



The
University
Of
Sheffield.

Analysis of biomimetic polymer brushes by XPS and optical spectroscopy

Abdullah A Sari

A thesis submitted in partial fulfilment of the requirements for the degree of
Doctor of Philosophy

The University of Sheffield

Faculty of Science

Department of Chemistry

Submission Date

31-January-2023

Declaration

I, Abdullah, confirm that this thesis is my own work. This thesis is submitted in fulfilment of the requirements of the degree of Doctor of Philosophy at the University of Sheffield. The work described in this thesis was undertaken between January 2019 and January 2023 under the supervision of Professor Graham Leggett. This work has not previously been presented for an award at this, or any other, university.

Signed:

Abdullah A Sari

January 2023

Department of Chemistry,

Dainton Building,

University of Sheffield,

Brook Hill,

Sheffield, UK.

S3 7HF

Acknowledgements

To start off, I would like to specially thank my supervisor Professor Graham J Leggett for giving me this great opportunity to be a part of his research group. Thanks for his patient, kind support and supervision during my research. Without his support, this thesis would not have been possible.

Secondly, I would like to thank all of Graham's group members. A special thank has to go to Anna Lishchuk for the great collaboration, help in the data modelling and providing plasmonic arrays of gold surfaces.

I would like also to specially thank Deborah Hammond and Jabra Alkorbi for their collaboration in collecting and analysing XPS depth profiling data for my samples.

I gratefully acknowledge the funding received towards my PhD from Umm Al-Qura University (UQU), Makkah Almokarramah, Saudi Arabia.

I would like to thank my father (1941-1993), My mother, my wife, and my son for their patience. I would not have been able to do this without their kind wishes.

Abbreviation

AFM	Atomic Force Microscopy
AINPs	Aluminum nanoparticles
APTES	3 – aminopropyltriethoxysilane
ATRP	Atom Transfer Radical polymerisation
AuNPs	gold nanoparticles
BE	binding energy
BIBB	2-bromoisobutyryl bromide
BIBUDT	Bromoisobutyrylundecanethiolate
CAG	Contact Angle Goniometer
Chl a	<i>Chlorophyll a</i>
Chl b	<i>Chlorophyll b</i>
CMPTS	4-(chloromethyl) phenyltrichlorosilane
CTAB	Cetyltrimethylammonium bromide
Cy3-NHS ester	Cyanine3 NHS ester
DCM	Dichloromethane
DMA	(2-dimethylamino)ethyl methacrylate)
DMF	Dimethylformamide
DTBU	bis[2-(2bromoisobutyryloxy)undecyl]disulfide
ESCA	Electron Spectroscopy for Chemical Analysis
GC-MS	Gas chromatography mass spectrometry
HMTETA	1,1,4,7,10,10-hexamethyltriethylenetetramine
IL	Interferometric lithography
INR	Iodinated Nile Red
KE	Kinetic energy
LCST	Lower critical solution temperature

LH1 and LH2	Light harvesting complexes 1 and 2
LSPR	Localised Surface Plasmon Resonance
MEEE	2,2-mercaptoethoxyethoxyethanol
MES	2- mercaptoethanesulfonate
MMA	Methylmethacrylate
MPS	Methacryloxypropyltrimethoxysilane
MS	Mass Spectrometry
NPPOC	N-[2-(2-nitrophenyl)propan-1-oxycarbonyl]
NR	Nile Red
OLEDs	Organic light emitting diodes
OSE	Organic Solvent Extraction
P2VP	Poly(2-vinylpyridine)
P2VP	Poly(2-vinylpyridine)
PCysMA	Poly(cysteine methacrylate)
PDDA	Poly(diallyldimethylammonium) chloride
PDEM	Poly(2-diethylamino)ethyl methacrylate)
PDMA	Poly(2-dimethylamino)ethyl methacrylate)
PDPA	Poly(2-dipropylamino)ethyl methacrylate)
PMDETA	N,N,N',N'',N''-Pentamethyldiethylenetriamine
PNIPAM	Poly(N-isopropylacrylamide)
POEGMEMA	Poly (oligo ethylene glycol) methyl ether methacrylate
POEGMEMA	Poly(oligo ethylene glycol) methyl ether methacrylate
PPE	Poly(p-phenyleneethynylene)
PS	Polystyrene
PTBAEMA	Poly(2-(tert-butylamino)ethyl methacrylate)
q-PDMA	Quaternised poly(2-dimethylamino)ethylmethacrylate)

RARF	Reversible Addition-fragmentation Chain Transfer
RDRP	Reversible-deactivation radical polymerization
RMS	Root mean square
R-X	Alkyl halide
SE	Spectroscopic Ellipsometer
SFE	Supercritical Fluid Extraction
SFM	Scanning Force Microscopy
SLBs	Supported lipid bilayers
SPM	Scanning probe microscopy
THF	Tetrahydrofuran
THPC	Tetrakis (hydroxymethyl) phosphonium chloride
TMAT	N,N,N-trimethylammoniumethanethiol
TOAB	Tetraoctylammonium bromide
UV-VIS	Ultraviolet and visible spectroscopy
XPS	X-ray photoelectron microscopy
<i>ZnChla</i>	Zinc phytylchlorophyllide a

Table of Contents

Acknowledgements	III
Abbreviation	IV
Table of Contents	VII
List of Figures	XII
List of Tables	XX
ABSTRACT	1
1 CHAPTER 1: INTRODUCTION	3
1.1 General introduction	3
1.2 Surface plasmons	5
1.2.1 Theoretical basis of LSPR.....	7
1.2.2 SPR importance	10
<i>Modelling of plasmon-exciton coupled system.</i>	17
1.3 Nanoparticles.....	21
1.3.1 Gold nanoparticles.....	21
1.3.2 Aluminium nanoparticles.....	38
1.4 Polymer brushes	45
1.4.1 <i>Grafting-to</i> and <i>Grafting-from</i>	45
1.4.2 ATRP Polymerisation	47
1.4.3 Properties of polymer brushes.....	55
1.4.4 Poly(2-(dimethylamino)ethyl methacrylate)	58
1.5 Dye-polymer complexes	61
1.6 <i>Chlorophyll</i>	64
1.6.1 <i>Chlorophyll</i> chemical structure.....	64
1.6.2 <i>Chlorophyll a</i> and <i>chlorophyll b</i>	64
1.6.3 <i>Chlorophyll</i> extraction and purification.....	66
1.6.4 <i>Chlorophyll a</i> and its derivatives.....	67
1.6.5 Central metal replacement	69
1.7 Nile Red.....	70
2 CHAPTER 2: AIMS AND OBJECTIVES:	72
3 CHAPTER 3: EXPERIMENTAL	74
3.1 Materials.....	74
3.2 Cleaning of glassware and substrates.....	75

3.3	Sample handling	75
3.4	Synthesis.....	76
3.4.1	Growth of PDMA via ATRP	76
3.4.2	Growth of PDMA brushes via ATRP from gold nanostructure.....	77
3.4.3	Synthesis of quaternised PDMA.....	77
3.4.4	Extraction of <i>chlorophyll a</i> from spinach leaves	77
3.4.5	Synthesis of polycrystalline gold film	78
3.4.6	Synthesis of AuNPs.....	79
3.4.7	AINPs synthesis	79
3.4.8	Synthesis of 2-(10-iododecyl) Nile Red.....	80
3.5	Deposition methods of the materials on solid substrates	80
3.5.1	Self-assembled monolayers (SAMs)	80
3.5.2	Dip coating	82
3.5.3	Spin Coating	82
3.5.4	Drop- casting, simple deposition	83
3.6	Surface modification.....	84
3.6.1	Photolithography of BIBB-APTES films.....	84
3.6.2	IL fabrication of AuNPs nanostructure.....	84
3.6.3	Drop-casting of <i>Chla</i> and J-aggregates onto PDMA grafted Au arrays	85
3.6.4	Functionalisation of polycrystalline gold film or Au nanoarrays with DTBU.....	85
3.6.5	Immobilization of AuNPs onto APTES-functionalised solid substrate.....	85
3.6.6	Attachment of <i>ZnChla</i> to PDMA brushes and q-PDMA	86
3.6.7	Incorporation of AuNPs into brush films	86
3.6.8	Incorporation of AINPs into brush films	86
3.6.9	Attachment of <i>ZnChla</i> to AuNPs-functionalised PDMA system.....	87
3.6.10	Attachment of <i>ZnChla</i> to AINPs-functionalised PDMA system.....	87
3.6.11	Attachment of INR to PDMA brushes	87
3.6.12	Spin-coating of <i>Chla</i> PDMA grafted from gold nanostructure arrays.....	88
3.6.13	Concentration-dependence of plasmon-exciton coupling	88
3.7	Analytical techniques.....	89
3.7.1	Atomic Force Microscopy AFM.....	89
3.7.2	Contact angle (CA) measurements:.....	91
3.7.3	Spectroscopic Ellipsometry (SE):	93
3.7.4	Total internal reflection ellipsometry TIRE	96
3.7.5	X-ray photoelectron microscopy (XPS)	101
3.7.6	UV-visible spectroscopy (UV-vis).....	104
3.7.7	Mass Spectrometry (MS)	106

3.7.8	Nuclear magnetic resonance (NMR)	106
3.7.9	Modelling of strong plasmon-exciton coupling	108
4	CHAPTER 4: PLEXCITONIC COMPLEXES: SYNTHESIS	112
4.1	Introduction	112
4.2	Experimental.....	114
4.2.1	Materials.....	114
4.2.2	Samples cleaning and handling.....	114
4.2.3	Synthesis of BIBB-APTES films	115
4.2.4	Photolithography	115
4.2.5	Growth of PDMA via ATRP	115
4.2.6	Synthesis of quaternised PDMA (q-PDMA).....	116
4.2.7	Extraction and derivatization of <i>chlorophyll a</i>	116
4.2.8	Attachment of <i>ZnChla</i> to PDMA brushes and q-PDMA.....	117
4.2.9	Surface analysis.....	117
4.3	Results and discussion	119
4.3.1	Formation and characterisation of initiator-functionalised surfaces.....	119
4.3.2	Kinetics of growth of PDMA brushes from initiator	123
4.3.3	Addition of <i>chlorophyll</i> to brush structures.....	134
4.3.4	Adsorption isotherm for <i>ZnChla</i> on PDMA.....	140
4.3.5	Quaternisation of PDMA brushes and Chl attachment to q-PDMA - regulation of binding. 147	
4.3.6	XPS Depth Profiling of PDMA quaternised with 1-iodooctadecane and PDMA reacted with <i>chlorophyll</i>	156
4.4	Conclusion	172
5	CHAPTER 5: PLEXCITONIC COMPLEXES: PLASMONICS	173
5.1	Introduction	173
5.2	Materials and methods.....	175
5.2.1	Materials.....	175
5.2.2	Sample cleaning and handling.....	175
5.2.3	Formation of BIBB-APTES films.....	175
5.2.4	Preparation of polycrystalline gold film.....	175
5.2.5	Interferometric lithography fabrication of gold nanostructure arrays.....	176
5.2.6	Functionalisation of polycrystalline gold thin films and plasmonic arrays of gold nanostructures using DTBU	176
5.2.7	Growth of PDMA via ATRP brominated surfaces	177
5.2.8	Extraction and derivatization of <i>chlorophyll a</i>	177
5.2.9	J-aggregates solution preparation.....	178

5.2.10	Drop-casting of Chl and J-aggregates onto gold nanostructure arrays.....	178
5.2.11	Spin coating of Chl and J-aggregates onto gold nanostructure arrays	178
5.2.12	Synthesis of 2-(10-iododecyl) Nile Red.....	178
5.2.13	Attachment of INR to PDMA brushes	179
5.2.14	Surface analysis.....	179
5.3	Results and discussion	181
5.3.1	Surface analysis of clean polycrystalline gold films.....	181
5.3.2	Surface analysis of BIBUDT-modified polycrystalline gold films	182
5.3.3	Surface analysis of PDMA-functionalised polycrystalline gold films	184
5.3.4	Morphology of Plasmonic arrays	185
5.3.5	J-aggregates-based plasmonic complexes	189
5.3.6	<i>ZnChla</i> -based plexcitonic complexes	191
5.3.7	Iodinated Nile Red (INR).....	200
5.4	Conclusion	214
6	CHAPTER 6: GOLD NANOPARTICLE FILMS.....	215
6.1	Introduction	215
6.2	Materials and methods.....	217
6.2.1	Materials.....	217
6.2.2	Samples cleaning and handling.....	217
6.2.3	Synthesis of BIBB-APTES films	218
6.2.4	Growth of PDMA via ATRP	218
6.2.5	Extraction and derivatization of <i>chlorophyll a</i>	218
6.2.6	Synthesis of AuNPs.....	218
6.2.7	Immobilization of AuNPs onto APTES-functionalised solid substrate	219
6.2.8	Incorporation of AuNPs into brush films	219
6.2.9	Attachment of <i>ZnChla</i> to PDMA-AuNPs system.....	219
6.2.10	Surface analysis.....	219
6.3	Results and discussion	221
6.3.1	Synthesis and characterisation of AuNPs.....	221
6.3.2	Incorporation of AuNPs into PDMA brushes	224
6.3.3	Attachment of <i>chlorophyll</i> to AuNPs-PDMA structure	231
6.4	Conclusion	239
7	CHAPTER 7: ALUMINIUM NANOPARTICLE FILMS	240
7.1	Introduction	240
7.2	Materials and methods.....	242
7.2.1	Materials.....	242

7.2.2	Samples cleaning and handling.....	242
7.2.3	Synthesis of BIBB-APTES films	242
7.2.4	Growth of PDMA via ATRP	242
7.2.5	Synthesis of quaternised PDMA (q-PDMA)	243
7.2.6	Extraction and derivatization of <i>chlorophyll a</i>	243
7.2.7	AINPs synthesis	243
7.2.8	Incorporation of AINPs into brush films	244
7.2.9	Attachment of <i>ZnChla</i> to PDMA-AINPs system	244
7.2.10	Surface analysis.....	244
7.3	Results and discussion	246
7.3.1	Incorporation of AINPs into PDMA brushes.....	249
7.4	Conclusion	258
8	CHAPTER 8: CONCLUSION AND FUTURE WORK	259
8.1	CONCLUSION	259
8.2	FUTURE WORK	262
9	REFERENCES	263

List of Figures

Figure 1-1: Schematic representation of the mechanisms of LSPR and propagated SPR.	6
Figure 1-2: Schematic description of the motion of electronic cloud around the particle under the effect of the electromagnetic field.	8
Figure 1-3: Optical properties of individual particle compared to a complex group of particles. ^[12]	9
Figure 1-4: Formation of plexcitonic states based on strong plasmon-exciton coupling.	11
Figure 1-5: Extinction spectra of LH2 (green), and AuNPs before (blue), and after the attachment of LH2 (red). ^[32]	13
Figure 1-6: Extinction spectra of 1 and 2 chlorin maquettes, where the more coupling strength was achieved by 2-chlorin Marquette. ^[25]	14
Figure 1-7: (a) extinction spectra of gold-PCysMA-Chla complexes in different temperature, (b) extinction spectra of gold-PCysMA-Chla complexes in different media. ^[33]	15
Figure 1-8: Representative diagram of Rabi splitting for the two coupling modes in both strong coupling (solid lines), and weak coupling (dashed lines).	18
Figure 1-9: Extinction spectra of plasmonic nano arrays coupled to LH2 with significant decrease of the fractional coverage. The coloured spectra represent the experimental data and the black lines represent the model data. ^[32]	20
Figure 1-10: Examples of AuNPs that have been found in products produced by humans. ^[20]	22
Figure 1-11: Illustration diagram of the difference between top-down and bottom-up approaches.	23
Figure 1-12: Schematic illustration of chemical reduction of gold salt with sodium citrate and sodium borohydride.	26
Figure 1-13: IL fabrication of Au nanostructure: (Top) experimental set-up. (Middle) single exposure. (Down) double exposure.	29
Figure 1-14: The effect of the particle size and shape on the shape and position of the plasmon band. ^[20]	31
Figure 1-15: (a) Colour of AuNPs solutions at different pH, and (b) protein-coated AuNPs at pH 4.0, 5.0, 5.5, 6.2, 6.7, 7.2, 8.3, 9.2, and 10.1, from left to right. ^[62]	35
Figure 1-16: Diagram showing the process of external and in situ addition of NPs to the polymer brush.	36
Figure 1-17: AFM images (A) PDMA brushes, and (B) AuNPs attached to PDMA brushes. ^[71]	38

Figure 1-18: Schematic of the formation of native oxide layer on aluminium nanoparticle (Top), and thin film of Al deposited on solid substrate (down).....	40
Figure 1-19: Schematic representation of different strategies of grafting polymer chains to a solid substrate. (a) Grafting-from, and (b) Grafting-to.	47
Figure 1-20: Most common examples of ATRP ligand; (left) PMDETA and (right) HMTETA.	50
Figure 1-21: ATRP mechanism. ^[130]	53
Figure 1-22: Schematic representation of different conformations of surface-tethered polymer: (a) polymer brush or extend polymer. (b) mashroom-like polymer. (c) pancake-like polymer.	57
Figure 1-23: Quaternization of PDMA with alkyl halide. ^[165]	59
Figure 1-24: Attachment of dye molecules to the polymer: (a) direct attachment. (b) polymerisation of dye molecules as a monomer. (c) the use of dye molecules as initiator. ...	63
Figure 1-25: (a) Typical chlorophyll structure; chlorophyll a (left) and chlorophyll b (right). (b) Representation of the optical transition of chlorins in chlorophyll.....	65
Figure 1-26: Representation of the most common conversion of chlorophyll a to its common derivatives Chlorophyllide a, pheophytin a, Pheophorbide a, and ZnChla derivative.....	68
Figure 1-27: Chemical structure of Nile Red and Nile blue.	70
Figure 3-1: illustration of sample handling.	75
Figure 3-2: Schematic illustration of the formation of SAMs.	81
Figure 3-3: Schematic illustration of dip coating process.	82
Figure 3-4: Schematic illustration of spin coating.....	83
Figure 3-5: Schematic illustration of simple deposition.	83
Figure 3-6: Schematic illustration of boil deposition.....	84
Figure 3-7: Schematic diagram of the effect of probe quality on AFM images where non-sharp tip can cause spatial obstruction and reflect fake images. ^[210]	90
Figure 3-8: Diagram of contact angle parameters and different liquids drops with different contact angles behaviour on solid surface. ^[212]	92
Figure 3-9: Schematic diagram illustrates the structure and significant component of ellipsometer.	94
Figure 3-10: Schematic diagram showing the setup of VASE technique.	96
Figure 3-11: Schematic diagram showing the setup of TIRE technique.	98
Table 3-1: The model used for spectroscopic ellipsometry data fitting of PDMA grown on continuous gold film and derivatized with chlorophyll.	99
Table 3-2: The model used for SE data fitting of PDMA grown on glass substrate, embedded with AuNPs and derivatised with chlorophyll.....	101

Figure 3-12: diagram showing the principle of XPS.	102
Figure 4-1: Schematic illustration of BIBB-APTES formation on a solid substrate.	119
Figure 4-2: XPS high resolution spectra of APTES and BIBB-APTES films: (a) C 1s spectrum of APTES. (b) N 1s spectrum of APTES. (c) C 1s spectrum of BIBB-APTES. (d) Br 3d spectrum of BIBB-APTES film.	120
Table 4-1: Measured contact angle and film thickness as a function of the change of surface chemistry.	121
Figure 4-3: Contact angle of BIBB-APTES films measured at (a) different concentrations of BIBB and (b) different immobilisation times.	122
Figure 4-4: Schematic of ATRP synthesis of PDMA brushes.	123
Figure 4-5: Growth profile of PDMA brushes: dry thickness as a function of polymerisation time.	124
Figure 4-6: XPS high resolution spectra of PDMA brushes: (a) C 1s spectrum. (b) N 1s spectrum. (c) O 1s spectrum. (d) Br 3d spectrum.	125
Figure 4-7: XPS Si 2p spectra of PDMA brushes grown for different polymerisation time; 5, 15, 60 min from top to bottom.	126
Figure 4-8: schematic illustration of debromination process of BIBB-APTES layers to create micropatterned PDMA brushes.	127
Figure 4-9: AFM contact mode images of micropatterned BIBB-APTESA film: (a) AFM height image with its cross section. (b) AFM friction image with its cross section.	129
Figure 4-10: (Blue points) Percentage of Br atoms of UV-modified BIBB-APTES layer at different exposure doses ranging from 0 – 6 J cm ⁻² across the whole surface. (Black points) Contact angle of UV-modified BIBB-APTES layer at different exposure doses ranging from 0 – 6 J cm ⁻² across the whole surface.	130
Figure 4-11: AFM tapping mode images of PDMA brushes grown on micropatterned BIBB-APTESA film: (a) AFM height image with its cross section. (b) AFM phase image with its cross section.	131
Figure 4-12: Thickness difference between exposed and non-exposed areas of PDMA brushes grown on micropatterned BIBB-APTES initiators measured by AFM tapping mode.	132
Figure 4-14: Schematic illustration of extraction and derivatization of ZnChla, R = phetyl group.	135
Figure 4-16: Schematic illustration of chlorophyll binding to amino group of PDMA brushes.	137
Figure 4-17: Absorption spectrum of ZnChla (Black) in DMF: water (1:3v/v) mixture. (Red) after immobilization on PDMA for 24 h for the same concentration.	138

Figure 4-18: XPS spectra of PDMA before and after addition of ZnChla: (a) and (b) Zn 2p spectra before and after the addition, respectively. (c) and (d) N 1s spectra before and after the addition, respectively. (e) and (f) C 1s spectra, before and after the addition, respectively.	139
Figure 4-19: Absorption spectra of a series concentrations ranging from 0.1 to 25 μM of ZnChla in a mixture of DMF: water in the ratio 1:3 v/v. (a) in solution, and (b) on PDMA brush polymerised for 15 min.....	141
Figure 4-20: calibration curve of ZnChla concentrations as a function of their maximum absorbance.	142
Figure 4-21: Concentrations of ZnChla within PDMA brushes as a function of the initial ZnChla concentration in solutions.	143
Figure 4-22: Fractional coverage of ZnChla within PDMA layers as a function of ZnChla concentration in the solution.	144
Figure 4-23: changes in number of excitons per polymer and fraction of monomers bound to ZnChla as functions of the initial concentrations of ZnChla in solution.	145
Figure 4-24: Variation in Zn 2p percentage on the surface as a function of chlorophyll concentration.	146
Figure 4-25: Quaternisation of DPMA with 1-iodooctadecane.	148
Figure 4-26: XPS N 1s high resolution spectra of (a) normal PDMA brush compared to q-PDMA with quaternization degree of (b) 16 %. (c) 65 %. (d) 92 %.....	149
Figure 4-27: Degree of quaternization (Red points) and measured contact angle (blue circles) as functions of 1-iodooctadecane concentration.....	150
Figure 4-28: XPS C 1s high resolution spectra of (a) normal PDMA brush compared to q-PDMA with quaternization degree of (b) 16 %. (c) 65 %. (d) 92 %.....	151
Figure 4-29: Growing iodine3d XPS spectra as a function of PDMA quarterisation degree.	152
Figure 4-30: Zn 2p and N 1s XPS spectra after attachment of ZnChla to PDMA before (a and b) and after quaternization with quaternization degree of 8% (c and d), and quaternization degree of 78% (e and f), respectively.	153
Figure 4-31: Absorption spectra of ZnChla after immobilization on to normal PDMA brush and q-PDMA with quaternization degree of 11%, 65%, 79% and 89%.	155
Figure 4-32: (a) N 1s and (b) C 1s XPS high resolution scans taken from depth profile at time 0, i.e., before any etching of pure PDMA. (c) N 1s and (d) C 1s XPS high resolution scans taken from depth profile at time 0, i.e., before any etching of q-PDMA.	157
Figure 4-33: XPS depth profile through the normal PDMA sample	158

Figure 4-34: High resolution scans of N 1s (left) and C 1s (right) taken from PDMA depth profile	159
Figure 4-35: (a) XPS depth profile through q-PDMA. (b) Scale limit to show I and N more clearly.	161
Figure 4-36: Curve fitted high resolution N 1s and C 1s spectra collected for depth profiling of q-PDMA.	163
Figure 4-37: (a) Surface concentration (%) of two nitrogen environments detected. (b) Surface concentrations (%) of two nitrogen environments detected shown on logarithmic scale.	165
Figure 4-38: Expected change in average composition as a function of quaternization (calculated).	166
Figure 4-39: XPS depth profile showing variation in elemental concentration as a function of number of clusters.	167
Figure 4-40: Selected high resolution N1s and C 1s spectra from ZnChla depth profile.....	169
Figure 4-41: Surface concentrations of two nitrogen environments as a function of number of clusters.	170
Figure 5-1: Schematic illustration of the growth of PDMA brushes onto brominated gold film and subsequent attachment of ZnChla.	174
Figure 5-2: XPS high resolution Au 4f spectrum collected from clean polycrystalline gold surface.....	181
Figure 5-3: XPS analysis of BIBUDT-modified Au surface. (a) schematic of BIBUDT-modified Au surface. (b) XPS high resolution S 2p spectrum. (c) XPS high resolution C 1s spectrum. (d) XPS high resolution Br 3d spectrum. (e) XPS high resolution Au 4f spectrum.	183
Figure 5-4: XPS analysis of PDMA grown from Au surface. (a) schematic of the growth of PDMA from Au surface. (b) XPS high resolution C 1s spectrum. (c) XPS high resolution N 1s spectrum.....	185
Figure 5-5: Tapping mode AFM images of typical plasmonic arrays of gold nanostructures (right, and cross section taken from this image (left)).....	186
Figure 5-6: (a) Typical extinction spectra of a number of samples of Au arrays. (b) Extinction spectra of typical plasmonic arrays of Au nanostructures measured at different angles of incidence.....	187
Figure 5-7: Typical extinction spectra of Au arrays before (black) and after (red) the growth of PDMA brushes (denoted by eV).	188
Figure 5-8: (a) Extinction spectra of Au arrays before (black) and after drop-casting J-aggregates measured at different incident angles. (b) Extinction spectra of Au arrays before	

(black) and after spin-coating J-aggregates measured at different incident angles. The sharp spectra observed at 585 nm in both (a) and (b) are extinction spectra of J-aggregates.	190
Figure 5-9: (a) Extinction spectra of Au arrays before (black) and after drop-casting ZnChla onto the surface of plasmonic arrays of AuNPs (green). (b) Extinction spectra of Au arrays before (black) and after spin-coating ZnChla onto the surface of PDMA grafted from plasmonic arrays of AuNPs (other spectra) measured at different incident angles.	192
Figure 5-10: Schematic of binding ZnChla to PDMA grown from Au surface.	193
Figure 5-11: Extinction spectra of clean Au arrays and PDMA-functionalised plasmonic arrays of AuNPs before and after the attachment of ZnChla.	196
Figure 5-12: Modelling of plasmon-exciton coupling in J-aggregates-based plexcitonic systems. Green spectrum is experimental data, and red is fitted data.	197
Figure 5-13: Modelling of plasmon-exciton coupling in ZnChla-based plexcitonic systems with different polymerisation times of PDMA; (a) 15 min and (b) 60 min. The black spectra are before the attachment of ZnChla and thick green spectra are collected experimentally after attachment of ZnChla. The short red lines represent the model data.	199
Figure 5-14: Synthesis of iodinated Nile Red via the reaction of hydroxylated Nile Red with 1, 10-diiododecane chains.	200
Figure 5-15: Extinction spectra of INR solutions with concentrations of 0.25, 0.5, 1, 2 and 4 mM from down to top.	201
Figure 5-16: Calibration curve for INR concentrations vs maximum absorbance.	202
Figure 5-17: Schematic of binding ZnChla to PDMA through quaternisation mechanism.	203
Figure 5-18: Extinction spectra of PDMA functionalised with different concentrations of INR.	204
Figure 5-19: Fractional coverage of INR onto PDMA brushes.	205
Figure 5-20: N 1s XPS spectra of INR-functionalised PDMA brushes with different INR concentrations. (a) 0.25 mM and (b) 8 mM.	206
Figure 5-21: Quaternisation degree of the amine groups of PDMA brushes with different concentrations of INR.	207
Figure 5-22: C 1s XPS spectra of INR-functionalised PDMA brushes with different INR concentrations. (a) 0.25 mM and (b) 2 mM (c) 8 mM.	208
Figure 5-23: I 3d XPS spectra of INR-functionalised PDMA brushes with different INR concentrations. (top) 2 mM and (down) 0.25 mM.	209
Figure 5-24: Iodine percentage on the surface of PDMA as a function of INR concentration.	210

Figure 5-25: Extinction spectra of INR spin-casted on the plasmonic arrays of gold nanostructures.	211
Figure 5-26: Extinction spectra of PDMA-initiated gold plasmonic arrays before and after attachment of INR.	212
Figure 5-27: Modelling of plasmon-exciton coupling in J-aggregates-based plexcitonic systems. Green spectrum is experimental data, and red is fitted data.	213
Figure 6-1: Schematic illustration of incorporation of AuNPs into PDMA and subsequent addition of ZnChla.	216
Figure 6-2: Extinction spectra of various concentrations of colloidal AuNPs prepared by chemical reduction. (Blue) concentrated as-prepared solution. (Black) diluted 1-1 solution in water. (Red) diluted 1-10 solution in water.	222
Figure 6-3: Extinction spectra of AuNPs adsorbed onto APTES-functionalised glass substrate acquired from three solutions with different concentrations (Blue) as-prepared solution. (Black) diluted 1-1 solution in water. (Red) diluted 1-10 solution in water.	223
Figure 6-4: AFM tapping mode images of AuNPs adsorbed onto APTES layer (a) height image (b) phase image, and their respective cross-section spectra (a1) and (b1).	224
Figure 6-5: illustration of electrostatic interaction between AuNPs and PDMA chains.	225
Figure 6-6: Extinction spectra of AuNPs adsorbed onto PDMA brushes from three solutions with different concentrations (Black) concentrated as-prepared solution 17 nM. (Blue) diluted 1-1 solution in water. (Red) diluted 1-10 solution in water.	226
Figure 6-7: Extinction spectra of AuNPs-embedded PDMA brushes with different thicknesses of the brush (Black) 15 nm. (Blue) 20 nm. (Red) 35 nm.	227
Figure 6-8: Schematic illustration of AuNPs embedded into PDMA brushes with different thicknesses ranging from 15 30 nm.	228
Figure 6-9: The multilayer-box-model used for ellipsometry data fitting of AuNPs-functionalised PDMA.	229
Figure 6-10: Spectroscopic ellipsometry Psi and Delta spectra acquired for AuNPs-functionalised PDMA brush.	230
Figure 6-11: (a) PDMA brush grown from glass substrate via ATRP. (b) AuNPs-embedded PDMA brush with immobilisation time of 4 h. (c) AuNPs-embedded PDMA brush with immobilisation time of 24 h.	231
Figure 6-12: Schematic diagram showing the proposed structure of plasmon-exciton coupling in AuNPs-ZnChla supported by PDMA brushes.	232

Figure 6-13: Extinction spectra of AuNPs-embedded PDMA brushes before the attachment of ZnChla (blue), and after the attachment of ZnChla with concentration of 100 μ M (red) and concentration of 50 μ M (green).....	233
Figure 6-14: Spectroscopic ellipsometry amplitude (Psi) spectra collected from AuNPs-functionalised PDMA brushes at variable incident angles ranging from 57 to 69, before the attachment of ZnChla (a) and after the attachment of ZnChla (b).....	235
Figure 6-15: Zn 2p percentage measured by XPS analysis of AuNPs-embedded PDMA brushes after the attachment of ZnChla with different concentrations ranging from 0 μ M to 5.9 μ M. The inset graph is Zn 2p spectrum collected from AuNPs-embedded PDMA brushes after the attachment of ZnChla with concentration of 100 μ M.....	236
Figure 6-16: Multilayer-box-model used for ellipsometry data fitting of AuNPs-functionalised PDMA after the addition of ZnChla.	237
Figure 6-17: AFM tapping mode images of AuNPs-embedded PDMA brushes after the attachment of ZnChla. (a) Height image and (b) Phase image.	238
Figure 7-1: (a) proposed structure of single AINP prepared by alane decomposition and coated by polyether molecules. (b) Extinction spectra of AINPs in wate. The black spectrum was aquired for a concentrated solution and The red spectrum for diluted solution.....	247
Figure 7-2: Refractive index sensitivity of the produced AINPs in different solvents.....	248
Figure 7-3: (a) XPS Br 3d Spectrum of AINPs incorporated into PDMA brushes showing Al peak at 74.5 eV. (b) AINPs percentage into PDMA brushes (red bar) compared to the percentage of Al of clean glass substrate (black bar).	250
Figure 7-4: AFM tapping mode images of AINPs incorporated into PDMA brushes. (a) height image, and (b) phase image.	251
Figure 7-5: Absorption spectrum of AINPs-coated PDMA brush, and inset photo of AINPs adsorbed onto PDMA brush.....	252
Figure 7-6: Contact angle of PDMA brushes AINP functionalised with AINPs with percentages ranging from 0 to 100%.....	253
Figure 7-7: Absorption spectrum of ZnChla-functionalised AINPs-coated PDMA brush.	254
Figure 7-8: Extinction spectra of AINPs synthesised via sono-solvo chemistry (a) after 1 day inocpation in ethanol/ ethylene glycol mixture. (b) after 14 days inocpation in ethanol/ ethylene glycol mixture.	255
Figure 7-9: Absorption spectrum of AINPs synthesised via sono-solvo chemistry and imbedded into PDMA brush.....	256

List of Tables

Table 3-1: The model used for spectroscopic ellipsometry data fitting of PDMA grown on continuous gold film and derivatized with chlorophyll.	99
Table 3-2: The model used for SE data fitting of PDMA grown on glass substrate, embedded with AuNPs and derivatised with chlorophyll.....	101
Table 4-1: Measured contact angle and film thickness as a function of the change of surface chemistry.	121

ABSTRACT

A grand challenge for the past two decades has been to discover how to achieve efficient long-range transport of excitation in molecular photonic materials. Excitons (electron-hole pairs) are transported via incoherent hopping processes, with the effect that recombination rates are high and exciton diffusion lengths are short. The goal of this PhD has been to explore a new approach to the design of molecular photonic materials that combines biologically-inspired design with strong light-matter coupling. In strong light-matter coupling, a confined optical mode such as a localised surface plasmon resonance (LSPR) is hybridised with molecular excitons to yield new states that mix the properties of light and matter. Recent work demonstrated that light-harvesting complexes from plants and photosynthetic bacteria are coupled strongly to LSPRs associated with gold nanostructure arrays, yielding large coupling energies and coherent, ultra-fast energy transfer. However, proteins are not suitable for applications in electronic and optical devices. Thus, the goal of this thesis is to explore the construction of biomimetic plexcitonic antenna complexes, in which a synthetic polymer scaffold is used to organise pigment molecules within the near field associated with a metal nanoparticle.

Chlorophyll a was isolated from spinach and the central magnesium ion replaced by Zn^{2+} to stabilise the molecule (*ZnChla*). The binding of *ZnChla* to poly(dimethyl aminoethyl methacrylate) (PDMA) was studied by X-ray photoelectron spectroscopy and optical spectroscopy. Concentrations of *ZnChla* of ~ 1 M were obtained, somewhat in excess of the concentrations found in plant light-harvesting complexes (~ 0.6 M). *ZnChla* is thought to coordinate to the PDMA scaffolds via the formation of coordination bonds from the tertiary nitrogens to the central metal ion. When these structures were formed on gold nanostructure arrays, splitting of the plasmon band was observed, consistent with the expected plasmon-exciton coupling. The coupling strength was found to be correlated with the concentration of *ZnChla* in the film, consistent with the expected behaviour if strong coupling occurred. However,

the largest coupling energy achieved was 0.16 eV, short of the strong coupling limit and suggesting that further optimisation of the system is required.

Nile Red (NR) was derivatised to introduce an iodo-alkane linker for quaternisation to the PDMA scaffold. Binding of the dye to the scaffolds was characterised by XPS and UV-Vis measurements. Extinction spectra of gold nanostructure arrays displayed dramatic changes after binding of iodinated Nile Red (INR), consistent with strong plasmon-exciton coupling. However, time did not permit a detailed investigation of the correlation between the coupling strength and the concentration of dye in the film.

As an alternative approach, scaffolds were grown from glass surfaces and metal nanoparticles were subsequently embedded in the polymer layer, after which *ZnChla* was attached to the scaffold. For gold nanoparticles (AuNPs), beside red shift of the LSPR of AuNPs, a new feature is observed at 2.48 eV, which is probably due to weak interaction resulted from possible interference between the LSPR of AuNPs and the vibrational transitions of *ZnChla*. For aluminium nanoparticles (AlNPs), obtaining useful optical properties of AlNPs that can be used to create plexcitonic complexes using this route is suppressed by the fast oxidation of AlNPs.

CHAPTER 1: INTRODUCTION

1.1 General introduction

Absorption of light by molecular materials leads to the formation of electron hole pair, known as excitons, through the promotion of an electron from the highest occupied molecular orbital to the lowest unoccupied molecular orbital in molecular materials. The control of excitons is important in the new and emerging technologies. For example, organic light emitting diodes (OLEDs) are incredibly attractive in applications such as electronics because they can be produced from earth abundant materials in low energy process. One example of this application is the use of OLEDs in the displays of the modern mobile phones. However, molecular materials have very high dynamic disorder (the rapid and random movement of the constituent molecules inside their solid or condensed phase). Consequently, excitons are transported via an incoherent process. Excitons can only travel a short distance, ~ 10 nm before the electron and hole recombine. The short exciton diffusion lengths associated with molecular materials impose serious constraints on the design of devices. The aim of this thesis is to develop methods for the formation of biomimetic materials, inspired by structures found in photosynthesis, and to combine these with strong plasmon exciton coupling, in order to create new molecular materials that use coherent excitation transfer to achieve efficient long-range transport of excitons.

Metal nanoparticles have surface electrons that oscillate with characteristic frequencies (plasma frequencies) typically in the visible region of the electromagnetic spectrum. Therefore, when metallic nanoparticles are irradiated with visible light and the frequency of the incident light matches the oscillation frequency of the surface electrons, strong absorption can be observed. The study of surface plasmons, which is now known as 'plasmonics',^[1] has been rapidly developing since the early 1990s. This development coincided with the development of nanotechnology and nanoscience. A large part of the literature on plasmonics is focussed on metallic nanostructures containing gold or silver, which exhibit plasmon resonances in the

visible spectral range. AuNPs are relatively resistant to oxidation, while silver, on the other hand, is more susceptible to oxidation but exhibits more intense and narrower LSP resonances. The plasmonic properties of aluminium nanomaterials in the UV range have also begun to attract interest too. Under certain conditions, a plasmon mode and an ensemble of excitons may exchange energy faster than their decay rates. This allows the system to enter the strong coupling regime where new hybrid light-matter states (plexcitons) are generated.^[2]

The chemistry of plasmonic metal nanoparticles is a rapidly growing field due to their potential applications in biosensing, catalysis, optics and electronics. Plasmon bands, due to the resonant coupling of light to the plasma oscillations of metal surface electrons at an air-electric interference, are strong features in extinction spectra. For nanoparticles larger than 2 nm, strong plasmon bands are observed.^[3] Both scattering and absorption contribute to the plasmon band. Plasmon bands are also known as Mie resonances because of the work of Gustav Mie, who provided a classical explanation for the origin of these features in optical spectra.^[4]

The shape, intensity and the position of surface plasmon bands (SPB) of metal nanoparticles are dependent on the dielectric constant of the medium, the electronic interaction between NPs and the capping agents, monodispersity, shape, size, dielectric environment, and orientation of the particles. Thus, it is possible to tune LSPR during formation processes by adjusting these factors by lithography techniques or by chemical syntheses.^[3,5] Quantum effects are common with cluster smaller than 2 nm, and for these smaller particles surface plasmon bands are not observed. Although all metals can exhibit SPB, Au, Ag and Cu have strong and intense SPB and additionally easy to use to form nanoparticles.^[3] Specifically, gold and silver nanoparticles display a unique plasmon band in the visible range, however, these are shifted by nanometre-scale changes depending on their sizes and shapes.^[6,7] The plasmonic properties of Au and Ag have been well reviewed.^[8-10]

1.2 Surface plasmons

Surface plasmons can be excited through several ways. One of them is to use metal nanomaterials, where the plasmons confined to the surfaces of the particles.^[11] The system undergoes a state known as surface plasmon resonance when the plasma frequency matches that of the incident radiation.^[3]

Surface plasmons (SPs) are collective oscillations of the conductive electrons at a metal surface. Resonant coupling of electromagnetic radiation to plasma oscillations at a metal-dielectric interface leads to the creation of surface plasmon polariton (SPP).^[12] The dielectric represents the positive permittivity, while negative permittivity material is represented by the metal. This phenomenon can generate an electromagnetic wave outside and inside the plasmonic metal, and the charge oscillations can be either localised (LSPR) in case of very small particles, or delocalised (SPR) in the case of thin films. The plasmon oscillation of the free electrons can be treated as a mechanical oscillation resulting from an external electric field. In bulk materials, the oscillations can propagate and occur at the plasma frequency when the size is larger than the wavelength of the light; such excitations are merely termed as surface plasmons (SP).^[13] See **Figure 1-1 (Top)**. However, in case of metallic nanoparticles when the size of the particles is close to the wavelength of the incident light, the free electrons are confined and participate in the collective oscillations, so this type of oscillations is described as localised surface plasmons (LSP),^[13] see **Figure 1-1 (Down)**. The frequency of this oscillation depends on the composition, shape and size of the particles. The light is then absorbed and scattered by the particles. This phenomenon enables single nanoparticles to be observed easily by dark field microscopy.^[5] SPR occurs when the light at a resonance angle is absorbed by thin metal less than 200 nm, which cause the conduction electrons to resonate leading to reduce the reflectivity. So SPR is sensitive to the change in refractive index of the medium.^[12] LSPR is usually generated on small nanoparticles leading to generation of localised electromagnetic fields with shorter decay length. The most significant feature of this LSPR is

its sensitivity to molecular binding particularly for small biological molecules.^[12] Both LSPR and SPR are susceptible to the alteration in the dielectric environment.^[12,14] The resonant frequency of SPs can be adjusted by the composition, geometry, size of the material, and the separation distance of the structures of materials.^[12] The particle size plays important role to maintain the frequency of LSP at visible wavelengths for metal nanoparticles.^[13]

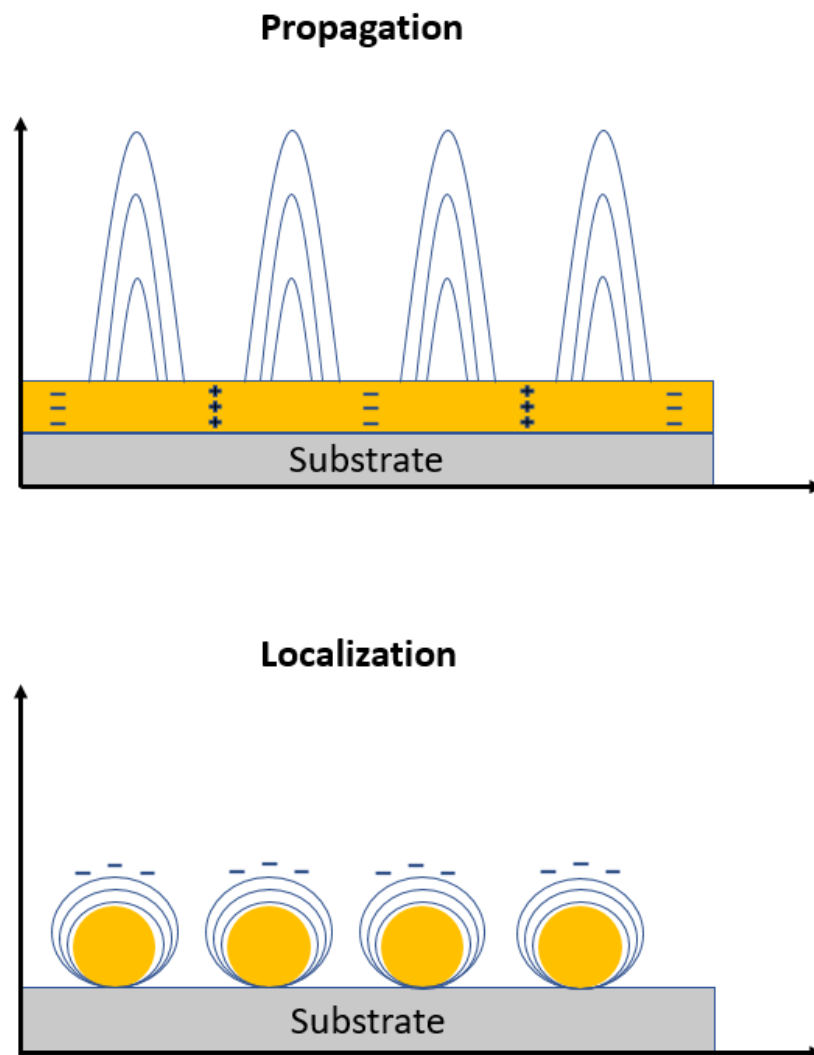


Figure 1-1: Schematic representation of the mechanisms of LSPR and propagated SPR.

Theoretically, LSPR can occur in any metal or alloys and semiconductors. Gold and silver are the most common metals which have been exploited in the study of LSPR. In contrast, aluminium has different surface chemistry, and its plasma frequency lies in the UV region of the electromagnetic spectra, where the light can be easily absorbed by some organic materials. In addition to this, Al has an advantageous refractive index sensitivity. In the case of copper, LSPR is strongly damped by the oxide layer that forms. The oxide layer can be removed by acetic acid to obtain a narrower linewidth.^[5] Plasmonic resonance are also exhibited by other materials, such as graphene due to the existence of conductive electrons.^[12]

1.2.1 Theoretical basis of LSPR

The resulting spectrum of light-matter interaction contains the fingerprints of the analyte describing its specific molecular details.^[13] Nanoparticles interact with incident light in a specific frequency domain, resulting in global scattering. The collective resonance of the nanoparticle's conduction electrons explains this macroscopic phenomenon. The dynamics of the electrons inside a metal are described by the Drude theory, where electrons are assumed to be independent and free. The motion of a cloud as a whole is then the total of the motions of individual electrons, resulting in a maximum coupling between them, with electrons acting in phase.^[4,15]

In nanoparticles, the goal is to determine the conditions that cause the electron cloud to resonate. The expression for the dielectric constant determined for the bulk is used for this purpose, and therefore the electron density in tiny particles (smaller than the wavelength of the incident light) is no longer uniform resulting in accumulating the charges at the edge of the particles, i.e., the electric field can cause displacement of the electron cloud leading to formation of surface charges. i.e. Negative charge where the electronic cloud is concentrated whereas positive charge where it is lacking,^[15] see **Figure 1-2**.

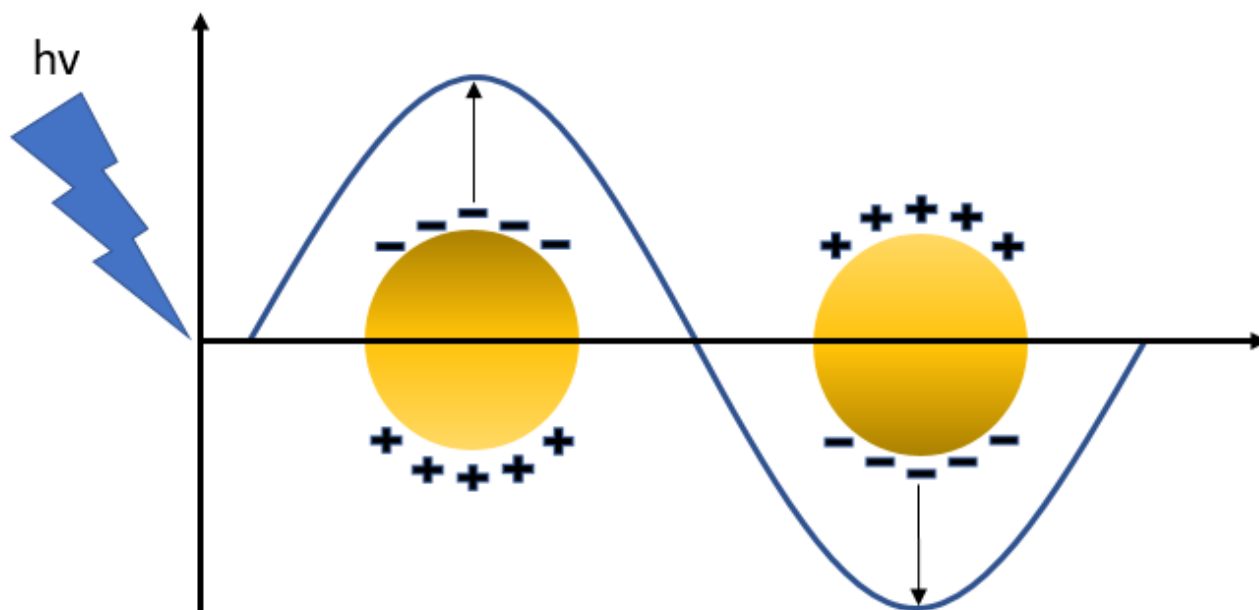


Figure 1-2: Schematic description of the motion of electronic cloud around the particle under the effect of the electromagnetic field.

Furthermore, because the NP size is small in comparison to the wavelength, it is reasonable to assume that all confined electrons in NP are subject to the same electric field at a specific time and that the electric field is independent of location. This hypothesis is referred to as the quasi-static approximation. Under the influence of the electric field, all the electrons oscillate collectively, resulting in plasmon polaritons in contrast to free plasmons in the bulk metal. These are analogous to confined gaseous plasmon oscillations; thus Shopper introduced the term plasmon.^[4] As a result of this dipolar charge redistribution, the electron cloud is subjected to a new force that is driven by a restoring force that conflict with the outer electric field. These considerations are only applicable when the particles are sufficiently apart to prevent their interaction. However, they are not applicable when the NPs are linked by oligomers, immobilised in a matrix, or self-organize.^[15]

Interaction of a group of NPs

Optical properties of individual particles can differ from those of a complex group of particles, because the presence of a group of particles close to each other leads to a strong plasmonic interaction, there can be a modification of the plasmon resonance frequencies.^[12] **Figure 1-3.** For example, in the case of single gold nanoparticle, the normal plasmon resonance is observed. However, the interaction between nearfields of the two neighbouring plasmonic particles can lead to coupling of the plasmon modes of metal nanoparticles at small separations. This coupling depends on the polarization of the light and appear in absorption spectra as shifts of wavelength.^[16,17] As interparticle distance decreases,^[12] the red shift increases.^[12]

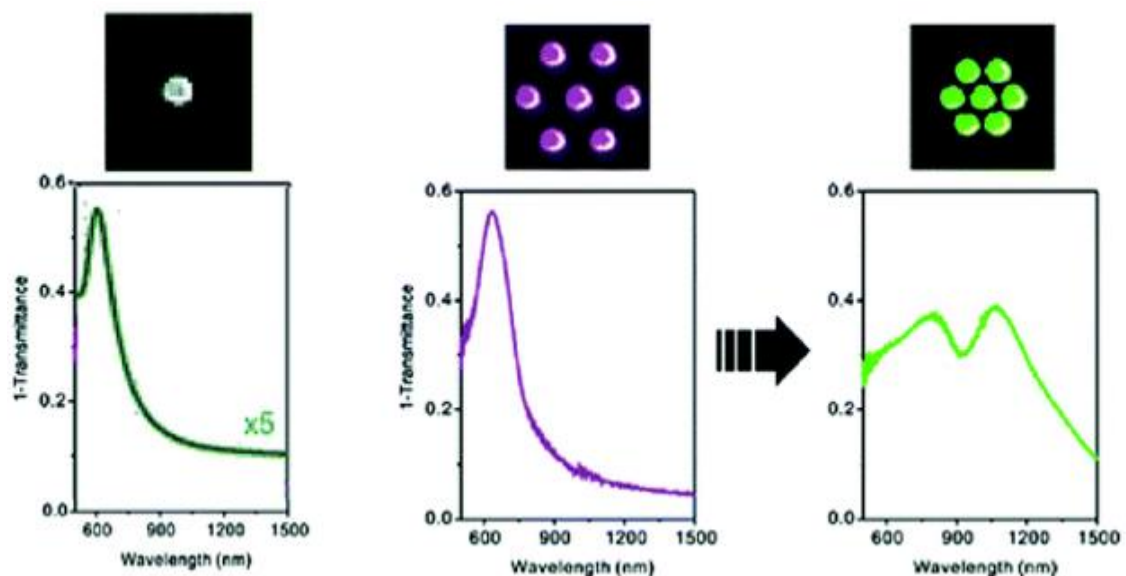


Figure 1-3: Optical properties of individual particle compared to a complex group of particles.^[12]

The coupling strengths of the coupled NPs depends strongly on numbers, spatial arrangements and interparticle distance of NPs. Thus, an enhanced utilization of NPs requires careful control over the structure and uniformity of NPs clusters.^[18] The physical mechanism of this coupling and Fano resonance (an asymmetric lineshape observed in spectroscopic

measurements, resulting from the interference between a discrete state and a continuum of states) are well explained in this review.^[12]

1.2.2 SPR importance

The interaction of the light with nanoparticle can change the optical properties of close molecules within the near field such as the natural emission rate.^[12,19] Thus, surface plasmon resonance (SPR) can be employed in order to detect environmental changes in a molecular system via measurement of change by interaction with light.^[20] For example, AuNPs can act as colourimetric sensors for triggering or detecting changes in the structure of the polymer such as non-ionic poly(N-isopropylacrylamide) (PNIPAM) and cationic poly-[2-(methacryloyloxy)ethyl] trimethylammonium chloride (PMETAC). The nature of the polymer and the AuNPs can control the detected properties.^[21] The environmental changes appear as a shift of the SPR band to a shorter (blue shift) or longer (red shift) wavelength depending on the refractive index of the medium.^[22] changes in both the distribution and the quantity of particles within a polymer system can result in variation of the optical properties.^[21] In addition, surface plasmons provide useful and unique properties due to the enhanced optical fields, that are confined spatially to an interface. This confinement is the result of the exponential decay of the electromagnetic fields and facilitates manipulating interface processes with high sensitivity.^[11] These characteristics make the plasmonic materials are widely applied in various fields such as biosensing, surface plasmon resonance microscopy, fluorescence spectroscopy, photovoltaics and surface-enhanced Raman spectroscopy, Recently, the plasmonics field has been one of the most active areas of research.^[11,23] This because plasmonic nanoparticles are effective and fundamental model of low-dimensional systems (materials that exhibit novel characteristics in comparison with bulk states by reducing their dimensions). Thus, plasmonics can be used to improve spectroscopic analysis by enhancing optical transitions of biological molecules where LSPR can join the properties of matter and light together.^[24] In addition, LSPR has been employed in several systems such as quantum dots, dye molecules and others^[25].

Also, noble plasmonic metals have been produced as biochemical sensors, and they have been used in subwavelength imaging and lithography.^[5]

Plexciton

In the strong coupling regime, the plasmon (metal) and the exciton (emitter) exchange the energy consistently faster than their respective decay rate, leading to the formation of new hybrid modes known as Plexcitons.^[11,26,27] These nanosystems can be obtained by the combination of plasmonic substrates such as nanoparticles or nanostructures with excitonic materials such as organic or inorganic dyes such as organic molecules or quantum dots, etc,^[28] as represented by **Figure 1-4**.

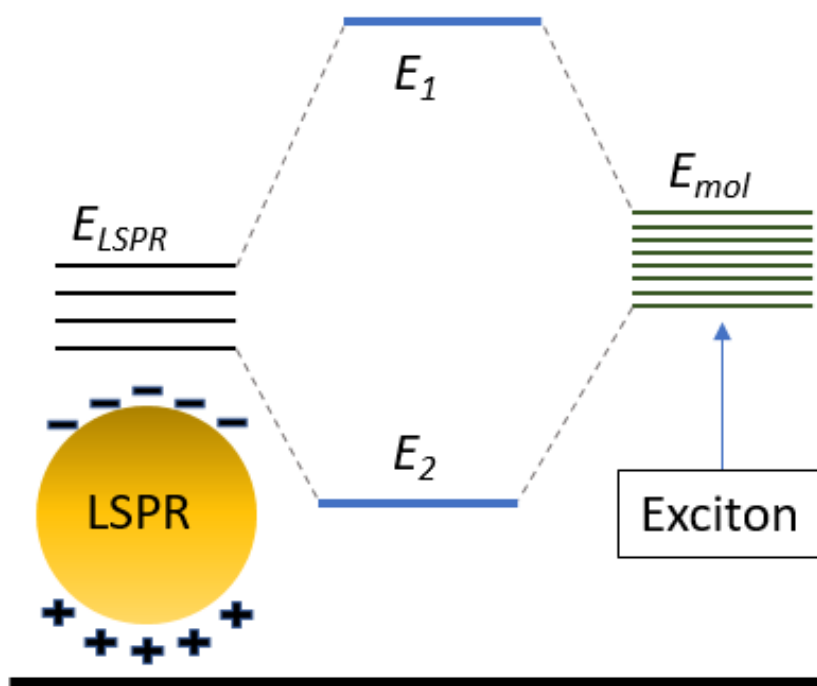


Figure 1-4: Formation of plexcitonic states based on strong plasmon-exciton coupling.

In strongly coupled systems, there is coherent energy exchange between the plasmonic and excitonic states. New eigenmodes are formed that are evidenced by the appearance of a

splitting in the absorption or transmission spectra.^[29–31] A comprehensive review of the literature on strong plasmon-exciton coupling was published by Torma *et al.*^[2], which also includes investigations of J-aggregates-based strong coupling and dye molecules-based plexcitonic systems during the period from 2004-2014.

In 2016, Tsargorodska *et al.*^[32] reported that the LSPR of Au nanostructures are split by the attachment of light harvesting complexes LH1 and LH2 from the purple bacteria. This splitting is attributed to strong coupling of the plasmon mode to excitons in the proteins. This coupling can lead to create new states that their energies are above and below LSPR energy. The strength of this coupling was found to be dependent on the electronic states in the LH complexes and the biomolecular coverage,^[32] see **Figure 1-5 – highlighted peaks**.

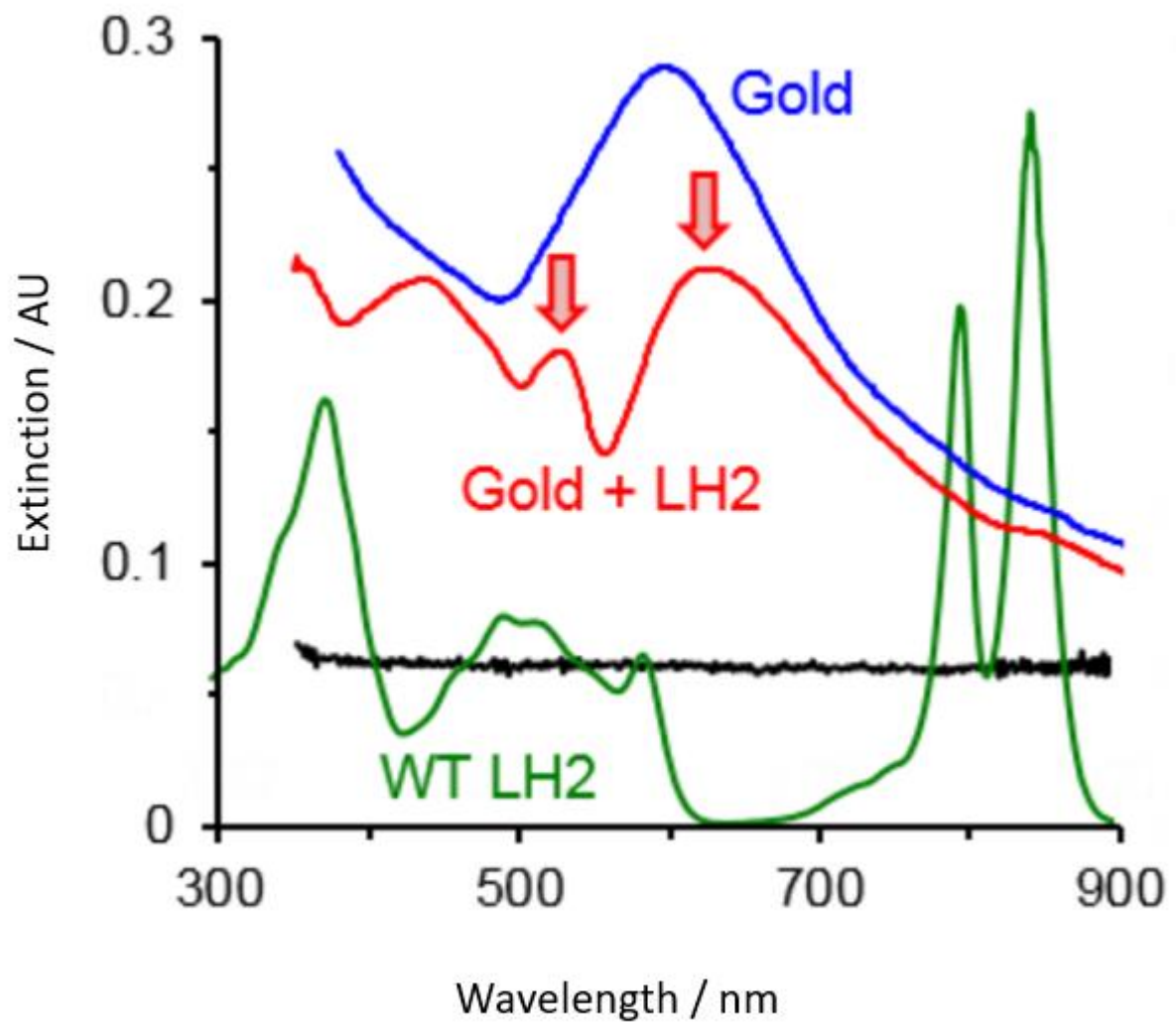


Figure 1-5: Extinction spectra of LH2 (green), and AuNPs before (blue), and after the attachment of LH2 (red).^[32]

In addition, strong plasmon-exciton coupling was achieved using artificial analogous *chlorophyll* in artificial protein structure,^[25] see **Figure 1-6**.

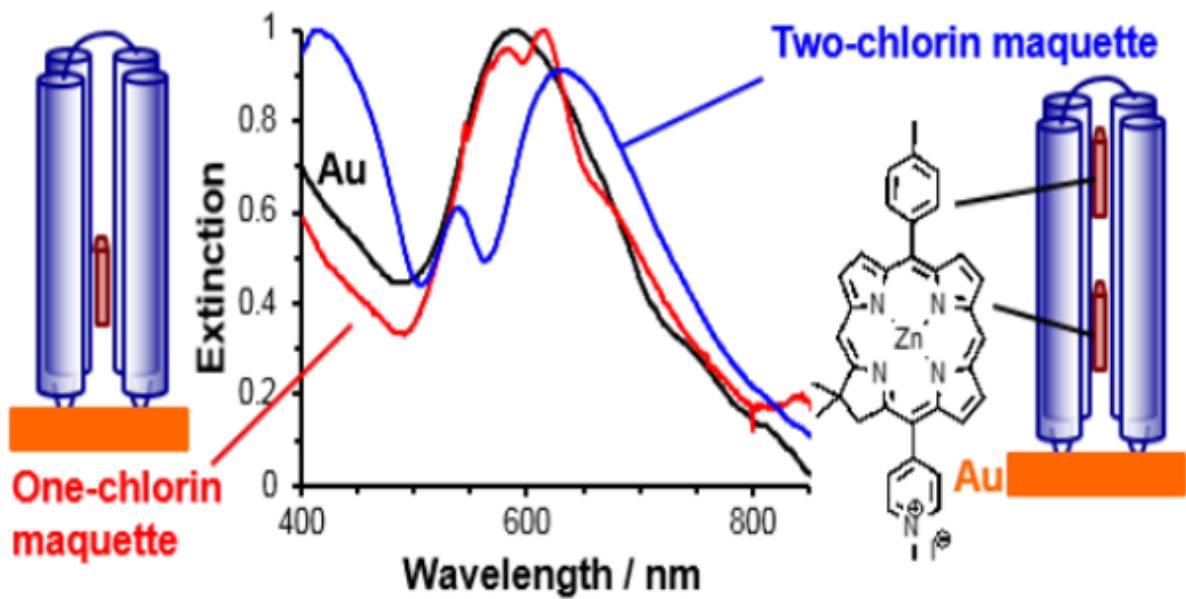


Figure 1-6: Extinction spectra of 1 and 2 chlorin maquettes, where the more coupling strength was achieved by 2-chlorin Maquette.^[25]

The protein acts as a scaffold to control the orientation of the dipole within the light field. By changing the protein structure, it was found that the energies of the coupled states could be manipulated. This opens up a new approach to the design of photonic materials, by using synthetic biology, and biologically-inspired design, to program the properties of coupled systems. However, proteins have fragile structure and are expensive to synthesise. Lishchuk *et al.* ^[33] designed pigment-polymer antenna complexes, in which the peptide scaffolds found in biological light harvesting complexes were replaced by surface-grafted polymers. They attached *chlorophyll* to these polymer scaffolds and were able to program the properties of the materials by controlling the grafting density, polymerisation time and *chlorophyll* coupling chemistry. Because the polymer scaffolds were stimulus-responsive, it was possible to achieve active control of strong plasmon-exciton coupling to regulate the concentration of excitons in the plasmon mode volume and hence to control the coupling strength,^[33] see **Figure 1-7**.

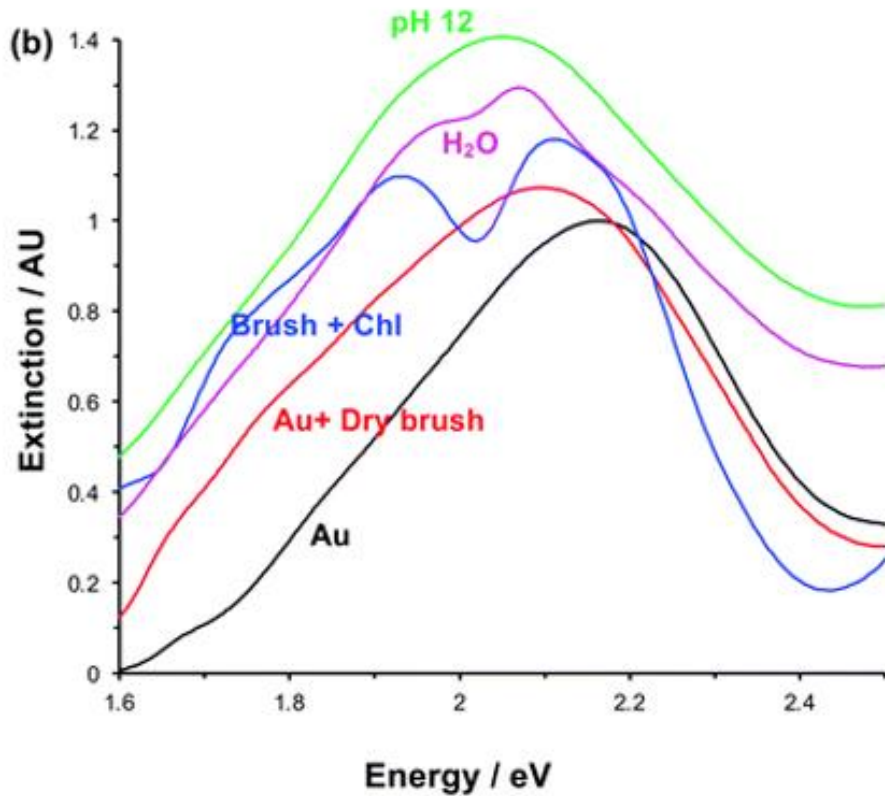
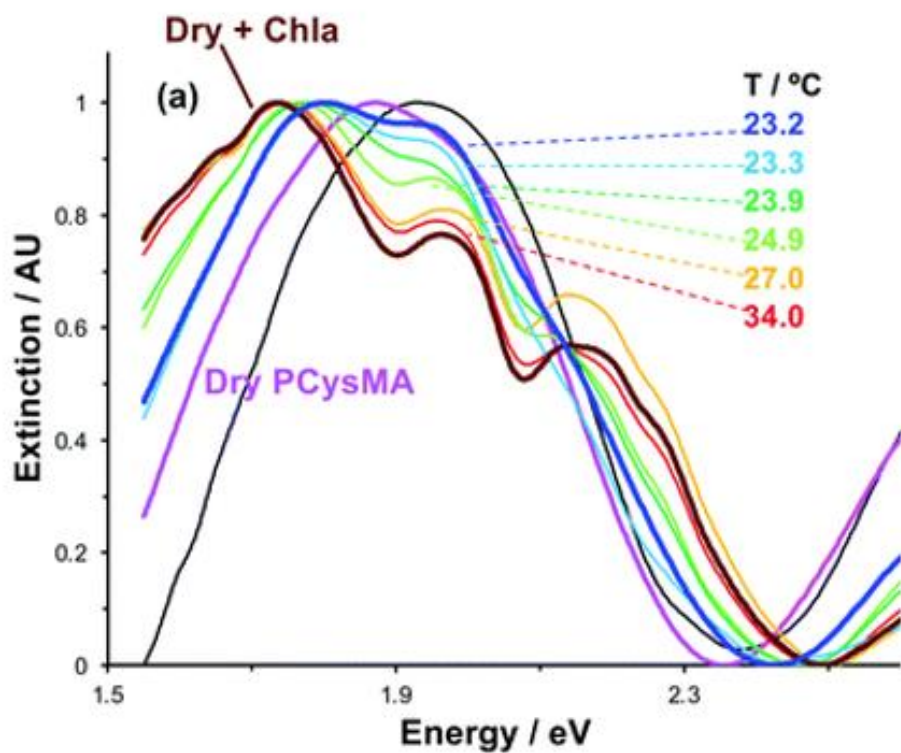


Figure 1-7: (a) extinction spectra of gold-PCysMA-Chla complexes in different temperature, (b) extinction spectra of gold-PCysMA-Chla complexes in different media.^[33]

The coupling strength can be determined by modelling the spectra. The coupling strength depends on the concentration of excitons in the plasmon mode and on the oscillator strength of the excitons.

Multiple splitting can be achieved as a result of large number of localised plasmons in AuNPs in the presence of two or more different types of dyes.^[29] Hybrid plexcitonic structures were formed using AuNPs and different types of dyes such as J-aggregates^[29]. Also, strong coupling of plasmon-excitons was achieved using nanoantennas.^[34] Similarly, the possibility of formation of strong coupled system involving naphthalene-type chromophore has been confirmed.^[35] The research on the optical properties of plexcitonic systems is important for better understanding of light-matter interactions and their practical applications and facilitates studies understanding essential quantum phenomena such as entanglement and coherent energy exchange, and develop significant applications.^[26] Nowadays, due to the distinctive characteristics of the plexcitonic systems, they attract great interest in particular applications such as data storages, solar cells, photonics (photovoltaics) and sensing.^[26]

Capping agent effect on the formation of plexcitonic states

NPs are usually stabilised with a capping layer to prevent the agglomerates and aggregates (These capping agents are also called coating layers and can be molecules, ions or polymers). They play an important role in the formation of plexcitonic systems. Where the self-assembly process can be influenced the intermolecular forces of the capping layers. Also, capping layers with long chains, such as positively charged 8-trimethylammonium octylthiol (TMAOt) and negatively charged 8-sulfate octylthiol (SOt), can affect the distances between plasmonic and excitonic moieties and form various aggregation states of the excitonic materials. So, the simple mixing of the plasmonic and excitonic materials in solution state is not sufficient for the

formation of the strong plexcitonic systems.^[28,36] Electrostatic interaction is the most common method that is exploited among all attractive reactions during the formation of plexcitonic system to enable the coating layer to act as a linker between the plasmonic materials and the excitonic molecules.^[28] However, the repulsion between the similar charges of the coating layers tends to prevent the assembly of plasmonic and excitonic materials as illustrated in the case of cyanine dyes and gold nanorods as demonstrated by Mohankumar *et al.*^[37] Moreover, the coating layer can be exchanged by the excitonic molecules. This exchange leads to a direct interaction between the plasmonic nanoparticles and the dyes, as it is shown in the case of citrate and borohydride.^[28] Nicola *et al.* have studied the possibility of the occurrence of plexcitonic coupling using more than ten different dyes and gold nanourchins (nanostars with short tips) with different sizes and coating layers. Among all the tests, plexcitonic systems were only resulted from five reactions. It was found that the citrate capping layer yielded in strong plexcitonic coupling, in contrast to thiol layers with a strong bound to the NPs. Thus, the coating layers have a great impact on the formation and the strength of the plexcitonic system.^[28]

Modelling of plasmon-exciton coupled system.

Figure 1-8 shows the dispersion of the modes in the coupled system. The horizontal line corresponds to the energy of the exciton, and the diagonal line correspond to the energy of the plasmon mode in an uncoupled system. At resonance, $E_{LSPR} = E_{mol}$ and the two lines should cross. However, when strong coupling occurs, an avoided crossing is observed; the energies of the plexciton modes are given by the solid curved lines, and the energy difference at resonance is equal to Rabi energy $\hbar\Omega$.^[2]

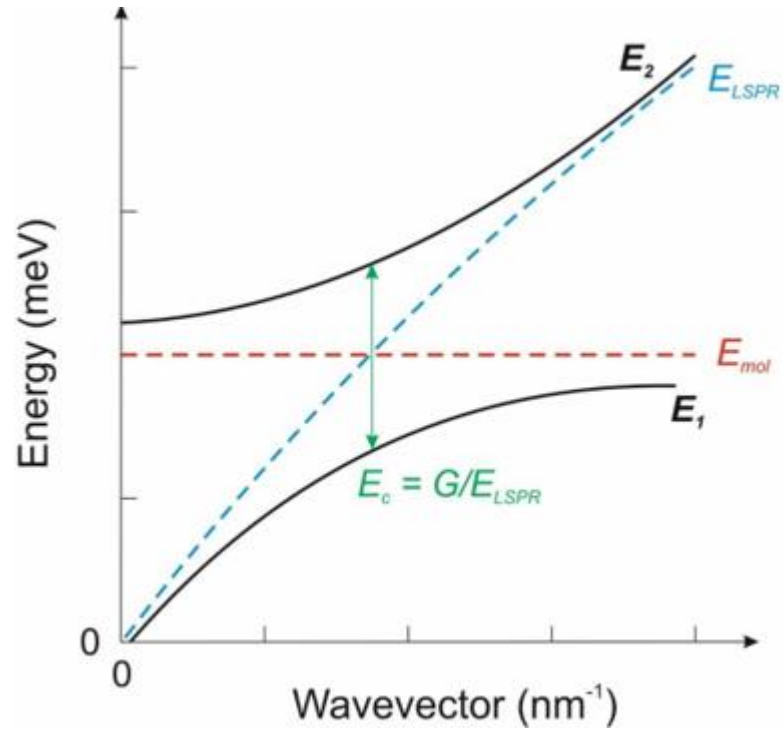


Figure 1-8: Representative diagram of Rabi splitting for the two coupling modes in both strong coupling (solid lines), and weak coupling (dashed lines).

To observe strong coupling, it is necessary that the linewidths of the plasmon and the exciton are small enough. If they are too broad, then a splitting of the plasmon band will not be observed. The system must satisfy the following equation:^[2,32]

$$E_c \geq \frac{1}{2}[\gamma_b - \gamma_{mol}]$$

where, γ_b is the linewidth of the plasmon mode, while γ_{mol} is the linewidth of the exciton mode.

Another significant factor is the density of excitons. Increasing the number of dipoles that coupled to plasmonic field results in increased coupling strength (Ω) and can be represented by the following equation:^[2]

$$\Omega = \sqrt{\frac{N}{V}} \frac{e}{\sqrt{\epsilon_0 m}}$$

where, N is the number of the dipoles, V is the volume occupied by the plasmonfield, and ϵ_0 is the permittivity of free space, and e and m are the charge and mass of the electron, respectively.

As noted above, coupling strength depends on the concentration of the excitons inside the plasmonic field (the square root of dipole number / unit volume),^[2] see **Figure 1-9**. Increase in the concentration of the excitons inside the plasmonic field leads to increase coupling strength,^[32] and it is obvious that the splitting is dependent on the number of dipoles present at the surface. This is due to that strong plasmon–exciton interaction is a collective phenomenon, in which the plasmon mode couples to an ensemble of excitons within the plasmon mode volume. Thus, linking E_{LSPR} , E_{mol} and the transition dipole moment (μ) is useful to give a good approximation for coupling energy E_c , and it should be proportional to the square root of the dipole density, see the following equation:^[33]

$$E_c \cong \sqrt{\frac{\mu^2 E_{mol}^2 N}{\epsilon_0 \epsilon_b E_{LSPR} V}}$$

where, ϵ_b is the permittivity of the background medium.

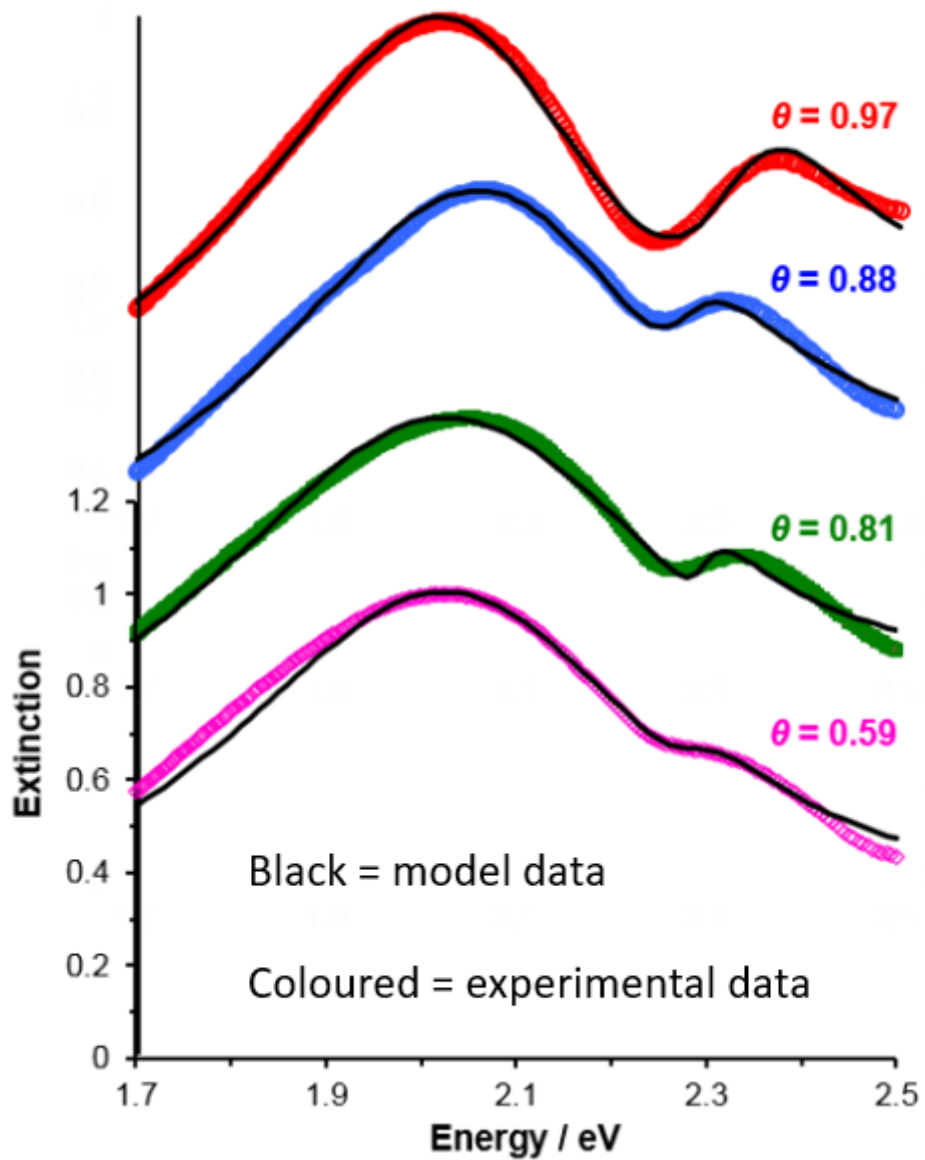


Figure 1-9: Extinction spectra of plasmonic nano arrays coupled to LH2 with significant decrease of the fractional coverage. The coloured spectra represent the experimental data and the black lines represent the model data.^[32]

1.3 Nanoparticles

The term 'nanoparticle' was attributed to Greek word 'nano' which means 'small'. Where, 1 nm = one billionth of meter = 1×10^{-9} m.^[38] NPs are known as a cluster of a number of atoms ranging from three to 10^7 with size between 1 and 100 nm in one dimension or more. NPs represent the main element in nanotechnology. NPs exhibit distinctive chemical, physical and biological properties compared to their bulk materials. This distinction is due to enhanced reactivity, stability and high surface area to volume ratio, etc.^[15,39]

NPs can be categorised, in general, into organic, inorganic and carbon-based nanomaterials. Organic NPs, such as micelles and dendrimers, are non-toxic and biodegradable. However, these organic NPs are sensitive to light and heat.^[40] Inorganic nanoparticles show interesting electronic, optical, and magnetic properties dependent on their shape, size and composition¹. Inorganic NPs include metal NPs and metal oxide NPs. Almost all metal can be reduced into their nanoscale size.^[41] Carbon-based NPs are only made up of carbon.^[42] Graphene, carbon black, carbon nanotube/ fibre and fullerenes are examples of carbon-based NPs. In recent years, nanoparticles have been generated from metals such as gold and silver, which led to the emergence of the term metal nanoparticles. Metal NPs can be modified into their respective metal oxides to increase their efficiency and reactivity.^[18,38,39]

1.3.1 Gold nanoparticles

1.3.1.1 History of AuNPs

Gold nanoparticles (NPs) were first synthesised in China and Egypt about the 4th or 5th century BC. Since then, their medicinal powers have been employed.^[15,43] AuNPs with sub-micrometre-size that are suspended in a liquid media such as deionised water, or an organic fluid are known as colloidal AuNPs.^[44] The optical properties of colloidal AuNPs were employed in colouration of glass, ceramics, china and pottery.^[15] For example, gold-plated

Archaeological Ivory (8th century BC), Lycurgus Cup (4th century), Teapot (1680) and Michael Faraday's original gold colloid samples (1852),^[20] see **Figure 1-10**.

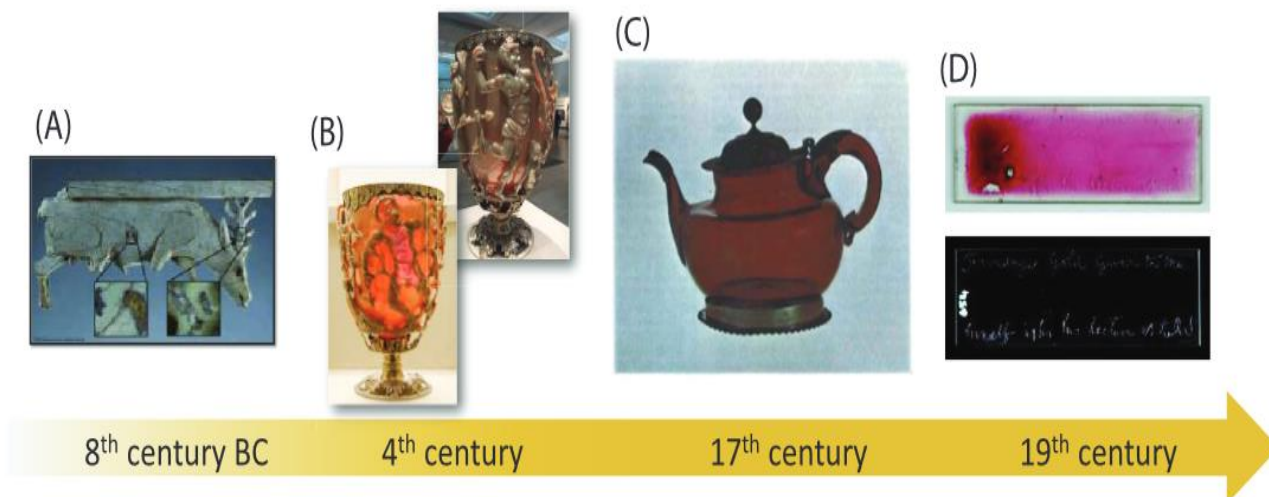


Figure 1-10: Examples of AuNPs that have been found in products produced by humans.^[20]

The most famous example of this application is the Lycurgus cup which is located in the British Museum in London. This cup was designed in the 4th century by the Romans. They discovered that incorporating small amount of gold into glass, it could be made to display surprising optical effects. the Lycurgus cup appears green when illuminated by reflected light, but a vivid red is visible in transmission. Analytical study revealed the existence of a mixture of gold and silver particles of about 70 nm in the glass vase, which was essential for the appearance of scarlet red colour.^[15] Michael Faraday's study in 1857, in which gold hydrosols were created by reducing an aqueous solution of the gold salt (HAuCl_4) with phosphorus dissolved in carbon disulfide, is credited with the first scientific synthesis of colloidal gold.^[45,46] This study attributes the optical properties of colloidal AuNPs to the change in particle sizes, where AuNPs can exhibit range of colours from ruby red to amethyst blue.^[44,47] Gustav Mie, in 1908, demonstrated the role of spherical metal particles in the phenomenon of scattering electromagnetic waves and absorption of light.^[44,48] Early in 20th century, Zsigmondy was awarded the Nobel prize for his role in the heterogeneously nature of colloidal solutions. In

1921,^[44,49] Svedberg elucidate the relation between shape and size of AuNPs and their properties.^[44,50] Significant methodologies for the preparation of AuNPs were improved during the other half of the 20th century.^[44] For example, In 1951, Turkevich used sodium citrate for the reduction of HAuCl_4 in water to establish one of the most widely used techniques for the synthesis of AuNPs.^[45,51] 40 In this procedure, citric acid serves as a reducing and stabilising agent, resulting in AuNPs with diameters of 20 nm with a narrow distribution of the size.^[44,45] The kinetics of the Turkevich reaction was developed by Chow and Zukoski.^[45,52] This reaction has been studied extensively and applied in a variety of ways^[45]. Further research by G. Frens provided control over the size of AuNPs by adjusting the ratio between gold salt and sodium citrate.^[45,53] In 1994, Shiffrin *et al.* developed the colloid synthesis of AuNPs using an immiscible alkanethiol and NaBH_4 .^[54] This was an opening of a promising research field on the functionalised AuNPs.^[44]

1.3.1.2 AuNPs synthesis

Metal nanoparticles are currently being extensively studied due to their unique properties, which mean that they can be used for a wide range of applications such as sensor technology.^[38] For the synthesis of metallic nanoparticles, a variety of techniques are used, which can be divided into two categories: bottom-up approaches and top-down approaches. The key difference between the two approaches is the starting material. In bottom-up methods, molecules or atoms are utilised as the starting material, whereas in top-down methods, bulk materials are reduced to nano-sized particles^[38]. Top-down procedures are destructive methods, while, bottom-up procedures are constructive methods,^[39] see **Figure 1-11**.

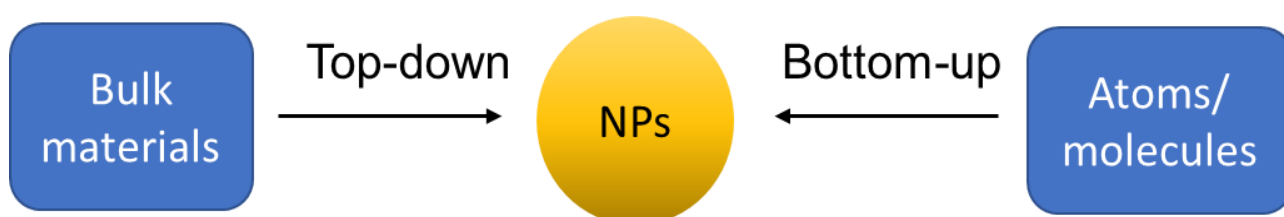


Figure 1-11: Illustration diagram of the difference between top-down and bottom-up approaches.

In top-down approach, nanoparticles are generated by reducing the size of the initial material using various chemical and physical processes. This approach includes mechanical milling and laser ablation. Although top-down techniques are simple, they are ineffective to produce irregularly shaped and very tiny particles. The main negative aspect of this approach is the change in physicochemical characteristics and surface chemistry of the produced nanoparticles.^[38,55,56] The bottom-up approach depends on the formation of nanoparticles from small atoms, molecules by joining the previously formed building blocks to generate the final nanoparticles. This method includes solid state, liquid state and gas phase strategies.^[38,57]

Specifically, AuNPs have been synthesized by several methods such as photolysis, thermolytic reduction, sonochemistry, radiolysis, two-phase synthesis procedure and chemical reduction. However, chemical reduction is the most popular and convenient method for preparing AuNPs. Briefly, a proper reduction agent is involved to reduce metal ions. In the usual, a protecting agent is used to avoid particles aggregation. For example, polyelectrolyte can be used as stabiliser for these types of nanoparticles.^[58] Chemical reduction procedure is based on reduction of ionic salt of the metal using suitable reduction agent and solvent in the presence of surfactant.^[59] For example, sodium borohydride can be used as a reduction agent in aqueous solution, while sodium lauryl sulphate (SLS) or trisodium citrate (TSC) can be used as capping layer or stabilization agent. The stabilization of nanoparticles can be monitored by the analysis of absorbance.^[60] Compared to other synthesis methods, this method is the simplest.^[59] Colloidal NPs formed by chemical synthesis are easy to prepare and inexpensive. However, there are several drawbacks associated with reducing agents, including poor reducing ability, toxicity and impurities.^[28,38,61]

In solution, the surface of NP is generally coated with capping and stabilising molecules such as thiols, amines, phosphine, and others, which inhibit agglomeration and continued growth of the NPs due to their affinity for the particle surface. These stabilization agents are usually referred to as ligands, and can significantly influence the behaviour of the particles,

because of their ability to modify the dielectric constant of the surrounding medium. Also, ligands can oxidise or partially reduce the NPs. The effect of these ligand is well studied.^[15]

Citrate-based reduction Methods

Citrate reduction is one of the most widely used methods for nanoparticle synthesis. Nanoparticles can be generated by direct addition of citrate into gold salts in boiling solvent.^[62] In addition to the simplicity of this method, the size of the particles can be controlled by adjusting the ratio between the metallic salts and the reduction agent, as well as the reaction time and temperature.^[13] In one study, range of different sizes of AuNPs from 25-50 nm was generated using sodium citrate. The size of the particles was controlled by adjusting the concentration of the reducing agent. Particles with diameter of 50, 35, 25, and 13 nm were produced using sodium citrate solutions with concentrations of 18, 18.2, 20.4 and 38.8 mM, respectively, considering the reaction conditions and experimental errors. In the same way, the sizes of AuNPs can be regulated by controlling the concentration of sodium borohydride during the solution-phase reduction reaction.^[63]

Thus, the size of the crystals decreases during the consumption of all monomers as long as the concentration of gold salt remains constant.^[63]

In a similar way, a fresh solution of NaBH_4 was used to reduce HAuCl_4 in media consisting of toluene mixed with tetraoctylammonium bromide (TOAB) under specific condition to produce AuNPs with size of approximately 5.2 nm.^[64] In this method, sodium borohydride was used as a strong reducing agent in order to form 5 nm AuNPs which then stabilised by sodium citrate.^[63] A mixture of $\text{Na}_3\text{C}_6\text{H}_5\text{O}_7$ and NaBH_4 was also used to generate AuNPs with particle size of 5 nm.^[65] The effect of both sodium citrate and sodium borohydride as reducing agents for tetrachloroauric acid (HAuCl_4) was investigated by reducing HAuCl_4 with both sodium citrate and sodium borohydride,^[66] separately, as shown in **Figure 1-12**.

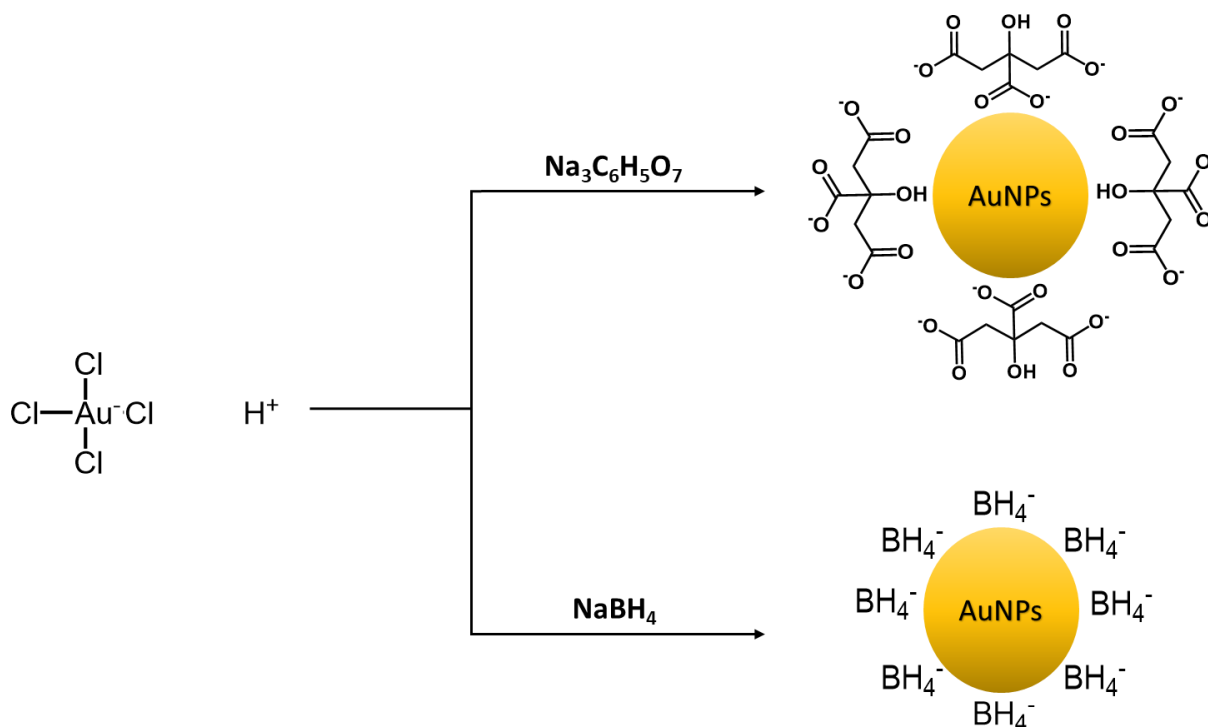


Figure 1-12: Schematic illustration of chemical reduction of gold salt with sodium citrate and sodium borohydride.

In a comparative study, AuNPs were generated using sodium citrate and sodium borohydride in order to investigate the efficiency of both reduction agents. It was found that formation of AuNPs using sodium borohydride is simple, but a reasonable size of nanoparticles cannot be obtained. However, sodium citrate exhibits higher efficiency where its reduction capacity was aided by heating the reactors.^[66]

Non-citrate-based reduction Methods

AuNPs with different particle sizes were also generated without the use of sodium citrate. Chen and co-workers have prepared polyelectrolyte-protected AuNPs with an average particle diameter of 12 nm by mixing $HAuCl_4$ with poly(diallyldimethylammonium) chloride (PDPA) which is exploited for both reduction and stabilization of AuNPs^[58]. AuNPs with 20 nm particle size were prepared by the reduction of $HAuCl_4$ in a solution of hydroxylamine –hydrochloride NH_2OH ^[65]. Larger AuNPs were also generated using silver nanocubes to react with $HAuCl_4$. The size of AuNPs was found to be 60 nm, which is 20% more than the size of Ag nanoparticles

[67]. Small AuNPs up to 2 nm were generated by reduction of HAuCl₄ with tetrakis(hydroxymethyl) phosphonium chloride (THPC). In this method, the size of the particles is controlled by controlling the concentration of gold salt.^[68] AuNPs were biologically prepared using *Diopyros (D.Kaka)* and *Magnolia (M. Kobus)* leaf extracts to reduce HAuCl₄ at different temperatures between 25 and 90 °C, and different leaf extracts concentrations in the range between 5 to 50% v/v. The formation of AuNPs was evidenced by the appearance of ruby-red colour.^[69] This study shows that the particle size can be decreased down to less than half from 110 to 40 nm with increasing of reaction temperature. Similarly, the size of particles was decreased with the increasing of reducing agent concentration.^[69] In a different approach, AuNPs were synthesized inside polymer matrix. For example, AuNPs were also synthesized by formation of gold complexes between poly(2-vinylpyridine) (P2VP) and HAuCl₄ in the polymer gel films. Then, AuNPs were formed by immersing the films inside boiled solution of sodium citrate.^[70]

1.3.1.3 AuNP nanostructures on solid surfaces

Accurate control of the optical properties of ordered metallic nanostructures can be advantageous in many research areas such as memory storage, nanosensors, surface enhanced Raman spectroscopy, and surface enhanced fluorescence. This control can be achieved by adjusting nanostructure parameters such as period, spacing, and morphology, which facilitates optimization of the performance of the nanostructure for further applications. There are different lithography techniques that have been used for fabrication of different metallic nanostructures. These techniques include nanoimprint lithography, electron beam lithography, colloid lithography, stencil lithography and photolithography.^[71]

As mentioned above, there are a number of methods that have been used to produce AuNPs in solution such as chemical reduction. However, formation of well-ordered assemblies of

AuNPs on a solid substrate is an essential for many applications such as AuNPs-based nanosensors. Nanoimprint lithography^[72] and electron beam lithography^[73] allow to obtain high precision, but depend on specialised and complex instrumentations. An alternative approach is to use a simple method such as colloidal lithography.^[74] Although the simplicity of this method is attractive, controlling specific characteristics such as size, particle spacing, and periodicity is limited. In 2014, Tsargorodska et al.^[23] used Interferometric lithography (IL) to combine the advantages of both of these two approaches using a double exposure methods, SAMs of octadecanethiol were patterned and used as resists to pattern films of gold supported on Cr-primed glass slides. The films were etched with mercapto compound to yield arrays covering $\sim \text{cm}^2$. Annealing of the samples results in recrystallization of the gold layer enabling to obtain strong plasmon absorption. The LSPR of the resulted structure can be controlled via varying the angle of sample rotation.^[23] Samples were robust and could be cleaned using cold piranha solution to allow repeated re-use. The process is shown schematically in **Figure 1-13**. The laser beam is directed onto a sample and mirror set at an angle 2θ relative to each other. Half the beam strikes the sample and the other half strikes the a mirror from which it is reflected onto the sample, where it interferes with the first half of the beam, leading to the formation of an interferogram, a pattern of alternating bands of constructive and destructive interference with a sinusoidal cross section and pitch $\lambda/2 \sin\theta$.^[23,75,76]

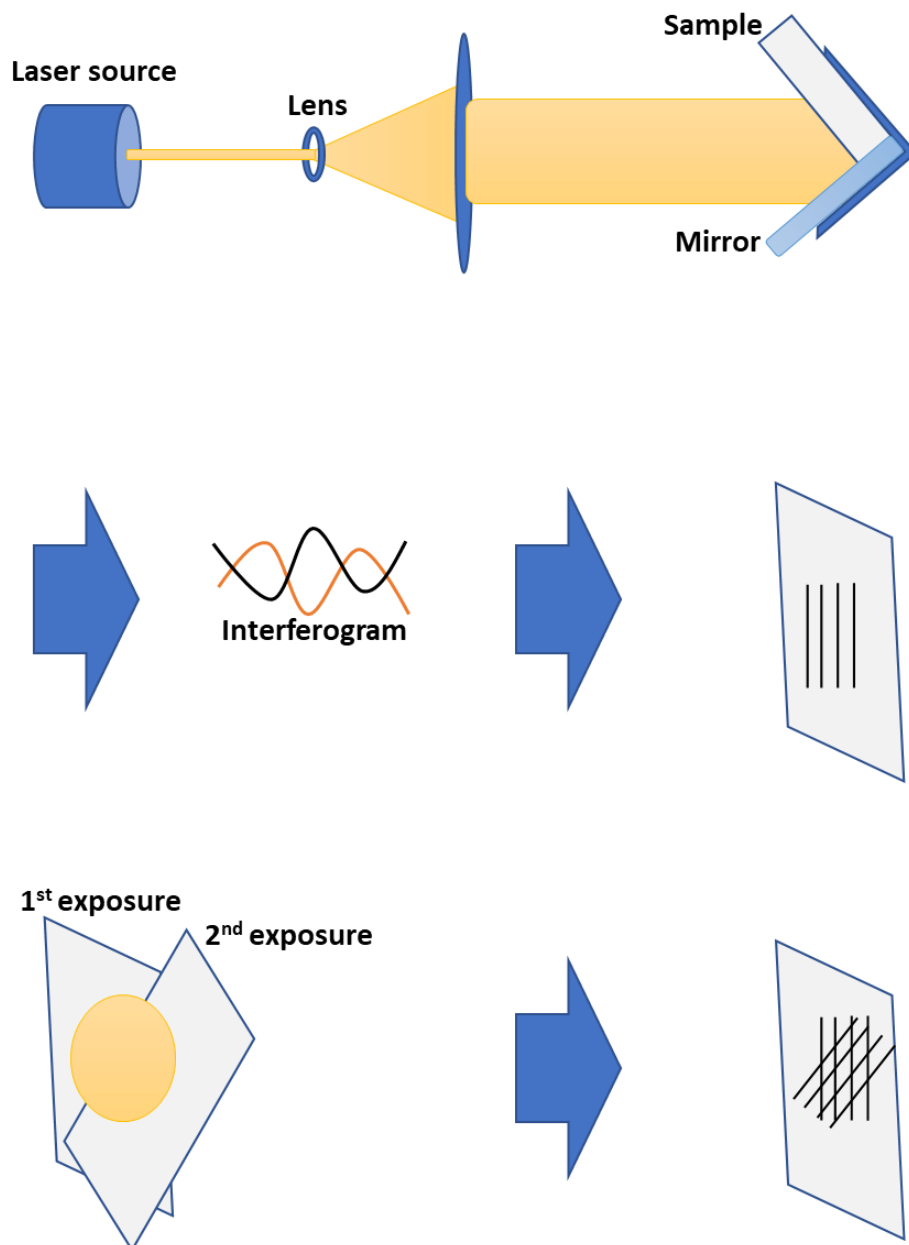


Figure 1-13: IL fabrication of Au nanostructure: (Top) experimental set-up. (Middle) single exposure. (Down) double exposure.

1.3.1.4 Gold nanoparticle properties

NPs are characterised by their size, surface area and morphology, composition, concentration, crystallography, shape and charge.^[39] Particle size reduction to the nanoscale reveals unique and improved features such as particle size distribution and shape that are not shown in bulk material and molecules.^[3,38] In comparison to bulk materials, the surface to

volume ratio of nanoparticles is about 40% higher. This significant surface area is a key factor in the size-dependent strong surface reactivity.^[38] The applications of NPs are highly dependent to their physical and chemical properties.^[39]

There is a clear difference in the optical properties of metal nanoparticles and bulk metals^[23]. A number of techniques have been used in order to characterise the properties and structures of nanoparticles. Among these, UV-vis has proved to be simple and useful tool for nanoparticles characterisation. For non-aggregated spherical AuNPs UV-Vis spectra display a strong features at around 520 nm,^[77] although the position of the plasmon band depends on the size and shape of the particle, see **Figure 1-14**, which shows different shapes and sizes of AuNPs with their respective absorption spectra, including spherical nanoparticles, cubic nanoparticles, nanostars and nanorods.

The colour of AuNPs can be in the range from ruby-red to blue depending strongly on the size and the structure of the particles. This relationship can be modified by nonradiative coupling between the particles themselves.^[23,69]

Generally, AuNPs can be selected to be either positively or negatively charged by choosing the appropriate stabiliser. For example, cetyltrimethylammonium bromide (CTAB)-coated AuNPs are positively charged, while citrate-coated AuNPs are negatively charged.^[78] Also, the charge can be tuned using aqueous-soluble ligand. Such as 2,2-mercaptoethoxyethoxyethanol (MEEE), N,N,N-trimethylammoniummethanethiol (TMAT) and 2-mercaptoethanesulfonate (MES) which can provide neutral, cationic and anionic charges respectively.^[79]

AuNPs can be prepared in different particle sizes, and different shapes and morphologies such as nanocubes, nanorod, nanobranches (Nanoparticles contain sharp tips of varying lengths. The number of branched tips per nanobranch ranges from 2 to 8), nanobipyramides,

nanospheres, nanourchins and nanostars. It was found that refractive index and absorption spectra of AuNPs are highly dependent to the shape and size of the particles.^[20,78]

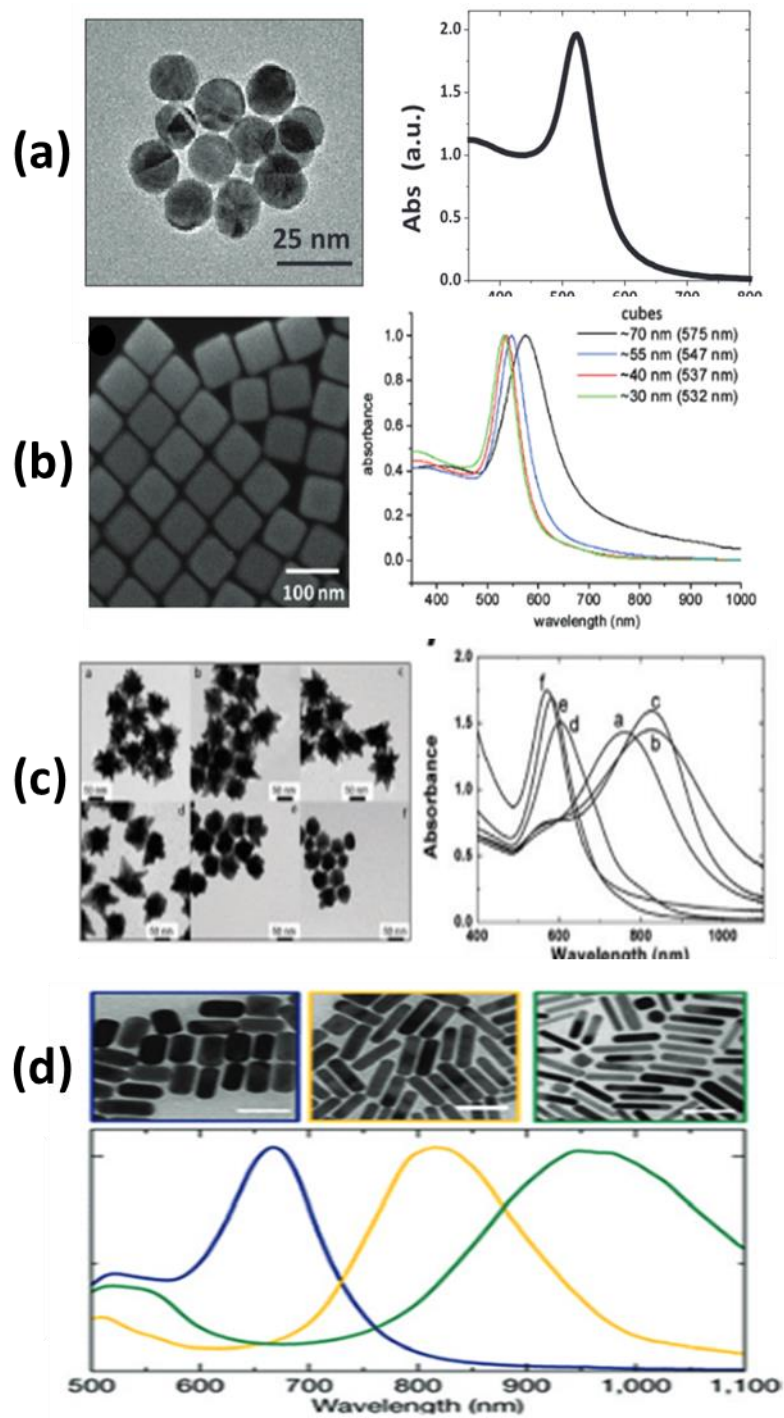


Figure 1-14: The effect of the particle size and shape on the shape and position of the plasmon band.^[20]

In comparison with Ag nanoparticles in aqueous solution, AuNPs exhibit more chemical stability than Ag nanoparticles.^[78] However, bare AuNPs are susceptible to aggregation due to their high surface energy, thus, citrate is usually used as stabilization and protective coating layer.^[80]

Aggregation of AuNPs can be suppressed using organic ligands as a capping agent. Thiol functionalities have a strong affinity for AuNP and are widely used. Dendrimers and polymers with mercapto groups and disulfides have also been used.^[63] Polymers represent an alternative class of surfactant that can be used as direct, reducing and stabilizing agents in seed-based methods of the preparation of AuNPs. For example, PDMA, has been employed as reducing and shape directing agent to produce AuNPs. This is because amine groups of PDMA can provide the essential active positions for ligands for the preparation of AuNPs with controlled size.^[44] The terms “aggregation” and “agglomeration” are commonly used for describing assemblages of particles that are found in liquid suspensions or in dry fine state. These processes can occur during filtration, milling, drying, storage or during crystallization operations as a consequence of sintering, fusion or interparticle bonding. A mass is called a lump (agglomerate) when the resulting shape of a mass can be described, while irregular shapes are resulted from aggregation process.^[81] In general, nanoparticles show a susceptibility to cluster through either agglomeration or aggregation processes. However, an agglomerate can be formed as a result of weak physical interactions which eventually lead to precipitate large size cluster, and this process is reversible. While aggregate is cluster of colloidal particles that irreversibly strongly bonded together.^[82] In solutions containing salts or other ions, citrate-protected AuNPs are unstable with a comparison to protein-functionalised AuNPs which show more stability at 4°C.^[63] XPS has been successfully applied to investigate nanoparticles aggregation, but it involves very complex analysis.^[82]

1.3.1.5 Applications

Nanoparticles are increasingly being used in a variety of domains, including organic and inorganic chemistry, physics, molecular biology, material science and medicine^[38]. The unique properties of NPs have facilitated applications in sensing, photonics, and energy harvesting^[18], nutrition, and medicine^[38], biochemistry and catalyst.^[15]

For example, immobilised AuNPs in oxide layers have been used as oxidation catalysts, with commercial application for anti-odour in Japan.^[15] Red colloidal solutions of AuNPs have been utilised as tonic medication. AuNPs have attracted interest for use in drug delivery, diagnostic applications and treatment of cancer hyperthermia.^[69] For example, AuNPs were used as a therapy to treat some nervous conditions. In addition, AuNPs were employed as antimicrobial agents. It was found that AuNP-coated aminoglycosidic antibiotics have antibacterial activity on both Gram-negative and Gram-positive bacteria. AuNPs can cause leakage of cell components (lysis) which is followed by cell death. They may also disable DNA by binding to it.^[83]

AuNPs were contributed to fabricate hybrid nanoassemblies by combination of AuNPs with poly(N-isopropylacrylamide) (PNIPAM).^[84] The use of Au NPs in optoelectronic tools is strongly reliant on the shape, size, nature of the protecting shell, interparticle distance and surrounding environment of the particles^[64]. AuNPs have been employed as photoprotector for *chlorophyll a*. This protection is achieved by bonding AuNPs with the nitrogen sites of *chlorophyll a* even during the dark, which leads to prevent the interaction of *chlorophyll* with reactive oxygen species that cause its decomposition in the light^[85]. Similarly, AuNPs have been employed to prevent photolysis of magnesium tetraphenylporphyrin (MgTPP),^[86] a molecule structurally similar to *Chla*.

nanosensors

Interest in AuNPs nanosensors has grown rapidly due to their high sensitivity and stability, fast response, ease of operation and their perfect suitability in detection and analysis.^[87] In sensors, any physical or chemical change that occurs to the environment surrounding the nanoparticles can lead to change in plasmonic resonance wavelength of maximum scattering or absorption. Therefore, highly sensitive surface plasmonic resonance is required. This sensitivity can be represented by the relation between the change in refractive index of surrounding molecules and the shift in resonance wavelength. It was found that this sensitivity can be effected by shape, size and metal composition.^[88] AuNPs have been employed to enhance the sensitivity of nanosensors for the detection of small molecule.

For example, Au NPs have been used as SPR signal amplification tags to detect small molecules. This detection typically exploit coupling between the surface plasmon polaritons and the localised surface plasmons (LSP) of the NP, leading to enhancement of the signal^[87]. Cationic AuNPs were selected as quenchers for anionic fluorescent poly(p-phenyleneethynylene) (PPE) in order to design a new sensor to analyze protein targets.^[89] AuNPs were also used as colourimetric sensors for identification of protein conformational alteration. Where it was found that the colour of protein-coated nanoparticles can be changed by alteration of solution pH,^[62] see **Figure 1-15**

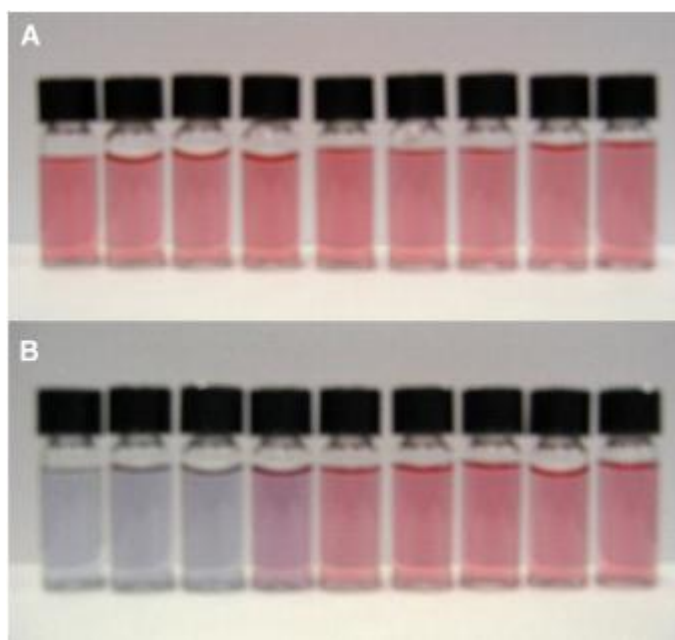


Figure 1-15: (a) Colour of AuNPs solutions at different pH, and (b) protein-coated AuNPs at pH 4.0, 5.0, 5.5, 6.2, 6.7, 7.2, 8.3, 9.2, and 10.1, from left to right.^[62]

Composite materials with colourimetric sensor properties can be produced by embedding AuNPs into polymer brushes. In order to increase the sensitivity of the brushes.^[21] Another example, Au NPs bounded to polystyrene (PS) brushes via hydrogen bonding were employed as nanosensors to detect different types of solutions in the media. In this reaction, collapse and swelling behaviors of PS toward different solutions can lead to change interparticle distance^[64]. Similarly, a novel nanosensor was constructed by adsorption of AuNPs onto poly(2-vinylpyridine) (P2VP) and polyglycidylmethacrylate (PGMA) together. This sensor was based on the behavior of the polymer brushes in different pH solutions.^[90] AuNPs were coated with streptavidin and coupled with biotinylated antibody-based bifunctional linkers through electrostatic interaction in order to enhance immunobiosensors.^[63]

Conventional SPR sensors that are based on SPP detection are use a Kretschmann configuration in which a thin layer of noble metal is deposited on a prism.^[91] In contrast, LSPR sensors are constructed on a substrate like a glass slide that coated with the noble metallic

nanoparticles.^[91] Thus, the requirement for equipment is more modest than with a conventional SPP-based detection systems. Optical fibre-based SPR and LSPR sensors offer a variety of advantages, including a small sensing tip that requires a small sample volume, and the ability for sensing remotely due to the simple optical design. In a comparison to SPR, LSPR technology has special advantages such as the ability to control and improve LSPR sensitivity by changing the shapes and sizes of nanoparticles.^[91]

1.3.1.6 Incorporation of AuNPs in Polymer brushes and PDMA

Recently, metal nanoparticles were introduced into polymer templates in several different ways, including hydrophobic interactions, hydrogen bonding interaction, covalent linkage, host-guest interaction, and electrostatic attraction as external addition or in situ synthesis of nanoparticles in polymers.^[71] See **Figure 1-16**.

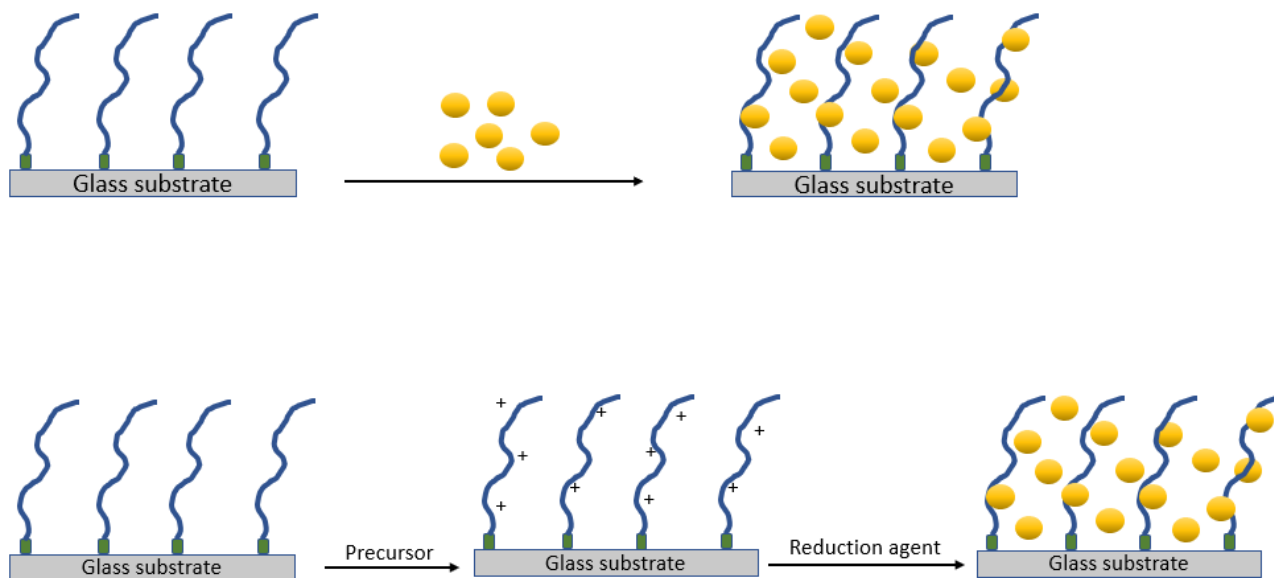


Figure 1-16: Diagram showing the process of external and in situ addition of NPs to the polymer brush.

Christau *et al.*^[92] used non-ionic poly(N-isopropylacrylamide) (PNIPAM) brushes to control the spatial distribution of hydrophobic 12-mercaptopdodecanoic acid (MDA)-coated AuNPs and hydrophilic citrate-coated AuNPs. Different solvents were used for incubation because of the different hydrophobicity of AuNPs, which resulted in different conformations of the polymer and different distributions of the particles. Here, the brush-particle interaction was driven by hydrogen bonding. Another possibility was reported by Bhat *et al.*^[93] where negatively charged AuNPs attached to positively charged poly(acryl amide) (PAAm) brushes via electrostatic attraction force. The charge density strength of AuNPs has a great impact on their distribution inside the polymer brushes. Variation in pH is the easiest approach to control the charge density.^[21] AuNPs distribution and their amount can be controlled by variation pH during the incubation of poly-[2-(methacryloyloxy)ethyl] trimethylammonium chloride (PMETAC) brushes in the suspension of AuNPs. At pH4, AuNPs formed aggregates due to decreased electrostatic stabilization. While at pH 8, the AuNPs were stabilised electrostatically allowing them to penetrate the brush instead of sticking to the surface as in pH 4. The interaction between the particles and the brush was driven by the electrostatic attraction leading to formation of colourimetric sensors with special optical properties.^[21,71] Polymers have many valuable properties, such as multifunctional groups, multiformity and well-defined structure, that have made them the preferred choice for fabrication of metal nanoparticle arrays using patterned polymer brushes models.^[71] Liping Fang *et al.*^[71] have fabricated a hybrid film by incorporation of AuNPs into patterned PDMA brushes using host-guest interaction method, and the interaction was confirmed by using PDMA monomer as competitive guest Using PDMA directly as a host for AuNPs immobilization is simple and there is no need for a complicated modification process. The absorption band of AuNPs was red shifted after the attachment to PDMA brushes, because the particles become close to each other, and dielectric constant is perturbed around the nanoparticles and the presence of PDMA can also increase the surrounding dielectric constant leading to red-shift.^[71] The surface morphology become more

rough after it was smooth before adding AuNPs and the root-mean-square (rms) roughness was changed from 0.45 to 2.49 nm,^[71] see **Figure 1-17**. Collapse state of the brushes caused by drying polymer brushes can cause adsorbed AuNPs to be close to each other, which is useful to control interparticle distance.^[94]

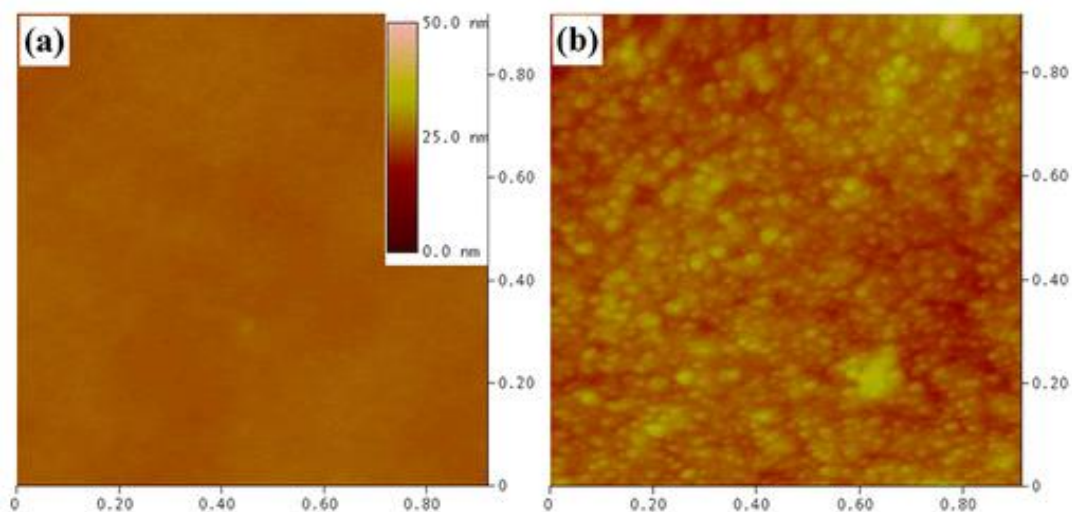


Figure 1-17: AFM images (A) PDMA brushes, and (B) AuNPs attached to PDMA brushes.^[71]

1.3.2 Aluminium nanoparticles

The study of surface plasmons has been rapidly developing in the past three decades. This development coincided with the development of nanotechnology and nanoscience. Most plasmonics studies have involved work on metallic nanostructures that contain Au or Ag. These nano metals exhibit plasmon resonances in the visible spectral range. AuNPs have relatively resistant to oxidation, while AgNPs could be more susceptible to oxidation but exhibits more intense and narrower LSP resonances. However, due to expansion of this field of research, the plasmonic properties of aluminium nanomaterials opened up a host of possibilities.^[95]

'Aluminium plasmonics' is not of the new age. it could be argued that the modern plasmonics began in 1957 with Ritchie's prediction of a peak in electron energy loss spectra (EELS) resulted from thin metal films due to surface plasmons,^[96] as well as Powell and Swan's

observation of such a peak in thin aluminium films in 1959.^[97] Thus, the study of aluminium plasmonics can be traced back to the beginning of plasmonics over half decade ago where the first LSPR peak was observed using small aluminium nanoparticles.^[98] The frequency of the plasmon bands of AlNPs is higher than that of AuNPs or AgNPs and thus allows for significant SPR coverage in the ultraviolet (UV) region of the spectrum, in contrast to Au, Ag, which typically exhibit SPR in the visible range. This feature of AlNPs is a key in applications such as photocatalysis and the detection of biological and organic systems that show strong UV absorptions. Another reason behind the interest in aluminium is that it is an abundant and inexpensive metal that can easily be produced in a variety of forms. Bulk Al is also a very stable material, because of the growth of a native oxide layer that protects the metal surface from contaminants and from further oxidation.^[95] AlNPs are interesting materials due to their rapid kinetics and high enthalpy of combustion, which add further enhancement of their reaction properties. Nano-sized aluminium particles are known to be a novel energetic material with extremely high reactivity due to enormous specific surface areas, and they are predicted to be used as a next-generation propellant in aerospace applications. The reactivity of AlNPs is size dependant. Aluminium nanoparticles with a diameter of 30-50 nm have been found to be the most sensitive. Aluminium nanoparticles have physical and chemical properties that make them suitable for a wide range of applications, including corrosion-resistance, heat shielding layers for aircrafts, heat reflecting paints, conductive and decorative plastics, etc. High-capacity hydrogen storage materials made of nanoscale Al particles are also being investigated.^[99]

1.3.2.1 Oxidation of AlNPs

Aluminium has a higher density of free electrons than gold and silver. There are 3 free electrons in the aluminium conduction band per atom, compared to 1 electron per atom for Au and Ag. Aluminium is frequently considered to be undesirable for plasmonics since it is thought

to oxidise quickly. However, upon exposure to air, a thin passivation layer of alumina (Al_2O_3) is formed on the surface of an Al particle or Al film within a few minutes, see **Figure 1-18**.

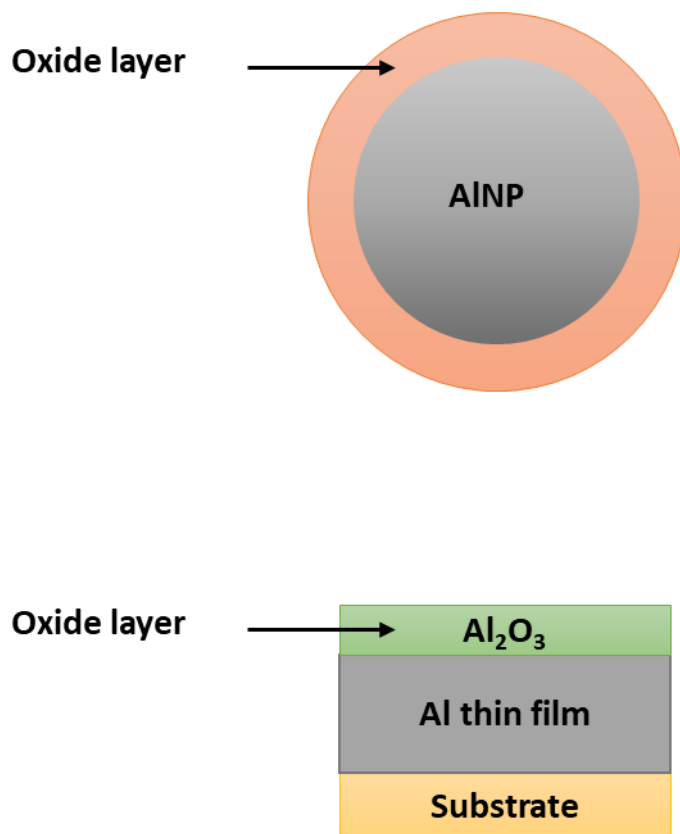


Figure 1-18: Schematic of the formation of native oxide layer on aluminium nanoparticle (Top), and thin film of Al deposited on solid substrate (down).

Angle-resolved x-ray photoelectron spectroscopy (AR-XPS) has been utilised to investigate the oxidation of aluminium nanofilm.^[100] It was found that over the course of several hours of exposure to the air, a stable oxide layer with a thickness of ~ 3 nm was formed. This layer remained stable for 30 days and acts as a protective layer to prevent further oxidation. As a result, no subsequent oxidation is detected by XPS, in contrast to the behaviour of silver nanostructures. Knight *et al.*^[101] have investigated the oxidation of AlNPs in depth. They investigated AlNPs with a diameter of 100 nm and various thicknesses of oxide layers. The thickness of the passivating oxide layer was controlled by introducing specific quantities of

oxygen during metal deposition. They found that increasing the level of oxidation caused a decrease in the scattering efficiency, with the result that λ_{\max} is red shifted. Thus, controlled oxidation can be utilised to control the energy of the plasmon mode. Furthermore, they found that the linewidth of the plasmon band does not increase significantly during the process. The plasmon resonance disappears as the oxidation level approaches 50%.^[95]

1.3.2.2 Synthesis of AINP

Understanding the principles of nanoscale chemistry and physics is a primary requirement for the production of nanoparticles. Chemical, physical, and biological methods can all be used to prepare and stabilise metal nanoparticles; chemical methods include electrochemical techniques, chemical reduction, photochemical reduction, and pyrolysis, while physical methods include physical vapour condensation (PVC), etc.^[99,102,103] Living organisms have enormous potential of generating nanoparticles and nanodevices with a wide range of applications^[104]. However, high purity active metals, Al for example, are difficult to produce due to their rapid oxidation. Aluminium nanoparticles with small sizes are extremely vulnerable to oxidation while being stored prior to application. Regardless of particle size, the thickness of an oxide layer on an aluminium particle typically ranges from approximately 2 nm to 6 nm.^[99] In general, the stability, size, morphology and properties of the metal nanoparticles are strongly sensitive to the kinetics of interaction of precursor with reducing agents, experimental conditions and adsorption of stabilizing agent. AINPs can be synthesized in a gas-state, liquid-state or solid-state.^[99]

Solid-state methods

Solid-state methods include mechanical and mechanochemical procedures. In both cases, ball milling equipment is used to reduce the size of the particles. In ball milling powdered metal is loaded into a container together with a number of heavy balls. Application of high-speed

rotation and vigorous shaking on the content leads to strong collision between the balls, which generates high mechanical energy, which in turn breaks up the particles into smaller size. Alternatively, mechanochemical milling may be used. Mechanochemical milling combines chemical and mechanical processes by changing the chemical composition of the metal precursor during the blending. The size of the particles synthesized by mechanochemical milling is typically smaller than that of mechanical synthesis. For example, AINPs have been produced by mechanochemical blending with size of 25-100nm^[105] using Li or Na as reduction agents, while the mechanical blending of Al powdered with magnesium can produce Al particles with raised size up to tens of micrometers.^[106]

Liquid-state methods

Liquid-state methods include chemical reduction and decomposition synthesis. In the chemical reduction route, a precursor of the metal is reduced by a suitable reduction agent, and catalyst, heat and stabilization agent can be involved. 110-210 nm AINPs have been synthesized by the chemical reduction of aluminium chloride using lithium aluminium hydride as a reducing agent at 164°C in mesitylene. However, AINPs produced by this method still contain impurities such as oxygen, carbon and chlorine. Similarly, 4–13 nm AINPs were produced using benzildiethylenetriamine as a reducing agent in ethanol.^[107] Also, NaBH₄ and LiAlH₄ have been used as reducing agents to produce 5–8 nm AINPs.^[108] In addition, bimetallic NPs of Au/Al were synthesized using reduction solution of sodium citrate, sodium carbonate and tannic acid.^[109]

In the decomposition process, alane complex is thermally or catalytically decomposed in the presence of a suitable passivation agent.^[110] The passivation agent here can be an organic reagent such as a perfluorinated carboxylic acid, or a metal coating layer. AINPs have been synthesised by catalytic decomposition of alane complexes using oleic acid or perfluorinated ionomer membrane as the surface passivation agent. Decomposition of alane amine H₃Al(NMe₂Et) at 164°C in mesitylene leads to formation of AINPs with particles sizes between

44-82 nm.^[111] The role of the passivation agents was investigated using 1-methylpyrrolidine alane and dimethylethylamine alane as aluminium precursors and molecules with single or double carboxylic acid groups as a capping agent. This study showed that dimethylethylamine alane is more reactive and can generate AINPs with high quality and well-defined properties. Furthermore, this study revealed that the passivation agents play an important role not only as a protection factor against the oxidation, but also act to trap the particles together to remain in the nanoscale during decomposition of the aluminium precursor.^[99]

Gas-state methods

This technique is based on condensation of evaporated molten aluminium inside a chamber containing an inert gas, where the gaseous metal condenses. Gas-state synthesis is the most prevalent method for the production of AINPs. However, AINPs obtained by this method are strongly influenced by the purity and type of the inert gas. This method has been modified by cooling the chamber to around 70 K (-203 °C) in order to speed up the condensation process. The modified process is called cryomelting.^[112] The oxide layer can be form during the condensation process with thicknesses up to 4nm covering 23 nm AINPs.^[113] In 2010, an electromagnetic modern system containing argon gas was built for the synthesis of AINPs.^[114]

Multi-state methods

These methods can be conducted in either the liquid state or the gaseous state, including wire fragmentation (flakiness, friability) and Laser ablation. In laser ablation, AINPs can be prepared by heating the target to the boiling point using a laser pulse leading to generate vapour atoms with adiabatic expansion. AINPs are generated during the condensation process. This process occurs in a liquid such as ethanol, ethylene glycol and acetone. Acetone is preferable due to its ability to generate AINPs with finer NPs with narrower size distributions.^[115] In addition to this, laser ablation can be performed using ambient gas such as argon, and the size of the produced particles can be controlled by tuning the ambient gas temperature.^[116] This method can generate particles with sizes in the range between 10-100 nm. However, the

main obstacle in this approach is that the ablation rate diminishes with longer ablation periods. When significant quantities of nanoparticles in a colloidal solution impede the laser path, a portion of the laser energy is absorbed by previously created nanoparticles rather than the target surface.^[115] In the wire fragmentation process, a powerful electrical current is applied to create an electromagnetic field around a metal causing a superheating of the metallic wire. Stopping the flow of current leads to dissipation of the electromagnetic field and the wire fragments into nanoscale particles. Similar to the laser ablation process, wire fragmentation can be performed in either liquid-phase or gas-phase. In liquid-phase, heavy alcoholic or water can be used as a suitable liquid-phase media for this process and the particles are collected by centrifugation.^[117] In the gas phase, superheating of the wire by electrical current leads to melt and evaporate and then, ionisation of the metallic material. Sudden cooling of the system leads to fragment the target and subsequently NPs is formed. Argon, nitrogen and helium are ideal atmospheres for this process.^[118]

1.4 Polymer brushes

In this thesis, polymer brushes are used to organise dye molecules within the light fields associated with metal nanoparticles. Polymer brushes are surface-grafted polymers, in which one end of the polymer chain is tethered to a suitable substrate.^[119] Polymer brushes are also known as tethered polymers^[119]. Interest in polymer brushes began with the emergence of a theoretical prediction of the brushes morphologies, which was a consequence of quantitative treatments of coil-polymers in 1980s.^[119] This special shape is the result of steric and electrostatic repulsion^[75] at low grafting densities, the polymer chains are collapsed, and form "mushrooms" whose dimensions are determined by the radius of gyration of the polymer. However, at high enough grafting densities, steric repulsion between neighbouring chains causes them to swell away from the surface to form a brush (extended state).^[120] The degree of swelling is determined by the nature of the interactions between neighbouring chains (for example, electrostatic repulsion can increase swelling), the interactions with solvent (highly solvated chains swell further) and the temperature.

Surface-grafted polymers may be formed either by *grafting-to* or *grafting-from*. In *grafting-to* pre-formed polymer is attached to a surface, while in *grafting-from*, polymer molecules are grown from a surface bound initiator^[119], See **Figure 1-19**. In general, *grafting-to* yields lower grafting densities because of the steric hindrance between the approaching chains and the already grafted chains of the polymer,^[121] so this in this thesis the focus will be on grafting-from and, in particular, surface-initiated polymerisation.

1.4.1 *Grafting-to* and *Grafting-from*

Grafting-to

Mansky *et al.* were the first users of the "*grafting-to*" method, which involves condensation of end-modified polymer chains with reactive groups on the surface.^[119,122] In *grafting-to* method, preformed functionalised polymer chains are attached covalently by reaction with

reactive groups on the surface.^[121] The major limitation of this approach is that it yields mostly low density polymer brushes, where a macromolecular barrier can be formed which, in turn, prevents the formation of new chains.^[119] Although *grafting-to* is simple method, molecular weight of the polymer can directly affect the thickness of the film. Moreover, attaching polymers to surfaces by non-covalent adsorption makes this process ineffective, leading to formation of unstable polymer brushes.^[123] The main limitation of this method is the impurity of non-grafted polymer chains with the grafted polymer, which is difficult to remove. However, this limitation can be overcome by centrifugation–redispersion cycle or simple washing in the case of attachment of a polymer to large particles. *Grafting-to* method is extensively employed grafting of a protein/peptide to a polymer to avoid contamination from the residual metal-halide salts^[121]. The best alternative to avoid these obstacles is to grow polymer brushes via surface-initiated polymerisation strategies which is also known as "*grafting-from*". Atom Transfer radical polymerisation (ATRP) is one of "*grafting-from*" polymerisation forms.^[123]

Grafting-from

"*Grafting-from*" method is attractive because it enables higher grafting densities to be achieved. In surface initiated polymerisation, polymers are grown from dense monolayers of adsorbates that terminate in an initiator.^[119] Thus, the steric problems associated with binding pre-formed polymers to surface are removed.^[121]

The grafting-from technique involves two main steps: (step 1) the initiator is firstly attached to a surface or polymer chain end, and (step 2) the polymer chain is grown from the initiator^[121]. The diffusion of monomers through the reaction mixture to the growing chain ends is the only limit to propagation^[119,124]. Grafting-from technique is versatile and is compatible with a wide range of monomers and polymerisation mechanisms.^[121]

Polymer brushes have been employed to improve the properties of materials for a variety of applications including control of biofouling, sensors, protein separation, tissue engineering, drug delivery and medical implants. In these applications, the higher grafting density achievable via the grafting-from approach is critical to the performance of the polymer film.^[125]

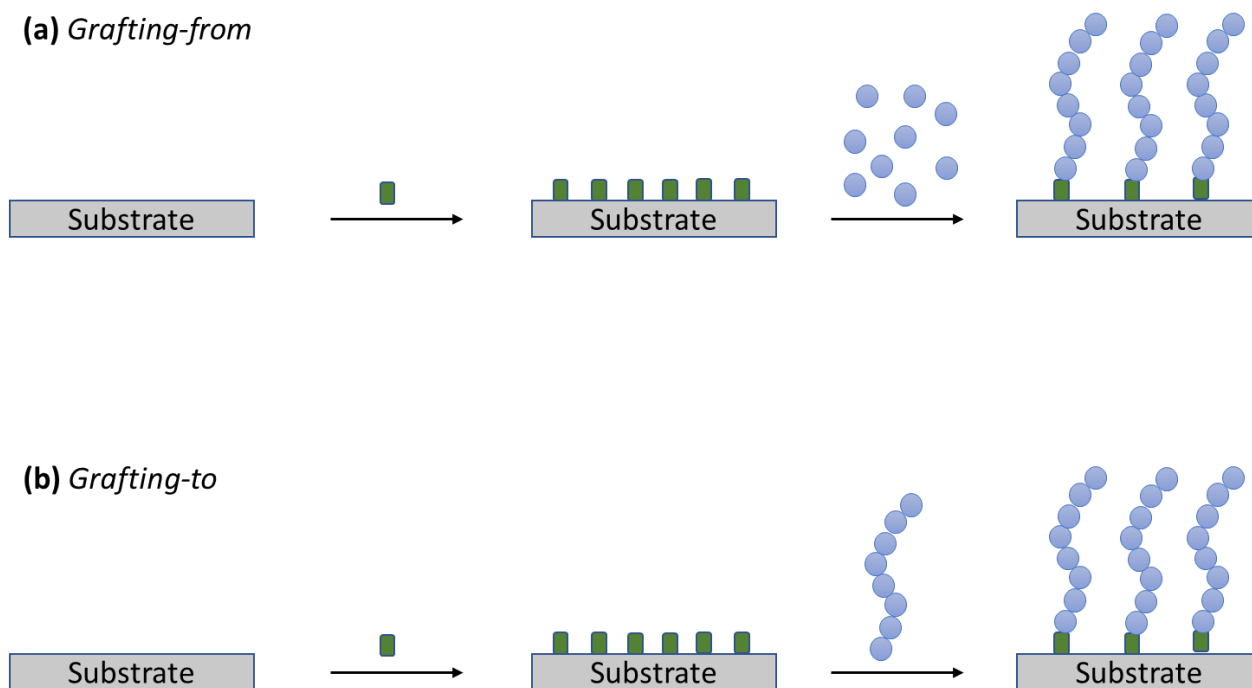


Figure 1-19: Schematic representation of different strategies of grafting polymer chains to a solid substrate. (a) Grafting-from, and (b) Grafting-to.

1.4.2 ATRP Polymerisation

Surface-initiated polymerisation techniques^[120] include surface-initiated nitroxide mediated polymerisation (SI-NMP),^[126] surface-initiated radical addition-fragmentation transfer (SI-RAFT)^[127] and surface-initiated atom-transfer radical polymerisation (SIATRP).^[128] ATRP is a rapid and simple technique for formation of different types of polymer brushes from solid surfaces.^[24,129] The term atom transfer radical polymerisation (ATRP) is derived from the atom transfer step, which is the fundamental process that allows polymeric chains to grow uniformly.^[130] In 1995, Sawamoto and Matyjaszewski reported ATRP for the first time independently^[121]. The first step is the modification of the surface of planar or colloidal substrate

using an active initiator. The modified surface is then exposed to a mixture of monomer solution and catalyst. In the most cases, a solvent must be used. Under optimum conditions monomers are joined together by the formation of covalent bonds to form polymer chains in a radical polymerisation process.^[123] ATRP is based on atom transfer radical addition (ATRA), a process that is catalysed by transition metal complexes and aims to create 1:1 adducts of alkyl halides and alkenes. ATRP is a type of living radical polymerisation mechanism: the initiator is transferred to the growing chain end after addition of each monomer unit. This transfer process can be sustained with high efficiency for long periods, before eventually terminations start to occur, and the rate of reaction slows.^[130] The mechanism of ATRP will be explained in detail in subsequent sections. The propagating radicals in ATRP are generated by transition metal-catalysed reversible atom transfer, a process that makes ATRP different from other reversible-deactivation radical polymerization (RDRP) approaches.^[121] In a comparison with other living polymerisation methods that include cationic or anionic polymerisations, living polymerisation methods are relatively difficult to use due to special experimental requirements.^[119] However, ATRP has been widely used to grow various types of polymer brushes from planar, colloidal and polymeric substrates such as gold, mica and silica.^[123,131]

ATRP components

The main components of an ATRP reaction system are the substrate, modified to introduce an active initiator, a monomer and a catalyst.^[130]

substrate

Glass has been widely used as a substrate for ATRP because of its good resistance and its low cost.^[76] Silica surfaces have been used for the growth of polymer brushes such as poly (oligo ethylene glycol) methyl ether methacrylate (POEGMEMA) via ATRP.^[132] The mechanism of grafting polymer chains onto the substrate differs depending on the type of substrate. For solid surfaces, either chemical bond formation or physical adsorption can be used.^[133]

Initiator

Alkyl halides have been used widely as ATRP initiator. To achieve well-defined polymer chains with narrow molecular weight distributions, the halide atom, X, must selectively and readily migrate between the transition-metal complex and the growing chain. Using bromine or chlorine results in the best control of the molecular weight. Iodine is preferable for acrylate and styrene polymerisation. Fluorine is not preferable because the C-F bond is extremely strong to undergo chemical cleavage. R-X bonds can be cleaved either homolytically or heterolytically depending on the initiator structure.^[130] 4-(chloromethyl) phenyltrichlorosilane (CMPTS), 3 – aminopropyltriethoxysilane-2-bromoisobutyryl bromide (BIBB-ATMS) and 3 – aminopropyltriethoxysilane-2-bromoisobutyryl bromide (BIBB-APTES) are the common examples of ATRP initiators.

Monomers

ATRP is suitable for the polymerisation of different types of functional monomers.^[134] Methylmethacrylate (MMA) is the most common monomer that has been utilised for growing polymer brushes by ATRP.^[123] However, many monomers have been effectively polymerised via ATRP. Typical monomers include (meth) acrylamides, (meth)acrylates, styrenes, and acrylonitrile. These types of monomers contain substituents that can stabilise the propagating radicals. Ring-opening polymerisation has been also successful. Under similar conditions and using the same catalyst, each monomer possess its unique atom transfer equilibrium constant for its active and dormant species (explained in detail under mechanism section). Also, each monomer has its unique intrinsic radical propagation rate. Therefore, for a particular monomer, the rate of radical deactivation and the concentration of propagating radicals must be adjusted to maintain the control of the polymerisation.^[130]

Catalyst

The catalyst is the most significant factor in ATRP and there are a number of metal complexes that have been effectively used as catalysts in surface initiated ATRP. The catalyst

determines the position of the atom transfer equilibrium and the dynamics of the exchange between the active and dormant species. An effective transition metal catalyst has various features. First, there must be at least two readily accessible oxidation states separated by one electron in the metal core. Second, the metal centre should have a strong halogen affinity. Third, when the metal is oxidised, the coordination sphere around it should expand to preferentially admit a (pseudo)-halogen. Fourth, the ligand should have a high level of metal complexation. The position and dynamics of the ATRP equilibrium should eventually be appropriate for the specific system. As ATRP catalysts, a number of transition-metal complexes have been investigated.^[130]

Ligands

The primary function of the ligand in ATRP is to solubilise the transition metal salt in the organic solvent and to modify the redox potential of the metal centre for suitable dynamics and reactivity for the atom transfer.^[130,135] HMTETA and PMDETA are the most widely used ligands in ATRP.^[136] **Figure 1-20** shows the chemical structure of both PMDETA and HMTETA.

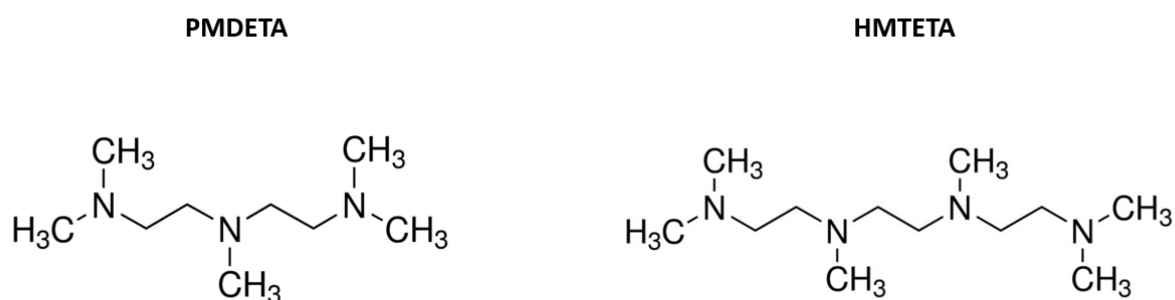


Figure 1-20: Most common examples of ATRP ligand; (left) PMDETA and (right) HMTETA.

Solvents

ATRP can be performed either in solution, in bulk, or in a heterogeneous media such as suspension or emulsion. In ATRP, various solvents have been used such as water, alcohol, acetone, dimethyl formamide (DMF), benzene, carbon dioxide, toluene, anisole, ethyl acetate,

ethylene carbonate, diphenyl ether, and many others. Solvent is a critical component in ATRP, particularly when the grown polymer is insoluble in its monomer such as polyacrylonitrile. The choice of solvent is usually influenced by several factors. There should be minimal chain transfer to the solvent. Interactions between the catalytic system and the solvent as well as catalyst poisoning by the solvent should also be considered. Also, solvent-promoted side reactions, such as the removal of H-X from polystyryl halides, which is more obvious in a polar solvent,^[137] which should be avoided.^[130]

Temperatures

Increasing temperature in ATRP leads to increase the rate of the polymerisation due to the increase of both the atom transfer equilibrium constant and the radical propagation rate constant. Thus, higher propagation/termination constants ratios and efficient control may be obtained at higher temperatures because of the activation energy for radical propagation in this case is higher than for radical termination. However, at higher temperatures, side reactions such as chain transfer become more obvious.^[137,138] Similarly, high temperatures lead to increase the solubility of the catalyst. Moreover, temperature increase may result in catalyst decomposition.^[139,140] The ideal temperature is determined by the monomer, catalyst, and molecular weight.^[130]

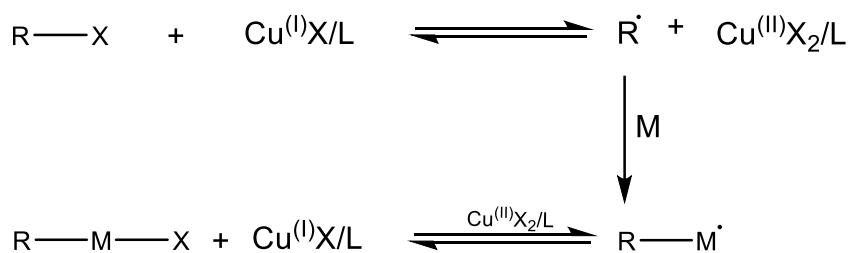
Additives

For effective ATRP, additives are often required. For the controlled polymerisation of MMA, a Lewis acid such as aluminium or other metal alkoxides is required. In the absence of the Lewis acid activator, extremely slow polymerisation was obtained. In the higher oxidation state, aluminium compounds can activate and stabilise the catalyst.^[141] The polymerisation rate can be enhanced in the presence of extremely polar solvents such as water.^[142] However, strong nucleophiles, such as phosphines, can sometimes stop the reaction.^[130,143]

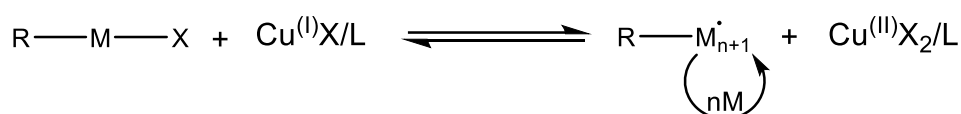
ATRP mechanism

ATRP is generally characterised as a reversible transfer of halide between transition metals and the growing chains via an inner sphere electron transfer (ISET) or outer sphere electron transfer (OSET).^[138] In general, formation of a polymer by ATRP consists of three main stages: initiation, propagation, and termination as illustrated in **Figure 1-21**. The initiation of ATRP reactions requires the transfer of the halogen atoms, such as bromine, from the initiator to the complex that formed between the catalyst Cu(I)Br and the ligand. This means that in the absence of the halogen atom, ATRP will be not initiated.^[120] The active species (radicals) are produced by a reversible redox process. This process is catalysed by a transition metal complex (Mtⁿ-Y/Ligand), where Y is the counterion or another ligand). The catalyst undergoes a one electron oxidation with abstraction of a halogen atom, X, from a dormant species, R-X. This process is driven with a rate constant of activation, k_{act} , and deactivation k_{deact} . Then, the chains of the polymer can be grown by the addition of the radicals to monomers with the rate constant of propagation k_p .^[130] The value of the equilibrium constant ($K_{eq} = k_{act}/k_{deact}$) defines the polymerisation rate in the absence of any side reactions other than radical termination by coupling or disproportionation. Too low equilibrium constant results in very slow ATRP. A high equilibrium constant, on the other hand, will result in a substantial degree of termination due to an increased radical concentration. This will be accompanied by a huge amount of deactivating higher oxidation state metal complex, shifting the balance toward dormant species and possibly causing the polymerisation to appear to be slower.^[130] It was found that long chains propagate faster than shorter chains, leading to expansion the molecular weight distribution.^[144,145] Finally, termination reactions (k_t) lead to oxidise metal complexes, X-Mtⁿ⁺¹, to reduce the growing radicals. An effective ATRP has a small contribution of terminating chains along with uniform growth of all chains, which is achieved through rapid initiation as well as fast reverse deactivation.^[130] It was found that polydispersity of polymer chains on the surface is greater than free chains in solution.^[145]

Initiation



Propagation



Termination



Overall reaction

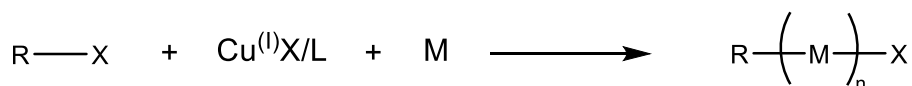


Figure 1-21: ATRP mechanism.^[130]

Throughout the formation of block copolymers by ATRP, the order of polymerised monomers is a significant issue, where the active monomers are polymerised firstly followed by less active monomers. This arrangement ordinarily follows the following order: acrylonitrile, methacrylate, styrene and acrylates and acrylamides, respectively from more active to less active. Also, vinyl chloride is more active than vinyl acetate. However, this arrangement can be changed due to halogen exchange process. In this process, alkyl halide is chain extended with an interactive monomer in the presence of metal complex catalyst. Since the equilibrium constant of ATRP for a bromo-(macro) initiator is larger than for a chloro-(macro) initiator, C-Br bond is reactivated

more faster than C-Cl bond leading to decrease the rate of second block growth. Thus, the initiation efficiency from bromo-initiator is preferable.^[146]

Advantages of ATRP

The primary objective behind ATRP is to achieve desired modification in surface properties such as biocompatibility, wettability, friction, resistance to corrosion and hydrophilicity and hydrophobicity^[147]. ATRP has several advantages compared to other polymerisation techniques. For example, ATRP is a simple procedure, and it is suitable for a wide range of both monomers and functional groups. Thus, ATRP can be performed in different types of media such as aqueous solution or emulsion, also it can be used for a wide variety of initiators^[121]. In general, the formation of polymer brushes with the highest grafting densities can be obtained the most easily using ATRP.^[148] A variety of types of polymers can be effectively and efficiently polymerised by ATRP, including linear, star, branched, gel/network and comb/brush.^[149] ATRP has also been used to form bottle-brush structures^[76]. Li X *et al.*^[150] concluded that a smoother topography of the polymer can be produced by ATRP compared to surface roughness of the polymer that prepared by conventional radical polymerisation.^[151] The simplicity of ATRP means that special equipment such as glove boxes and Schlenk are not required, making the synthesis of polymer brushes more accessible to a broader diversity of scientists.^[120]

Disadvantages of ATRP

ATRP is to some extent sensitive to oxygen, despite the fact that polymerisation can tolerate a small amount of oxygen, because the effect of a small amounts of oxygen can be eliminated by the presence of the catalyst at a higher concentration than the growing radicals.^[130,138] However, the concentration of the catalyst can be reduced by the strong oxidation process, which leads to reduce the rate of polymerisation. In some cases, peroxides can be produced due to the presence of oxygen which can actually catalyse the reaction. For example,

methacrylate can be polymerised with high molecular weight products and relatively low polydispersity in the presence of Cu(I) or Cu(II) complexes and small amounts of oxygen.^[130,152]

1.4.3 Properties of polymer brushes

Polymer brushes can be acidic (for example, poly methacrylic acid (PMAA) and poly(acrylic acid) (PAA)), basic (for example, PDMA, poly(2-diethylamino)ethyl methacrylate(PDEM) and poly(2-dipropylamino)ethyl methacrylate (PDPA))^[153] and zwitterionic when the brush chains can carry both positive and negative charges together, in addition to being non-ionic and neutral.^[131] However, charged polymer brushes stretch away from the surface due to the osmotic pressure caused by trapped counterions and repulsion, while the neutral polymer brushes swell due to internal excluded volume interactions^[154].

Binary brushes, consisting of two different monomers, can be formed as co-polymers, by including two monomers in the reaction mixture to form random copolymers, or by carrying out sequential polymerisation steps, to produce block copolymer brushes. Patterned binary brushes, in which different in which different monomers are polymerised in spatially defined regions of a surface pattern, may also be produced at the micrometre and nanometre scale by using nanolithographic techniques to deposit initiators selectively.^[155]

Film thickness, molecular weight, chemical composition, dispersity and grafting density are the most significant features of the brushes.^[156]

Grafting density

Grafting polymers by (ATRP) is a powerful way to modify surface properties via control of the surface grafting density, thickness and chemical structure. The grafting density of the polymer is usually modified by controlling the initiator density.^[145] The grafting density (σ) can be calculated in chains / nm² using the following equation:^[156]

$$\sigma = h\rho N_A / M_n$$

where, h is the dry film thickness of the polymer brush, ρ is the polymer density, N_A is Avogadro's constant, and M_n is the number-average molecular weight of the surface-tethered polymers. The change in the grafting density can lead to various height of polymer brushes^[157]. Thus, grafting density is directly affect polymer properties.^[119] For example, nanotribological properties of poly (PCysMA) brushes were found to be dependent on the grafting density. Where with the reduced grafting density, there is noteworthy increase in surface shear stress as it reported by Omed *et al.*^[157]

Dry thickness and molecular weight

In the case of flat substrates, the dry thickness of polymer layer depends on the total number of monomers and its mass balance, as shown in the following equation:^[145]

$$h = \frac{M_n \sigma}{N_A \rho}$$

where, h is the dry thickness, σ is the grafting density, M_n is the number-average molecular weight, and N_A is the Avogadro's constant, and ρ is the density of the brush. Polymer brushes can be formed in either mushroom-like, pancake structures or extended chains depending on the grafting density.^[156] At higher grafting densities, steric repulsion cause chains to stretch away from the surface, forming brushes. However, as the grafting density decreases, the chains become increasingly collapsed, eventually reaching the mushroom state, in which the thickness of the film is effectively determined by the radius of gyration of the polymer. At very low grafting densities, flattened "pancake" structure may be formed,^[119] see **Figure 1-22**. Film thicknesses can be easily measured by ellipsometry, although it does not provide direct information about dispersity and molecular weight.^[156] However, molecular weight of tethered chains is often measured by Gel Permeation Chromatography GPC analysis after cleavage of the chains.^[156]

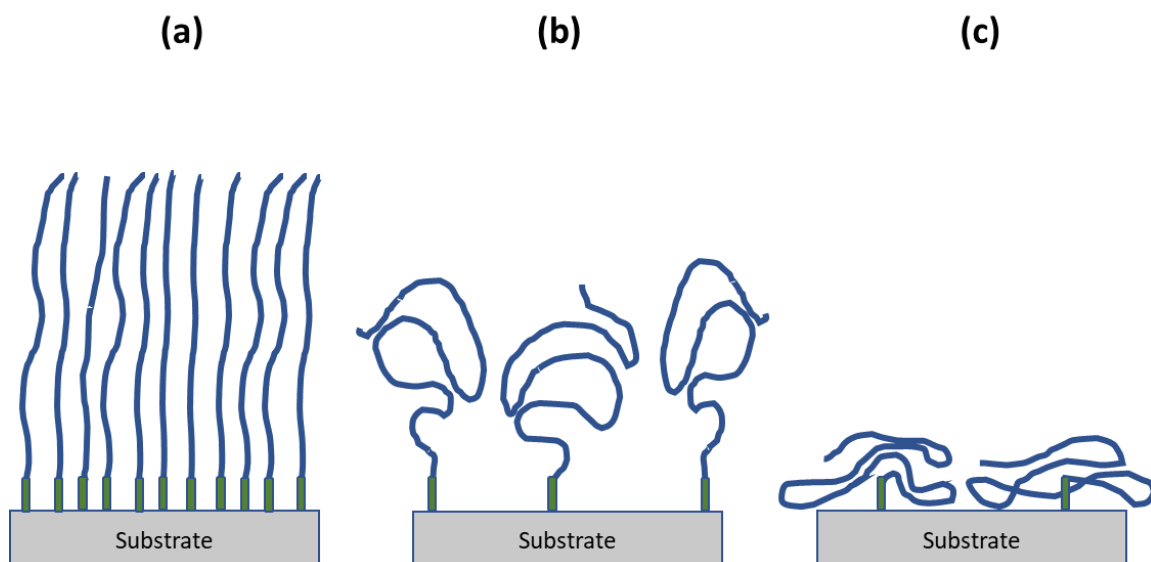


Figure 1-22: Schematic representation of different conformations of surface-tethered polymer: (a) polymer brush or extend polymer. (b) mushroom-like polymer. (c) pancake-like polymer.

Applications of polymer brushes

Integrating chemical and physical properties such as stiffness, self-healing, hydrophobicity and stimulus response, is a common purpose in many applications of modern biomaterials. polymer brush is one of the common strategies for engineering such properties.^[125] Polymer brushes offer simple, versatile and effective means to control interfacial interactions. For example, high levels of biocompatibility and lubricity have been reported for poly2-methacryloyloxyethyl phosphoryl choline (PMAOEPc) brushes in aqueous media. Exceptional resistance to protein adsorption can be achieved using poly oligoethylene glycol methacrylate (POEGMA) brushes.^[76] By comparison to other surface modification techniques, polymer brushes have been extensively and effectively employed to enhance the surface properties such as biocompatibility, wettability, antimicrobial effect and corrosion resistance.^[158] Polymer brushes have been utilised to produce surfaces with tailored chemical and biological functionalities in order to impart the desired interfacial characteristics.^[120] For example, (PCysMA) brushes were used as a suitable cushion for supported lipid bilayers (SLBs).^[159,160]

Polymer brushes can be utilised for smart coatings and can interact with surrounding environment. Recently, polymer brushes become more attractive for sensors fabrication due to their high sensitivity, to pH, temperature or ionic strength and the sensor conditions can be determined by the nature of the polymer.^[21,155] In general, they can be used as platform for fluorescent sensors.^[159] Recently, complex systems have been formed by embedding gels surfactants, or nanoparticles into polymer brushes.^[161]

1.4.4 Poly(2-(dimethylamino)ethyl methacrylate)

Tertiary amine methacrylate-based polymers such as poly(2-(dimethylamino)ethyl methacrylate) PDMA, (PDEA), and (PDPA) are the widely used basic polymers. In particular, PDMA is a widely used weakly basic polymer because of its responsiveness to both pH and temperature. Tertiary amine-base polymers synthesized by different polymerisation techniques are commercially readily available.^[162] PDMA is a weak polyelectrolyte polymer that responds to pH and temperature by changing its conformation.^[163,164] PDMA possess a partial charge with (pKa 7.5) in (pH 5.5) which leads to prevent the dehydration in the same way as for PNIPAM brush.^[161] PDMA brushes tend to be stretched away from the surface below pH 3 due to the large osmotic driving force, the degree of the swelling of the chains is inversely proportional to the grafting density, where the more swollen brushes can be obtained with low grafting density.^[153] PDMA as a weak homopolybase, it is water-soluble. However, solubility of PDMA depends on the pH value of the solution. Reduced solubility is observed at pH more than 9 and below 7. PDMA is a cationic polyelectrolyte around pH 8. At this pH, it displays lower critical solution temperature (LCST) behavior, and becomes desolvated at temperatures between 32 and 50 °C.^[153] The precise form of temperature responsiveness varies with the pH. The cloud point (the temperature below which a transparent solution undergoes either a liquid-liquid phase separation to form an emulsion or a liquid-solid phase transition to form either a

stable solution or a suspension that settles a precipitate) decreases from 76 °C to 38 °C when the pH is increased from 7 to 10.^[163]

PDMA Quaternization

PDMA brushes have been modified by quaternisation by reaction with alkyl bromides, such as, 1-bromohexane, 1-bromododecane, and 1-bromoethane. PDMA brushes were quaternised by other halogenated reagents such as 1-iodooctadecane.^[148,164] PDMA brushes formed on PVBC microspheres have been quaternised by 1-bromododecane or 1-bromohexane. The quaternisation reaction leads to the formation of a cationic polymer that is coordinated I-counterions as represented^[158] in **Figure 1-23**. Because of the high surface charge density, q-PDMA has been used as cationic antibacterial agent.^[148] q-PDMA brushes were also employed as a supportive pH-responsive platform for facile formation of highly mobile supported lipid bilayers SLBs on solid surface. The response of (q-PDMA) toward changing solution pH was investigated in two different solvents. In n-hexane that is non-solvent for the brushes, (q-PDMA) brushes were found to be pH-responsive. On the contrary, q-PDMA were non pH-responsive in tetrahydrofuran (THF) which is a good solvent.^[164] Marco *et al.* have investigated the kinetic parameters of the formation of q-PDMA, and found that the higher quaternization rate was achieved at increased temperature.^[165]

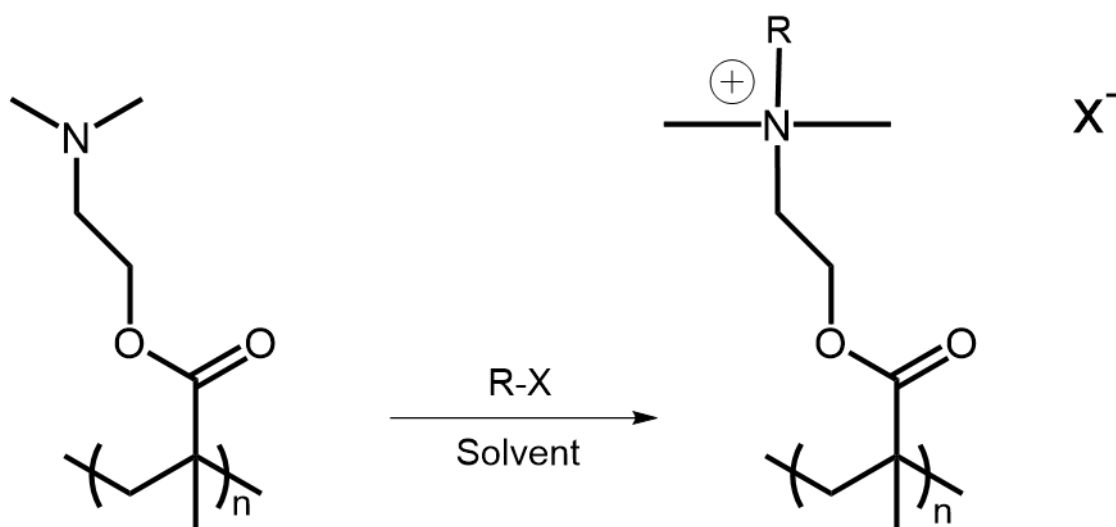


Figure 1-23: Quaternization of PDMA with alkyl halide.^[165]

PDMA synthesis and applications

PDMA brushes have been grown on a planar surface using ATRP. For example, Chen and co-workers have used ATRP to grow PDMA brushes.^[164] Antimicrobial activity of these brushes was examined on *E. coli* and *S. aureus*.^[166] There are different solvents that have been used to grow PDMA brushes via ATRP such as DMF and acetone and polymerised using HMTETA^[148] and PMTETA^[167] as examples of ATRP ligands. In addition, PDMA was prepared also via Reversible Addition-fragmentation Chain Transfer (RAFT) at 70°C. It was used as macroagent of RAFT for polymerisation of methacryloxypropyltrimethoxysilane (MPS) monomers.^[168] PDMA can also be used as cationic condensing factor for gene transfection of DNA. As a result, PDMA-coated nanoparticles can be used for DNA delivery.^[168] PDMA was grafted onto poly(vinyl chloride) (PVC) using ATRP initiated by allylic and tertiary chlorines. This copolymer was applied as positively charged nanofiltration membrane for dye separation. Compared to pure PVC membrane, PVC-g-PDMA membranes have higher hydrophilicity and permeability due to ability of PDMA to be protonated and partially quaternised.^[136] In addition, PDMA can be used as a template for mineralization of some inorganic oxides, such as titanium dioxide, silica and calcium phosphate^[71]. PAMA was polymerised in anisole with AMA, Cu(I) Br, and PMDETA under a vacuum after three freeze–thaw cycles and terminated by exposing the solution to air.^[167] PDMA was used to functionalise AuNPs to stabilise Pickering emulsions which can be reversibly broken by altering the pH as an application in control release.^[163] PDMA brushes applications can be extended by growing the chains using different types of substrates, such as silica, silicon, glass, polyethylene terephthalate (PET) and gold and others. Similarly, its application can be extended using different initiators such as BIBB-APTES^[164] and BIBB-ATMS.^[71]

1.5 Dye-polymer complexes

Organic dyes have been the subject of extensive research in recent decades. Their primary advantages were extended from the colouration of bulk material in the 19th century to tailor-made functional dyes today^[169]. There are numerous applications available, ranging from organic dye sensitised solar cells to selective protein labelling, synthetic polymers and light harvesting. Moreover, an estimated 70 000 tonnes of organic dyes are produced annually worldwide in the fields of hair colouring, textiles, paper production, food technology, leather tanning, and agricultural research. Recently, dyes-functionalised polymer structures have stimulated a great deal of interest due to their fundamental applications in organic electronic devices, particularly, in organic light emitting diodes (OLEDs) and white polymer light emitting diodes (WPLEDs) as well as in sensor molecules in environmental and biochemical applications.^[169]

One way to introduce dyes into a polymer is to attach the dye to the pre-formed polymer, either through the side chain or the end chain binding, See **Figure 1-24a**. For example, oregon green 488 fluorophores were chemically attached onto the PMEP polymers grafted onto gold substrates. These structures were used to investigate the conformational changes of the polymer in water and KCl. In water, the brushes emit strong fluorescence in the extended conformation. The addition of KCl increases charge screening effects along the polymer chains, resulting in partial collapse, which was evidenced by strong quenching of the obtained fluorescence^[170]. In another example, 4-(2-acryloyloxyethylamino)-7-nitro-2,1,3-benzoxadiazole (NBDAE) as donor and 1-(2-methacryloxyethyl)-3,3-dimethyl-6-nitro-spiro(2H-1-benzo-pyran-2,2-indoline) (SPMA) as acceptors were used to label thermos-responsive poly(N-isopropylacrylamide) (PNIPAM) brushes grafted on to silica nanoparticles. Irradiation of this system by UV light leads to transfer SPMA from nonfluorescent form to fluorescent form, which can act as a sensitive radiometric fluorescent thermometer.^[171] PNIPAM brushes were grown from protein filament and derivatised to introduce fluorescent

reports. This system was found to be responsive to change in temperature leading to a switch in the structure of the polymer between swollen and collapsed forms.^[172] pH-responsive dye-labelled polymer brushes were synthesised by co-polymerisation of fluorescein O-methacrylate with n-butyl acrylate via ATRP. This structure showed fluorescence properties under basic conditions, which were not shown in neutral or acidic conditions.^[173] In a similar way, Nile blue dye labelled PMPC homopolymer and PMPC-co-PDPA were also used as pH sensors. In these sensors, the dye molecules were attached covalently to already polymerised monomers.^[174] Fluorescent nanotags were synthesised by using a bottlebrush polymer from which extend hundreds DNA strands that can bind to hundreds of covalently attached or thousands of non-covalently introduced fluorescent dye molecules through side chain attachment. This fluorescent nanotag can detect protein targets with a remarkably bright signal that is favourable compared to commercial antibodies labelled with organic dyes.^[175] A common serious limitation in these structures is the aggregation of dye molecules.^{23–25} To solve this problem, Maciej *et al.* suggested that attaching the dye molecules at the chain-end of a polymer chain may result in lower aggregation instead of attaching the dye molecules in each repeating unit of the polymer chain. In their work, alkynylated fluorescein was used to functionalise micropatterned PMMA brushes grown by ARGET-ATRP through the end chain, which can be useful in light harvesting applications.^[176] In 2022, plexcitonic complexes were designated by using *chlorophyll* molecules to functionalise PCysMA brushes. The brushes were used as a scaffold to support the pigment to achieve strong plasmon-exciton coupling. The density of the pigment molecules attached to the system plays an important role in controlling the strength of the coupling. In addition, these plexcitonic dye-polymer complexes show temperature- and pH-responsive properties allowing to active the control of the plasmon-exciton strong coupling.^[33]

Alternative approach to the introduction of dye to the polymer is first to label the polymerisable monomers with dye molecules, and second to carry out polymerisation using the labelled monomers^[177] as illustrated in **Figure 1-24b**. For example, azo dye-labelled acrylic

and methacrylic monomers were polymerised by ATRP. Chemical activities of azo-labelled methacrylate polymers are more than that of azo-labelled acrylate polymers.^[177]

Also, organic dyes can be used as initiator in ATRP as demonstrated in **Figure 1-24c** Rhodamine 6G derivative was used initiate ATRP in order to generate homopolymers from 2-(methacryloyloxy)ethyl phosphorylcholine (MPC) monomers. In addition, Rhodamine 6G derivative was also used to form pH responsive PMPC-co-PDPA copolymers via sequential addition process.^[178]

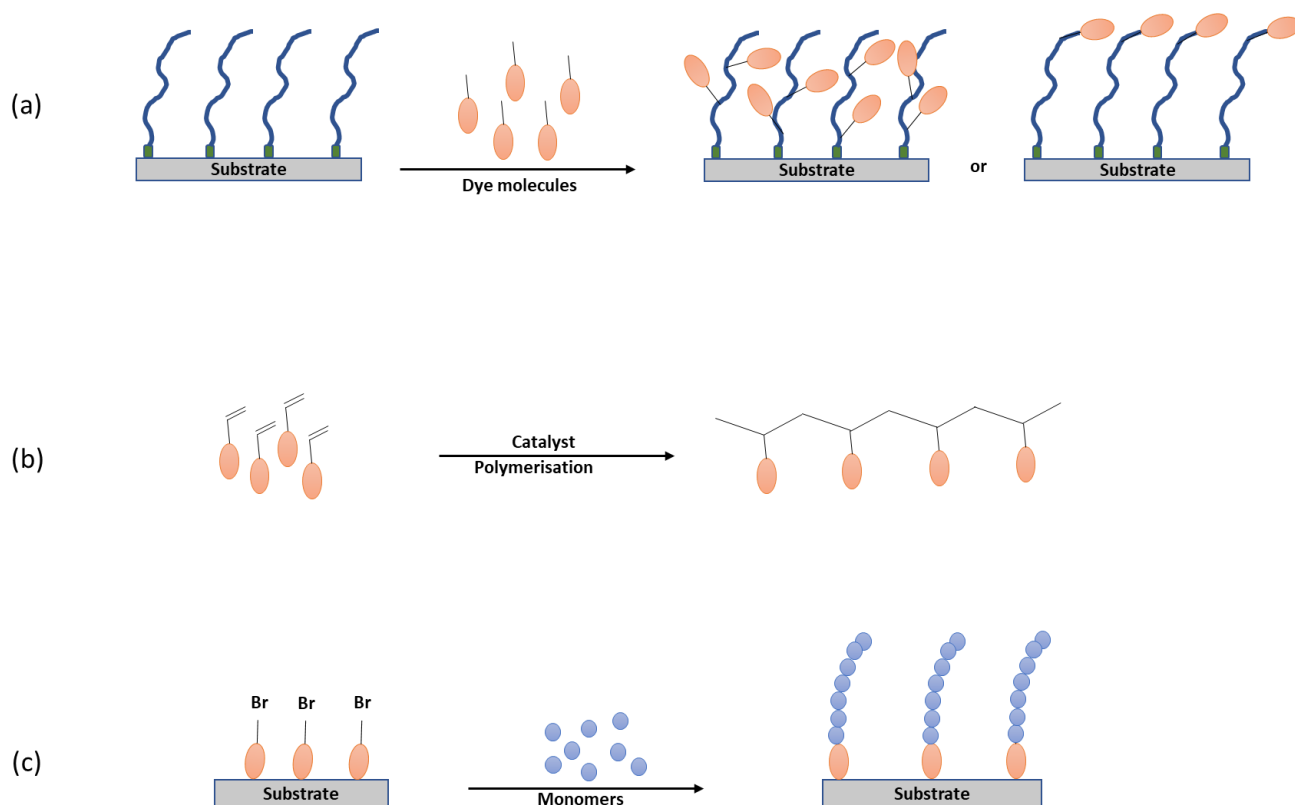


Figure 1-24: Attachment of dye molecules to the polymer: (a) direct attachment. (b) polymerisation of dye molecules as a monomer. (c) the use of dye molecules as initiator.

1.6 Chlorophyll

Chlorophyll is one of the most abundant pigments in plants.^[179] It is a bioactive compound that has antimutagenic and antioxidant properties.^[180] It was discovered in 1818 by Pelletier and Caventou. Since then, many studies have been conducted on how *chlorophyll* can be extracted and purified.^[179] It plays an important role to provide fundamental physiological information of the self-feeding organisms^[181]. It enables plants and some unicellular organisms such as microalgae to yield chemical energy from solar energy by photosynthesis.^[180]

1.6.1 Chlorophyll chemical structure

The primary *chlorophyll* molecule consists of central metal cation that bound co-ordinately to chlorin ring (tetrapyrrole structure). An additional pentagonal ring is located at one corner of the tetrapyrrole structure, while a variety of side groups are bond to the carbon atoms on the outer side of the structure. The other significant component is hydrocarbon tail, phytol chain, which is attached to the structure by ester linker.^[182]

1.6.2 Chlorophyll a and chlorophyll b

Chlorophyll can be found as one of two main structures that are *chlorophyll a* and *chlorophyll b*. *chlorophyll a* is a green/blue with absorbance in the range of 660-665 nm, while *chlorophyll b* is a greenish yellow with absorbance from 642-652 nm^[180]. *Chla* and *Chlb* exist naturally in the ratio of 3:1. The methyl group at the position C3 is a characteristic in *chlorophyll a*, while in chl b a formyl group is found in this position, see **Figure 1-25a**. In terms of thermal stability, it was found that *Chlb* is more stable than *Chla*.^[183]

The most vital feature of *Chla* is its π – electron structure. In each *Chla* molecule, there are 20 π – electrons from 10 double bonds and 4 from H-substituted or metal-substituted nitrogen atoms. π – electron structure in *chlorophyll* play an important role in the spectroscopic properties of *Chla*. Absorption of light promotes the transition of π – electrons from highest

occupied molecular orbitals (HOMO) to the lowest unoccupied molecular orbitals (LUMO) creating π - π^* transitions (excited state).^[182,184]

Due to the unsymmetrical aromatic structure of *Chla*, there are two different types of π – electrons transitions. The first is the transition from HOMO-1 and HOMO to LUMO+1, which generates strong absorption bands known as Soret bands. The second is the transition from HOMO-1 and HOMO to LUMO, which gives rise to a series of weak absorption bands known as Qx and Qy,^[184,185] see **Figure 1-25b**.

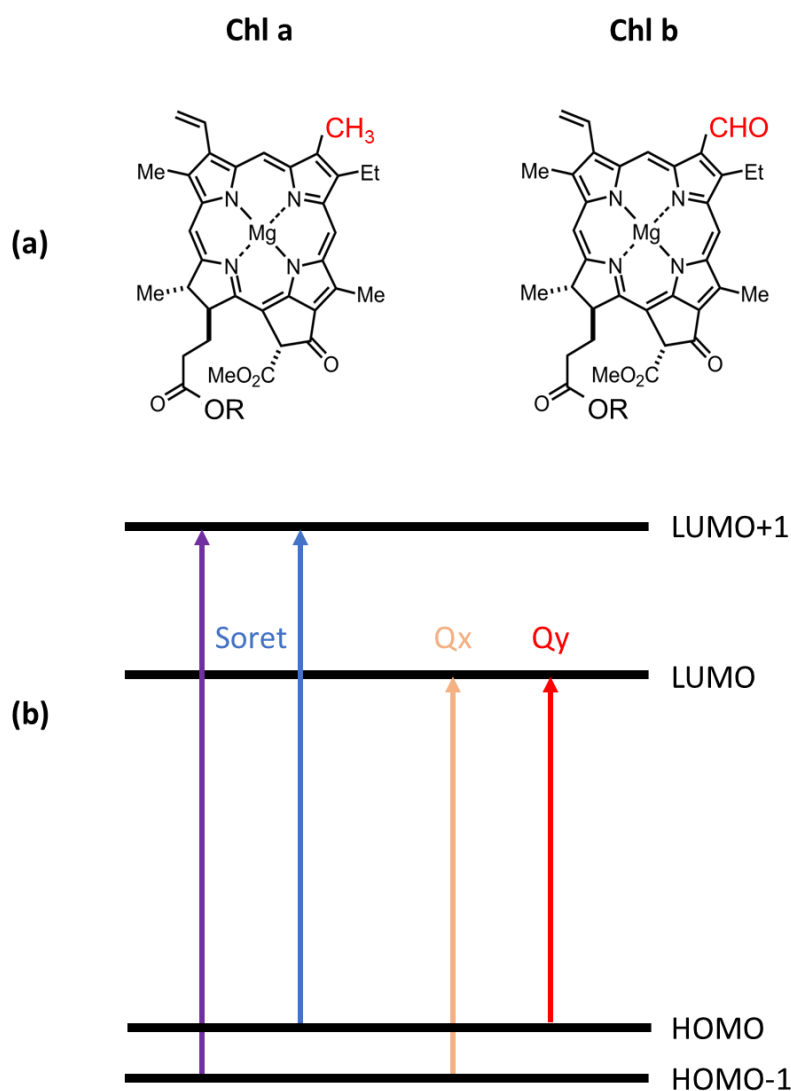


Figure 1-25: (a) Typical chlorophyll structure; chlorophyll a (left) and chlorophyll b (right). (b) Representation of the optical transition of chlorins in chlorophyll.

In photosynthetic light-harvesting antenna complexes, light is captured by pigment molecules, including *chlorophylls*. The energy is funnelled into reaction centres where charge separation occurs to drive the photosynthetic pathway. *Chlorophyll* excited states in light harvesting complexes are ~ 4 ns *in vivo*, and slightly longer (6 ns) *ex vivo*.

Recently, *Chlorophyll* has been widely used as food colours and phototherapeutic drugs, in addition to its important role as quantitative references in physiological studies.^[179] *Chlorophylls* were applied in organic electronic devices such as organic photovoltaics (OPVs) or organic light-emitting diodes (OLEDs). However, in these applications, *Chlorophylls* have a significant limitation due to high and fast photodegradation. This is because *chlorophyll* is the best natural photoreceptor.^[85]

1.6.3 *Chlorophyll* extraction and purification

A variety of methods have been reported for extracting *chl a* from its source such as Supercritical Fluid Extraction (SFE)^[186] and Organic Solvent Extraction (OSE).^[187] An effective method for extracting *chlorophyll* must produce fully separated *chlorophyll* in solution without a significant change in its composition.^[179] Production of highly purified *chlorophyll* in large quantities remains a major challenge. Aliphatic and aromatic hydrocarbons are highly ineffective in extracting *chlorophyll*.^[179] However, OSE is the most common method, where the organic solvent is used to dissolve lipids and lipoproteins.^[180,188] In general, it is difficult to state that there is a good organic solvent which can extract *chlorophyll* from all plants species. The choice of solvent varies for different species of plant.^[181] Methanol, ethanol, acetone and dimethylformamide (DMF) are examples of organic solvents that have been used in OSE. Although it was found that methanol, ethanol and DMF are more efficient than acetone in extracting high amount of pigments, acetone was preferable because it strongly inhibits the formation of *chlorophyll a* degradation products.^[180] Thus, acetone and then methanol are the most widely employed solvents for this purpose.^[179] Iriyama *et al.* have extracted *chlorophyll* using a mixture of dioxane/ water based on formation of dioxane-*chlorophyll* complexes that

can be selectively precipitate leaving other forms of pigments in the solution.^[189] Pure *chlorophyll* was extracted successfully using acetone and precipitated by dioxane-water mixture. It was qualitatively and quantitatively separated from high plants as well as bacteria and microalgae by thin-layer chromatography (TLC).^[179] During separation of *chlorophyll a*, a number of chemical transformations are possible, leading to poor yields.^[190,191] It was found that extracted chl is not affected by the storage of plant tissue up to 3 days at three different temperatures with or without solvent.^[192] *Chlorophyll* can be purified using simple column chromatography^[193]. However, this technique requires a good level of technical skill, in addition to consumption of time and solvents.^[179] Size exclusion chromatography and ion-exchange chromatography techniques have been combined in order to be used in *chlorophyll* purification process.^[179,194,195]

1.6.4 Chlorophyll a and its derivatives

Although *chlorophyll* is highly stable in nature, when it is isolated from its natural source, it may be degraded by light, acids, heat, oxygen and enzymes. This degradation process can result in formation of derivatives such as *chlorophyllide*, pheophorbide and pheophytin.^[196] *Chlorophyll* has been widely analysed by inexpensive, quick and accurate spectroscopic methods. However, the conventional methods have some limitations in measuring a mixture of different pigments as a result of interfering in the absorption spectra from the various components of the mixture. Ideally, the components should be separated before the analysis. When HPLC is used to separate the components of the mixture, *chlorophyll* molecules can be easily cleaved into *chlorophyllide* and phytol chain. However, because of the similarity of absorption spectra of *chlorophyll* and *chlorophyllide*, *chlorophyllide* cannot be easily separated and leads to inaccurate analysis. Thus, *chlorophyll* must be extracted by a method that produces a minimal amount of conversion of *chlorophyll* to *chlorophyllide*.^[181] The formation of *chlorophyllide* from *chlorophyll* is induced by either the extraction solvent or *chlorophyllase*, a hydrolase enzyme. *Chlorophyll a* can also be converted into *pheophytin a* derivative using MCS

or weak acid for de-metalation the molecules to remove the central magnesium. Hydrolysis of pheophytin leads to the cleavage of the phytol chain to form pheophorbide a.^[181] **Figure 1-26** summarise the most common conversions of *Chla* to its derivatives.

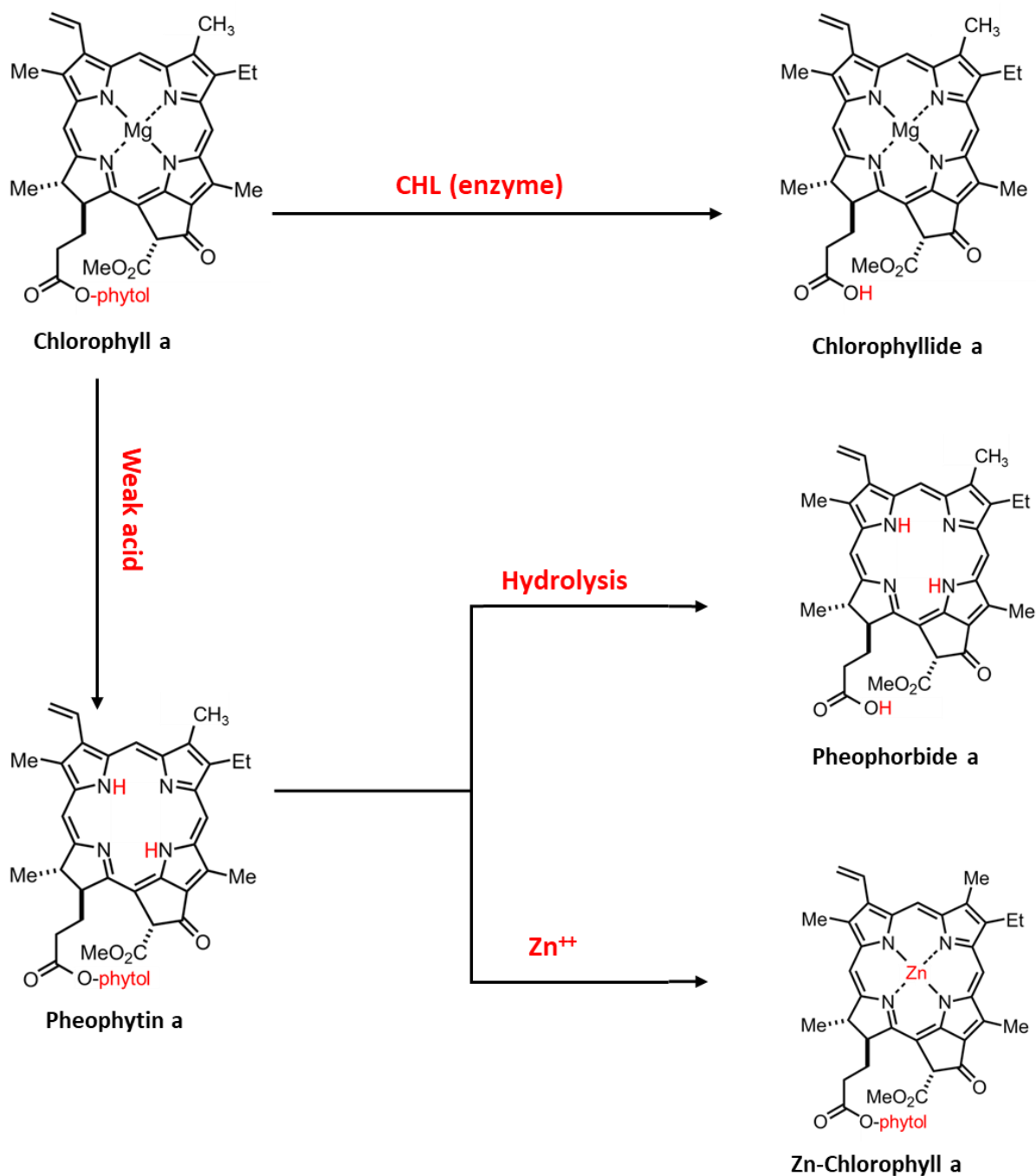


Figure 1-26: Representation of the most common conversion of chlorophyll a to its common derivatives Chlorophyllide a, pheophytin a, Pheophorbide a, and ZnChla derivative.

1.6.5 Central metal replacement

Because of the high reactivity of *chlorophyll* it could be easily effected by exposure to light, high temperature, oxygen and basic or acidic conditions.^[180] It was found that the *metallochlorophyll* derivatives are more stable than the natural *chlorophyll* itself. Zinc (Zn) and copper (Cu) ions were used to replace magnesium (Mg) ions in the central *chlorophyll* ring to resolve this problem. However, Zn *chlorophyll* derivatives are widely used, despite the simplicity of formation of Cu complexes, because of the toxicity of copper ions.^[196] Zn-*chlorophyll a* derivative (*ZnChla*) is a stable form of *chlorophyll a*, which exhibits excellent resistance to degradation. Moreover, *ZnChla* can effectively absorb red light at nearly 670 nm, in contrast to other *chlorophyll* derivatives. As a result, the properties of *ZnChla* are potentially useful in the construction of synthetic of light response materials.^[197] For example, it was found that *ZnChla* can be used as photosensitizer to produce biohydrogen from sucrose.^[198] However, Mg-*Chla* was reported to be absorbed light at approximately 660 nm.^[198]

1.7 Nile Red

The demand for synthetic dyes for artificial fabric colouration was one of the early drivers of the modern chemical industry. Since then, small-molecule dyes have been used in a variety of cutting-edge technologies and industrial applications. For example, solar cells, metal sensing and organic light emitting diodes (OLEDs), which are now being developed to meet current needs.^[199] Many common chromophores are employed in medicine, academia, and business, such as coumarin and rhodamine-based dyes. Every dye has advantages and disadvantages in terms of optical characteristics, solubility, photo/chemical stability, and synthetic access to analogues. Benzophenoxazine dyes are well-known in the literature for their bright colours and lipophilicity. Nile Red and Nile blue are two fluorescent compounds that belong to the benzophenoxazine family,^[199,200] see **Figure 1- 27**.

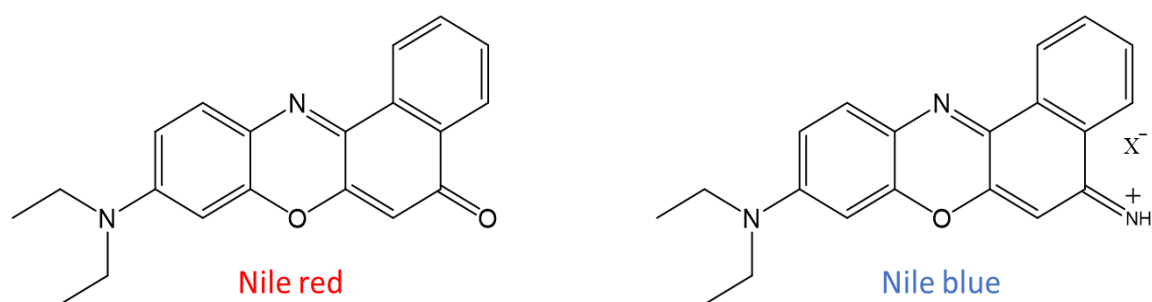


Figure 1-27: Chemical structure of Nile Red and Nile blue.

Nile Red is neutral dye containing carbonyl group and is poorly soluble in water. It is extremely fluorescent with a high quantum yield in a polar solvent but does not show any fluorescence in water. Its chromophore is extremely vulnerable to changes in medium polarity and dielectric constant. Nile blue is a cationic dye with iminium moiety and thus has more solubility in water compared to Nile Red resulting in its sensitivity to pH changes. Nile Red exhibits absorption maxima at 550 nm in methanol while Nile blue exhibits absorption maxima at 630 nm. This large difference is attributed to strength of the donor–acceptor systems of the

two dyes, i.e. because Nile blue is cationic, it has much stronger acceptor (cation) than Nile Red, which has amine (donor) and carbonyl group (acceptor), uncharged group. The first synthesis of Nile Red and Nile blue was reported in 1896 by Möhlau and Uhlmann. Notably, Nile Red can be derivatised from Nile blue by harsh boiling in H_2SO_4 . However, this method is no longer used. Alternatively, nitrosylated precursor is used to generate Nile Red.^[199]

CHAPTER 2: AIMS AND OBJECTIVES:

Gold NPs exhibit strong plasmon absorption in the visible range and they have consequently attracted an interest in applications in analytical science. Recently, there has been interest in a new phenomenon, strong plasmon-exciton coupling. It has been shown that such strong coupling can occur in biological system, in particular when bacterial light harvesting proteins are coupled to arrays of plasmonic gold nanostructure. The coupling here is a quantum optical phenomenon in which a plasmon mode couples collectively to an ensemble of excitons, to form macroscopically extended excited state. Such mechanism could be useful in solving the problem that exciton diffusion lengths are small in molecular materials. Proteins are inappropriate for this due to their instability and high cost (including suitable storage, transportations and raw materials for synthesis). The goal of this project is to fabricate biologically inspired, biomimetic structures that can be used to achieve similar strong coupling without the use of proteins. In particular, polymer brushes will be used as scaffolds upon which to support and organise excitons attachment, rather than polypeptides. To achieve this aim, PDMA will be grown via atom transfer radical polymerisation ATRP from brominated solid substrates under simple, cheap and environmentally friendly conditions. *Chla* will be extracted from spinach leaves and will be converted into more stable form by replacing Mg ions by Zn ions. Then, *Chla* will be used to functionalise PDMA brushes through coordination bonds between the tertiary amine groups of PDMA brushes and the central Zn ions of Zn derivative of the *chlorophyll* molecules. This *ZnChla*-PDMA antenna complexes will be constructed onto plasmonic arrays of gold nanostructures to explore the possibility of achieving strong plasmon-exciton coupling instead of using PCysMA brushes that need several chemical processes to create a suitable chemical linker for the attachment of *Chla*. PDMA brushes possess stimulus responsive properties that could be exploited to facilitate active control of the coupling by changing pH of the coupling media.

In addition, polymer brush will be used to regulate the packing of gold nanoparticles, instead of growing PDMA from gold nanostructure. So, novel solution processing routes to the formation of quantum-optical films based on these structures will be explored. To achieve this aim, PDMA will be grown from brominated solid substrates. Colloidal AuNPs will be synthesised in one step via chemical reduction method and will be imbedded into PDMA brushes. This will be followed by functionalisation of the structure with *chlorophyll a*.

A similar solution processing route will be used to synthesis plasmonic structure based on the packing of AINPs into PDMA brushes. AINPs will be synthesised via decomposition of alane complex with titanium isopropoxide. Then, AINPs will be imbedded into PDMA brushes. LSPR will be controlled via sono-solvo chemistry. The possibility of obtaining plasmon-exciton coupling by the attachment of *ZnChla* to PDMA-AINPs structure was investigated.

UV-Vis spectrophotometer (UV-VIS) will be used to record the change in the optical properties. The thickness of the structure will be measured by Spectroscopic Ellipsometry (SE). Atomic Force Microscopy (AFM) will be used to study the morphologies of the surfaces, X-ray Photoelectron Spectroscopy (XPS) will be used to study the change in the chemical composition of the samples. Contact Angle goniometer (CA) will be used to monitor the surface energy changes.

CHAPTER 3: EXPERIMENTAL

3.1 Materials

Glass substrates (cover slips glass slides, Menzel-Glazer/ 22*60# 1.5), tetrahydrofuran (99.7%, HPLC grade), petroleum ether 40-60 °C, hydrochloric acid (35%), sodium hydroxide and silica gel powder were provided by VWR. Quartz coverslips, fused, (25.4*25.4*0.25 mm), 1, 10-diiodooctane 98% and copper I bromide ($\geq 98\%$) were supplied by Alfa Aesar. Chloroauric acid (gold(iii) chloride hydrate, 99.9% trace metals basis) HAuCl_4 , trisodium citrate (sodium citrate tribasic dihydrate, 99%), 3-aminopropyltriethoxysilane ($\geq 99\%$), 2-bromoisobutryl bromide (98%), triethylamine ($\geq 99\%$), dichloromethane (99.9%, HPLC grade), 2-(dimethylamino)ethylmethacrylate (98%), 1,1,4,7,10,10-hexamethyltriethylenetetramine (97%), 1-iodooctadecane (95%), glacial acetic acid (99%), n-hexane (97%, HPLC grade), diethyl ether (99.8%), zinc acetate dehydrate, titanium isopropoxide (97%), alane N,N-dimethylethylamine complex, 0.5 M in toluene, 1,2-epoxyhexane (97%), silver nitrate, sodium borohydride powder ($\geq 98.0\%$) and bis[2-(2-bromoisobutyryloxy)undecyl]disulfide (DTBU) were purchased from Sigma Aldrich. Ethanol, absolute (99.8%, HPLC grade), acetone (99.8%, HPLC grade), methanol (99.8%, HPLC grade), toluene (99.8%, HPLC grade), isopropan-2-ol (99.5 % HPLC grade), hydrogen peroxide (30% w/v), sulfuric acid (95%), dimethylformamide (99%), magnesium sulphate anhydrous, sodium hydrogen carbonate, sand low iron and sodium chloride were supplied by Fisher Scientific. Silicon wafers 6" (150 mm) was purchased from Pi-KEM.co.uk. Spinach leaves were obtained from a local supermarket. Fresh water was deionised by Elga PURELAB Nano-pore system operates with a resistivity of 15 $\text{M}\Omega$ cm. Copper mesh electron microscope grids (1000-2000 mesh Cu) were used for micropatterning purpose and obtained from Agar Scientific (Cambridge). Dry toluene and dry diethyl ether were obtained from an onsite Grubbs dry solvent system. All these materials were used as received without any further purification. Copper bromide was stored under vacuum. DMA was stored at 4 °C after removal of the inhibitor. Chloroauric acid was stored between 3-8 °C in the dark.

3.2 Cleaning of glassware and substrates

Piranha solution (30:70 H₂O₂:H₂SO₄) was used to clean substrates and glassware. All substrates and glassware were placed in a large beaker on a metal plate inside a fume cupboard. 30% hydrogen peroxide was added, followed by the addition of a 95% sulfuric acid to cover the glassware. After 2 h, the piranha solution was removed into a water bath at high dilution. The glassware was rinsed with copious amount of deionised water and the acidity was tested using pH litmus paper to confirm the removal of the acid. The glassware was placed in an oven overnight to dry. After drying, the substrates and glassware were wrapped with aluminium foil until use. *Note: Piranha solution is a dangerous solution and extremely strong oxidising agent that may react with organic substances violently. Therefore, it is necessary to use special gloves, face shield, and goggles for Piranha cleaning procedures along with the rest of the necessary precautions for the lab.* Laboratory tools such as tweezers and suba-seals were washed with acetone and deionised water, then immersed in isopropanol under sonication for 30 min. This was followed by washing with deionised water and drying under a stream of nitrogen gas.

3.3 Sample handling

Piranha-cleaned substrates were cut into about 5x10mm pieces using diamond scribe, metallic ruler and glass stage, which have been cleaned previously with ethanol. The slides were cut asymmetrically assist in identifying which slide was being modified or analysed, see **Figure 3-1**.

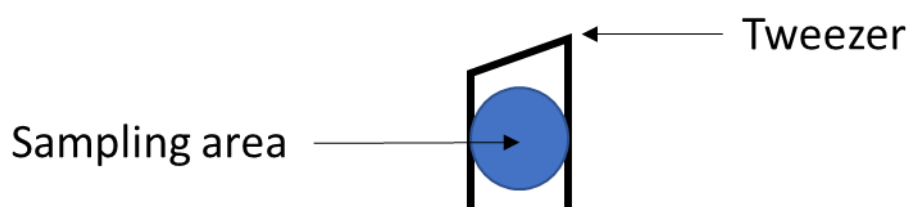


Figure 3-1: illustration of sample handling.

Dust created while cutting slides was removed by a stream of nitrogen gas. The slides were only handled with care using tweezers that had been previously cleaned with ethanol. The same protocol was used for handling silicon wafers and quartz chips.

3.4 Synthesis

Formation of self-assembled BIBB-APTES layer onto solid substrate

Amine-functionalised substrates were prepared by immersion of piranha-cleaned glass slides in a freshly prepared solution of 2.0% v/v APTES in ethanol, which had been aged for 5 min. The immersion time was 30 min. The modified glass substrates were then washed thoroughly with ethanol and dried under a nitrogen stream. This was followed by annealing the samples inside a vacuum oven at 120°C for 30 min. APTES-functionalised substrates were then derivatised in a solution of BIBB (0.37 mL, 3 mmol) dissolved in a mixture of TEA (0.41 mL, 3 mmol) and 60 mL dichloromethane. The resulting BIBB-APTES initiated glass substrates were rinsed with ethanol, dried under a nitrogen stream and stored in a fridge until used. BIBB-APTES samples were characterised by XPS, AFM and CA.

3.4.1 Growth of PDMA via ATRP

In a 100 mL round bottom flask, 50 mL of DMF was used to dissolve 50.48 mL of DMA (47.1 g, 30 mmol) at 90°C under stirring. The mixture was deoxygenated via three cycles of vacuum/nitrogen for around 20 min. HMTETA (0.30 mL, 0.15 mmol) was added to the mixture with further deoxygenation for approximately 10min. This was followed by the addition of Cu(I)Br (0.14 g, 0.10 mmol), which leads to a change in the colour of the solution from colourless to light brown within several seconds. The mixture was deoxygenated for further 10 min. Then BIBB-APTES functionalised samples were placed in Schlenk tubes under nitrogen. 4 mL of DMA/ catalyst solution was added to each sample under nitrogen at 90°C. The growth of PDMA was allowed to proceed for different polymerisation times ranging from 1 min to 2 h. Finally, the polymerisation was terminated by removing the slide from the mixture, and removal

of the residual of monomer and catalyst by rinsing with isopropanol and ethanol, followed by drying with nitrogen. The structure of PDMA brushes was analysed by XPS and the thicknesses of the polymerised brushes were measured by SE.

3.4.2 Growth of PDMA brushes via ATRP from gold nanostructure

PDMA brushes were grown from Au-coated glass slides following the procedure described above. However, for gold surfaces, DTBU was used to form the adsorbed layer of initiator rather than forming BIBB-APTES film as was used for polymerisation from glass substrates.

3.4.3 Synthesis of quaternised PDMA

A fresh 200 μ M solution of 1-iodooctadecane was prepared in tetrahydrofuran. The previously prepared PDMA-coated slides were immersed in the 1-iodooctadecane solution for 18 h at room temperature. After that, the quaternised PDMA brushes were removed from the 1-iodooctadecane solution, followed by rinsing with ethanol and sonication for 10 min in THF and dried under nitrogen gas. The same procedure was repeated using different concentrations of 1-iodooctadecane to find out the optimal conditions for maximum quaternisation.

3.4.4 Extraction of *chlorophyll a* from spinach leaves

The twigs and middle veins of the spinach leaves were removed from the spinach leaves, and the leaves were washed with deionised water and dried with paper towel. This was followed by vigorous blending of the leaves in acetone (300 mL) for 10 min. The mixture was allowed to settle. After appearance of the dark green pigment at the top of the solid sediment, the pigment was separated and washed with acetone several times, and the solvent was removed by rotary evaporator. For further extraction of *chlorophyll a* from the organic and oily impurities, the pigment was dissolved in petroleum ether 40-60°C (150 mL), then a mixture of 60% methanol in water was used to wash the product three times. A solid portion MgSO₄ was added to the product for drying, and the mixture was filtered to remove MgSO₄ and the aqueous

layer. Petroleum ether was evaporated by rotary evaporator to give *chlorophyll a* (dark green pigment).

3.4.4.1 Conversion of *chlorophyll a* into *pheophytin a*

Chlorophyll a was converted into *pheophytin a* by dissolving the dark green pigment in 25 mL acetic acid under stirring for 3 h. Then, 5 mL of concentrated solution of sodium hydrogen carbonate was added to neutralise the pH to 7. DCM was used to separate the product from the mixture. The organic layer was washed with deionised water and dried with solid MgSO_4 which was removed by filtration. DCM was evaporated by rotary evaporator to give *pheophytin a* (dark blue pigment). *pheophytin a* was purified by column chromatography using a mixture of hexane, diethyl ether and acetone in the ratio 6:3:1 as mobile solvent. The formation of pheophytin was analysed by MS.

3.4.4.2 Conversion of *pheophytin a* into *Zn-chlorophyll a (ZnChla)*

The dark blue pigment was dissolved in DCM (50 mL), and the resulting solution was mixed with solution of zinc acetate dehydrate (0.25g) in 4 mL methanol. The mixture was refluxed under argon at 35°C for 1 h. The product was extracted using 20 mL diethyl ether and washed with diethyl ether three times and with water three times before being dried with solid MgSO_4 . MgSO_4 was removed by filtration, and the solvent then was removed under reduced pressure. The resulting *ZnChla* was purified by column chromatography using a mixture of hexane, diethyl ether and acetone in the ratio 6:3:1 as mobile solvent. The formed *ZnChla* was analysed by MS, NMR and UV-Vis spectroscopy.

3.4.5 Synthesis of polycrystalline gold film

Piranha cleaned glass slides were coated with a 2-5 chromium followed by 20 nm gold in an Edwards Auto 306 bell jar vacuum coater system with a base pressure of 8×10^{-7} mbar. Evaporation rates of ca. 0. nm s⁻¹ and ca. 0.4 nm s⁻¹ were used for Cr and Au, respectively. The samples were allowed to cool for 30 min and rinsed with ethanol prior to use. The

substrates were immersed in a 1 mmol solution of octadecanethiol in degassed ethanol overnight and rinsed with ethanol and dried with nitrogen before use.^[23]

3.4.6 Synthesis of AuNPs

In an Erlenmeyer flask, 500 mL of HAuCl_4 (0.17, 1 mmol dm^{-3}) was boiled under reflux. The solution was stirred vigorously using magnetic stirrer-hot plate. Then, 50 mL of trisodium citrate (0.59g, 38.8 mmol dm^{-3}) was added in a single addition under vigorously stirring. The yellow solution was turn first dark blue and finally deep red colour within a few minutes, indicating the formation of AuNPs. The reactants were continuously stirred under boiling temperature for 15 minutes. Then, the mixture was allowed to cool. Finally, the volume was adjusted to 500 mL using fresh deionised water. The solution of AuNPs was stored in the dark between 3-8 °C.

3.4.7 AINPs synthesis

3.4.7.1 Chemical decomposition

Using a Schlenk system, 13 mL of alane N,N-dimethylethylamine complex (0.0065 mol) in toluene was transferred into a double necked round bottom flask using a Luer lock syringe under nitrogen. This was followed by addition of 25 mL of dry ethyl ether DEE under vigorous stirring. 16 μL of titanium isopropoxide was dissolved in 1.6 mL of toluene and added to the alane/ DEE mixture in the flask. The addition of titanium isopropoxide leads to a change the colour of the mixture to a dark brown, promptly, indicating the formation of AINPs. After that, 0.15 mL of 1,2-epoxyhexane was added to the prepared AINPs immediately as a capping agent. The particles and the capping agent were allowed to mix properly for 30 min under stirring. The solvents were removed under vacuum.^[201]

3.4.7.2 Sono-Solvo chemistry

1 g of Al foil was cut into small pieces and sonicated in a mixture of 60 mL ethanol and 30 mL of ethylene glycol using an ultrasonic bath at 50 °C for 6 h. During this process the colour changed to dark grey gradually. The large parts were allowed to precipitate overnight. The

supernatant was collected into round bottom flask that was connected to Schlenk system. After the removal of ethanol under vacuum at 110 °C, 10 mL of ethylene glycol was added to the mixture. The reaction was allowed to proceed under 197 °C for 14 days. During this period, the solution colour turned to yellow indicating the formation of AINPs. In order to purify the product, 0.5 mL ethanol was added to 0.5 mL of the reaction mixture and centrifuged to remove the large particles. The top part of the supernatant was collected to obtain AINPs in ethanol.^[202]

3.4.8 Synthesis of 2-(10-iododecyl) Nile Red

Nile Red (100 mg, 0.3 mmol), K₂CO₃ (250 mg, 1.81 mmol) and 1,2-diiodooctane (1.18 g, 3.22 mmol) were dissolved in 2 mL DMF. The reaction mixture was stirred at 60 C for 2 h under nitrogen. The product was then extracted with ethyl acetate (30 mL) and washed 3 times with water (3*20 mL) and brine (30 mL) and dried to afford dark red solid product. The produced iodinated Nile Red was purified by column chromatography using a mixture of 1:2 ethyl acetate and petroleum ether to yield 60 mg iododecyl Nile Red.

3.5 Deposition methods of the materials on solid substrates

3.5.1 Self-assembled monolayers (SAMs)

SAMs are self-organised and well-ordered molecular assemblies that can be produced by spontaneous adsorption of an active surfactant on a variety of solid substrates.^[124] SAM formation results in a structure that is at or near thermodynamic equilibrium, which promotes self-healing and defect rejection, as well as a densely packed and well-ordered stable surface configuration.^[203] The general structure of SAMs consists of three main parts: head-group, backbone and end-group, see **Figure 3-2**. The head-group has strong, specific interaction with substrate. The backbone is made up of aliphatic chains or aromatic oligomers that control molecular self-assemblies. The end-group or the terminal group determines the functionality of the SAM as well as the topography and surface energy of the modified surface.^[124]

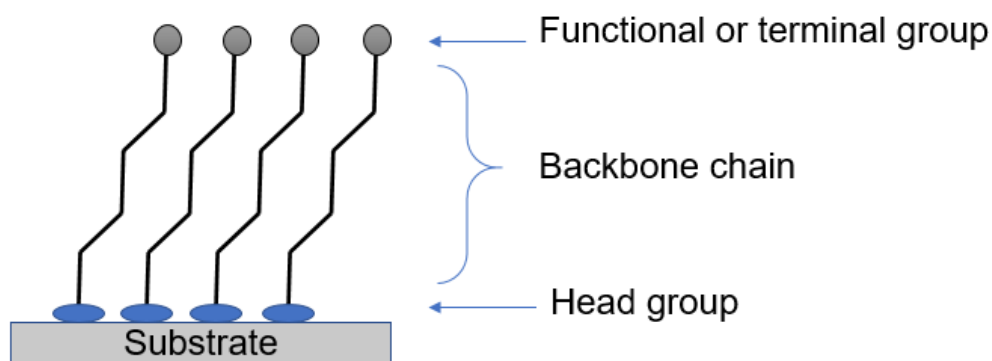


Figure 3-2: Schematic illustration of the formation of SAMs.

Many self-assembly systems have been examined. SAMs of alkyl thiolates on gold are the most researched to date. Silanes on hydroxylated surfaces are significant systems for many technological applications, forming not only on glass or silica, but also on the native oxide of many materials.^[203] The synthesis of polysiloxane in situ, which is coupled to the surface silanol groups ($-\text{SiOH}$) via $\text{Si}-\text{O}-\text{Si}$ interactions, is the driving force behind the formation of a SAM monolayer using alkylalkoxysilanes, alkylchlorosilanes and alkylaminosilanes.^[203] Functionalised long hydrocarbons chains are the most used as SAMs building block, although these two-dimensional systems are not limited to long chains materials.^[124] SAMs can be formed mostly on metals, such as Au, Ag, and Cu, using thiol chemistry, or alkyl siloxanes on hydroxyl-terminated substrates, such as glass surfaces, Si/SiO_2 and $\text{Al}/\text{Al}_2\text{O}_3$ using siloxy linkages.^[203] SAMs have been successfully utilised to modify a number of hydroxylated substrates. For example, glass, quartz, silicon oxide, aluminium oxide, zinc selenide, mica and germanium oxide.^[203] Recently, functional SAM systems have gained great attention as significant interfacial systems for sensing and other analytical applications.^[203]

In the case of particles deposition, a colloidal solution is used to immerse the substrate for a specified time, after that the substrate is removed from the solution and dried. The deposited particles are bound strongly to the substrate and do not aggregate upon drying. Thus, Stable

colloids allow for a uniform deposition with almost little or no aggregation, although surface preparation requires high level of experience.

3.5.2 Dip coating

Dip coating is a procedure in which the substrate to be coated is submerged in a liquid and then extracted at a predetermined temperature and air pressure, see **Figure 3-3**. The coating thickness is primarily determined by the liquid's viscosity, solid content, and withdrawal speed. A new angle-dependent dip coating method has recently been developed. For optical coatings, layer thickness control is critical. The angle between the substrate and the liquid surface determines the coating thickness. The dipping angle can be used to measure layer thickness, and different layer thicknesses can be achieved on both the top and bottom sides of the substrate.^[204]

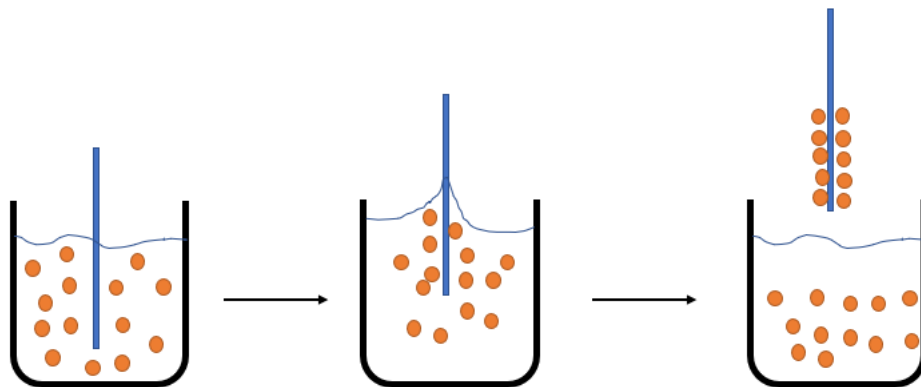


Figure 3-3: Schematic illustration of dip coating process.

3.5.3 Spin Coating

The acceleration of a liquid droplets on a spinning substrate is known as spin coating. A droplet of the coating material is manually or robotically placed in the centre of the substrate. Then the droplet is spread over the top of the wafer by spinning at around 500 rpm for the first few seconds, then at higher speed, see **Figure 3-4**. The mechanics of spin coating

requires a delicate balance of centrifugal forces regulated by spin speed and viscous forces defined by solvent viscosity. Also, there are some variable parameters that can be involved in spin coating such as, solid content, solution viscosity, angular speed and spin speed and time.^[205]

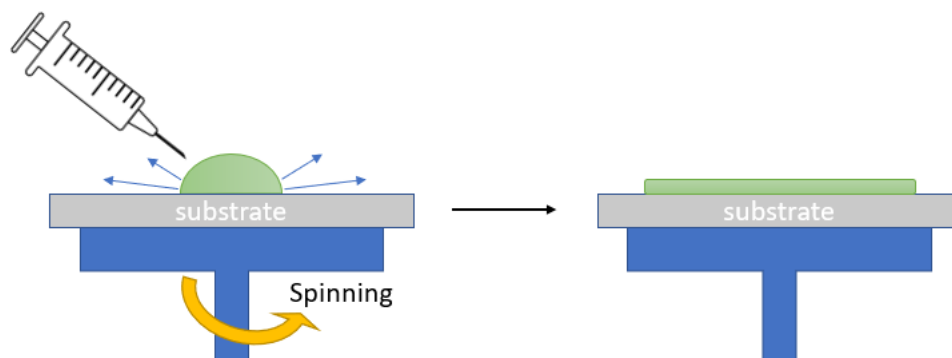


Figure 3-4: Schematic illustration of spin coating.

3.5.4 Drop- casting, simple deposition

Depending on the desired density of the material to be deposited, a drop of the solution was placed on the substrate and left to dry by naturally, often between a few minutes to hours, or using nitrogen stream. After this treatment, the sample can be used immediately, see **Figure 3-5**. In this process, unmodified substrates can be utilised, and basic cleaning process are often enough. Compared to self-assembly that typically last for few hours to days, this technique allows faster preparation with less effort.^[206]

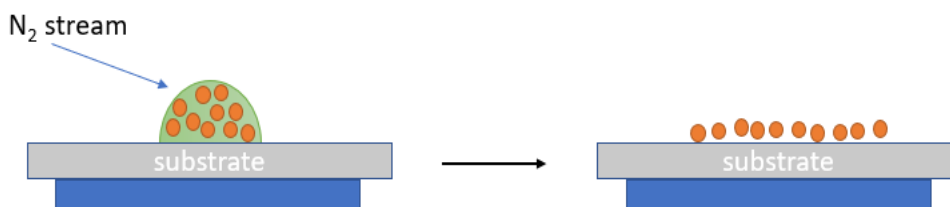


Figure 3-5: Schematic illustration of simple deposition.

Lee *et al.* introduced a fascinating deposition process to enhance the drop-casting method. After heating the substrate to 150°C, a drop of the solution was dropped onto preheated substrate leading to fast evaporation of the liquid content leaving a uniform dispersion of nanospheres and rods, see **Figure 3-6**. The boil deposition method produces superior outcomes with low aggregates and less dependence on solvent viscosity.^[207]

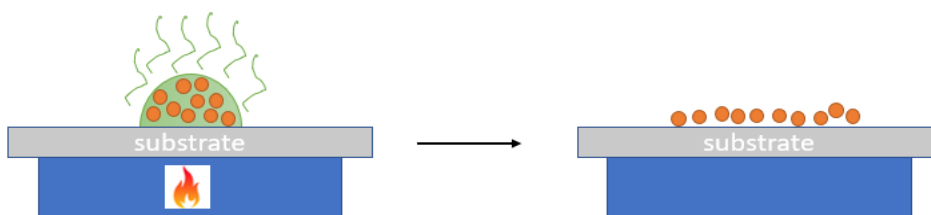


Figure 3-6: Schematic illustration of boil deposition.

3.6 Surface modification

3.6.1 Photolithography of BIBB-APTES films

A frequency-doubled argon ion laser beam (Coherent Innova) FreD300C was used to expose the samples at wavelength of 244 nm. A beam expander was used to expand the exposed area to 0.8 cm². BIBB-APTES films were exposed to a series of exposure doses ranging from 0.1 to 6 J/cm². Cu electron microscope grid obtained from Agar, Cambridge, UK were used to achieve micropattern scale.^[76]

3.6.2 IL fabrication of AuNPs nanostructure

A Coherent Innova 300C FreD frequency-doubled argon ion laser was employed as the light source for photolithography, emitting UV light at 244 nm. To create a coherent beam, a spatial filter with an aperture of 5 μm was employed to focus the laser beam through a lens and the edge of the coherent beam was cut using a mask with an appropriate aperture. Modified ODT

SAMs on gold films were etched by immersion the samples in a solution of (0.2 mol dm⁻³) 2-mercaptoethylamine hydrochloride in 8% v/v of 35% of ammonia solution in ethanol. After that, the samples were rinsed with ethanol and dried with nitrogen. Annealing of gold layer was carried out using a muffle furnace (Carbolite) in air at 450-560°C for different period of times (50-120 min). The heating rate was ca. 7 °C min⁻¹. The annealed samples were allowed to cool at room temperature. Cold piranha solution was used to clean the sample allowing them to be reused several times.

3.6.3 Drop-casting of *Chla* and J-aggregates onto PDMA grafted Au arrays

Au-coated glass slides were placed on a previously cleaned glass stage facing upwards. 70 μL of 250 μM *Chla* solution was spread onto the surface of the sample. The droplet of the solution was allowed to dry naturally. After that, the sample was blown dry with nitrogen. This procedure was used to deposit J-aggregates on Au-coated glass slides.

3.6.4 Functionalisation of polycrystalline gold film or Au nanoarrays with DTBU

Cr/Au-coated coverslip glass slides were immersed in a 2 mM solution of (DTBU) in nitrogen-degassed ethanol. The reaction was allowed to proceed in a fridge at temperature of 4 °C for 24 h to form a bromine-terminated initiator monolayer. The slides were then removed from the solution and rinsed with ethanol and blown dry with nitrogen stream. This procedure was followed to functionalise Au nanoarrays samples with DTBU.

3.6.5 Immobilization of AuNPs onto APTES-functionalised solid substrate

APTES-functionalised glass slides were immersed in suspensions of AuNP with three different concentrations (saturated, diluted 1-1 and diluted 1-10) of AuNPs for the desired

immobilization time in the dark at room temperature. Then the samples were rinsed with deionised water, dried by a nitrogen stream, and characterised via UV-vis spectroscopy and AFM.

3.6.6 Attachment of *ZnChla* to PDMA brushes and q-PDMA

Concentrations of *ZnChla* ranging from 0-500 μM were used to functionalise PDMA brushes. This was performed by immersion of PDMA samples in the solutions of *ZnChla* in the dark at room temperature overnight. Then the samples were rinsed with deionised water and dried by nitrogen stream. *ZnChla*-functionalised PDMA were characterised by UV-Vis spectroscopy, AFM, SE and XPS.

3.6.7 Incorporation of AuNPs into brush films

PDMA-coated glass substrates prepared as described previously were immersed in a suspension of AuNPs for the desired immobilization time using 1.5 mL Eppendorf tubes. The reaction was allowed to proceed in the dark at room temperature to form glass-BIBB-APTES-PDMA-AuNPs layers. Then the samples were rinsed with deionised water and dried by nitrogen stream. AuNPs-functionalised PDMA brushes were analysed by UV-Vis spectroscopy, AFM and SE.

3.6.8 Incorporation of AINPs into brush films

PDMA-coated glass substrates prepared as described previously were immersed in AINP suspension for the desired time in 1.5 mL Eppendorf tubes. The reaction was allowed to proceed in the dark at room temperature to form glass-BIBB-APTES-PDMA-AINPs layers.

Then the samples were rinsed with diethyl ether and dried by nitrogen stream. AuNPs-functionalised PDMA brushes were analysed by UV-Vis spectroscopy, AFM and XPS.

3.6.9 Attachment of *ZnChla* to AuNPs-functionalised PDMA system

ZnChla was attached to AuNPs-functionalised PDMA brushes by immersion of the samples (glass-BIBB-APTES-PDMA-AuNPs) in a solution of *ZnChla* for the desired immobilization time in the dark at room temperature to form glass-BIBB-APTES-PDMA-AuNPs-*ZnChla* structures. Then the samples were rinsed with deionised water and dried under a stream of nitrogen. *ZnChla*-functionalised systems were characterised by UV-Vis spectroscopy, AFM, SE and XPS.

3.6.10 Attachment of *ZnChla* to AuNPs-functionalised PDMA system

ZnChla was attached to AuNPs-functionalised PDMA brushes by immersion of the samples (glass-BIBB-APTES-PDMA-AuNPs) in a solution of *ZnChla* for 24 h in the dark at room temperature to form glass-BIBB-APTES-PDMA-AuNPs-*ZnChla* structures. Then the samples were rinsed with diethyl ether and dried by nitrogen stream. *ZnChla*-functionalised systems were characterised by UV-Vis spectroscopy.

3.6.11 Attachment of INR to PDMA brushes

Different concentrations of INR ranging from 0.25 mM - 8 mM were used to functionalise PDMA brushes. The derivatisation reaction was conducted by immersion of PDMA grown from BIBB-APTES initiator in the solutions of INR overnight in the dark at room temperature. Then the samples were rinsed with ethanol and dried by nitrogen stream. INR-functionalised PDMA were characterised by UV-vis spectroscopy, SE and XPS. This procedure was followed to

attach INR to PDMA that grown from Au-coated glass slides that functionalised with bromoisobutyrylundecanethiolate (BIBUDT).

3.6.12 Spin-coating of *Chla* PDMA grafted from gold nanostructure arrays

PDMA-functionalised Au nanoarrays fabricated by IL sample was placed on the stage of spin-coater directed upwards. Then, 5 μL of *Chla* solution was spin-coated onto the surface of the sample at 800 rpm. This procedure was performed using different concentration of *ZnChla* including 1.67, 2.5 and 3.35 mM. After that, the sample was blown dry with nitrogen.

3.6.13 Concentration-dependence of plasmon-exciton coupling

PDMA brushes were polymerised for 15 min and functionalised with AuNPs as described previously. Then the structures were immersed in a series of different concentrations of *Chla* solutions in the range from 0 to 25 μM for 24h at 25 °C in the dark to functionalise PDMA brushes.

3.7 Analytical techniques

3.7.1 Atomic Force Microscopy AFM

Atomic Force Microscopy (AFM) is a member of the scanning probe microscopy family of technique. It is also known as Scanning Force Microscopy (SFM). In AFM, a sharp tip attached to a flexible cantilever is scanned across the sample surface. Changes in the interaction force lead to change in the deflection of the cantilever which are measured using an optical deflection (detection) system. This is based on the principle of measuring the force between tip and surface which can be demonstrated by Hooke's law, see the following equation.

$$F = -K * X$$

where, F is the force, K is the spring constant and X is the distance.

The main components of an AFM system are the laser source, scanner, analysing unit and controlling software. AFM can be operated in one of three main modes: contact mode, non-contact mode and tapping mode. In contact mode there is direct physical contact between the tip and the surface. In non-contact mode, there is no contact between the tip and the sample surface, and the tip oscillates with a constant amplitude at frequency slightly higher than cantilever's resonance frequency. AFM measures repulsive force in contact mode and attractive force in non-contact mode. However, non-contact measurement is technically difficult. Tapping mode may be considered to be an intermediate between contact and non-contact modes being based on soft and intermittent contact with the sample. The tip gently taps on the surface sample while the oscillation amplitude remains constant. Contact mode is suitable for rough mechanically robust samples, and it is relatively faster than other modes, but it can damage soft samples due to direct contact which may cause scratch on the surface. Compared to contact mode, non-contact mode is appropriate for hydrophobic samples, but it is the slowest mode. However, non-contact mode is a specialised mode usually performed in ultra-high vacuum, and not widely used because of the experimental difficulties (although it can

achieve highest resolution of any AFM technique. Tapping mode is less harmful due to low friction between the tip and the sample and it has almost higher resolution.^[208]

AFM can provide different types of data such as friction, height, phase, amplitude which is particularly in tapping mode and deflection in contact mode. These data can be displayed through a number of channels that can be easily managed.^[209] AFM can also provide 3D images of the analyte surface. Although AFM has been proven to be a powerful tool that used to analyse a wide range of samples such as metals, plastic, glasses, cells walls and bacteria, it subject to some limitations. In particular, the finite size of the probe can impact the analysis of very small structures. For surface features that approach the dimension of the AFM tip, the sample profile becomes convoluted with that of the tip, leading to an apparent increase in surface feature sizes, as illustrated by **figure 3-7**.^[210] In addition, a variety of artefacts may be observed in images, due to aberrations in tip manufacturing, tip damage and the transfer of contamination to the probe.

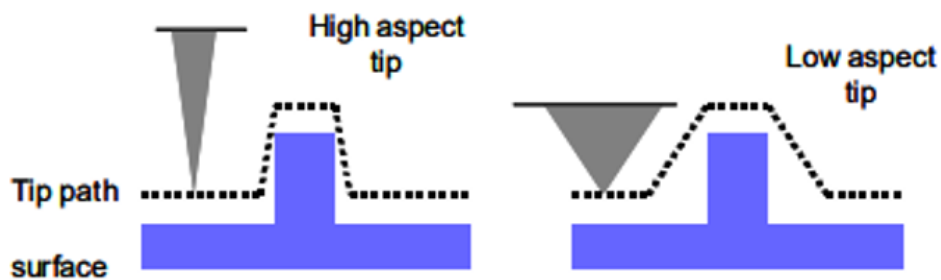


Figure 3-7: Schematic diagram of the effect of probe quality on AFM images where non-sharp tip can cause spatial obstruction and reflect fake images.^[210]

3.7.1.1 AFM experimental procedure

AFM contact mode and tapping mode images were obtained using a Digital Instruments NanoScope 5 multimode atomic force microscope (Bruker, Coventry, UK) fitted with a “J” scanner. Silicon nitride nano-probes (Bruker, Coventry, UK) with nominal spring constants ranging from 0.06 to 0.350 N m⁻¹ were used for contact mode imaging, while silicon nano-probes (Bruker, Coventry, UK) with nominal spring constants of 26 N m⁻¹ were used for tapping mode imaging. All measurements were conducted in air at room temperature. AFM data analysis was performed using NanoScope Analysis (v.1.5). The analysed images were flattened to the 3st order.

3.7.2 Contact angle (CA) measurements:

Several surface properties such as wetting, adhesion and surface free energy have been studied using expensive, time consuming and spatialised equipment. From this point of view, there was a need to develop simple technique to reduce these obstacles. Contact angle goniometry (CAG) provides a simple, inexpensive means to investigate the thermodynamics of surfaces. When a drop of liquid is placed in contact with a solid surface, the resulting contact angle depends on the thermodynamics of the solid, liquid and vapor interaction at the perimeter of the spreading drop. CA has been considered as a quantitative technique in same research, although its main use is as a qualitative technique to detect some specific properties.^[211] In this technique, a drop of liquid is place on the solid surface using syringe equipped with a thin needle. The drop is illuminated from behind and imaged using a travelling telescope. The angle between the surface and the tangent to the drop surface where in meet the solid can be measured manually by an optical goniometer or via image analysis of a photographs of the liquid drop. When the drop touches the solid surface, it begins to spread until the equilibrium is reached. The contact angle at equilibrium depends on the free energy of solid-liquid, solid-vapor and liquid- vapor interactions as shown in **Figure 3-8 (Top)**. Equilibrium contact angle can be expressed by the following “Young’s equation”.^[212]

$$\gamma_{sv} = \gamma_{sl} + \gamma_{lv} \cos \theta$$

where, γ is free energy of the surface and θ is CA. Measurements of contact angles provide a useful and sensitive tool for determining a variety of surface properties such as hydrophilicity and hydrophobicity, roughness, liquid surface tension, solid surface energy and surface heterogeneity. Notably, the value of the contact angle depends on the nature and properties of both phases; liquid and solid surface, where CA takes value from zero to 180°, i.e., drops of the same liquid act in a different manner with different substrates, and vice versa, where resulting contact angles are different in case of different liquids drops with identical surface. For example, mercury, water, and silicone oil drops form three different contact angle values on the same glass substrate. This is because of the differences in the surface tensions of these liquids. for water drops, the surface is said to be hydrophilic for contact angles less than 90°, and hydrophobic for contact angles greater than 90°. Where the drop does not wet the surface at all, the material is said to be "superhydrophobic", see **Figure 3-8 (Down)** .^[212]

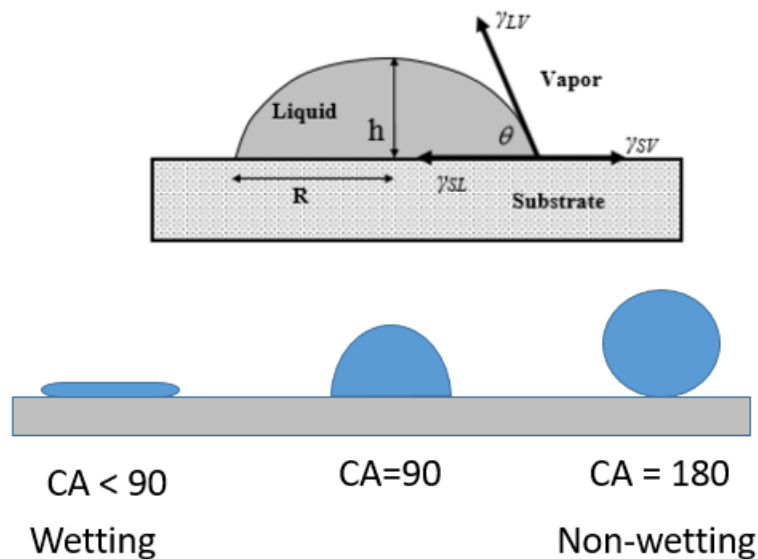


Figure 3-8: Diagram of contact angle parameters and different liquids drops with different contact angles behaviour on solid surface.^[212]

3.7.2.1 Contact angle experimental procedure:

Advancing sessile drop water contact angles was measured using a Rame Hart sessile-drop model 100-00 goniometer. The instrument was equipped with a micro-litre syringe that was used to place a 2 μL drop of deionised water (18.2 $\text{M}\Omega\cdot\text{cm}$) on the surface to be analysed. A telescope with an integral goniometer is used to measure the contact angle from the right and left sides, after adjusting the base line in a parallel and congruent manner with the drop line contact with the surface. The obtained contact angle values are the mean of at least three different measurements.

3.7.3 Spectroscopic Ellipsometry (SE):

Spectroscopic Ellipsometry SE is useful optical method for characterisation of thin films and surfaces. It is a member of a small group of techniques that have been employed for measuring film thicknesses to a high degree of precision and accuracy.^[213] The term 'ellipsometry' refers to the fact that the technique involves illuminating the sample with elliptically polarised light^[214]. The light that is reflected from the surface is analysed using a rotary polariser. Polarised light can be characterised by measuring the alteration of the amplitude ratio φ and phase deference \emptyset of it. These two parameters are reported to be sensitive to a number of sample properties which include refractive indexes and layers thicknesses of both substrate and deposited films taking into consideration incidence angle, wavelength of the light and the permeation depth through the sample.^[213] Ellipsometer consists of monochromatic and collimated light source which is supplied with a polariser, sample stage, an analyser and photodetector as represented in **Figure 3-9**.^[215]

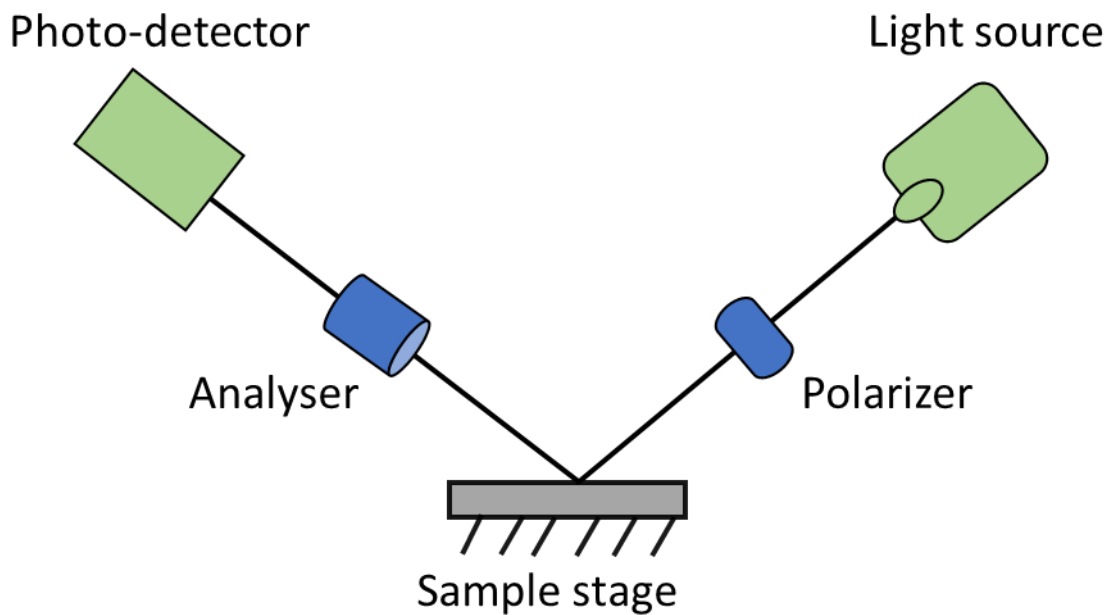


Figure 3-9: Schematic diagram illustrates the structure and significant component of ellipsometer.

In SE, a Quartz Tungsten Halogen (QTH)^[216] light source is used to cover the UV-VIS spectral range. Beside this light source usually a He-Ne laser beam is used at 70° incidence angle with wavelength of around 628 nm.^[217] There are many applications that involve SE such as the examination of optical characteristics of both bulk materials and thin films in addition to monitoring thin layers growth. Data that obtained by SE are complex to interpret and an appropriate model must be constructed in accordance with characteristics of the material in order to analyse the data. Moreover, it is important to note that the optical characteristics of thin layers are completely different from the properties of bulk materials. This means that by proper and careful modelling of SE data, they can be used to characterise the properties of thin films with high precision.^[218] On the other hand, it is considered as relatively slow experimental technique. Also, there are some limitations that should be considered during SE measurement. Firstly, the data must be taken at inclined incidence. Secondly, surface of the sample should be at a small degree of roughness.^[214]

3.7.3.1 Variable angle spectroscopic ellipsometry VASE

Ellipsometry is a highly accurate and repeatable method that does not require any reference material because it measures the ratio of two values. It is extremely sensitive to the presence of even very thin coatings because it detects a phase shift between polarizations along with an amplitude ratio. Another feature of ellipsometry is that it measures multiple parameters of the film at the wavelength of interest. The combination of spectroscopic capability with multiple angles measurements generates additional information and improves the sensitivity to the unidentified parameters. In variable angle spectroscopic ellipsometry (VASE), ellipsometry data are collected at variable incident angles, see **Figure 3-10**. This technique is a potential method for studying novel materials and procedures. For the most demanding research applications, sophisticated instruments and software are available for the collecting and interpretation of VASE data, in addition to its simplicity that makes it possible to use VASE for standard measurements as well. VASE analysis can be used to extract a variety of the desirable material characteristics, such as layer thickness, surface and/or interfacial roughness, and optical constants.^[219]

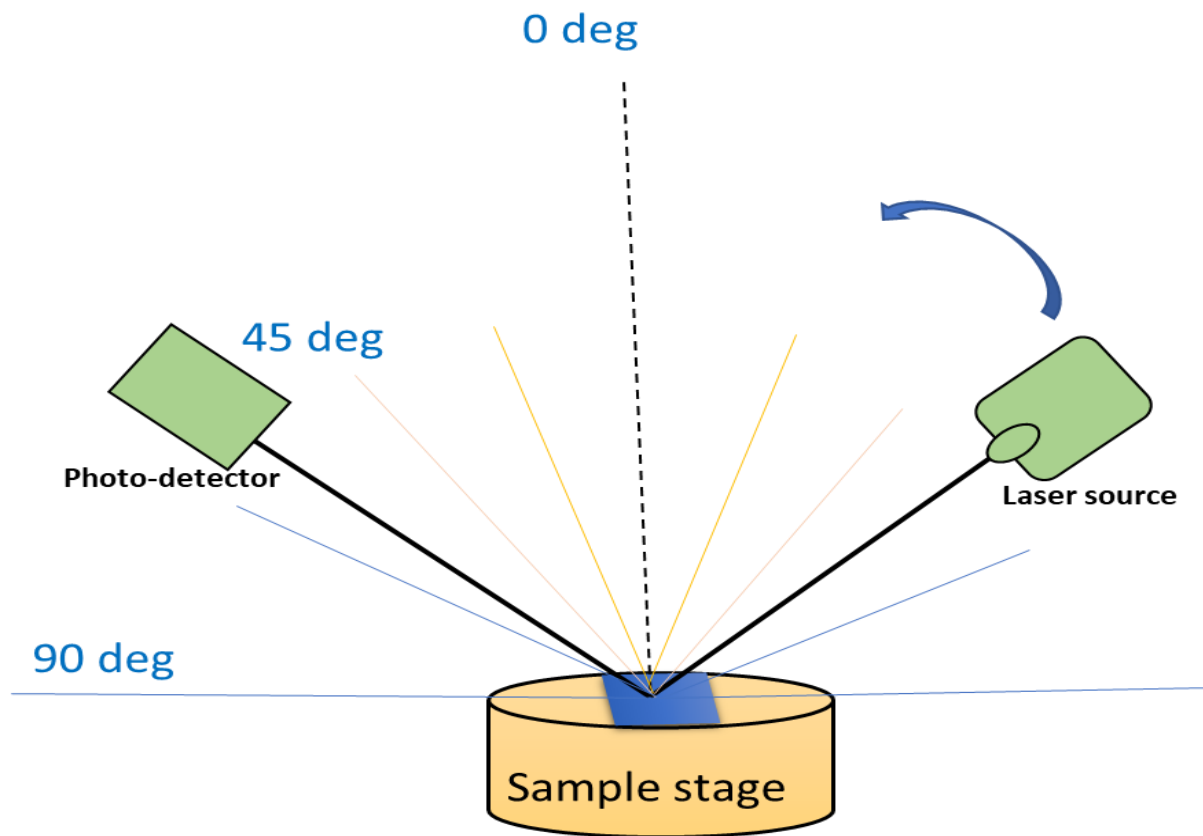


Figure 3-10: Schematic diagram showing the setup of VASE technique.

3.7.4 Total internal reflection ellipsometry TIRE

Total internal reflection ellipsometry (TIRE) is measurement technique, that is a combination of internal reflection and ellipsometry. Internal reflection in this context refers to a condition where light is reflected at an interface where the refractive index of the incident media is greater than that of the reflecting material. Here, the incident semi-infinite medium is made of glass and is normally transparent. In most simulations, the reflecting semi-infinite media will be a gas or a liquid, typically water-base, and this medium can typically be opaque depending on how the refractive index complex is valued. The intensity changes are the main focus of SPR-based approaches. However, in this case, the ellipsometry principle is used to assess the polarisation changes caused by reflection.

Figure 3-11 shows the experimental set up of TIRE. In this method the sample is placed upside down on the top of a designated cell, which allows the measurements in different media, in a direct contact with the measurement media. a drop of index matching liquid is then spread on the top side of the sample with no air bubbles. a prism is mounted on the top of the set up in direct contact with index matching liquid which prevent any unwanted reflections or refractions.^[220]

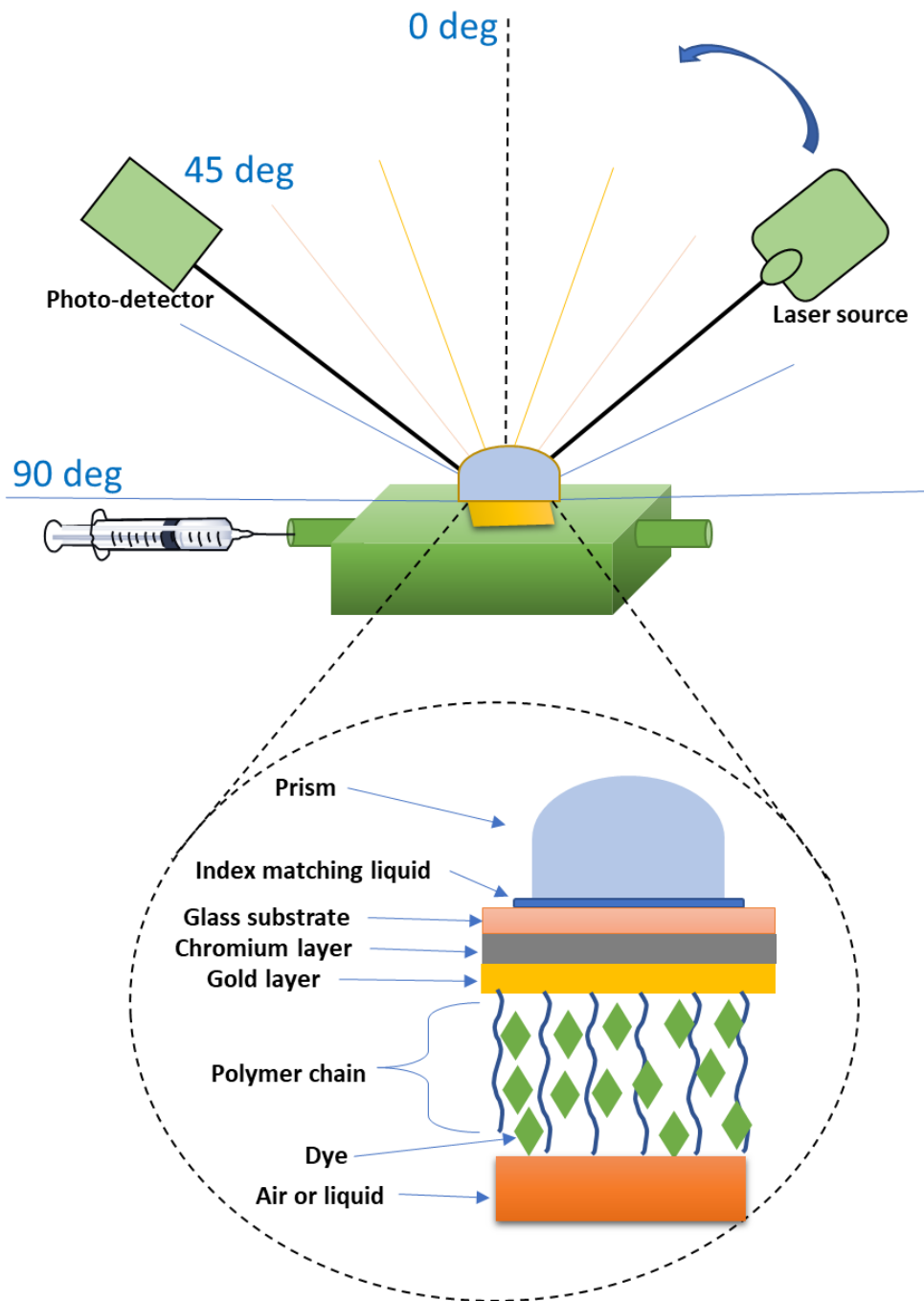


Figure 3-11: Schematic diagram showing the setup of TIRE technique.

3.7.4.1 Ellipsometer experimental procedure:

Ellipsometric spectra were collected using an Alpha-SE ellipsometer (J.A. Woollam Co., Lincoln, NE) with a Quartz Tungsten Halogen (QTH) light source to cover the UV-VIS spectral range, supplied with a He-Ne laser at wavelength of $\lambda = 633 \text{ nm}$, and at an incident angle (Φ) of 75° from the normal. Measurements were conducted from 300 to 700 nm, and modelling

was performed using Complete-EASE software (J.A. Woollam Co., Lincoln, NE). Root-mean-square error (RMSE) between the modelled and measured ellipsometric constants Δ and Ψ was used to assess the fit quality over all measured wavelengths. The thickness was measured in at least three different areas on each sample and stated as the mean \pm standard error.

To evaluate the thickness of dry PDMA brushes derivatized with chlorophyll grown on continuous gold surface or from glass, an optical multilayer-box-model was applied (see **Table 3-1**). Values for optical constants n and k of glass, chromium and gold were taken from the standard material library.

Table 3-1: The model used for spectroscopic ellipsometry data fitting of PDMA grown on continuous gold film and derivatized with chlorophyll.

Layer	Material	Fitted parameters
Layer 4	EMA: Material 1: Cauchy (PDMA brushes) Material 2: Chlorophyll	thickness h of the EMA layer in nm Fraction of Material 2 Depolarization
Layer 3	Cauchy_Wvl (initiator)	thickness h of the initiator in nm Refractive index n and parameters $B_n=0.01$ and $C_n=0$ were fixed during the fitting.
Layer 2	Au	thickness h of the evaporated gold film in nm
Layer 1	Cr	thickness h of the evaporated chromium film in nm
Substrate	BK7 glass	

A Cauchy dispersion function ($n = A_n + \frac{B_n}{\lambda^2} + \frac{C_n}{\lambda^4}$ and $k = 0$, where A , B , and C are constants, A sets amplitude, B and C give dispersion shape) for the non-absorbing initiator (i.e. BIBUDT or BIBB-APTES) layer was used for modelling the adsorbed SAMs layer of initiator and PDMA brushes. Refractive indices n of the initiator used in this model, were measured previously with the Abbe refractometer. BIBUDT film thicknesses on continuous gold surface were fitted considering the previously measured Cr/Au layer thickness.

For the PDMA brush layer, a Cauchy relation in combination with an Effective Medium Approach (EMA) according to Bruggeman was used to describe the dependence of the refractive index n on the wavelength for this non-absorbing polymer. The refractive index of PDMA was assumed according to *Chen et al.* [164] and set to ca.1.53. The second material in EMA model was either void (before derivatization of PDMA brushes with chlorophyll) or *ZnChla* (after derivatization). During modelling, the thickness and the optical constants of the underlying initiator layer were fixed to the values determined to avoid parameter correlations.

In the case of PDMA grown from glass and embedded with AuNPs, the first material in EMA was PDMA, the second material was AuNPs and the third material was *ZnChla* after derivatization. This model and fitted parameters are represented in **Table3-2**. Here, linear optical mode was chosen for AuNPs, and Bruggeman optical mode was chosen for *ZnChla*.

The change in the Delta and Psi optical properties of AuNPs-embedded PDMA before and after the attachment of *ZnChla* was recorded by conducting ellipsometry measurements by variable angle spectroscopic ellipsometry (VASE) between 46° – 87°.

Table 3-2: The model used for SE data fitting of PDMA grown on glass substrate, embedded with AuNPs and derivatised with chlorophyll.

Layer	Material	Fitted parameters
Layer 2	EMA: Material 1: Cauchy (PDMA brushes) Material 2: AuNPs Material 3: ZnChla (after the attachment)	PDMA: $n = 1.53$, $B = 0.03$ and $C = 0$ AuNPs: $\% = 61.7$ ZnChla: $\% = 81.5$ and $depolarisation = 0$
Layer 1	Cauchy_Wvl (initiator)	thickness h of the initiator in nm refractive index n and parameters $B_n=0.01$ and $C_n=0$ were fixed during the fitting.
Substrate	BK7 glass	

3.7.5 X-ray photoelectron microscopy (XPS)

X-ray photoelectron microscopy XPS is non-destructive analytical technique that has been widely used to analyse and characterise different type of surfaces and biomedical polymers. It is also known as Electron Spectroscopy for Chemical Analysis (ESCA). XPS can detect all elements except helium (He) and hydrogen (H) and allows determination of the elemental composition of a material. In addition, it is also able to provide chemical bonding information.^[221]

Among all surface analysis techniques, XPS is the most efficient tool in terms of chemical information and data interpretation.^[221] XPS is based on the photoelectric effect^[222]. However, principle of XPS has been well reviewed.^[223] When a material is irradiated using X-rays, electrons are ejected from core shells in the atoms in the material. The kinetic energies E_k of the emitted photoelectrons are given by the following equation.

$$E_k = h\nu - E_B - \phi$$

where, $h\nu$ is the photon energy, E_B is the binding energy of the orbital from which the photoelectrons are emitted (effectively the first ionisation energy) and ϕ is the work function (the energy barrier to emission of the photoelectron). XPS is a highly surface sensitive technique because the inelastic mean free paths of photoelectrons are short, meaning that they only escape from the top 10 nm. **Figure 3-12** shows simplified principle of XPS.

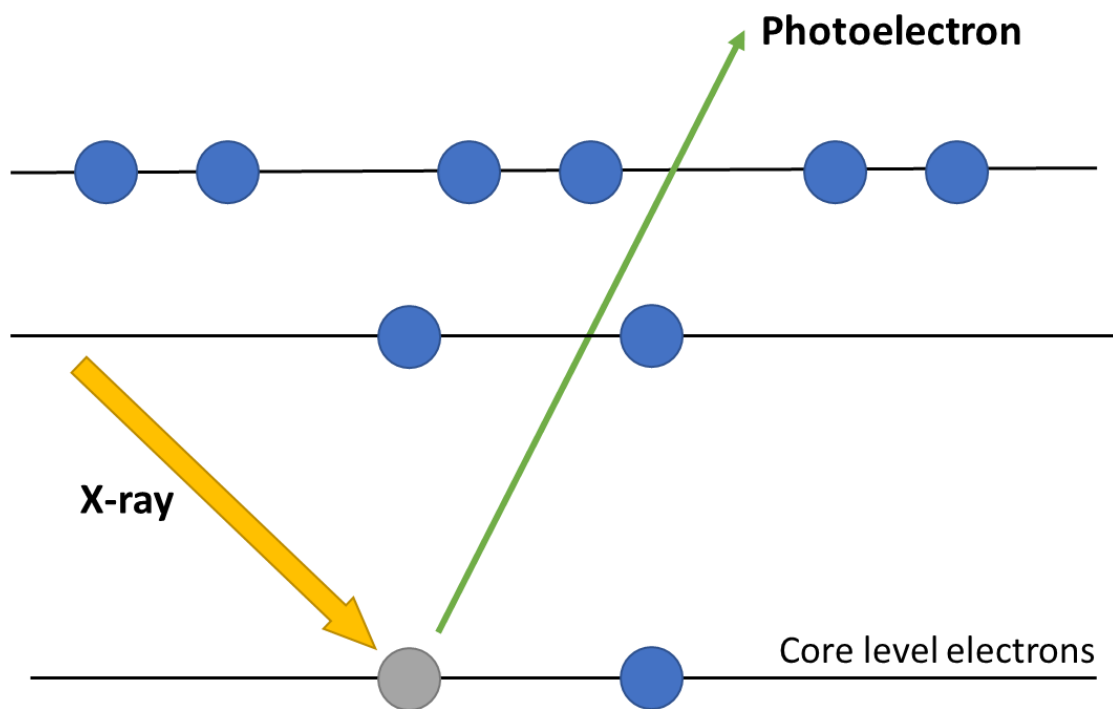


Figure 3-12: diagram showing the principle of XPS.

After ejection core shell electron, its place will be vacancy and it can be filled by a higher energy electron coming from a higher energy level. This process can generate another photoelectron which is known as "Auger photoelectron". The number of photoelectrons is plotted as a function of the photoelectron kinetic energy, or, more usually as a function of the BE which is more informative about surface composition and structure. The photoelectron binding energies are element-specific, enabling quantitative and qualitative analysis of the surface composition, and they are also subject to small chemical shifts that depend on their local binding environment. Analysis of these chemical shifts enables detailed analysis of surface structure and bonding.

By repeatedly accessing sub-surface compositional layers, depth-profiling tests can be used to characterise composition of the sample as a function of penetration depth.^[224] Monatomic depth profiling reveals subsurface information by using an ion beam to remove layers of the surface or surface contaminants. Quantified information as well as layer thicknesses are produced by combining an array of ion gun etch cycles with XPS studies. A spectrum, or group of spectra, are captured from the sample's surface prior to material removal. By rastering an ion beam across a square or rectangular section of the sample, the surface is etched. The ion beam is blanked following the etch cycle, and another set of spectra are taken. Etching and spectrum capture are repeated until the appropriate depth of profiling has been reached.^[225]

3.7.5.1 XPS experimental procedure:

XPS analyses were carried out using a Kratos Supra instrument with a monochromated aluminium source and an argon cluster source. XPS data were analysed using the CASAXPS software. All binding energies were calibrated relative to the primary hydrocarbon C 1s signal at 285 eV. The samples were mounted onto the XPS sample holder with double sided carbon tape. In order to collect an XPS depth profile, XPS spectra are first collected from the analysis

area before any etching has occurred. The sample is then etched for a set amount of time before the XPS analysis is repeated. The sample is then re-etched, the analysis collected once more, and the cycle is continued for a prescribed number of depths. The conditions used for etching are that the argon cluster source was set to produce Ar_{3000}^+ clusters at 10 keV. The ion gun is left to stabilise for two hours before use. The ion beam current is typically about 8 nA but can vary between different experiments, and consequently the specific ion beam current is measured before use. The data is then plotted as a function of the number of clusters to hit the sample surface (dose). The cluster source was allowed to raster over an area 2 mm by 2mm to produce an etch crater. The X-ray analysis was collected from an area 110 micrometres in diameter at the centre of the etch crater. The X-ray emission current used was 25 mA, and at 15 kV. High resolution scans were collected from the $\text{Zn}2p^3$ or $\text{I}3d^{5/2}$ (as appropriate for either quarternised with 1-iodooctadecane or reacted with *chlorophyll*), O 1s, N 1s, C 1s and Si 2p transitions, with one 30 second sweep for the O 1s, one 60 second sweep for each of $\text{I}3d^{5/2}$ or $\text{Zn}2p^{3/2}$ and Si 2p, and four 60 second sweeps for both C 1s and N 1s. All data was collected at a pass energy of 40 eV. Charge neutralisation was used throughout at 0.4 A.

XPS database available in (<https://www.thermofisher.com/uk/en/home/materials-science/learning-center/periodic-table.html>) was used as a reference for peaks assignments.

3.7.6 UV-visible spectroscopy (UV-vis)

When a beam of light is passed through a sample, the intensity of the transmitted beam will be reduced at a given wavelength if the sample contains molecules that absorb at that particular wavelength. The absorbance A at this wavelength is given by the Beer-Lambert law:^[226]

$$A = \epsilon lc$$

where, ϵ is the extinction coefficient at the wavelength of interest, l is the path length and c is the concentration of the absorber.

In this context, "absorbance" refers to the decrease of light density due to the absorption of light leading to transitions in the analyte molecules from the ground state to higher states. In contrast, the "extinction" expresses the total loss of intensity and includes losses from scattering as well as absorption.^[227] When the sample is measured in quartz or glass cuvette, the cuvette surface will reflect part of light leading to provide misleading data. In order to overcome this error, a reference measurement is required. This can be achieved by using blank cuvette that does not contain any sample as baseline. The typical instrument consists of light source, monochromator, sample chamber and detection unit with an amplifier. Tungsten and deuterium lamp are used to cover the spectral region in the UV and Visible range with a variation of wavelength from 190 to 900 nm.^[228]

3.7.6.1 UV-VIS experimental procedure:

UV-visible absorption spectra at typical incidence were measured using Cary50 spectrophotometer (Agilent Technologies, USA) at a scan speed of 600 nm/min with a bandwidth of 10 nm. The wavelength scan range was 350 – 800 nm (unless otherwise stated). For suspension samples measurements, about 3 mL of the solution were loaded in a standard cuvette with 10 mm optical path length and were measured in succession at room temperature many times. The solid samples were measured in air and in liquid. Air measurements were conducted using a home-made PTFE holder to enable measurements of the same area on the surface during all experimental stages. During the measurements of the solid surface in liquids with different pH values, the holder with fitted sample was placed in a standard quartz cuvette (10 mm transmitted path length). Then about 1.5 mL of desired solvent was injected to immerse the sample inside the cuvette to investigate the response behaviour of the system to pH modification between 0.1M HCl (pH 1.0 ± 0.20) and 1M NaOH (pH 12.0 ± 0.2).

3.7.7 Mass Spectrometry (MS)

Approximately 10 mg of *pheophytin a* or *ZnChla* were dissolved in acetone and analysed with a Waters LCT classic ToF liquid-chromatography mass spectrometer (LC-MS). The same procedure was followed to analysed INR with LC-MS

Analytical data of *pheophytin a*:

$R_f = 0.33$ (6:3:1 hexane: diethyl ether: acetone); LC-TOF-MS ES+, observed. $m/z = 872$ (17.191 min). Calculated = 871.22 [(M + H)+, M=C₅₅H₇₄N₄O₅].

Analytical data of *ZnChla*:

$R_f = 0.37$ (5:4:1 hexane: diethyl ether: acetone); LC-TOF-MS ES+, observed. $m/z = 933.5$ g/mol. Calculated = 934.57 g/mol [(M + H)+, M= C₅₅H₇₂N₄O₅Zn].

Mass spect analysis of final product of Zn-chl shows very close molecular weight of 933.5 g/mol.

Analytical data of INR:

$R_f = 0.38$ (1:2 petroleum ether: ethyl acetate); LC-TOF-MS ES+, observed. $m/z = 600.18$ g/mol. Calculated = 600.54 g/mol [(M + H)+, M= C₃₀H₃₇N₂O₃].

3.7.8 Nuclear magnetic resonance (NMR)

¹H NMR spectra of *chlorophyll a* derivatives or INR were collected using Bruker NMR (Avance and Avance III HD) spectrometers operating at a 400 MHz radio frequency. Samples were dissolved in approximately 5 mL of chloroform-d and filtered before measurement prior to NMR analysis.

Analytical data of *pheophytin a*:

^1H NMR (400 MHz, in CDCl_3) δ (ppm) = 0.09, -1.60 (broad singlet, 1H, NH), 0.69-0.97 (multiplet, pythyl CHCH_3) 0.96-1.41 (multiplet, pythyl CH_2), (multiplet, pythyl vinyl, 2H) 1.82 (doublet, $J = 6.29$, 3H), 1.90 (multiplet, 3H), 2.08 (multiplet, 3H), 2.19 (trace of acetone), 2.36 (multiplet, 2H), 2.50, 2.64 (multiplet, 2H), 2.83 (broad triplet, $J = 5.39$, 2H), 3.26 (singlet, 3H, methyl), 3.42 (singlet, 3H, methyl), 3.71 (broad singlet, 3H, methyl), 3.71 (broad singlet, 2H, $\text{CH}_2\text{-CH}_3$) 3.90 (singlet, 3H, COOCH_3), 4.23 (broad doublet, $J = 7.71$ Hz, 1H) 4.31 (multiplet, 2H, pythyl CH_2), 4.46 (m, 1H HC-CH_3), 4.50 (multiplet, 3H, CH_3) 5.15 (multiplet, 1H, pythyl vinyl), 5.14, 5.38 (multiplet, multiple H, aggregation), 6.18 (d, $J = 9.16$, 1H, vinyl), 6.22 (singlet, 1H, CH-COOCH_3), 6.31 (doublet, $J = 19.21$ Hz, 1H, vinyl, cis), 8.02 (dd, $J = 11.28$, $J = 5.97$, 1H, vinyl, trans) 8.58 (singlet, 1 H, ring $\delta\text{-H}$), 9.45 (singlet, 1H, ring $\alpha\text{-H}$), 9.5 (singlet, 1H, ring $\beta\text{-H}$).^[229]

Analytical data of *ZnChla*:

NMR study of *ZnChla* shows similar profile of *pheophytin* with broader peaks with slight shift over most of the peaks and more pronounced shift from 9.45 to 9.6 (singlet, 1H, ring $\alpha\text{-H}$), and from 9.5 to 9.7 (singlet, 1H, ring $\beta\text{-H}$).

Analytical data of INR:

^{13}C NMR (101 MHz, CDCl_3) δ the carbon (C_{23}) at 183.35 ppm, (C_{11}) 161.91, (C_{18}) 152.08, (C_{14}) 150.72, (C_{21}) 146.88, (C_{20}) 140.17, (C_{15}) 134.08, Ring carbons (C_{12} , 13, 16, 17, 19, 22, 24, 25, 26) (131.05, 127.75, 125.55, 124.70, 118.30, 109.47, 106.68, 105.34, 96.34), CDCl_3 77.35, 77.24, 77.04, 76.72, (C_{10}) 68.39, (C_{27}) 45.08, (C_2 to C_9) (33.57, 30.51, 29.47, 29.36, 29.34, 29.23, 28.54, 26.06), (C_{28}) 12.64, (C_1) 7.37. Imp 29.72 ppm. The numbers of carbon atoms stated in ^{13}C NMR analysis are shown in **Figure 3-13**.

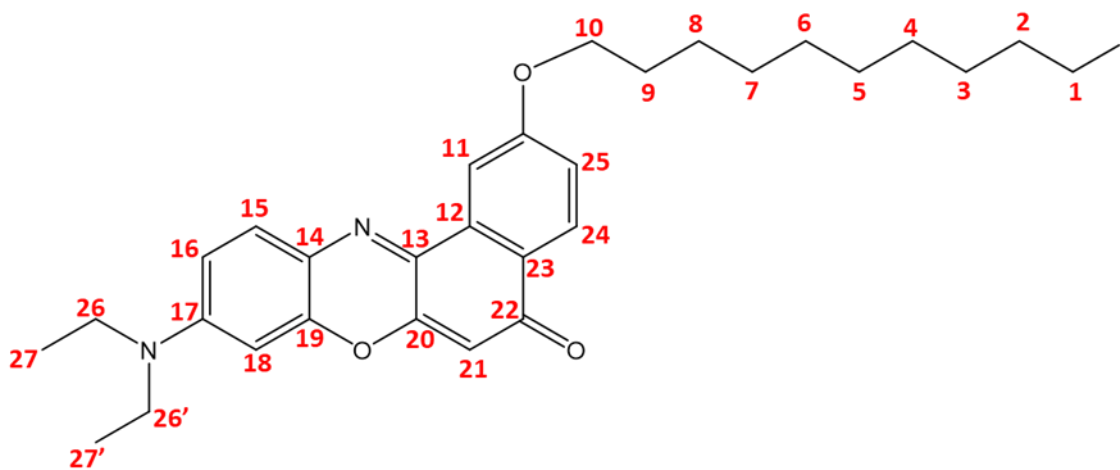


Figure 3-13: Clarification of the intended numbers of carbon atoms numbers in ^{13}C analysis.

3.8 Modelling of strong plasmon-exciton coupling

Following the method outlined by Lishchuk et al.^[33] plasmon-exciton coupling in plexcitonic complexes was modelled as coupled oscillators. Specifically, the coupled systems were modelled as consisting of a broad mode with resonance frequency ω_b and damping γ_b coupled to a second narrow mode with resonance frequency ω_d and damping γ_d . **Figure 3-14.**

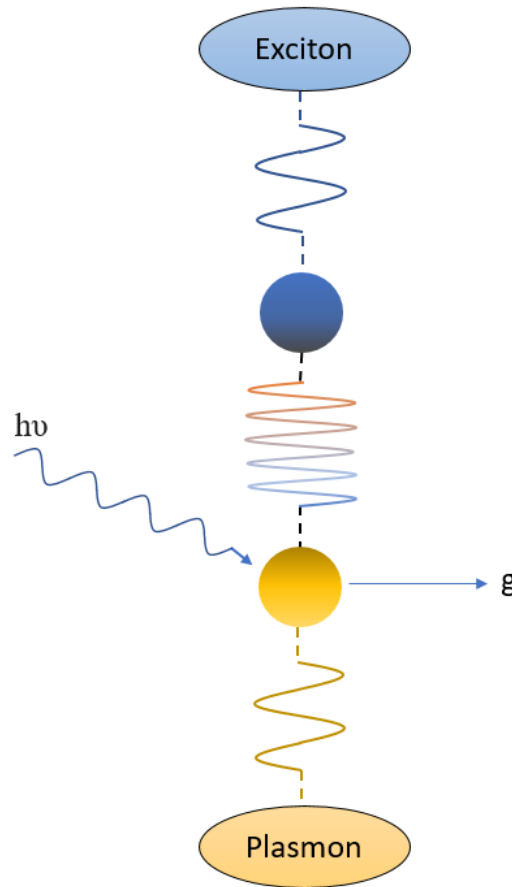


Figure 3-14: Schematic illustration of the plasmon and exciton coupling system as a coupled harmonic oscillator with a coupling strength g under an external light effect.

The coupling between the two oscillators in this model is g and the highly damped oscillator is driven by an external harmonic force with amplitude $fe^{i\omega t}$. In this model, the broad, highly damped mode is the LSPR, and the narrow line width mode is the exciton. The equations of motion are:

$$\ddot{x}_b + \gamma_b \dot{x}_b + \omega_b^2 x_b + gx_d = fe^{i\omega t}$$

$$\ddot{x}_d + \gamma_d \dot{x}_d + \omega_d^2 x_d + gx_b = 0$$

For harmonic oscillators these equations generate solutions $x_b = c_b e^{i\omega t}$ and $x_d = c_d e^{i\omega t}$, where the coefficients c_b and c_d can be solved analytically. The extinction becomes proportional to the imaginary part of

$$\alpha(\omega) \propto \frac{1}{\tilde{f}(\omega) + i\omega\tilde{\gamma}(\omega)}$$

where,

$$\tilde{f}(\omega) = \omega_b^2 - \omega^2 - \frac{g^2(\omega_d^2 - \omega^2)}{(\omega_d^2 - \omega^2)^2 + \gamma_d^2 \omega^2}$$

and

$$\tilde{\gamma}(\omega) = \gamma_b + \frac{g^2 \gamma_d}{(\omega_d^2 - \omega^2)^2 + \gamma_d^2 \omega^2}$$

The experimental results can be modelled using these equations. These equations were scaled to have units of energy rather than frequency. In a similar way, the energy of the exciton (E_{mol}) corresponds to ω_d and the energy of the LSPR (E_{LSPR}) corresponds to ω_b . The quantity $E_C = G/E_{\text{LSPR}}$ is approximately equal to the splitting in the coupled harmonic oscillator model when the two oscillators are at resonance with each other, where $G = \hbar^2 g$ is the scaled coupling which has the dimensions of energy squared. Similarly, the energy of the exciton E_{mol} corresponds to ω_d and the energy of the localised surface plasmon resonance E_{LSPR} corresponds to ω_b . The quantity $E_C = G/E_{\text{LSPR}}$ is approximately equal to the splitting in the coupled harmonic oscillator model when the two oscillators are at resonance with each other.

Several criteria are used for determining whether a system is in the strong coupling regime. In order for a normal mode splitting (Rabi splitting) at resonance to be visible, in the case where

the linewidths of the modes are similar, the coupling energy E_c should be roughly the same as or larger than the average of the linewidths of the two modes/oscillators (modes 1 and 2). However, this is only an overall criterion since the visibility also depends on the shapes of the linewidths. In case of one large and one small linewidth, a double-peak structure (on and slightly off resonance) becomes more easily visible and sometimes the condition $E_c \geq \sqrt{\gamma_1 \gamma_2}$ is used as a guideline. In that case it is important to consider the fundamental criterion of strong coupling, namely that $E_c \geq \frac{1}{2} (\gamma_1 + \gamma_2)$. This guarantees that the term giving the splitting between two modes at resonance, $\sqrt{E_c^2 - \frac{1}{4} (\gamma_1 - \gamma_2)^2}$ stays real and indeed two different normal modes exist.

CHAPTER 4: PLEXCITONIC COMPLEXES: SYNTHESIS

4.1 Introduction

Excitons are electron–hole pairs that can be created as a result of absorption of light by molecules leading to the promotion of an electron from the highest unoccupied molecular orbital (HOMO) to the lowest unoccupied molecular orbital (LOMO). However, the design of devices is considerably limited by the exciton diffusion lengths, which are of the order of 10 nm or, under extreme circumstances, a few tens of nm.^[230,231] Consequently, the development of design principles for the efficient long-range transport of excitons in molecular materials has remained an unsolved grand challenge. In order to solve this problem, there has been much interest in the utilisation of photosynthetic light-harvesting antenna complexes (LHCs) from bacteria and plants as a pigment-protein model for the effective transfer of excitons in molecular structures.^[33] In these antenna complexes, precise spatial organisation of pigment molecules (*chlorophylls* and carotenoids) is achieved by peptide units, which also control networks of energy transfer process with a high degree of precision.^[232] However, proteins are not suitable for potential photonic material applications due to the high expense of large-scale production and their natural vulnerability to processing damage. Hence, there is a crucial need to discover new systems that incorporate the attractive properties of LHCs into photonic devices such as sensors. In order to achieve this, Lishchuk *et al.*^[33] suggested that biomimetic systems can be designed by incorporating dyes into surface-grafted polymer brushes - pigment-polymer complexes by analogy with pigments protein complexes found in photosynthesis. In their study, PCysMA brushes were used as a scaffold to support *chlorophyll* molecules. The *chlorophyll* density in these pigment-polymer antenna complexes was controlled by varying the polymerisation time and grafting density of PCysMA brushes. Although there has been a large number of studies on the construction of dyes-polymer structures, obtaining high concentrations of the binding dye to the polymer remains a challenge.

In the present work, a new approach to the synthesis of pigment-polymer antenna complexes was examined. In particular the possibility of using surface-grafted PDMA brushes formed by ATRP as a scaffold to support *chlorophyll* molecules was investigated. The aim was to achieve simpler synthetic route than that reported previously by Lishchuk *et al.* Thus, it was hoped to achieve more efficient control of the biomimetic structure. ATRP was chosen to grow PDMA brushes from planar substrates due to its ability to generate high dense and well-controlled thick polymer brush with low termination rates. Due to the presence of the central double charged ion in the *chlorophyll* ring, it was hypothesised that *chlorophyll* might bind to the tertiary amine group on the pendant chains of PDMA brushes through a coordination bond in a similar mechanism to the binding of tetrapyrroles by haem binding sites in proteins.^[233] The density of the *chlorophyll* that bound to PDMA brushes was controlled by varying the concentrations of the *chlorophyll* solutions and, also, by regulating the number of the binding sites on the polymer chains by partial converting of the amine group to the quaternary ammonium.

4.2 Experimental

4.2.1 Materials

Glass substrates (Coverslips glass slides, Menzel-Glazer/ 22*60# 1.5), tetrahydrofuran (99.7%, HPLC grade), petroleum ether 40-60 °C, hydrochloric acid (35%), Sodium hydroxide and silica gel powder were provided by VWR. 1, 10-diiodooctane 98% and copper I bromide ($\geq 98\%$) were supplied by Alfa Aesar. Aminopropyltriethoxysilane (APTES) ($\geq 99\%$), 2-bromoisobutyryl bromide (98%), trimethylamine (BIBB) ($\geq 99\%$), dichloromethane (99.9%, HPLC grade), 2-(dimethylamino)ethylmethacrylate (DMA) (98%), 1,1,4,7,10,10-hexamethyltriethylenetetramine (HMTETA) (97%), 1-iodooctadecane (95%), glacial acetic acid (99%), n-hexane (97%, HPLC grade), diethyl ether (99.8%), zinc acetate dehydrate, were purchased from Sigma Aldrich. Ethanol, absolute (99.8%, HPLC grade), acetone (99.8 %, HPLC grade), methanol (99.8%, HPLC grade), isopropan-2-ol (99.5% HPLC grade), hydrogen peroxide (30% w/v), sulfuric acid (95%), dimethylformamide (DMF) (99%), magnesium sulfate anhydrous, sodium hydrogen carbonate, sand low iron and sodium chloride were supplied by Fisher Scientific. Silicon wafer (150 mm) was purchased from Pi-KEM.co.uk. Spinach leaves was obtained from a local supermarket. Deionised water was obtained from an Elga PURELAB Nano-pore system with a conductivity of 15 M Ω cm. Copper mesh Electron microscope grids (1000-2000 Mesh Cu) was used for micro-patterning. All these materials were used as received without any further purification. However, copper bromide was stored in a vacuumed atmosphere and DMA was stored at 4 °C after removal of the inhibitor.

4.2.2 Samples cleaning and handling

All glass slides and silicon wafers were cleaned as described in chapter 3. The substrates were immersed in Piranha solution (30% H₂O₂: 98% H₂SO₄, 1:3, v/v) for around 2 h.^[234] *Caution: Piranha solution reacts violently with organic matter and should be handled with extreme caution!*^[167] After the appropriate disposal of piranha solution, the slides were washed several

times with deionised water and dried in piranha oven overnight. The slides were cut into small pieces with their size being selected to be appropriate for the characterisation technique. The used slides were handled using clean tweezers and stored in sealed Eppendorf tubes prior to use.

4.2.3 Synthesis of BIBB-APTES films

BIBB-APTES films were prepared in two steps as described previously in chapter 3. Briefly, 2% solution of APTES in ethanol is used to immerse substrates for 30 min to form APTES films which were removed from the solution and rinsed with ethanol and were then dried by nitrogen stream. This was followed by placing annealing the samples on a hot plate for 30 min at 120 °C. To form bromine-functionalised ATRP initiators, APTES films were immersed in a mixture of bromoisobutryl bromide and triethylamine in dichloromethane for 30 min at room temperature. Then BIBB-APTES functionalised substrates were rinsed with ethanol and then dichloromethane and finally blown dried by nitrogen.^[76]

4.2.4 Photolithography

A frequency-doubled argon ion laser beam (Coherent Innova) Fred300C was used to expose BIBB-APTES samples at wavelength of 244 nm. A beam expander was used to expand the exposed area to 0.8 cm². Copper electron microscope grid (Agar, Cambridge, UK) was used to achieve micropattern scale.

4.2.5 Growth of PDMA via ATRP

PDMA brushes were grown from BIBB-APTES initiated glass and silicon substrates as described with more details in chapter 3. The inhibitor was removed from DMA monomers by

filtration of the monomers through silica in small column. DMA monomers was dissolved in DMF. HMTETA and Cu(I)Br were used to catalyse ATRP at 90 °C. Then 4 mL of monomer/catalyst solution was added to each BIBB-APTES sample in Schlenk tubes. The reaction was performed at nitrogen atmosphere using three cycles of vacuum/nitrogen after each addition of the reaction components. The growth of PDMA was allowed to proceed for different polymerisation times ranging from 1 min up to 2 hours. The polymerisation was terminated by removing the slide from the mixture. This was followed by the removal of the residual of monomer and catalyst using isopropanol and ethanol. After rinsing, PDMA samples were blown dry with nitrogen. The same procedure was also followed to grow PDMA brushes from micropatterned BIBB-APTES initiator.

4.2.6 Synthesis of quaternised PDMA (q-PDMA)

Quaternised PDMA (q-PDMA) was prepared by immersing previously prepared PDMA-coated glass and/or silicon slides in a freshly prepared solution of 1-iodooctadecane for 18 h at room temperature. After that, the q-PDMA brushes were removed from the solution and rinsed with ethanol and sonicated in THF and dried under nitrogen gas. More details can be found in chapter 3.

4.2.7 Extraction and derivatization of *chlorophyll a*

A detailed description of *ZnChla* synthesis can be found in chapter 3. Briefly, chl *a* was extracted from spinach leaves by acetone. After the removal of acetone under reduced pressure, further extraction of *chlorophyll a* from the organic and oily impurities was performed using petroleum ether. Petroleum ether was removed by rotary evaporator, yielding a dark green pigment, *chlorophyll a*. The extracted *chlorophyll a* was converted into pheophytin *a* (dark blue pigment) by dissolving the dark green pigment in acetic acid under stirring for 3 h.

Pheophytin a was purified by column chromatography using a mixture of hexane, diethyl ether and acetone in the ratio 6:3:1. The formation of pheophytin was analysed by MS and NMR. Zinc acetate dehydrate dissolved in methanol was used to convert pheophytin into *ZnChla* under reflux in argon atmosphere at 35 °C for 1 hour. The produced *ZnChla* was purified by column chromatography using a mixture of hexane, diethyl ether and acetone in the ratio 6:3:1. The formed *ZnChla* was analysed by MS, NMR and UV-Vis absorption spectroscopy.

4.2.8 Attachment of *ZnChla* to PDMA brushes and q-PDMA.

PDMA brushes were functionalised with *ZnChla* by immersion of PDMA samples in a series solutions of *ZnChla* with different concentrations ranging from 0 - 25 µM for the desired immobilization times at room temperature to form glass-BIBB-APTES-PDMA - *ZnChla* film. *ZnChla* -functionalised-PDMA samples were rinsed with deionised water and dried by N₂ stream. *ZnChla* -functionalised PDMA were characterised by UV-Vis spectroscopy, AFM, SE and XPS. This procedure was followed to attach *ZnChla* to q-PDMA in order to form *ZnChla* -functionalised q-PDMA films.

4.2.9 Surface analysis

A Cary 50 UV-vis spectrophotometer was used to obtain extinction spectra in the range 400 – 800 nm, unless otherwise is stated. *ZnChla* samples were measured in a standard quartz cuvette with 10 mm optical path length at room temperature at least 2 sampling areas. Glass substrate-based samples were measured in air. Air measurements were conducted using home-made PTFE sample holder which was allowed to perform measurements of the same area on the surface during all experimental stages.

X-ray photoelectron spectroscopy (XPS) spectra were obtained using a Kratos Axis Supra spectrometer (Kratos Analytical, Manchester, UK). All binding energies were calibrated relative

to the primary hydrocarbon C 1s signal at 285 eV. XPS data were analysed using the CASAXPS (v. 2.18) software.

AFM images were obtained using a Digital Instruments (Nanoscope 5 Multimode Atomic Force Microscope), (Veeco, Santa Barbara, CA) fitted with a “J” scanner (0–125 μm). All measurements were conducted in air at room temperature. AFM data analysis was performed using Nanoscope Analysis software (v.1.5).

Ellipsometric spectra were collected using an M-2000VI ellipsometer (J. A. Woollam Co., Inc., USA) operating in a spectral range from 370 to 1000 nm, at an incident angle (Φ) of 75° , unless otherwise is stated. Modelling ellipsometric data was performed using CompleteEASE software (v.6.6). At least three measurements per sample were carried out in air to obtain an average.

Water contact angles measurements were performed using a Rame Hart sessile-drop model 100-00 goniometer. The obtained contact angle values are the mean of at least three different measurements. All contact angle values were denoted by $\cos \theta$.

4.3 Results and discussion

4.3.1 Formation and characterisation of initiator-functionalised surfaces

ATRP initiators on solid substrates were prepared by reaction of the acyl bromide BIBB with films of adsorbed APTES as represented in **figure 4-1**.

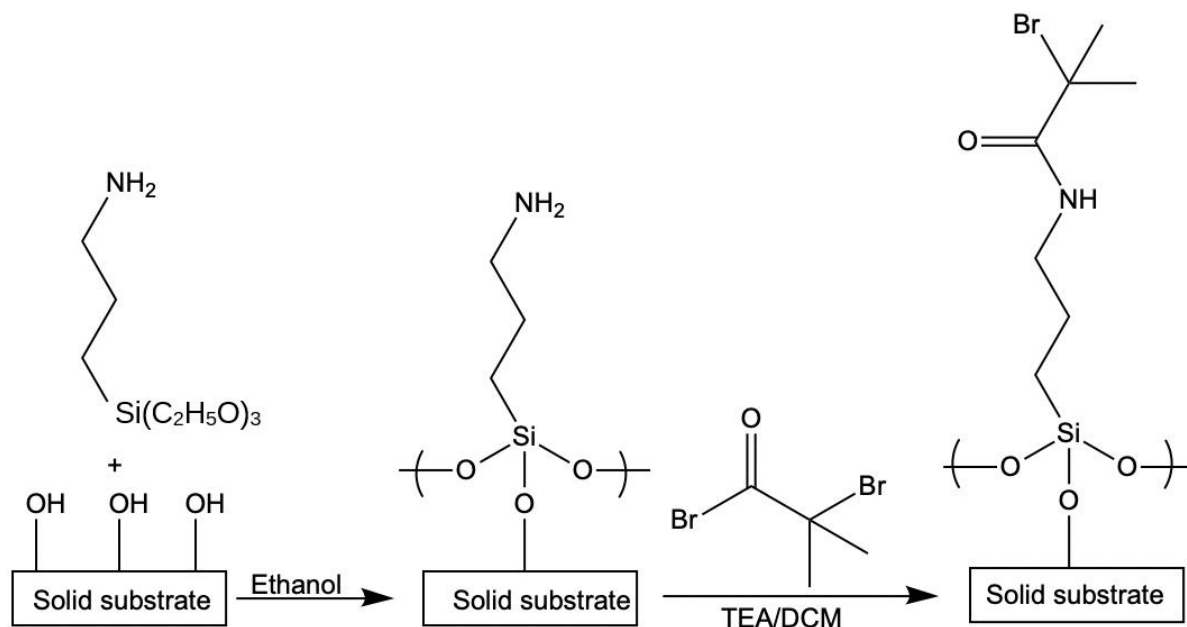


Figure 4-1: Schematic illustration of BIBB-APTES formation on a solid substrate.

After each step in the process, samples were characterised using X-ray photoelectron spectroscopy (XPS), contact angle goniometry and ellipsometry. High-resolution C1s and N1s XPS spectra are shown in **Figure 4-2**.

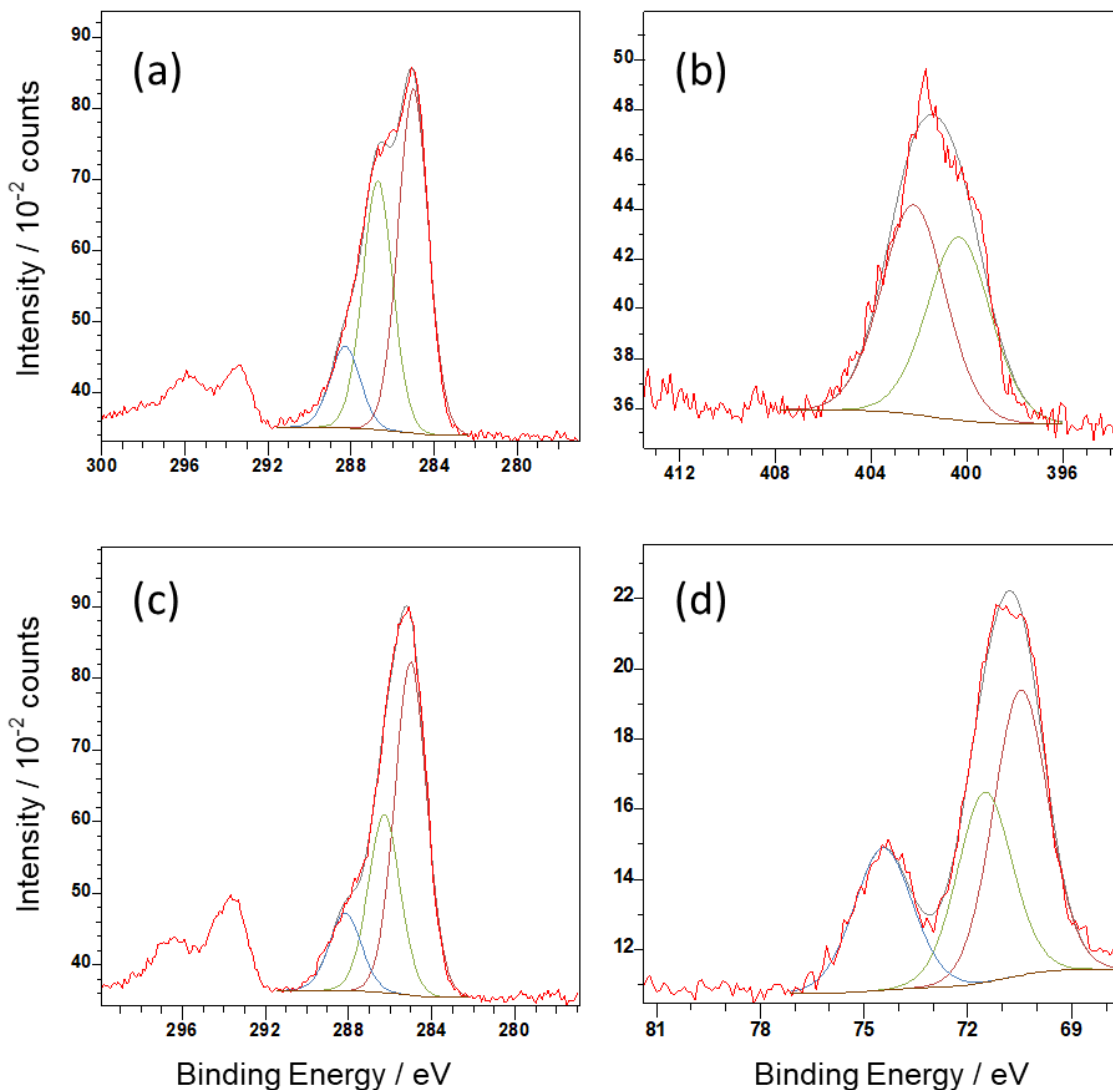


Figure 4-2: XPS high resolution spectra of APTES and BIBB-APTES films: (a) C 1s spectrum of APTES. (b) N 1s spectrum of APTES. (c) C 1s spectrum of BIBB-APTES. (d) Br 3d spectrum of BIBB-APTES film.

Three peaks at 285.0 eV, 286.6 eV and 288.56 eV are shown in C1s spectrum for APTES film. The first two peaks (at 285.0 eV and 286.6 eV) were attributed to the saturated carbon and carbon bonded to the amino group of APTES. The third peak (at 288.5 eV) is most likely attributed to the presence of the carbamate/carbamic acid groups produced as a result of the well-known reaction of PTES with CO₂, which is evidenced by the appearance of a protonated amine group (NH₃⁺) peak at 402.5 eV next to the amine peak at 399.8 eV on the spectrum of N 1s of APTES film,^[235,236] see **Figure 4-2a and 4-2b**.

XPS analysis of the BIBB-APTES layer^[76] shows three peaks at 285.0, 286.7 and 288.7 eV, corresponding to C-C-C, C-Br/CNCO and O=C-N, respectively, as shown in **Figure 4-2c**. The small features between 293-298 eV is attributed to the presence of K in the glass substrate. Successful halogenation of the film with Br was confirmed by the appearance of Br 3d doublet peaks at 70eV and 72eV, as shown in **Figure 4-2d**. The extra peak at 74.5 eV in the Br spectrum is attributed to Al³⁺ presented in the glass substrate.

The change in surface chemistry was also monitored by contact angle measurements. The contact angle was reduced after Piranha cleaning from 25° to 9° indicating the change in hydrophilicity due to hydroxylation process as mentioned previously.^[237] Then salinization of the surface by APTES increases the hydrophobicity due to the presence of amino terminated end groups.^[237] The measured contact angle of APTES film was 46°, which increased to 70 ± 5° after the functionalisation of the surface by BIBB layer as expected for full density and smooth brominated surface. The average thickness of BIBB-APTES was measured by SE to be 1.0 ± 0.4 nm for full density layer, See **Table 4-1**.

Table 4-1: Measured contact angle and film thickness as a function of the change of surface chemistry.

Samples	Average CA / degree	Thickness / nm
Clean glass substrate	9 ± 3	----
Glass-APTES	46 ± 5	----
Glass-BIBB-ABTES	70 ± 5	1.10 ± 0.13

To evaluate the best conditions for forming the BIBB-APTES film, BIBB-APTES was prepared using different concentrations of BIBB. As expected, 2% immersion of the sample in a solution of BIBB in DCM is sufficient to obtain full density BIBB-APTES film. This was

confirmed by contact angle measurements. The highest contact angle was achieved under these conditions, and it does not increase further at higher concentrations, see **Figure 4-3**.

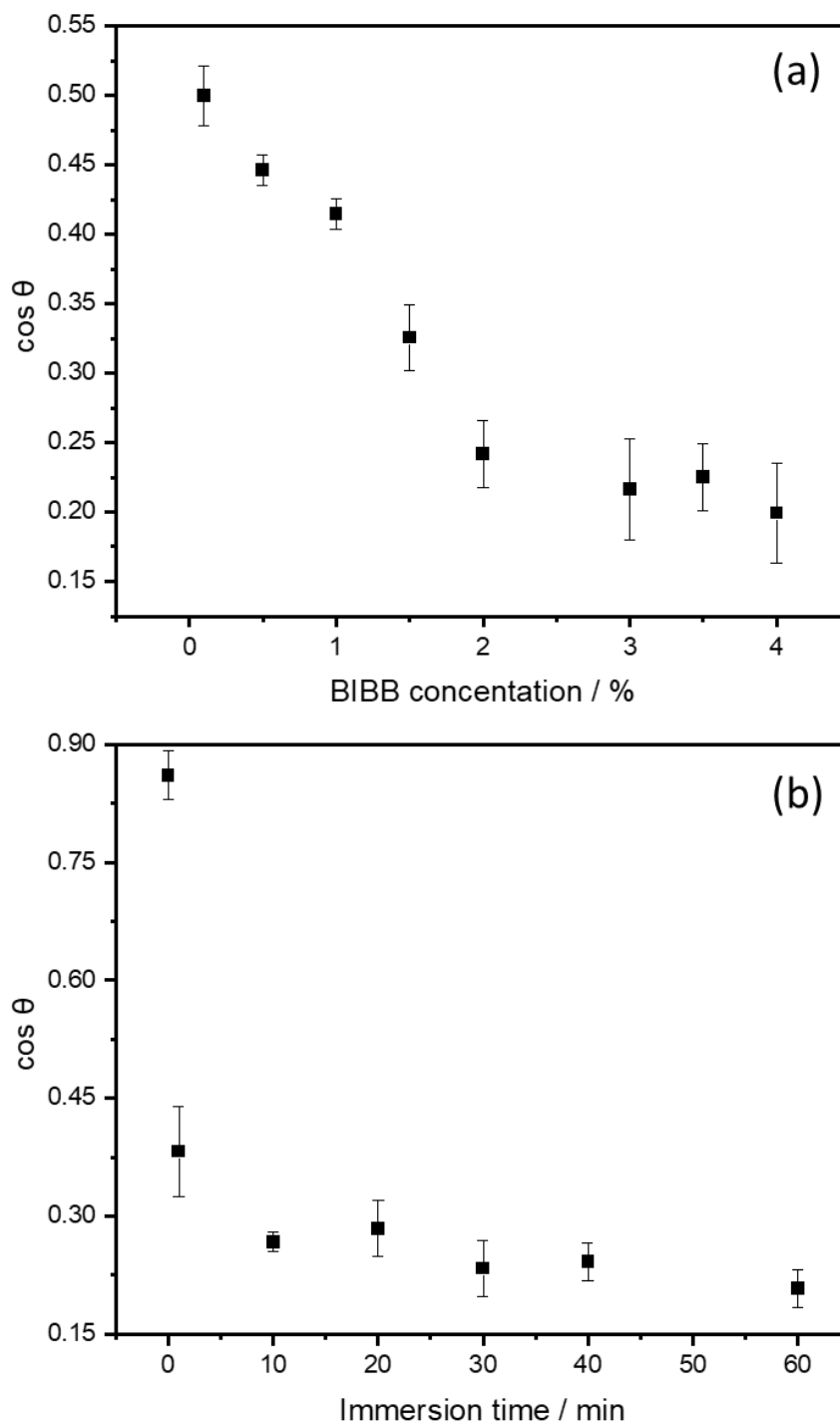


Figure 4-3: Contact angle of BIBB-APTES films measured at (a) different concentrations of BIBB and (b) different immobilisation times.

4.3.2 Kinetics of growth of PDMA brushes from initiator

PDMA brushes were grown bromine-terminated surface by ATRP using the protocol reported by Cheng *et al.*^[164] as shown in **Figure 4-4**.

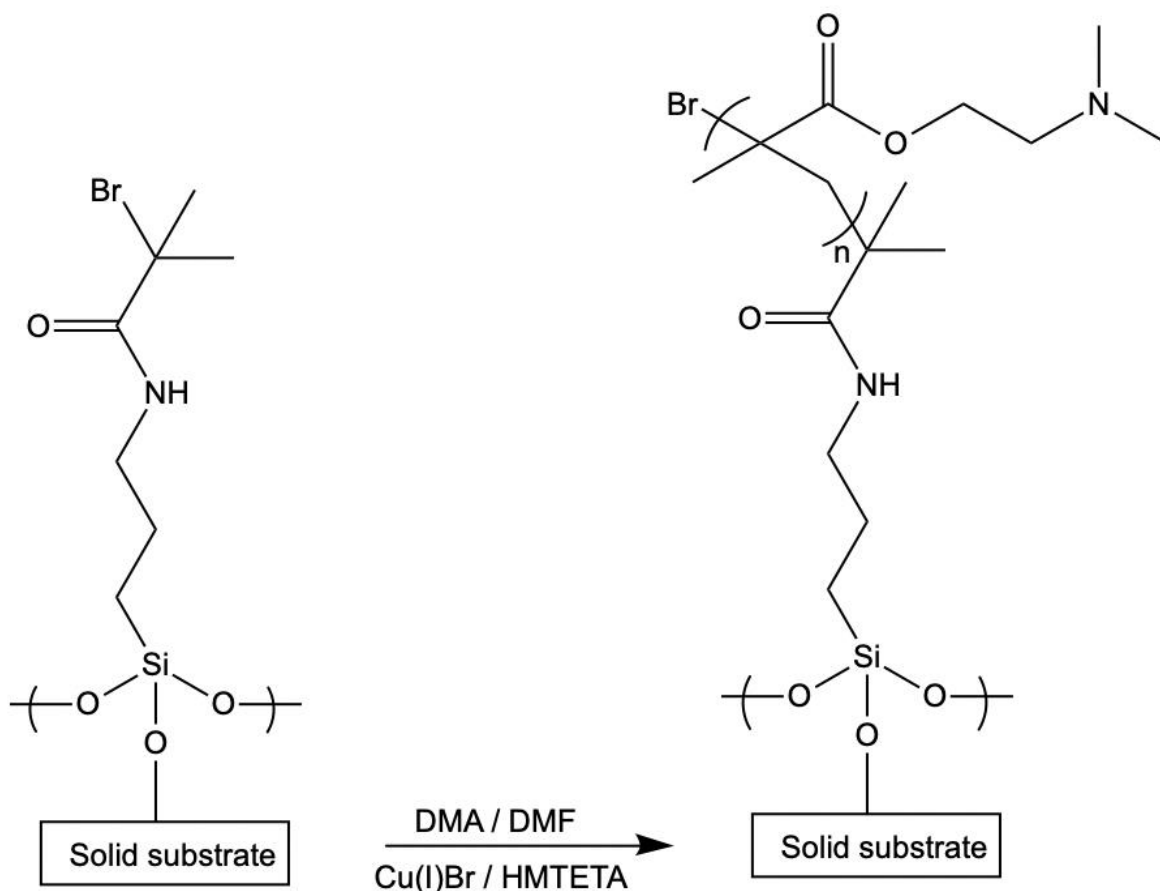


Figure 4-4: Schematic of ATRP synthesis of PDMA brushes.

PDMA brushes grown from BIBB-APTES films were characterised by XPS, contact angle goniometry and spectroscopic ellipsometry. **Figure 4-5** shows the dry film thickness as a function of time, as determined by spectroscopic ellipsometry. There was approximately linear increase in the height of the polymer brush during first 30 min of the polymerisation, reaching a thickness of 20 ± 1 nm. Thereafter, the rate of the polymerisation was slowed until a maximum

thickness of 31 ± 3 nm was reached after 60 min. After this time, no significant increase in the height was observed over the next three hours, which was resulted by the termination process.

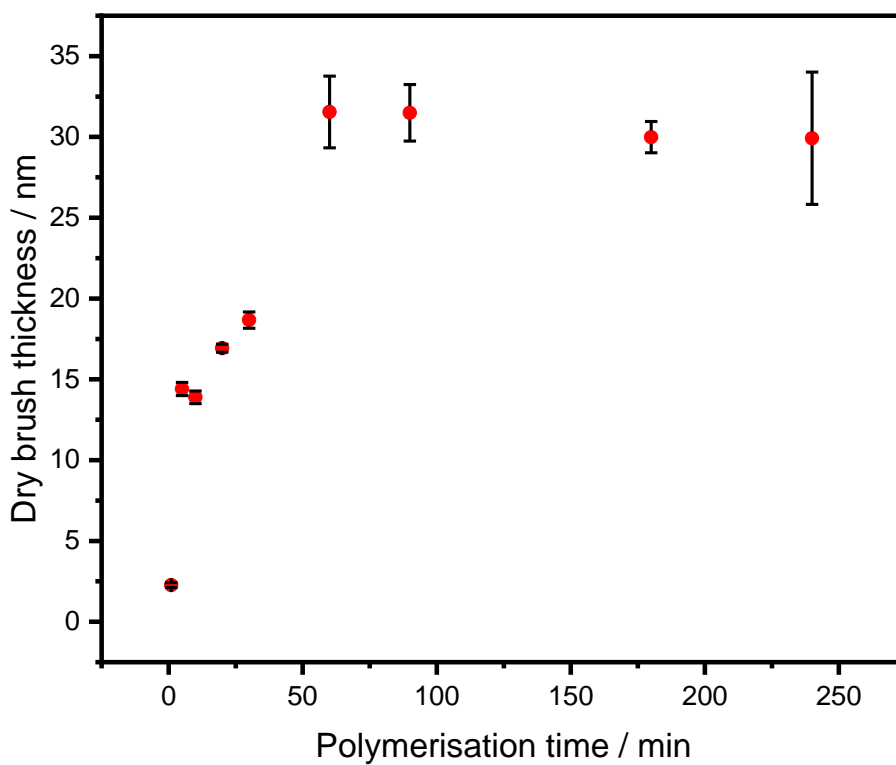


Figure 4-5: Growth profile of PDMA brushes: dry thickness as a function of polymerisation time.

Water contact angle measurements show a dramatic increase in contact angle from 9° for unmodified piranha cleaned substrate to 75° after 1 h polymerisation time. Thereafter, the contact angle changed very little even after much longer polymerisation times.

The PDMA brushes were characterised using XPS as shown in **Figure 4-6**.

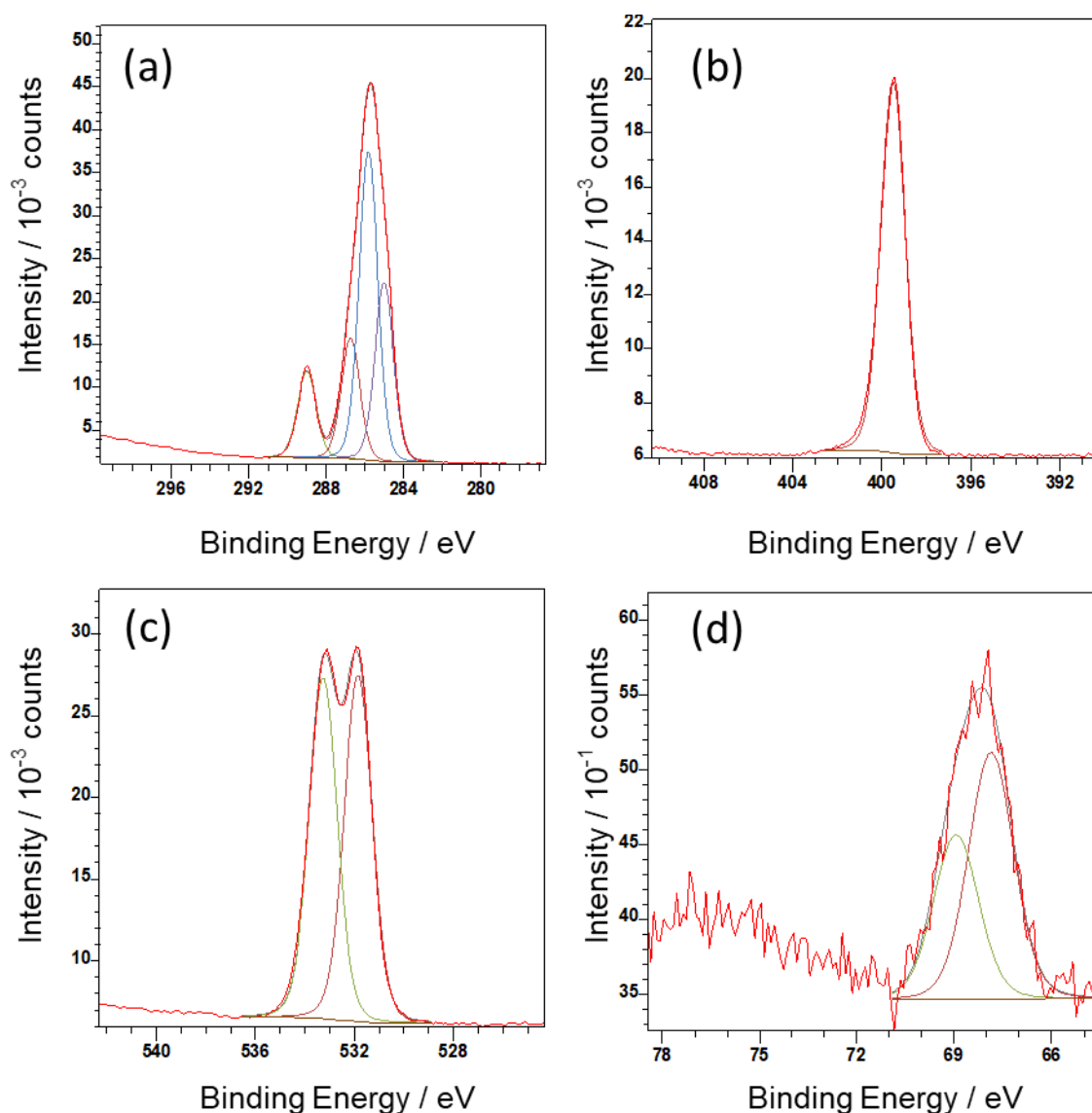


Figure 4-6: XPS high resolution spectra of PDMA brushes: (a) C 1s spectrum. (b) N 1s spectrum. (c) O 1s spectrum. (d) Br 3d spectrum.

The high resolution C1s spectrum of PDMA brushes polymerised for 15 min was fitted using four components (**Figure 4-6a**). These components correspond to the hydrocarbon -C-C- peak at 285.0 eV, -CO-N at 285.9 eV, the -C-N- at 286.8 and the ester carbonyl -CO-O- peak at 288.9 eV, in good agreement with data reported by Cheng *et al.*^[164] The N1s spectrum exhibits a high intensity peak at 399.6 eV, (**Figure 4-6b**), which correspond to -C-N- of PDMA^[164]. XPS O1s spectrum shows doublet signal at 532.1 eV and 533.7 eV (**Figure 4-6c**), which attributed

to -CO-O- and -C-O- respectively. The Br 3d peak in **Figure 4-6d** is attributed to the terminal halogen atom. This peak was fitted with two components, representing the doublet ($3d_{3/2}$ and $3d_{5/2}$) that resulted from spin-orbital coupling.

XPS Si 2p high resolution spectra were collected from PDMA samples that were grown for different polymerisation times as illustrated in **Figure 4-7**.

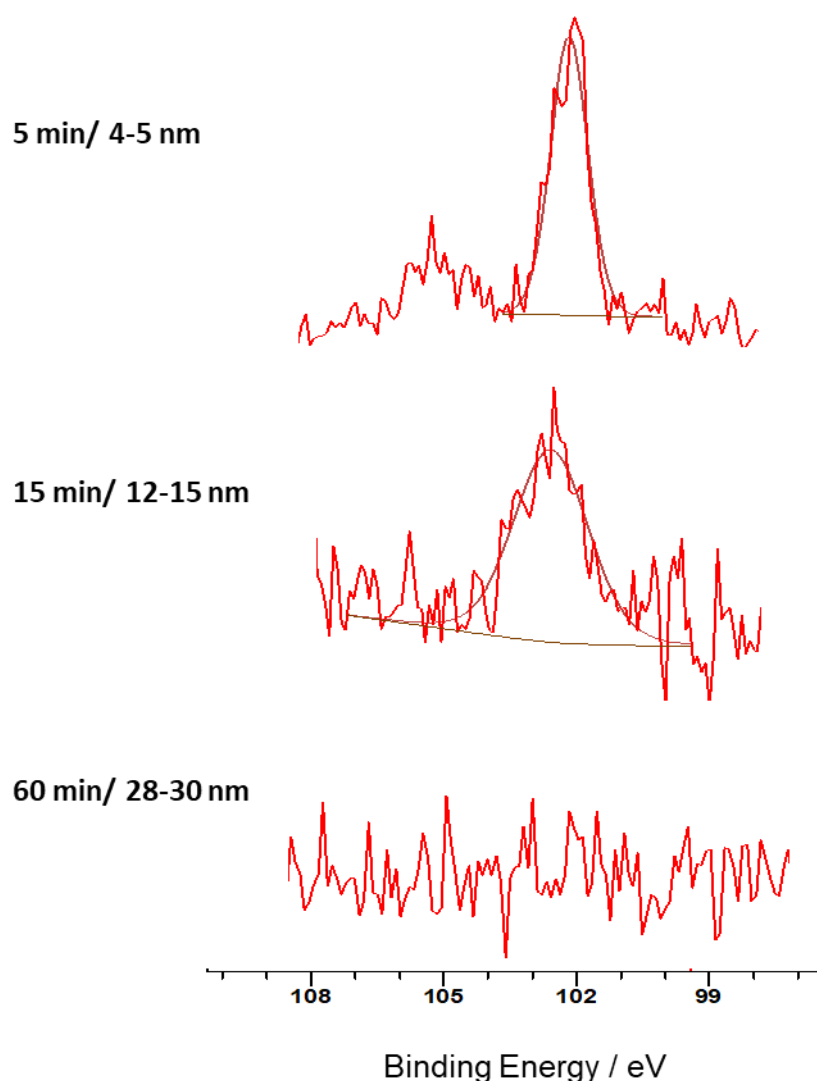


Figure 4-7: XPS Si 2p spectra of PDMA brushes grown for different polymerisation time; 5, 15, 60 min from top to bottom.

As it can be seen from **Figure 4-7**, Si 2p peak, which attributed to the substrate, diminished as the polymerisation time increased. That is, the scanned area raised away from the substrate surface.

4.3.2.1 Reduced density PDMA

Preparation of patterned functional surfaces is a vital element in applications such as sensing, nanoelectronics, cell adhesion, etc. Among the different patterning techniques, photolithography of polymer brushes provides fast, simple, and cost effective way for surface modification and preparation of hybrid materials.^[176]

Here, BIBB-APTES initiators were firstly micropatterned by partial removal of bromine atoms from the initiators. The micropatterned initiator was used to grow PDMA brushes via ATRP. It was hypothesised that removal of Br from the exposed regions should lead to growth of brushes with reduced dry thicknesses. The micropatterning process was illustrated schematically in **Figure 4-8**.

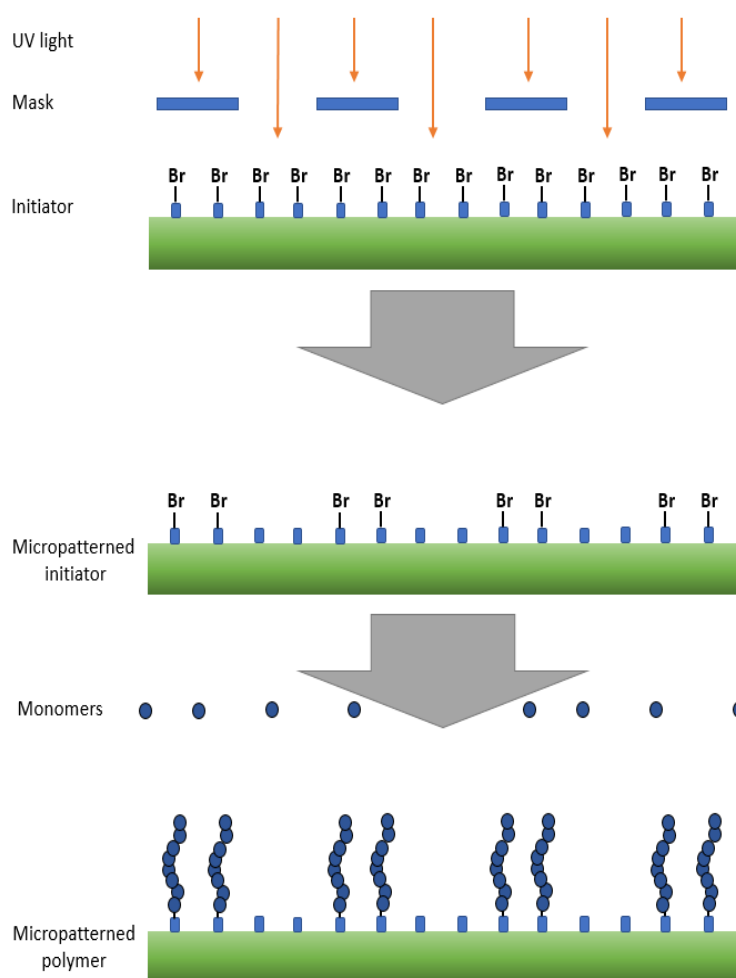


Figure 4-8: schematic illustration of debromination process of BIBB-APTES layers to create micropatterned PDMA brushes.

Micrometer scale patterning of Br-functionalised initiator was achieved by the exposure of BIBB-APTES layer to UV light at wavelength of 244 nm through a copper mesh electron microscopy grid using a frequency-doubled argon ion laser beam. The diameter of the illuminated area was 0.5 cm and the exposure doses was in the range 0.1 to 6 J cm⁻². The exposure to UV results in removal of the halogen atoms from the exposed areas.

Micropatterned BIBB-APTES films were characterised by contact mode AFM. **Figure 4-9a** shows contact mode height image of micropatterned BIBB-APTES film after a dose of 6 J cm⁻². There is a negligible contrast between exposed regions in which the Br initiator was removed by UV exposure (dark area) and intact regions at unexposed area on the surface. However, a friction force image (**Figure 4-9b**) exhibits a clear contrast between exposed areas (squares) and the masked areas (bar). The regions displaying brightest contrast correspond to the more polar exposed areas, from which Br has been removed. Removal of halogen atom probably leads to the introduction of polar groups to which the AFM probe adheres more strongly as it travels across the surface, causing an increase in the rate of energy dissipation and a higher coefficient of friction. The root mean square roughness Rq/Ra (roughness value that can be measured by AFM) of BIBB-APTES was measured to be 0.7 nm, consistent with previously reported roughness data for such surfaces by Ahmed *et al.*^[76] AFM analysis indicates the successful dehalogenation of the initiator without degradation of the initiator itself.

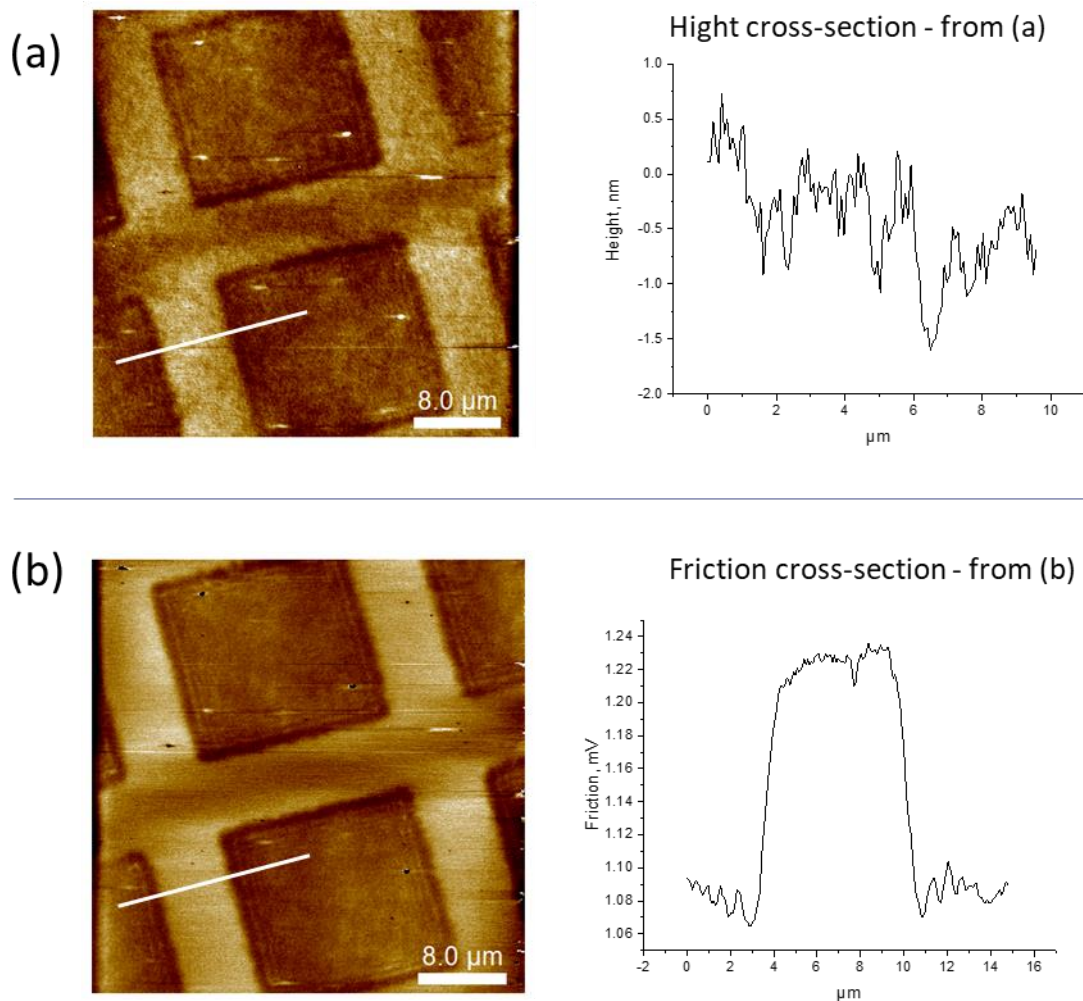


Figure 4-9: AFM contact mode images of micropatterned BIBB-APTESA film: (a) AFM height image with its cross section. (b) AFM friction image with its cross section.

Dehalogenation across the whole initiator surface was achieved through maskless UV modification of such BIBB-APTES layers following the procedure reported by Ahmed *et al.*^[76] The diameter of the exposed area was 0.5 cm and the exposure doses were ranged from 0.1-6 J cm⁻². The UV modified initiator was characterised by XPS and contact angle measurements.

XPS analysis confirmed the photodegradation of the Br-functionalised initiator. The percentage of the Br atoms was rapidly decreased with increasing exposure dose and became

slowly decreased after the exposure to 1 J cm^{-2} , demonstrating complete removal of Br atoms

Figure 4-10 blue circles.

The water contact angle decreases rapidly with dose up to 1 J cm^{-2} , with the rate of decrease slowly thereafter, to yield a limiting value of 46° in agreement with data reported previously by Ahmed et al.,^[76] as shown in **Figure 4-10 black squares.**

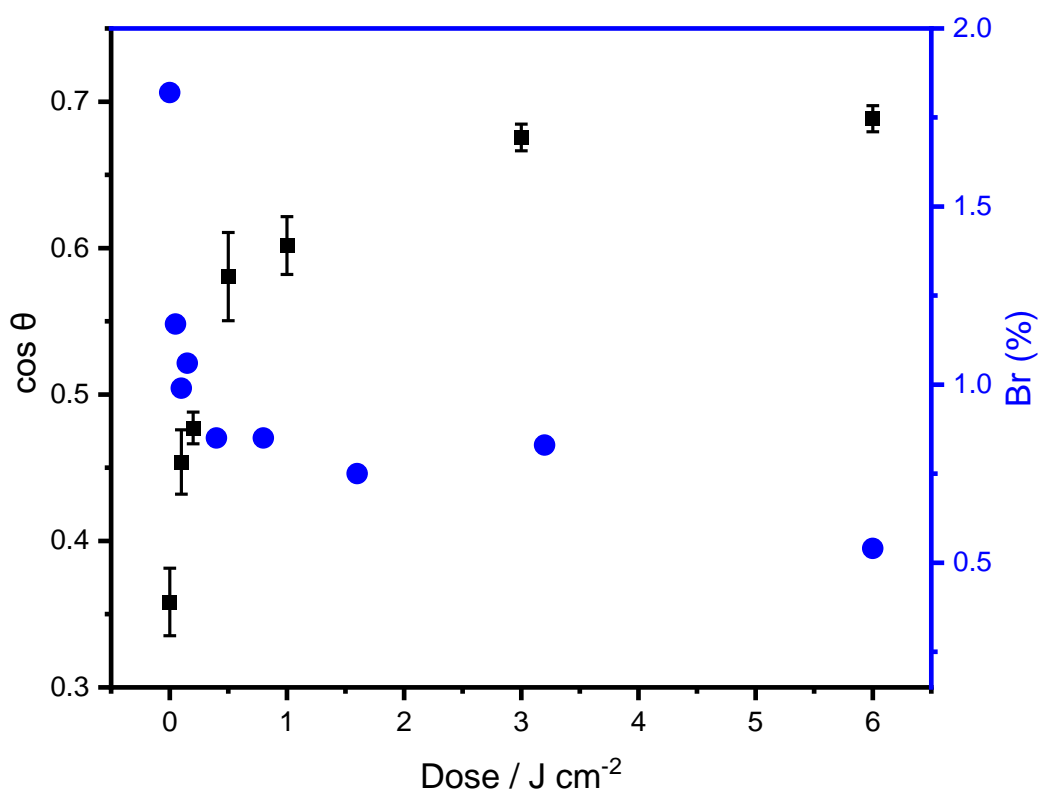


Figure 4-10: (Blue points) Percentage of Br atoms of UV-modified BIBB-APTES layer at different exposure doses ranging from 0 – 6 J cm^{-2} across the whole surface. (Black points) Contact angle of UV-modified BIBB-APTES layer at different exposure doses ranging from 0 – 6 J cm^{-2} across the whole surface.

Micropatterned BIBB-APTES initiated surfaces were used to create patterned PDMA brushes at the micro-scale. AFM Hight image of micropatterned PDMA brushes shows a clear difference in height between exposed regions (squares) and masked regions (bars), see

Figure 4-11a. However, the masked areas display greater height contrast than exposed areas. This confirms the growth of PDMA brushes from the non-exposed areas, as expected which further approved by the clear contrast in the AFM phase image between exposed and non-exposed areas as shown in **Figure 4-11b.**

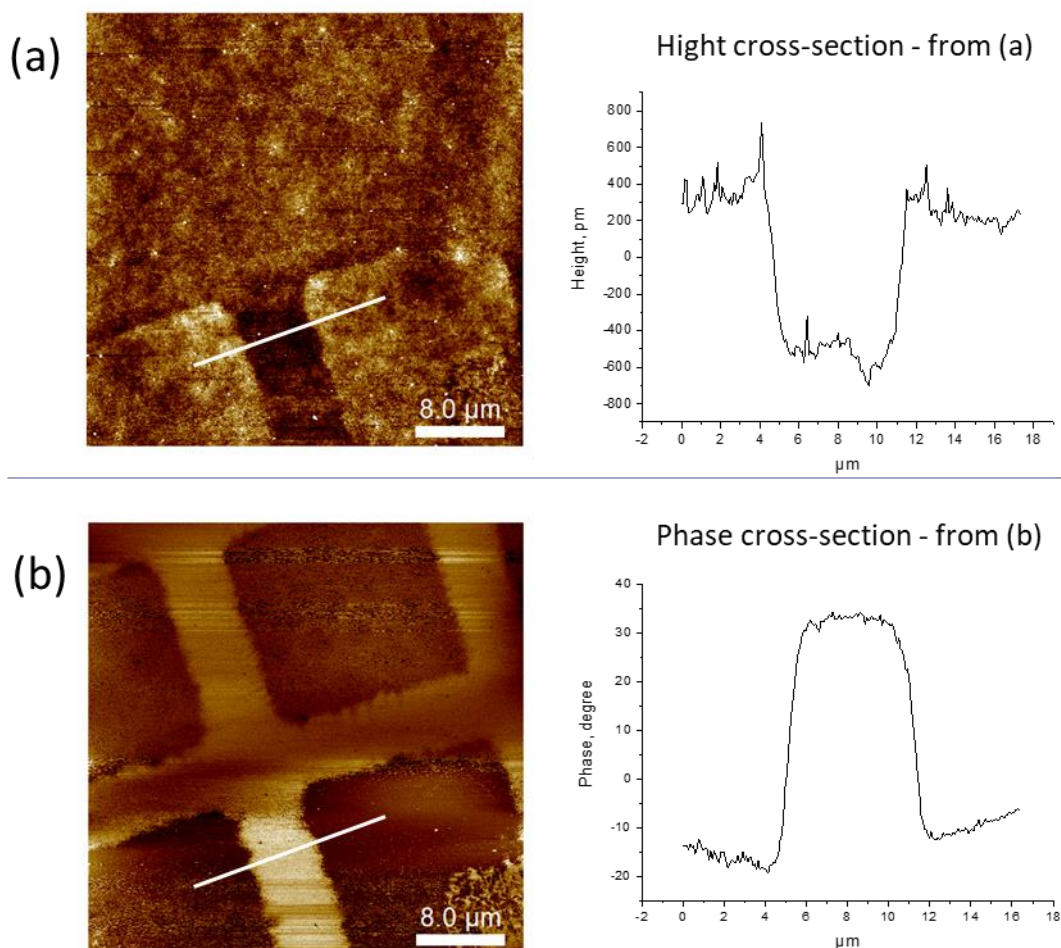


Figure 4-11: AFM tapping mode images of PDMA brushes grown on micropatterned BIBB-APTESA film: (a) AFM height image with its cross section. (b) AFM phase image with its cross section.

Height differences between the PDMA brushes polymerised for 15 min in non-exposed areas and the exposed areas were measured in order to estimate the mean PDMA thickness. As it can be seen in **Figure 4-12.** The Height difference significantly increased by increasing the exposure dose before it tends to be stabilised. This is due to the increase the partial

removal of Br from the initiator leading to decrease the brushes densities in the exposed areas and then to decrease the height in these areas.

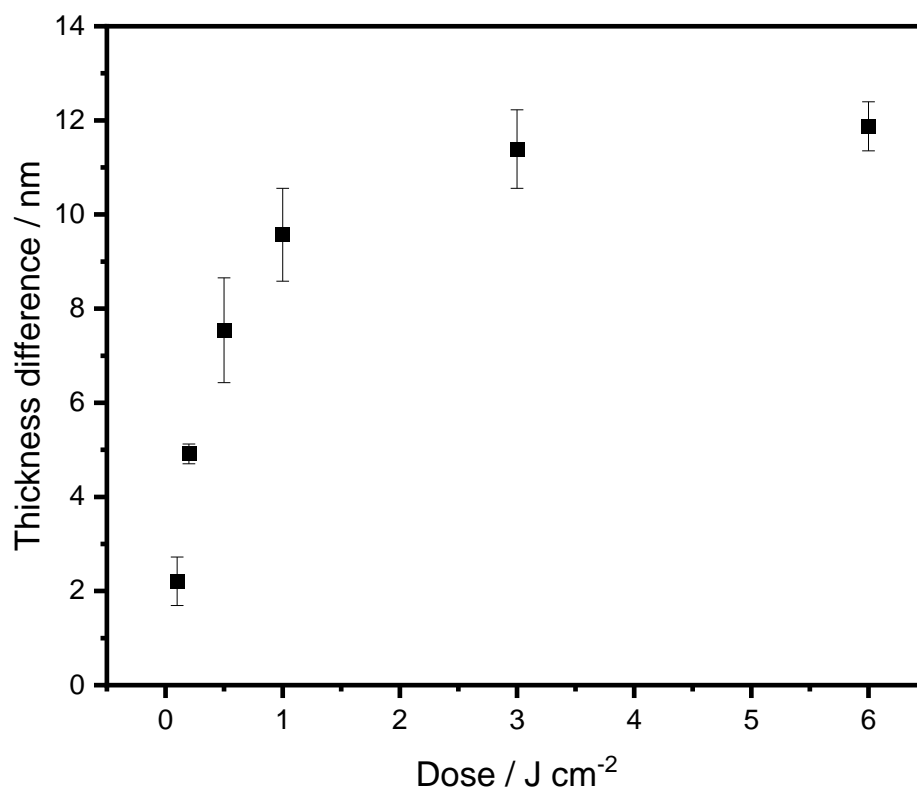


Figure 4-12: Thickness difference between exposed and non-exposed areas of PDMA brushes grown on micropatterned BIBB-APTES initiators measured by AFM tapping mode.

PDMA brushes were grown from BIBB-APTES films modified by exposure to variable irradiation doses, thus yielding varying grafting densities. A reduction in the polymer grafting densities leads to a reduction of the concentration of amine groups at the surface, which reduces the surface free energy, as confirmed by contact angle measurements as shown in **Figure 4-13a**. The thicknesses of reduced density PDMA brushes were measured by ellipsometry. As expected, the average thickness of the reduced density PDMA layer was found to decrease with increasing dose (**Figure 4-13b**).

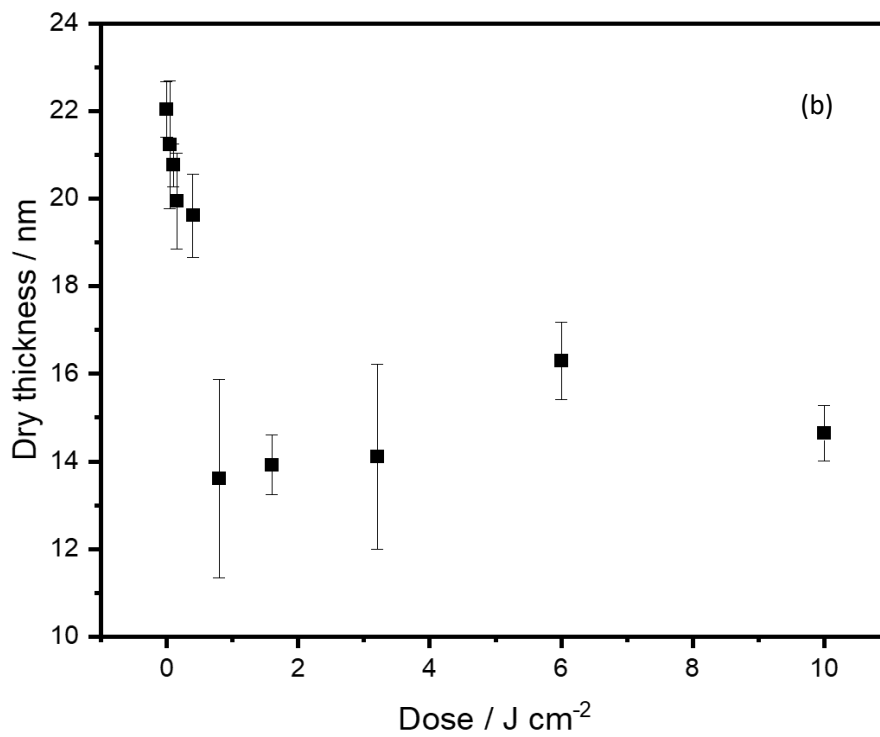
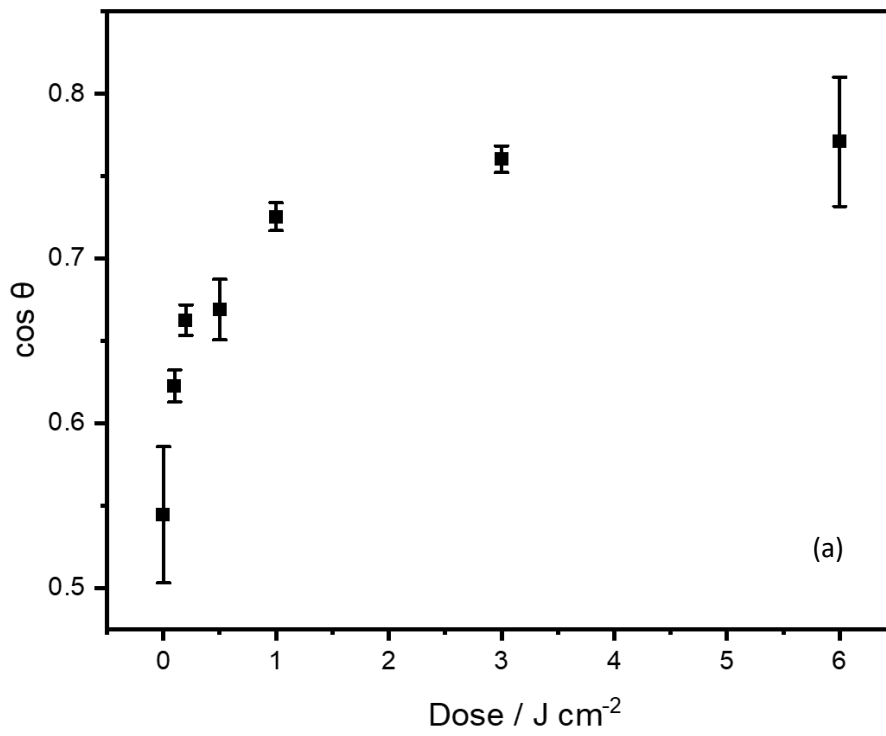


Figure 4-13: (a) Mean contact angle of reduced density PDMA brushes as a function of different exposure doses. (b) Mean dry thickness of reduced density PDMA brushes as a function of different exposure doses measured by ellipsometry.

4.3.3 Addition of *chlorophyll* to brush structures

4.3.3.1 *Chlorophyll* synthesis and characterisation

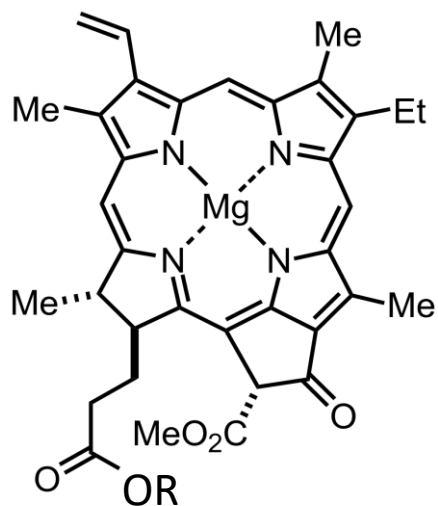
In this work, *chlorophyll a* was extracted from spinach leaves as a cost-effective natural source due to *chlorophyll* abundance in such plants. Although there are several ways to extract *chlorophyll*, organic solvent extraction (OSE) method was used in this project due to its efficiency. 99.9% acetone was chosen for this purpose because of its ability to reduce side reactions unlike diluted aqueous acetone such as 80% acetone which may result in degradation of *chlorophyll a* and occurrence of side reactions. Methanol and ethanol are similar to aqueous acetone and can lead to form undesirable products.^[181] Due to instability of *chlorophyll* outside its natural environment, it was chemically converted into more stable derivatives. Here, *chlorophyll a* firstly was converted into pheophytin a by protonation of nitrogen atoms using weak acid (acetic acid) which leads to remove magnesium ions from chlorin ring center to yield pheophytin.

Because the chemical structure of *chlorophyll a* is similar to that of *chlorophyll b*, they were separated as pheophytin a and pheophytin b by column chromatography system using 6:3:1 hexane: diethyl ether. The dark green pigment was collected and metalated with Zn ions using zinc acetate monohydrate to produce *Zn-chlorophyll* form. **Figure 4-14** summarise the extraction and derivatization processes of *ZnChla* synthesis.



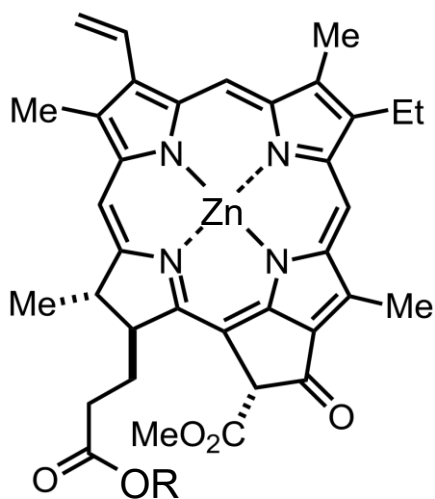
Spinach

Acetone



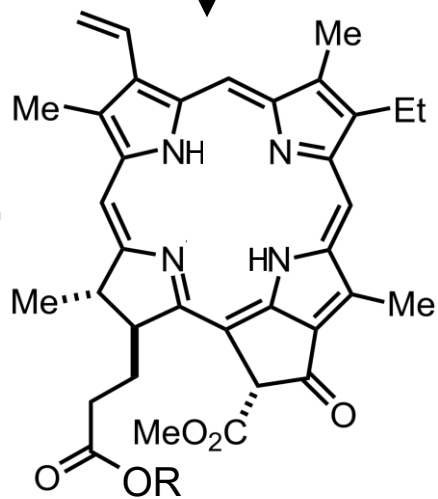
Chl

Acetic acid



Zn-chl

$Zn^{++} / MeOH$
30 min / 35 °C



Pheophytin a

Figure 4-14: Schematic illustration of extraction and derivatization of ZnChla, R = phetyl group.

UV-Vis spectrum of extracted Znchl was measured in a mixture of 1:3 DMF:water. *ZnChla* molecules absorb light in the blue (around 430nm) and red (around 665nm) spectral ranges with a narrow bands due to solet transitions and $Q_{x,y}$ transitions, respectively showing a good agreement to reported spectra of *chlorophyll* in the literature,^[238] see **Figure 4-15**.

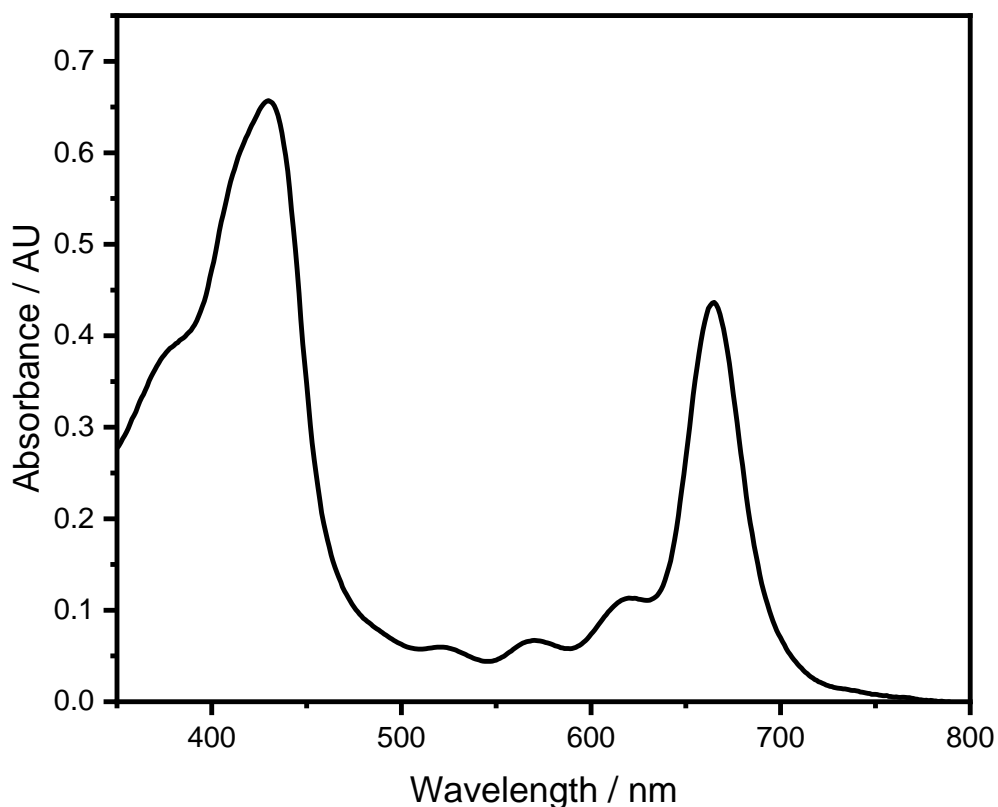


Figure 4-15: Absorption spectrum of *ZnChla* in DMF: water (1:3 v/v) mixture.

4.3.3.2 Attachments of *ZnChla* to PDMA

In light natural harvesting complexes, peptide units are used to organise *chlorophyll* and *carotenoids* in 3D.^[33] In the present work, surface-grafted PDMA brushes formed by ATRP were used as a scaffold to support *chlorophyll* molecules in order to design more readily active biomimetic structure. ATRP was chosen due to its ability to generate a well-controlled thick polymer brush with low termination rates.

Due to the presence of the central double charged zinc ions in the *chlorophyll* ring, *chlorophyll* molecules were expected to bind to the tertiary amine group of PDMA brushes through coordination bonds via a similar mechanism to that by which heme binding sites coordinate to other tetrapyrroles as it can be seen in **Figure 4-16**.

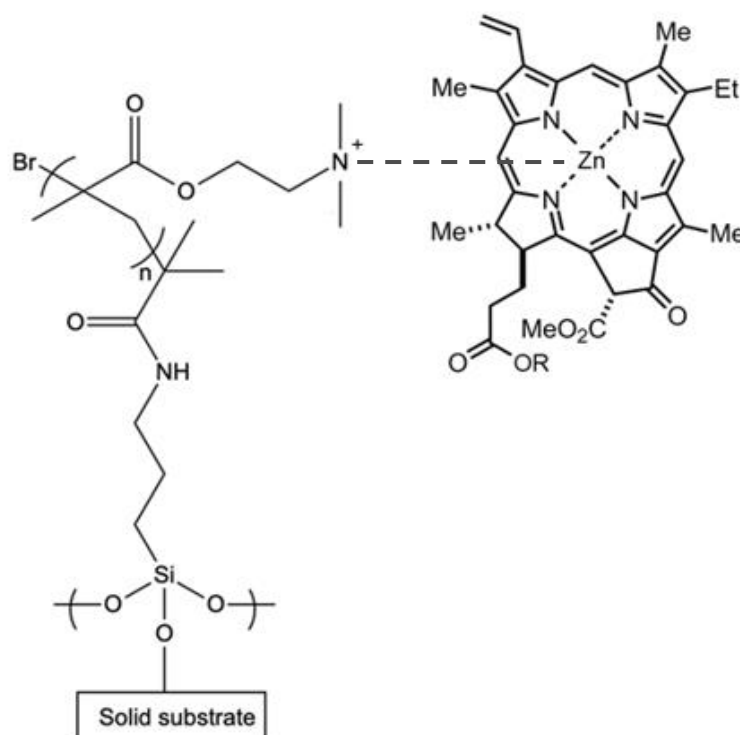


Figure 4-16: Schematic illustration of chlorophyll binding to amino group of PDMA brushes.

PDMA brushes were grown from brominated surfaces and incubated in solutions of *ZnChla*. The resulting *ZnChla*-functionalised PDMA-grafted surface structures were characterised by UV-vis spectroscopy and XPS. **Figure 4-17.** shows the absorption spectrum of a *ZnChla*-functionalised PDMA brush (**Figure 4-17 red spectrum**) together with the absorption spectrum of *ZnChla* solution (**Figure 4-17 black spectrum**). *Chla* absorption spectrum exhibit strong features at 430 nm and 665 nm, corresponding to the soret and Q_y transitions. The same peaks are observed in the spectrum of *Chla*-functionalised PDMA scaffold, confirming the binding of *Chla* to the polymer. The intensities of the absorption bands are reduced as expected given that the polymer film is only 15 nm thick, whereas the solution phase spectrum was acquired for *Chla* dissolved in solvent in a standard 1 cm cuvette.

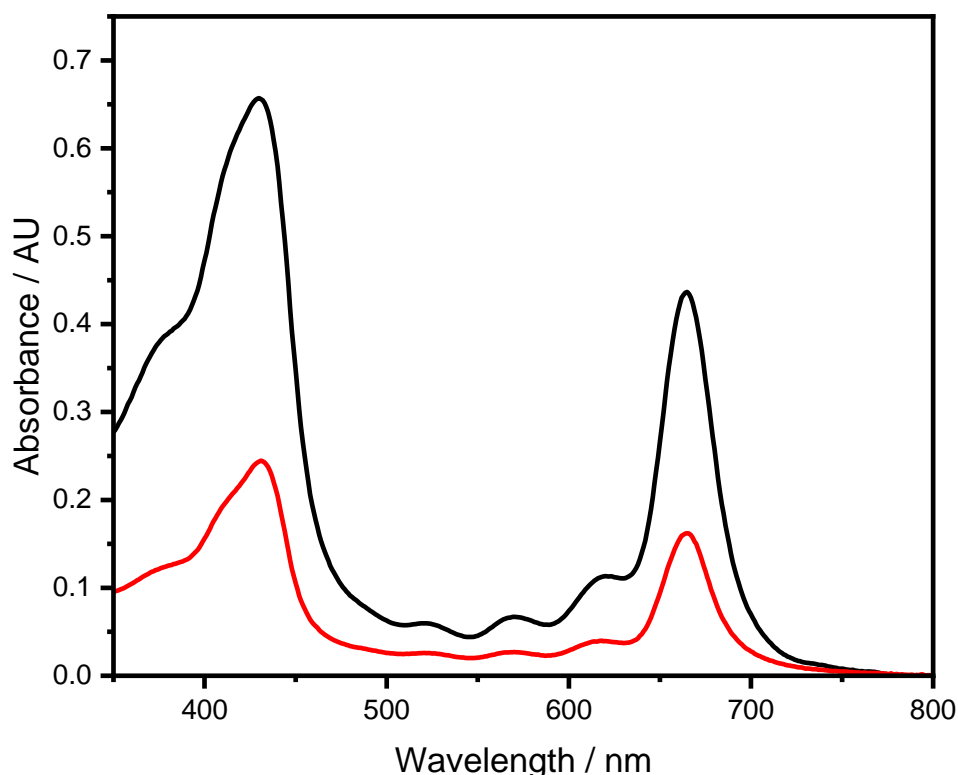


Figure 4-17: Absorption spectrum of *ZnChla* (Black) in DMF: water (1:3v/v) mixture. (Red) after immobilization on PDMA for 24 h for the same concentration.

PDMA samples were also characterised by XPS. Zn is absent from the as-prepared polymer, but after incubation of the polymer in a solution of *Chla*, a strong Zn 2p peak is observed, confirming the binding of *Chla*,^[33] (Figure 4-18 a and b).

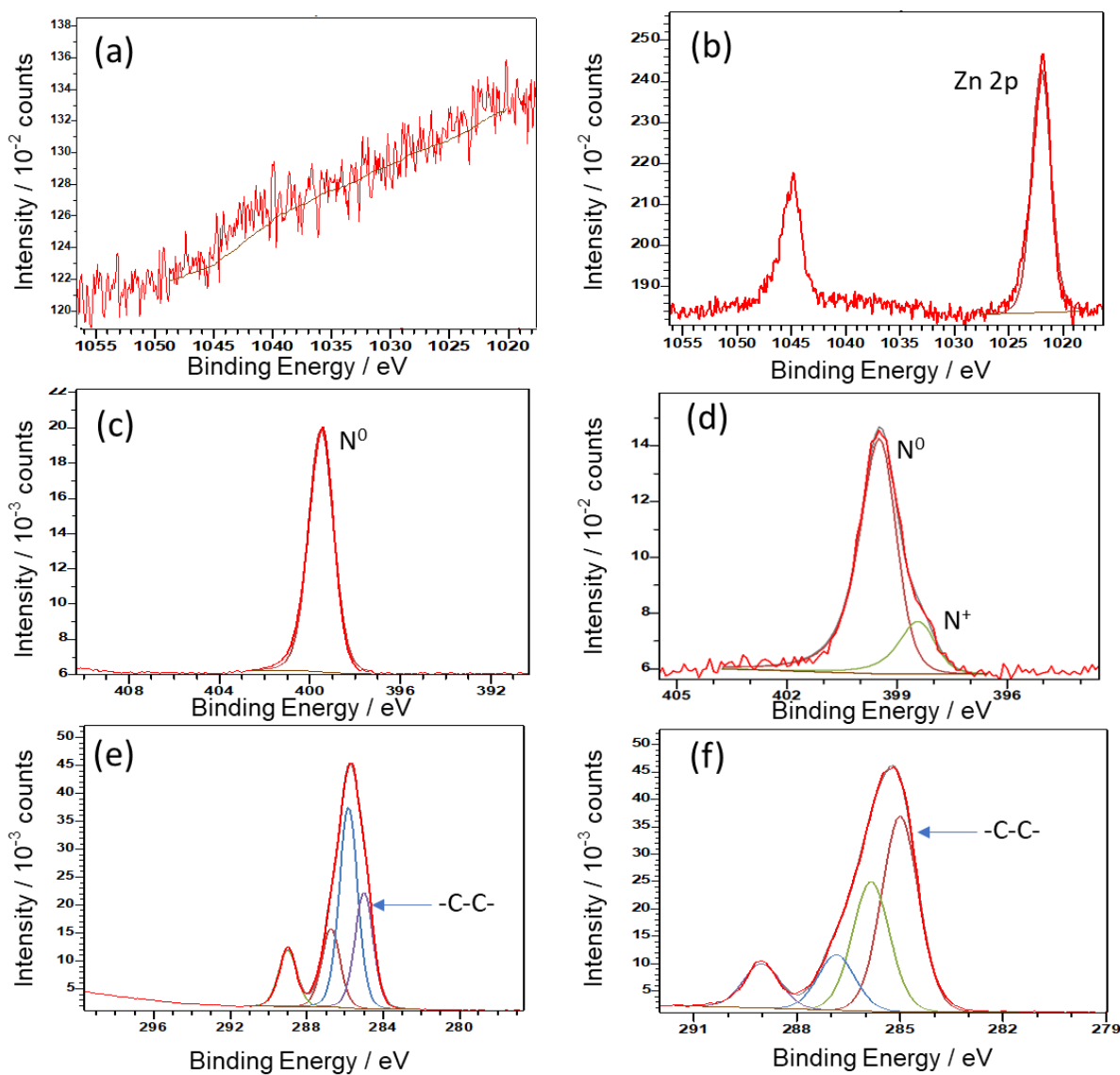


Figure 4-18: XPS spectra of PDMA before and after addition of ZnChla: (a) and (b) Zn 2p spectra before and after the addition, respectively. (c) and (d) N 1s spectra before and after the addition, respectively. (e) and (f) C 1s spectra, before and after the addition, respectively.

Pronounced changes also observed in the N 1s region of the XPS spectrum. For the as-prepared polymer, a single peak is observed at 399.6 eV. However, after binding of *Chla*, two peaks are observed. First peak is at 398.5 eV, which was attributed to Nitrogen bounded coordinately to Zn ions at the centre of *chlorophyll* ring.^[33] The second peak that at 399.5 eV was attributable to -C=N-C-, from chlorin ring and tertiary amino group of PDMA (**Figure 4-18 c and d**). Addition of *ZnChla* additionally causes an increase in the intensity of the C 1s peak at 285 eV, due to the presence of phytol chain in every *ZnChla* molecule, as it can be seen in **Figure 4-18 e and f**.

4.3.4 Adsorption isotherm for *ZnChla* on PDMA

The kinetics of adsorption reactions can be studied conveniently by measuring adsorption isotherms. The amount of adsorbate at equilibrium is measured as a function of the concentration of the adsorbate molecules in solution at constant temperature.^[239,240] In order to study adsorption isotherm of *Chla* adsorbed on PDMA brushes, PDMA films were immersed in a series of *Chla* solutions with concentrations ranging from 0- 25 μM for 24h. The amount of *Chla* bond to the brushes was determined by using Uv-vis spectroscopy and XPS.

Figure 4-19a shows the absorption intensity of the *Chla* in the solutions with different concentrations. As expected, the absorption intensities were linearly increased with increasing solution concentration. **Figure 4-19b** shows absorption spectra of PDMA films following immersing in *Chla* solutions of different concentrations. It can be seen that the intensities of the main *Chla* peaks increase with concentrations, as expected.

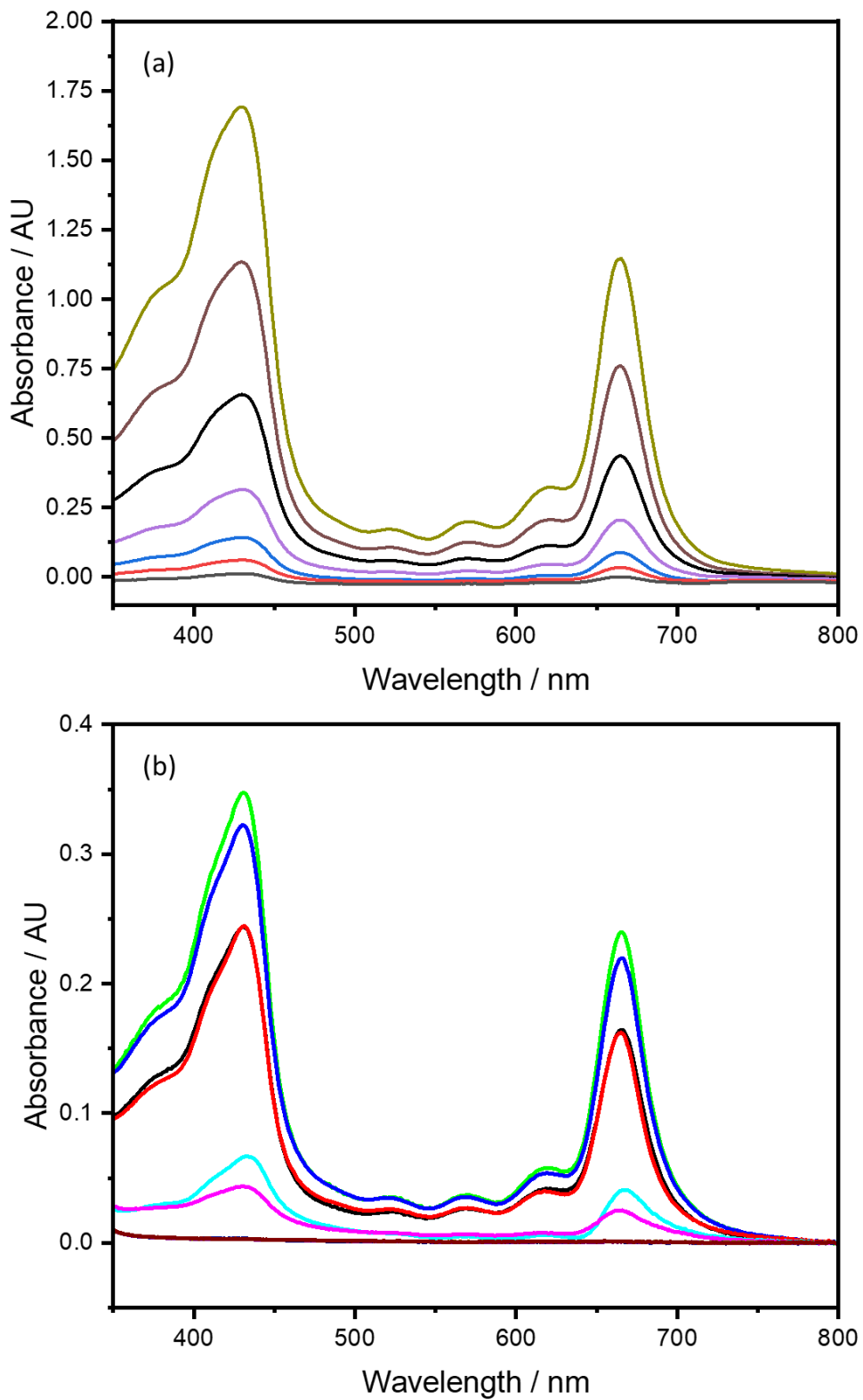


Figure 4-19: Absorption spectra of a series concentrations ranging from 0.1 to 25 μM of ZnChla in a mixture of DMF: water in the ratio 1:3 v/v. (a) in solution, and (b) on PDMA brush polymerised for 15 min.

There was a linear relation between the concentrations of *ZnChla* solutions and their respective maximum absorbance as shown in **Figure 4- 20**.

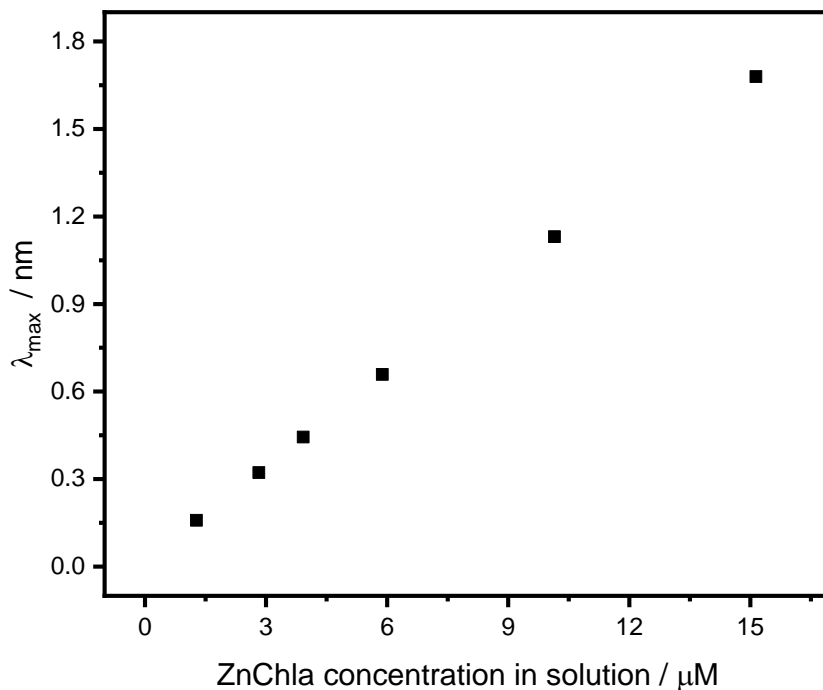


Figure 4-20: calibration curve of ZnChla concentrations as a function of their maximum absorbance.

Concentration of *ZnChla* within PDMA layer was calculated using Beer-Lambert law

$$A = \varepsilon cl$$

where, A is absorbance, ε is the molar extinction coefficient, c is the concentration, and l is the path length, here, is the thickness of the brush layer d . The relation between the initial concentration in the solution and after adsorbed within the brush layer is plotted in **Figure 4-**

21

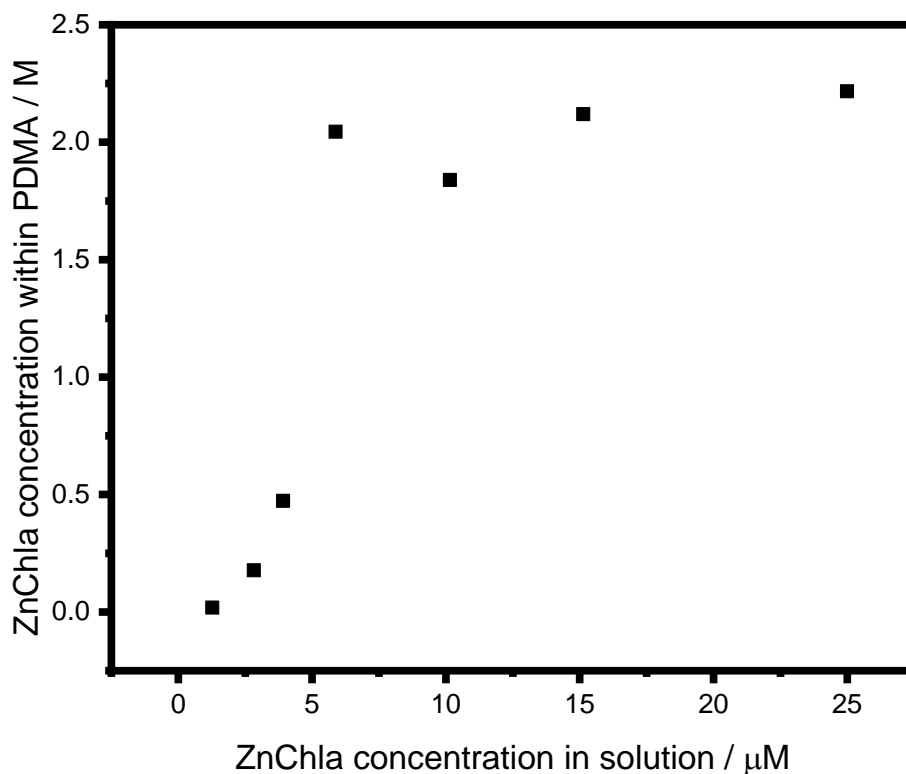


Figure 4-21: Concentrations of *ZnChla* within PDMA brushes as a function of the initial *ZnChla* concentration in solutions.

The fractional coverage (the concentration of the adsorbate in relative to the maximum concentration of the adsorbate on the surface) of adsorbed *ZnChla* molecules onto the surface-grafted PDMA brushes was calculated and presented in **Figure 4-22**. There is a monotonic relationship between the concentration of the used *ZnChla* solution and the amount of adsorbed *ZnChla* on the surface of the structure between 0.1 μM to approximately 5.8 μM . Thereafter, the rate of increase slows, and it approaches a limiting value at a concentration of 5 μM .

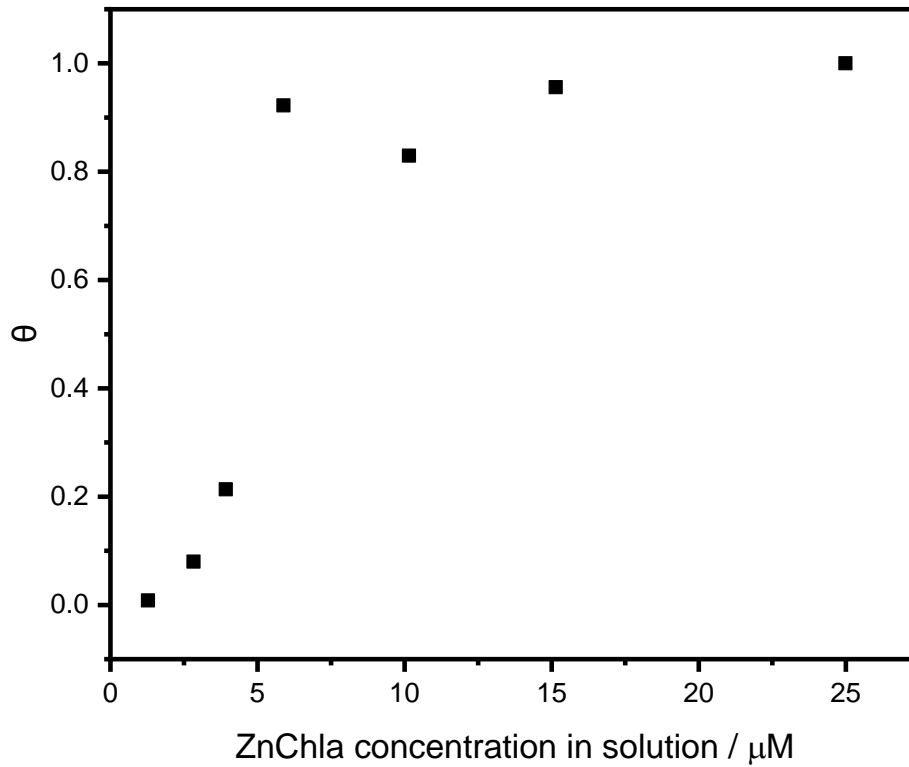


Figure 4-22: Fractional coverage of ZnChla within PDMA layers as a function of ZnChla concentration in the solution.

The number of excitons (*chlorophylls*) per polymer n_p can be calculated using the following equation:

$$n_p = \frac{NA}{5 \times 10^{14} \epsilon}$$

where, N is Avogadro's number. A is absorbance and ϵ is the molar extinction coefficient. Then, it is possible to estimate the fraction of monomers χ that are bound to a Chl as follows. A reasonable assumption is that there are 4 repeat units per nm of polymer chain. Thus, the degree of polymerisation (number of monomers per chain) is $\sim 4 \times d / \text{nm}$, and $\chi = n_p / (4d / \text{nm})$. **Figure 4-23**

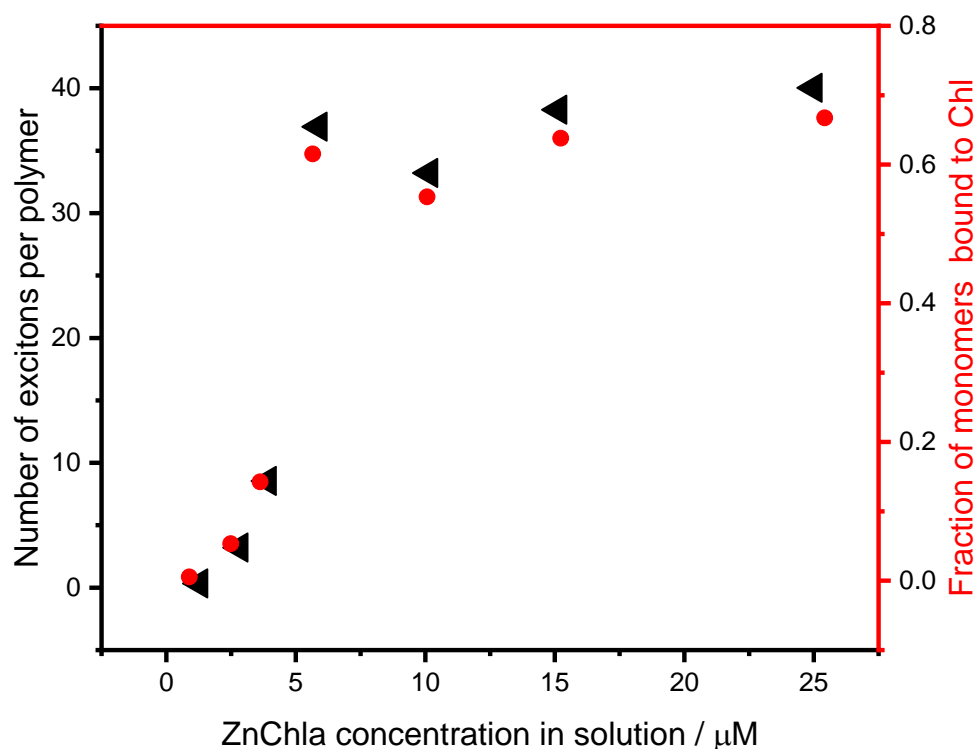


Figure 4-23: changes in number of excitons per polymer and fraction of monomers bound to ZnChla as functions of the initial concentrations of ZnChla in solution.

These calculations assume a fully-stretched chain confirmation, which is unlikely. So, to solve this, calculations based on the molecular weight of the polymer can be used instead of calculating chain length. However, this can be complicated and may not be directly applicable to determining the number of monomers in polymer brushes grown on solid substrates. This is because polymer brushes on substrates are typically thin films or surface-confined structures, and traditional bulk characterization techniques (such as gel permeation chromatography) may not be suitable. Also, the uniformity of the chain length across the entire surface must be considered.

After immersing in *Chla* solutions, PDMA samples were analysed using XPS, and the Zn 2p peak area was measured. The variation in the Zn 2p area with the *Chla* concentration is shown in **Figure 4-24**. This observation indicates that the more *chlorophyll* molecules the more binding sites on the PDMA chains are occupied by *ZnChla* molecules until reaching saturation state.

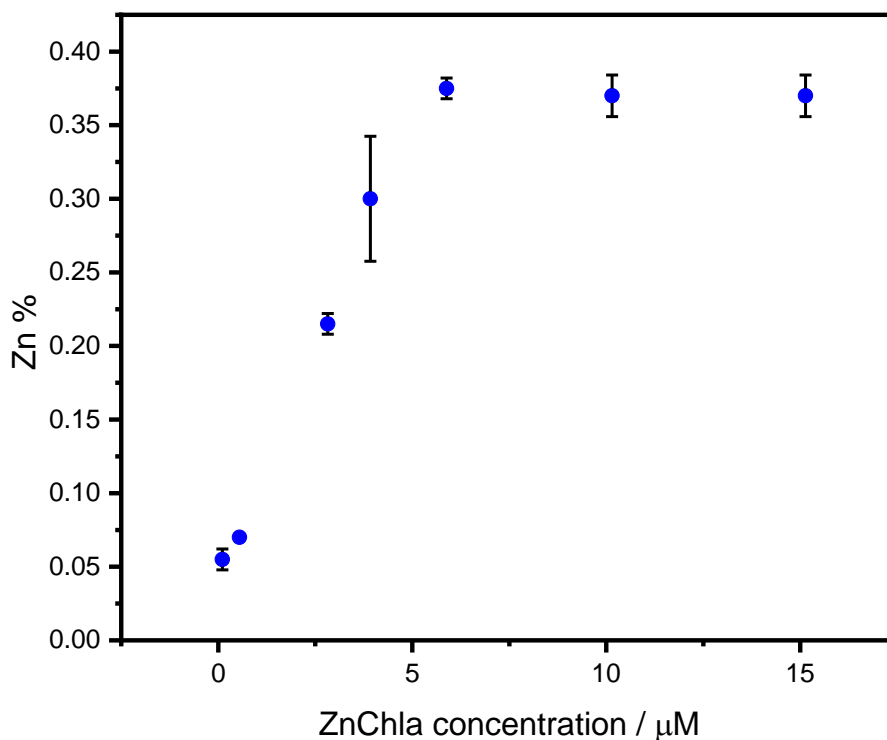


Figure 4-24: Variation in Zn 2p percentage on the surface as a function of chlorophyll concentration.

4.3.5 Quaternisation of PDMA brushes and Chl attachment to q-PDMA - regulation of binding.

Because PDMA possesses tertiary amine functionality in every repeated unit on the polymer chain, it is possible to conduct Menshutkin reaction in which tertiary amine are converted into quaternary ammonium salts using an appropriate alkyl halide. However, the quaternization efficiency depends on the used solvent used in this process. Using a poor solvent for the brushes such as n-hexane leads to confinement of the quaternization to the upper portion of the brush chains. It also maintains pH-responsive behaviour unlike the use of good solvents such as THF which allows for uniform quaternization throughout the polymer chains layer causing the polymer brushes to lose their pH-responsive properties. Moreover, the degree of polymer quaternization can be controlled by variation of alkyl halide concentration. It was hypothesised that if *Chla* binding was via coordination to the tertiary amine groups in PDMA, blocking of the amines by quaternization with 1-iodooctadecane should yield a reduction in *Chla* binding. So, in this section, partial quaternization of the amine groups of PDMA brushes was achieved using 1-iodooctadecane in THF. This process was used to regulate the binding of *chlorophyll* by blocking the binding sites via converting the amine group to the positively charged ammonium salt. **Figure 4-25** shows the schematic illustration of the quaternization of DMA with 1-iodooctadecane.

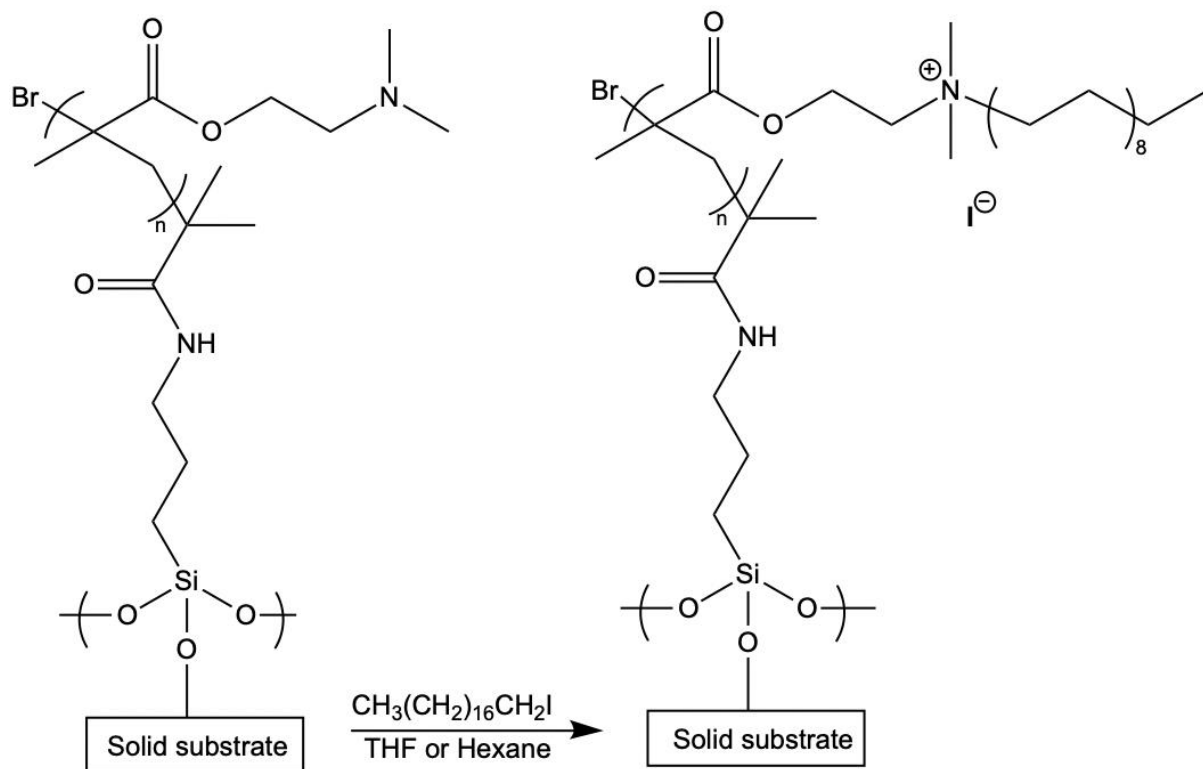


Figure 4-25: Quaternisation of DPMA with 1-iodooctadecane.

The degree of PDMA quarterisation was determined by XPS because this technique can efficiently distinguish between normal (neutral) and quaternised (cationic) nitrogen atoms, which can be quantified by XPS peak-fitting. **Figure 4-26** shows N 1s high resolution XPS spectra recorded for PDMA brushes before quaternisation (**Figure 4-26a**). A series of quaternised PDMA brushes with a quaternization degree of 16%, 65%, and 92% were obtained using 1-iodooctadecane with concentrations of 25, 50, 100 μM , respectively (**Figure 4-26 b, c and d**). There is only one peak at around 399.54 eV in pure PDMA XPS spectrum, which attributed to the neutral nitrogen atom of the amine group of PDMA brush. However, the emergence of N^+ peak at around 402.5 eV in N 1s spectra confirms the quaternization process. This peak became more pronounce corresponding to the increase of the concentration of 1-iodooctadecane.

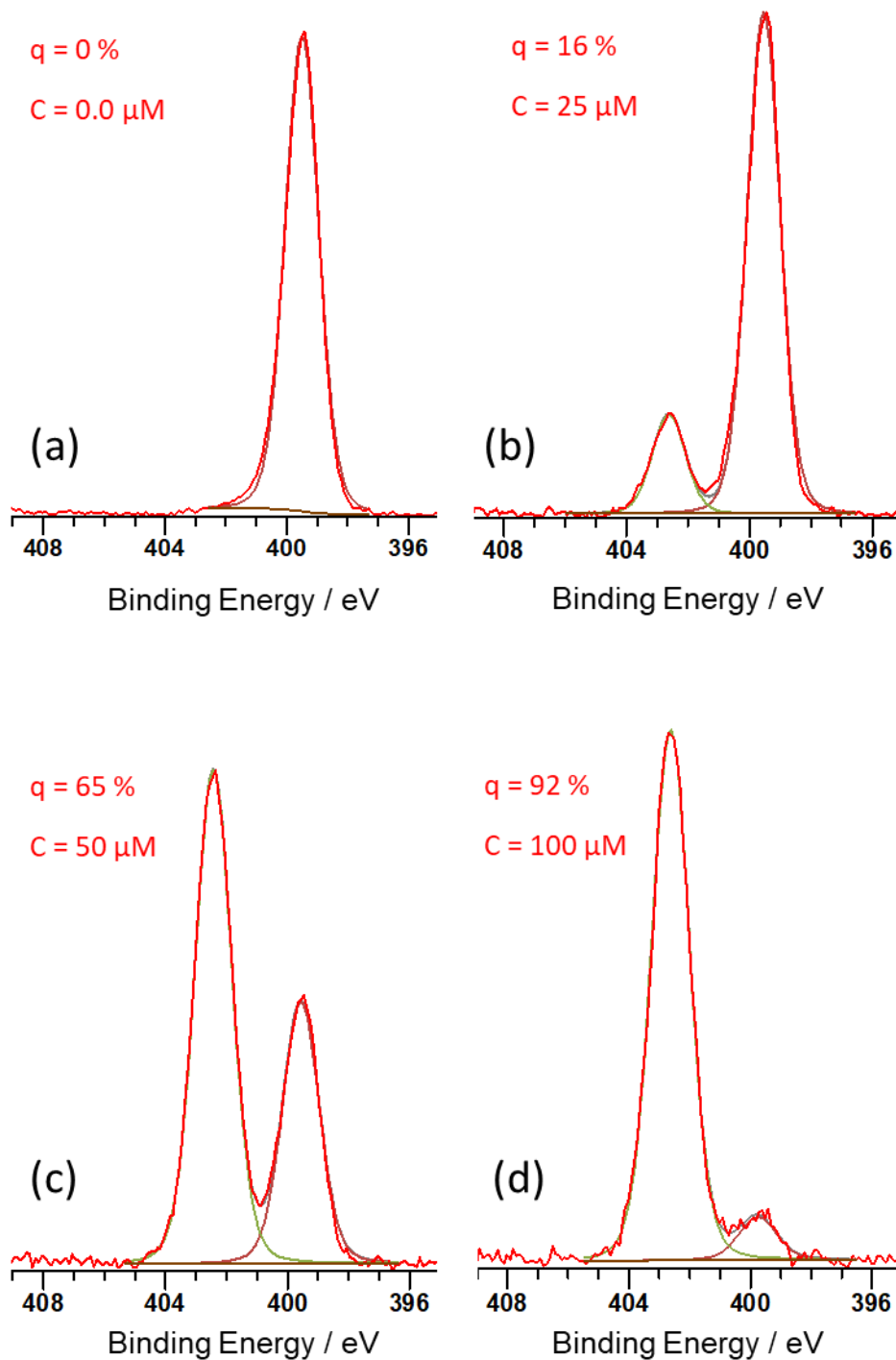


Figure 4-26: XPS N 1s high resolution spectra of (a) normal PDMA brush compared to q -PDMA with quaternization degree of (b) 16 %. (c) 65 %. (d) 92 %.

Noticeably, the degree of quaternization was increased with the concentration of 1-iodooctadecane used to derivatise the brushes from 0 μM to 75 μM . However, a limiting value was measured for concentrations between 100 μM and 400 μM . 92% was the highest degree of quaternization that was achieved. See **Figure 4-27 red points**.

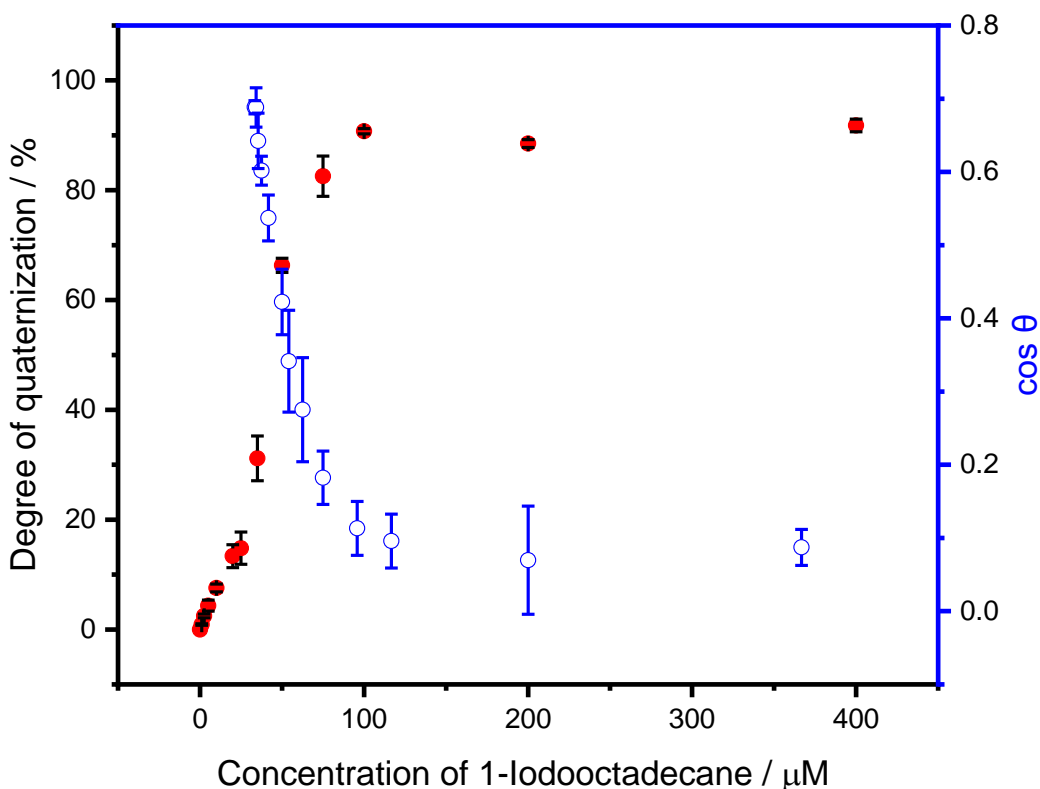


Figure 4-27: Degree of quaternization (Red points) and measured contact angle (blue circles) as functions of 1-iodooctadecane concentration.

As the degree of PDMA quaternization is increased, the measured contact angle increased from about 46° for un-quaternised PDMA to approximately 85° at the concentration of 100 μM for quaternised PDMA (**See Figure 4-27 blue circles**). The increase in hydrophobicity of the quaternised PDMA brushes can be attributed to the introduction of the relatively hydrophobic 1-octadecyl group into the PDMA brushes, which can be inferred by the growing C1s peaks corresponding to the increase of the concentration of 1-iodooctadecane as illustrated in **Figure 4-28**.

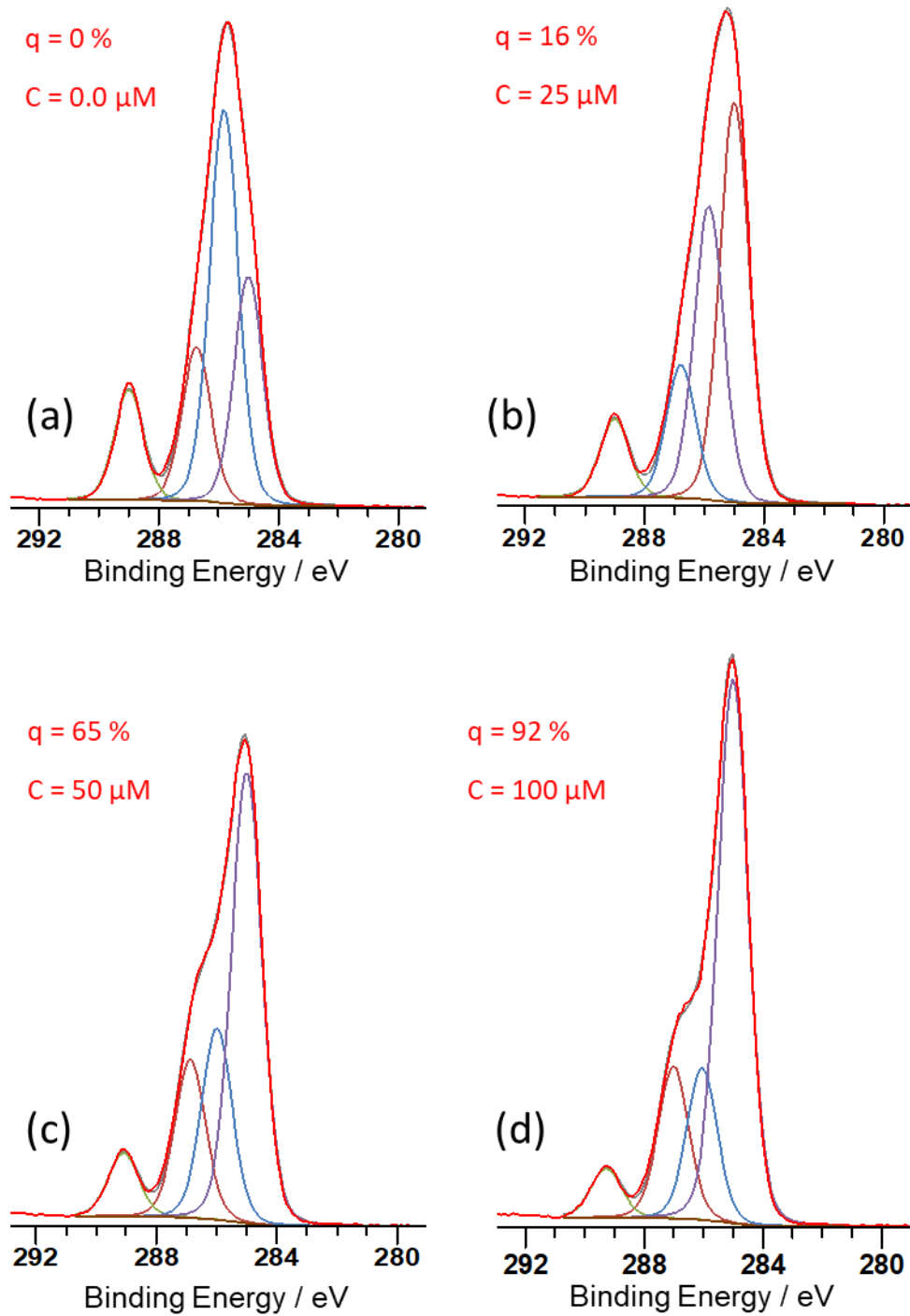


Figure 4-28: XPS C 1s high resolution spectra of (a) normal PDMA brush compared to q-PDMA with quaternization degree of (b) 16 %. (c) 65 %. (d) 92 %.

The percentage of iodine on the surface increased with the degree of quaternisation As expected (**Figure 4-29**). This is due to the introduction of iodide ions as counter-ions to the quaternised nitrogen atoms.

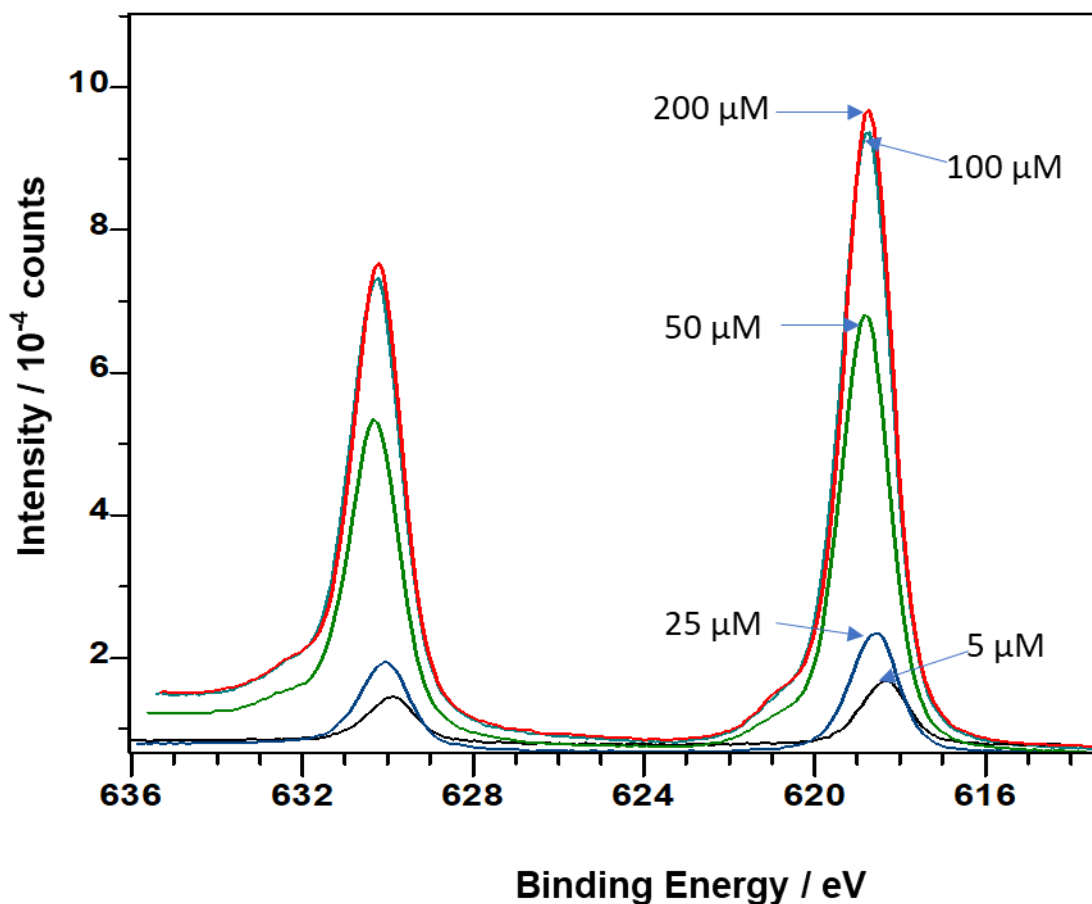


Figure 4-29: Growing iodine3d XPS spectra as a function of PDMA quaternisation degree.

4.3.5.1 Addition of *chlorophyll* to quaternised PDMA brushes

In order to explore the feasibility of regulating the binding of *ZnChla* molecules to PDMA brushes, *ZnChla* was used to functionalise a series of quaternised PDMA brushes with different degree of quaternization. **Figure 4-30** shows XPS Zn 2p and N 1s spectra of *ZnChla*-functionalised pristine PDMA **Figure 4-30 a and b**, respectively. **Figure 4-30** also shows XPS Zn 2p and N 1s spectra of *ZnChla*-functionalised q-PDMA brushes with quaternisation degree of 8% (**Figure 4-30 c and d**), and quaternisation degree of 78% (**Figure 4-30 e and f**). The

pronounced Zn 2p peak in the case of pristine PDMA was diminished by 8% when PDMA quaternised. This diminution continues increasing the quaternization. As expected, the higher degree of quaternization, the less *ZnChla* bound to PDMA brushes.

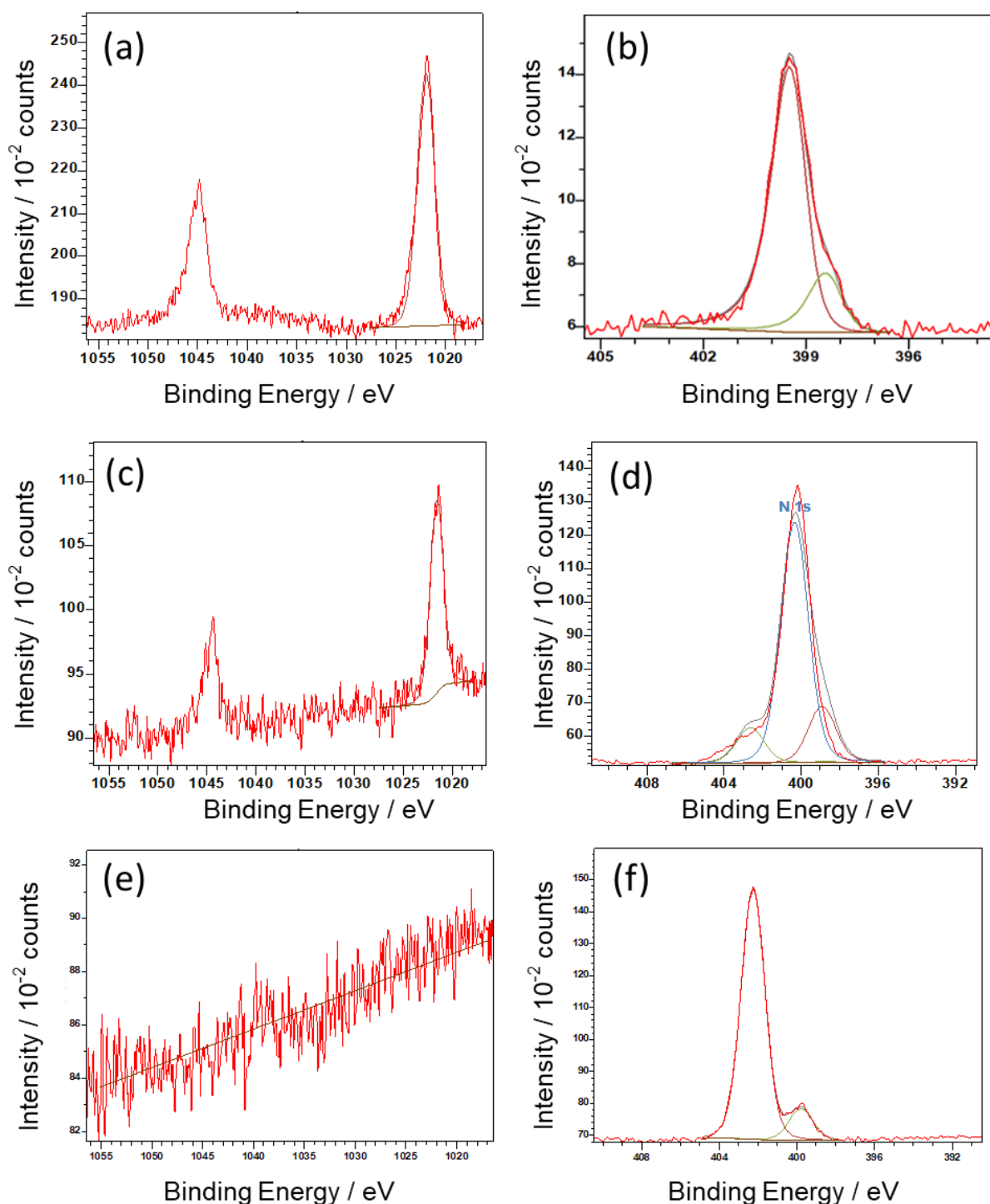


Figure 4-30: Zn 2p and N 1s XPS spectra after attachment of *ZnChla* to PDMA before (a and b) and after quaternization with quaternization degree of 8% (c and d), and quaternization degree of 78% (e and f), respectively.

Absorption spectra of *ZnChla*-functionalised pristine PDMA and *ZnChla*-functionalised q-PDMA brushes with quaternization of 11%, 65%, 78% and 89% were recorded and are presented in **Figure 4-31**. In good agreement with the XPS observations, the intensity of the *Chla* absorption bands decreased as the fraction of quaternised monomers increased, with *Chla* being undetectable at 89% quaternization. It is notable that although these spectra span a wide range of concentrations and degree of quaternizations, there is no significant in the positions of the *Chla* absorption bands, suggesting that *Chla* is not aggregated in any of these structures. This is consistent with hypothesised *Chla* binding mechanisms in which the tertiary nitrogen atoms on PDMA coordinate to the metal centre of The *Chla*. The significant decrease of the absorption intensities to less than the half of the original intensity by first few quaternization degree (11%) from around 0.4 to 0.18 can be attributed to the spatial hindrance caused by 1-octadecyl chains.

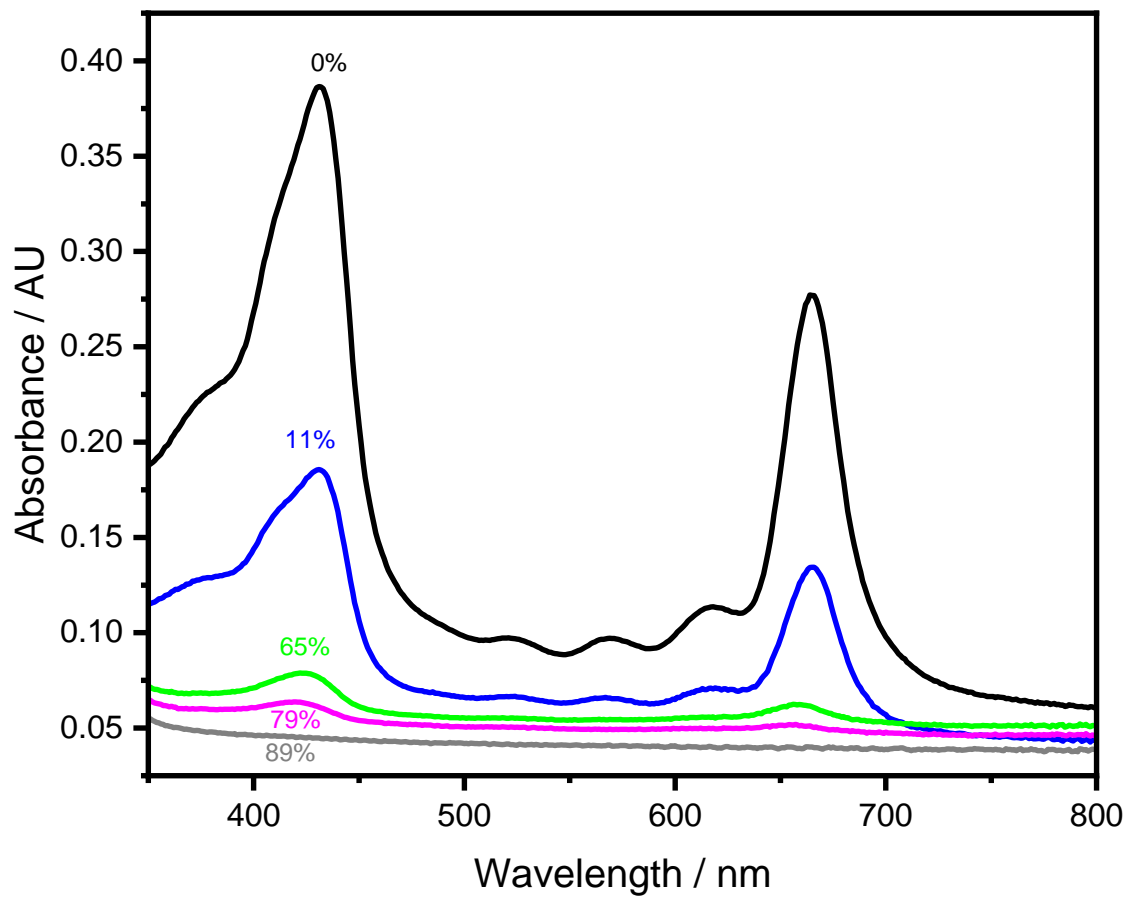


Figure 4-31: Absorption spectra of ZnChla after immobilization on to normal PDMA brush and q-PDMA with quaternization degree of 11%, 65%, 79% and 89%.

4.3.6 XPS Depth Profiling of PDMA quaternised with 1-iodooctadecane and PDMA reacted with *chlorophyll*

In this section, data analysis and fitting obtained spectra were conducted by collaboration with Deborah Hammond and Jabra AlKorbi.

4.3.6.1 XPS Depth Profiling of PDMA quaternised with 1-iodooctadecane

To obtain a better understanding about distribution of quaternization throughout the brush chains, XPS depth-profiling analysis were performed to iteratively access sub-surface compositional layers. Here, PDMA sample was left in a 140 μM solution of 1-iodooctadecane for 18 hours. Untreated PDMA brush was also analysed as a control sample. THF was chosen as being a good solvent for PDMA. The extent of quaternization achieved was much less than that expected based on the original isotherm, and it is believed this is a result of the cool temperatures in the laboratory when the samples were manufactured or could related to the low efficiency of 1-iodooctadecane the 3-month-old since it was opened.

An initial survey scan collected from unmodified PDMA thin film showed the layer thickness was greater than the penetration depth of the XPS experiment, which was inferred by the non-appearance of silicon peak. **Figure 4-32** shows the C 1s and N 1s spectra collected from the PDMA and q-PDMA samples before any etching. In the N 1s spectra the additional peak at approximately 402.7 eV can be seen for the quaternised samples and is consistent with a protonated amine group, (**Figure 4-32 a and c**). Changes to the C 1s spectrum can also be seen with a substantial increase in the C-C/C-H component at 285.0 eV compared to normal PDMA (**Figure 4-32 b and d**).

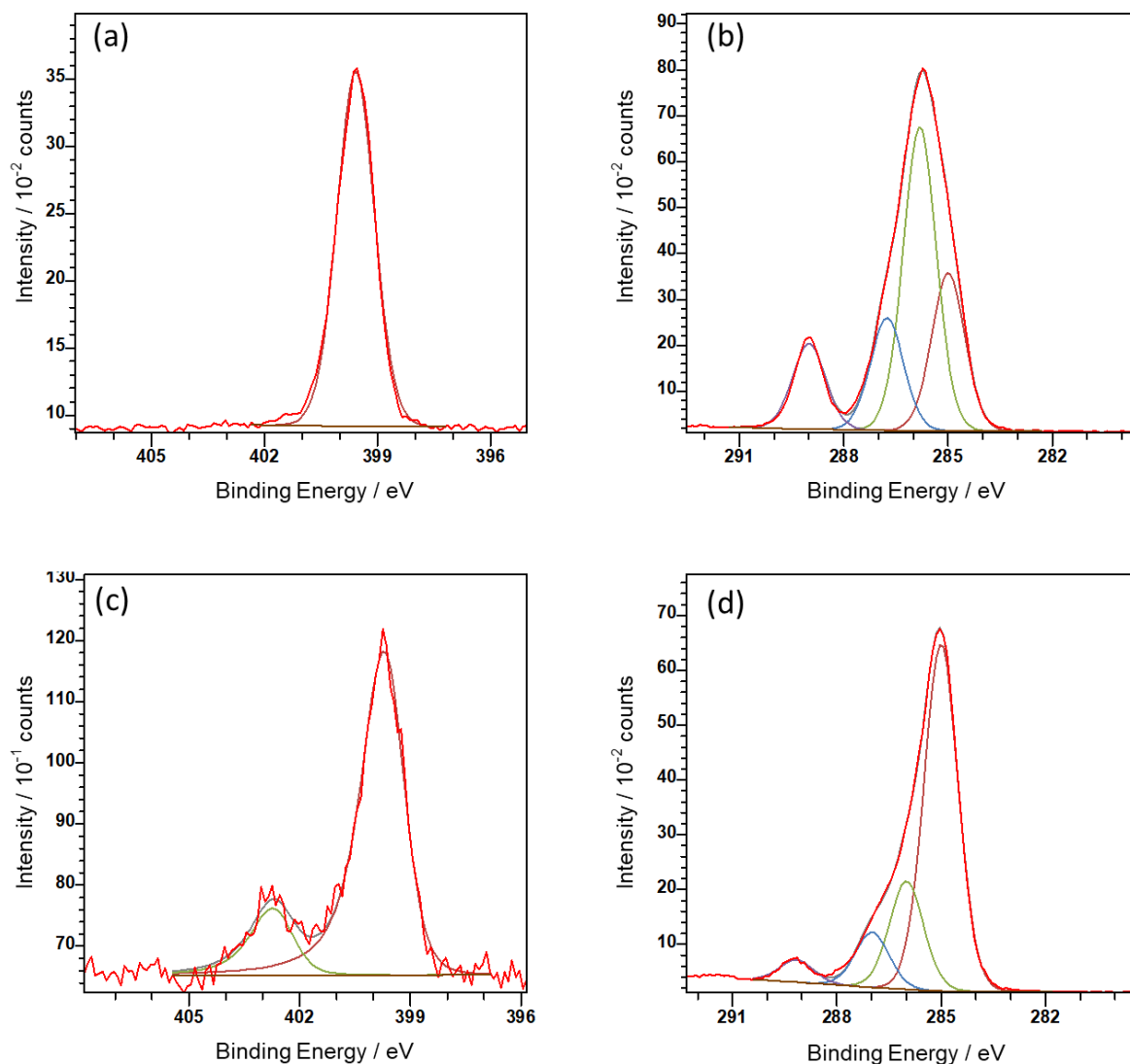


Figure 4-32: (a) N 1s and (b) C 1s XPS high resolution scans taken from depth profile at time 0, i.e., before any etching of pure PDMA. (c) N 1s and (d) C 1s XPS high resolution scans taken from depth profile at time 0, i.e., before any etching of q-PDMA.

Figure 4-33 shows a depth profile through the normal PDMA sample. The brush was fully penetrated within only a few depths, so the etch time per analysis was reduced for the quarternised samples. The interface is sharp, i.e. there is a rapid transition between polymer brush and substrate suggesting a uniform polymer brush thickness. The initial surface concentrations of 74 at% C, 9 at% N and 17 at% O are close to those expected for normal PDMA being 73 at% C, 9 at% N and 18 at% O.

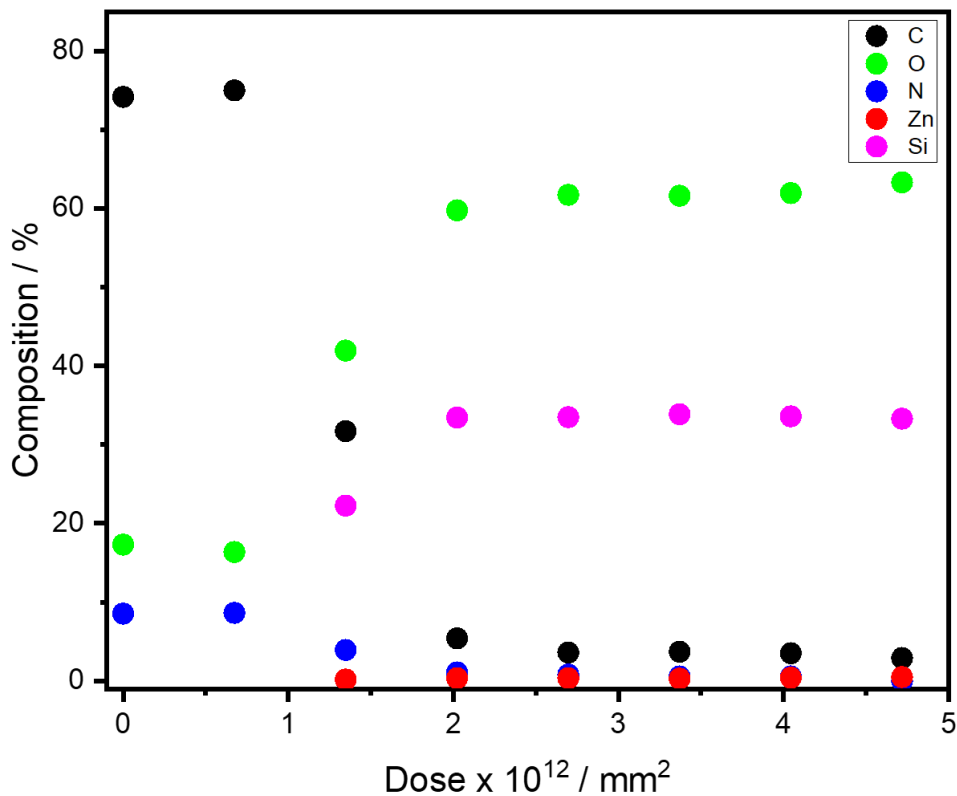


Figure 4-33: XPS depth profile through the normal PDMA sample

Nitrogen was only detected in one environment, as shown in **Figure 4-34** where the individual N 1s and C 1s spectra are shown for the first four analyses. There is little variation in the carbon chemistry until the fourth analysis where the polymer brush has been largely removed and at this point is difficult to make a confident curve-fit with the four peaks typical of PDMA.

For the discussion of *chlorophyll* treated PDMA later on, it important to note that for untreated PDMA, zinc was only detected once the glass substrate was reached, and at a constant concentration of approximately 0.4 at%.

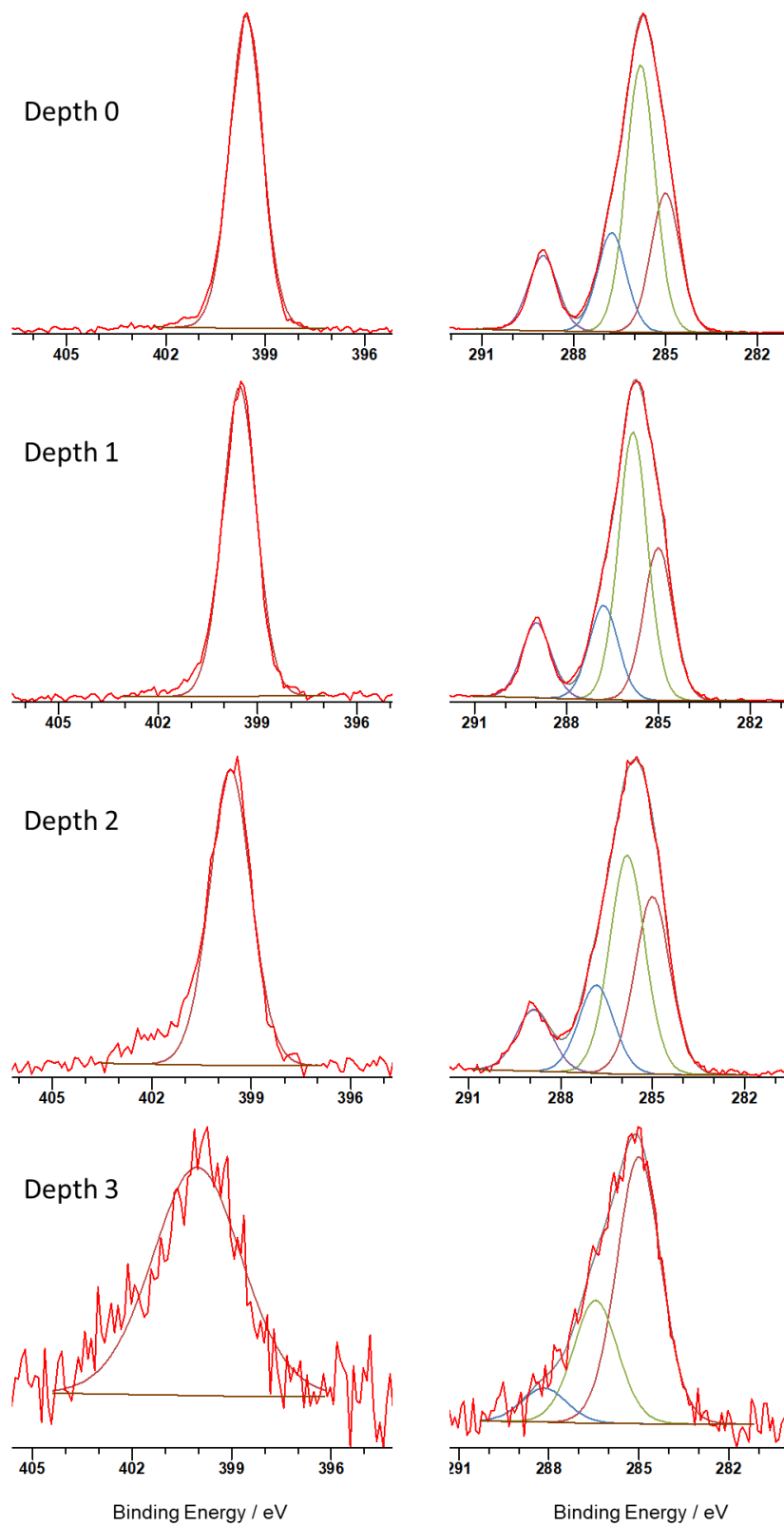


Figure 4-34: High resolution scans of N 1s (left) and C 1s (right) taken from PDMA depth profile

Figure 4-35a shows a depth profile collected from the quaternised sample. The same data is shown in **Figure 4-35b**, but the vertical scale has been limited to show the iodine and nitrogen concentrations more clearly. It can be seen that the initial carbon concentration is very high at approximately 85 at%. Oxygen is present in the PDMA but is present at a much larger concentration in the glass substrate. The carbon and oxygen profiles cross after the samples has been etched with nearly 3×10^{12} clusters/mm² after quaternization compared to approximately 1×10^{12} clusters/mm² for normal PDMA, suggesting either a much thicker or more dense organic film after quaternization. The nitrogen and iodine concentrations increase as the sample surface is penetrated, before decreasing as the substrate begins to give a more significant contribution to the intensity detected, in contrast to the expected stable concentrations along the depth. The reason behind this behaviour of nitrogen and iodine on the surface is not clear.

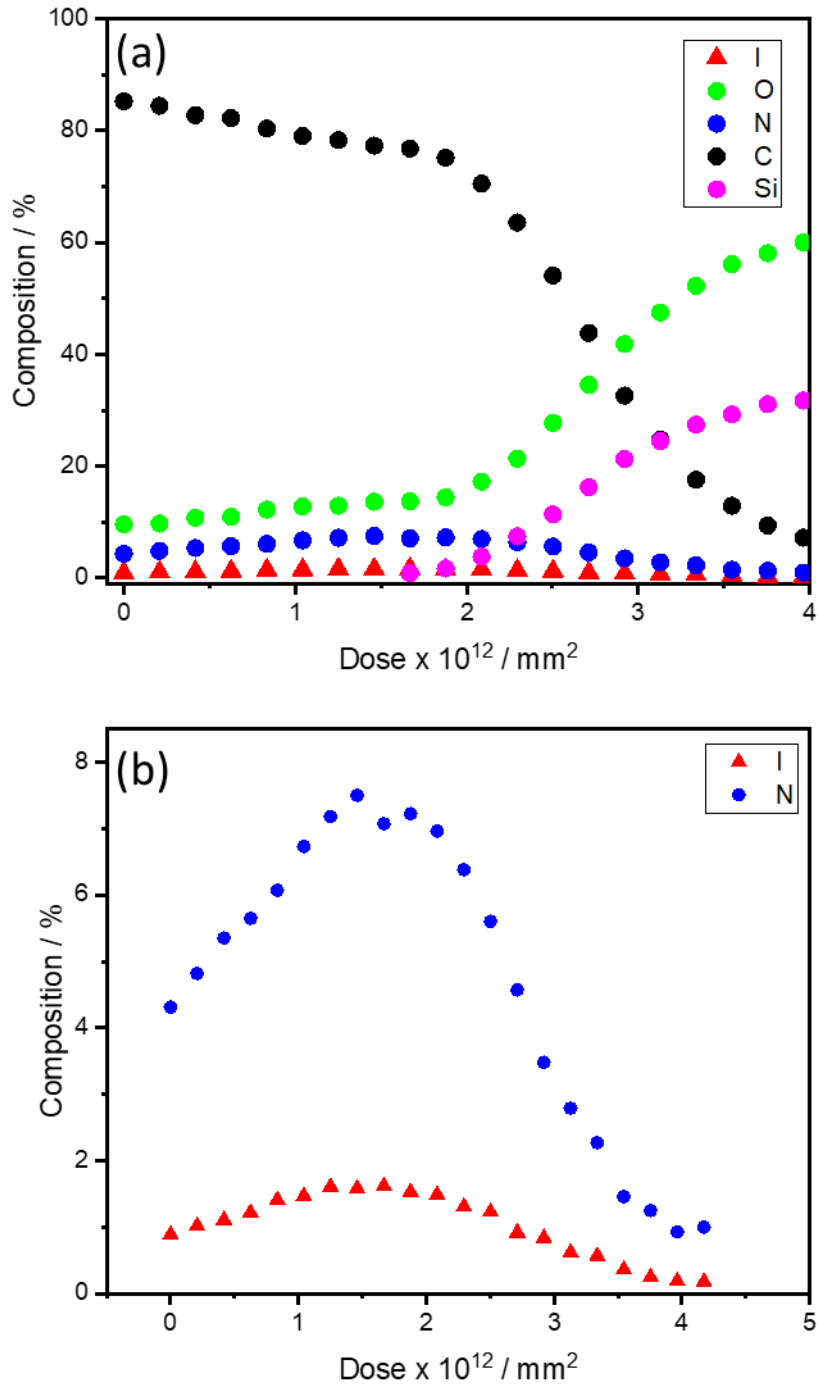


Figure 4-35: (a) XPS depth profile through q-PDMA. (b) Scale limit to show I and N more clearly.

The high-resolution scans collected during the depth profile have all been curve fitted. The N 1s scans were best fitted as two components, corresponding to the tertiary amine of the untreated PDMA and the protonated amine after quaternization. Example spectra are shown in **Figure 4-36**.

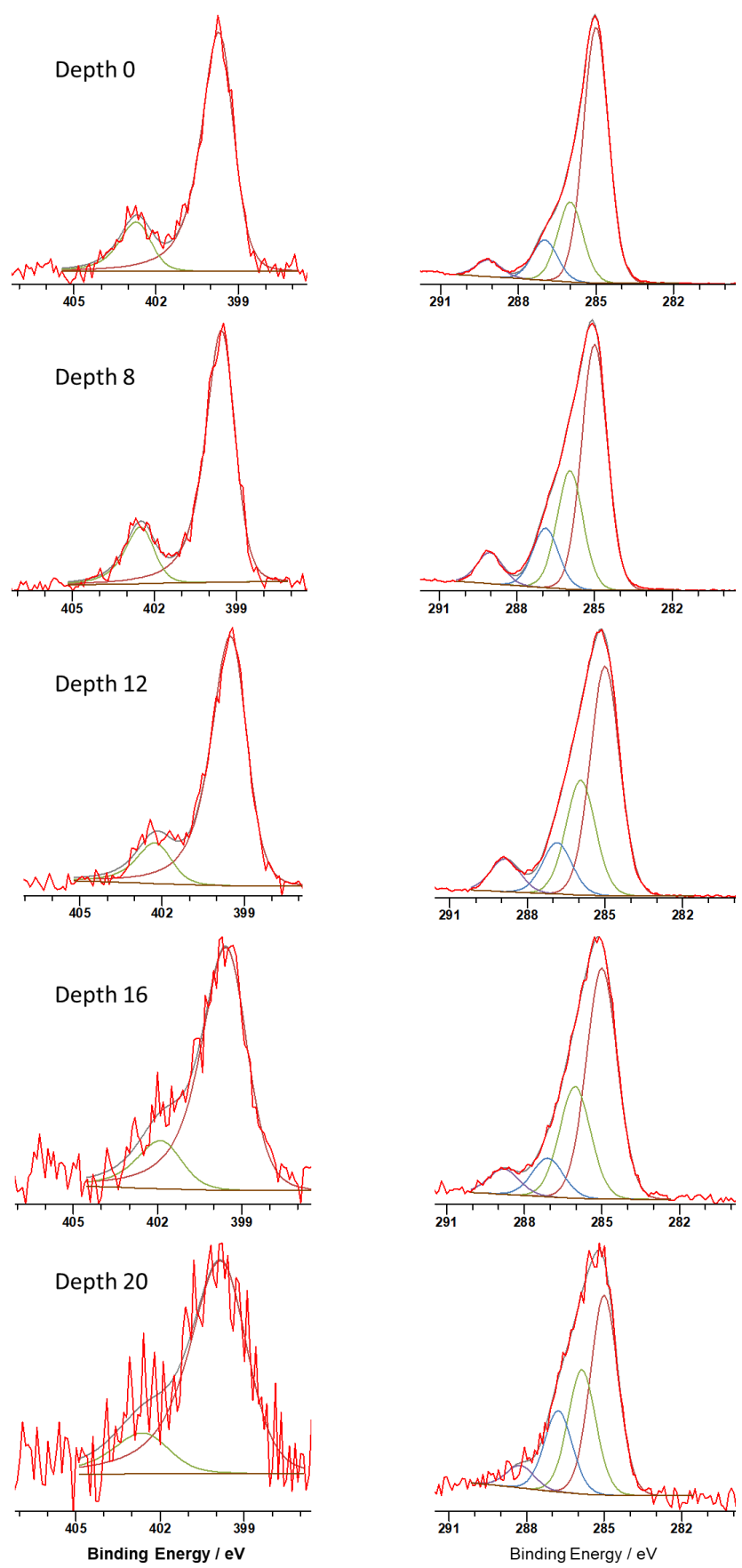


Figure 4-36: Curve fitted high resolution N 1s and C 1s spectra collected for depth profiling of q-PDMA.

Figure 4-37a shows N 1s components (normal nitrogen and quaternised nitrogen) plotted as surface concentrations (i.e., the sum of the two components gives the total nitrogen concentration shown in **Figure 4-35**). If these components are replotted on a logarithmic scale, the concentrations of the two components are seen to be parallel; suggesting the extent of quaternization is constant throughout the brush thickness (**Figure 4-37b**). It is noted these samples were produced in THF which is a good solvent for PDMA polymer brushes.

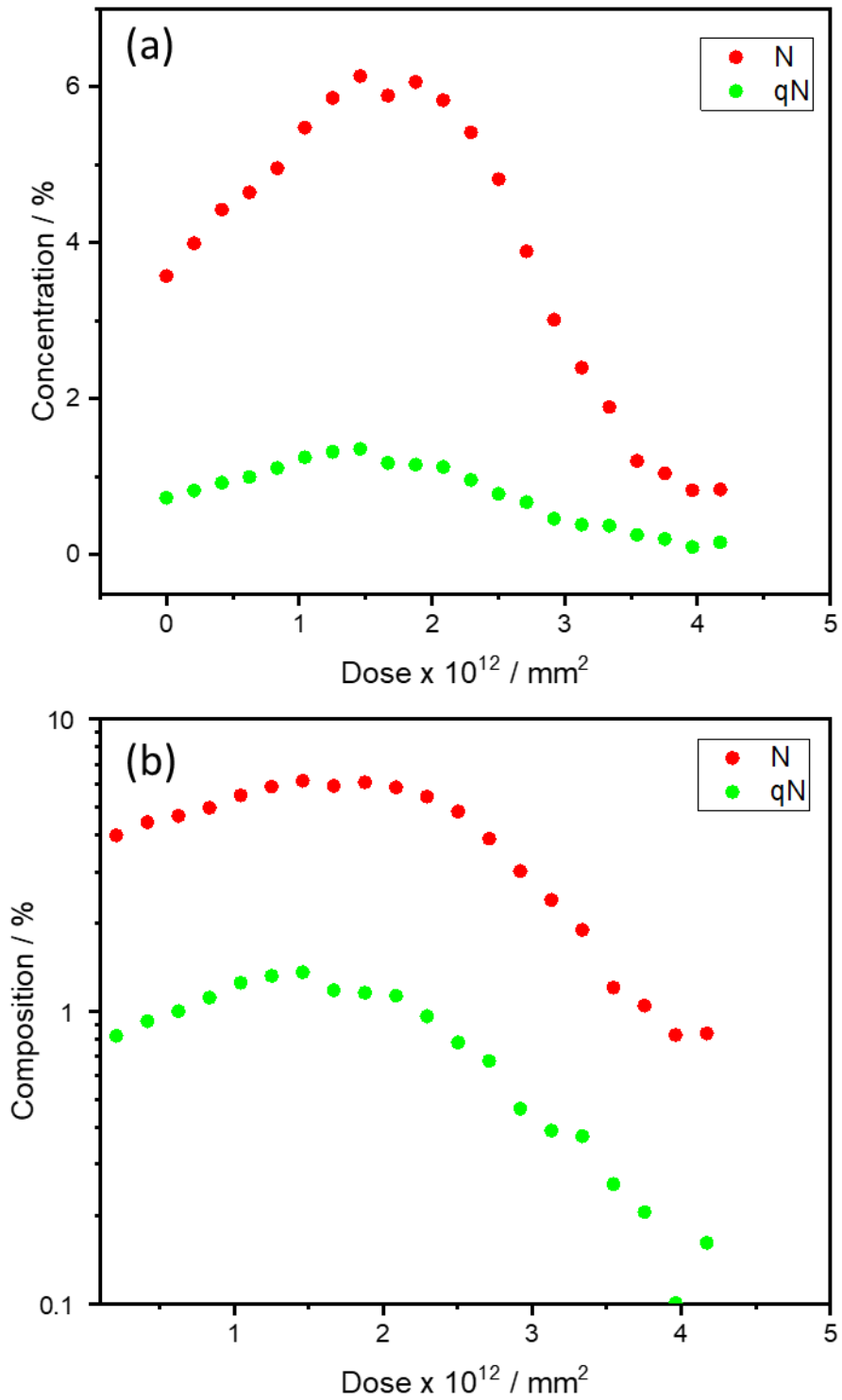


Figure 4-37: (a) Surface concentration (%) of two nitrogen environments detected. (b) Surface concentrations (%) of two nitrogen environments detected shown on logarithmic scale.

The initial N 1s analysis before any etching took place suggested approximately 17% quaternization of all nitrogen atoms. Control charts have been calculated to show how the average film composition is expected to vary with the degree of quaternization, **Figure 4-38**.

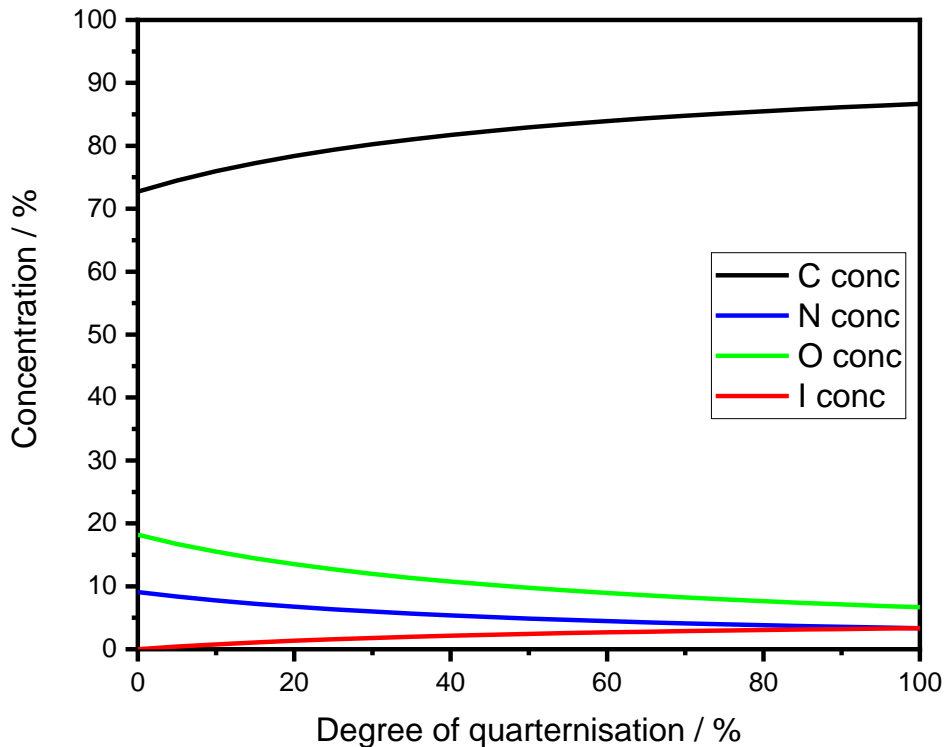


Figure 4-38: Expected change in average composition as a function of quaternization (calculated).

It can be seen that at approximately 17% quaternization, the composition is expected to be 77.7 at% C, 7.0 at% N, 14.1 at% O and 1.2 at% I. These are in a reasonable agreement to the values seen in the depth profile shown in **Figure 4-35** when the nitrogen concentration is at its greatest. From **Figure 4-38**, if the increased carbon seen on the unetched sample, approximately 85 at%, was due to quaternization then 75% or more quaternization would be required – and this does not agree with the nitrogen spectra collected. In order to explain this excess of carbonaceous material at the surface, it is suggested that there is excess unreacted

1-iodooctadecane on the surface of the sample which has likely been photobleached reducing the associated iodine concentration.

From these observations, it could be concluded that quaternization occurs at a similar level throughout the polymer brush when THF is used as the solvent. Excess carbonaceous material was found on the surface of the polymer brush sample, which was most likely attributed to unreacted photobleached 1-iodooctadecane.

4.3.6.2 XPS Depth Profiling of PDMA Treated with *Chlorophyll*

PDMA sample treated with *ZnChla* was depth profiled using XPS. The change in elemental composition as a function of the dose of total number of clusters to have bombarded the surface is shown in **Figure 4-39**. The initial carbon concentration is greater, and similarly nitrogen and oxygen concentrations lower, than a PDMA polymer brush only, suggesting there is a change in the chemistry of the surface in addition to PDMA on the surface.

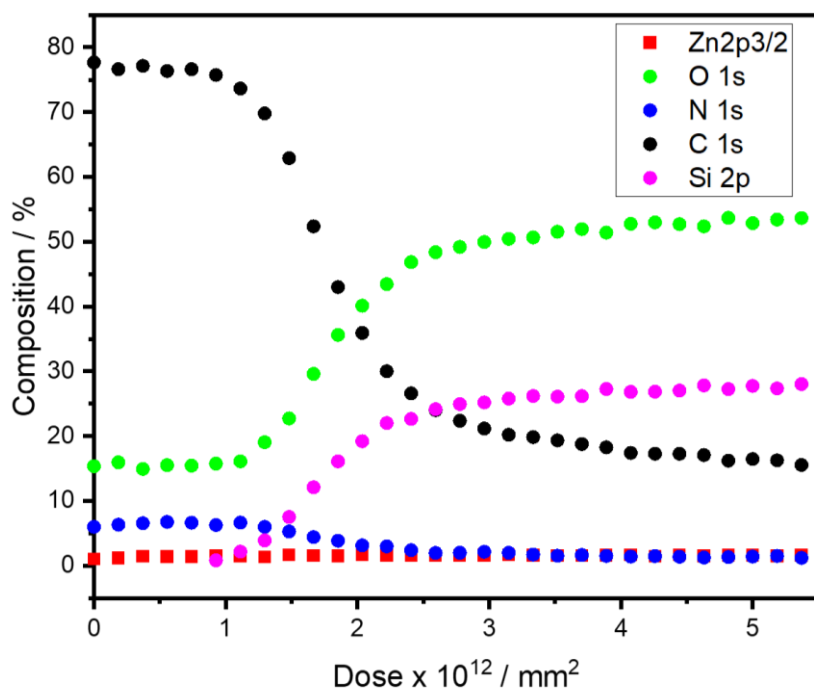


Figure 4-39: XPS depth profile showing variation in elemental concentration as a function of number of clusters.

The glass substrate is beginning to contribute to the XPS analyses from about 1×10^{12} clusters onwards, suggesting material is being removed and the substrate exposed, however the rate of increase of silicon and oxygen due to the substrate and decrease in carbon, nitrogen and zinc slows dramatically from approximately 3×10^{12} clusters. The residual carbon concentration in this region is higher than is typically seen in other polymer brush depth profiles, e.g., for an untreated PDMA polymer brush the carbon concentration <3 at% after 4×10^{12} clusters.

The surface zinc concentration does not drop below 1.4 at% beyond the 2×10^{12} clusters point in **Figure 4-39**. This may be because of Zn from origin composition of the glass substrate.

Selected curve fitted high resolution N 1s and C 1s spectra are shown in **Figure 4-40**. Depth 0 is before etching, depth 3 is within the initial region where the elemental composition of the surface is approximately unchanging, depth 6 is at the interference as the glass starts to contribute to the XPS analysis, depth 9 is two depths before where the oxygen and carbon profiles cross whereas depth 12 is two depths after this same point, depths 24 is in the long tail of the depth profile where concentrations of the elements were seen to change much more gradually.

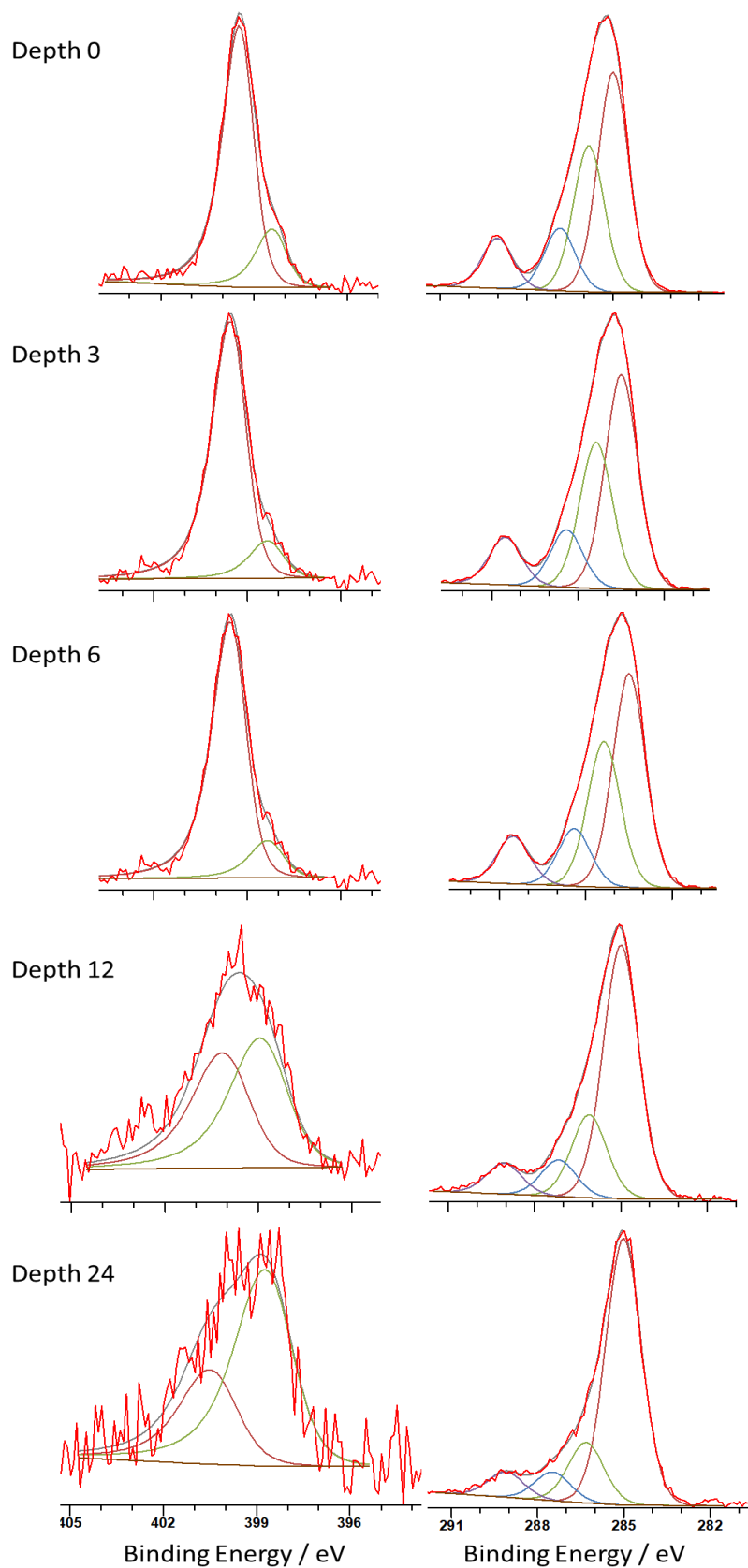


Figure 4-40: Selected high resolution N1s and C 1s spectra from ZnChla depth profile.

These spectra can be compared to those collected from a PDMA polymer brush seen previously in q-PDMA depth profiling discussion. Before any etching, N 1s spectrum shows two components, a large peak at approximately 399.5 eV consistent with the tertiary amine in the PDMA polymer brush and a smaller peak at approximately 398.5 eV consistent with the amine group bonded co-ordinately with central *chlorophyll* zinc. The nitrogen spectra are little changed whilst the nitrogen concentration is approximately constant. However, as the carbon concentration begins to rapidly decrease, from 1.3×10^{12} clusters, the nitrogen concentration also decreases leading to noisier spectra, but spectra where the *chlorophyll* component appears to increase. This can be seen in **Figure 4-41** which plots the contributions of what are believed to be the PDMA tertiary amines and the bonded Zinc from *chlorophyll* to Nitrogen from PDMA to the total nitrogen surface concentration as a function of the dose of number of argon clusters to hit the surface. Although the data is noisy, due to the small concentrations involved it is suggested that the concentration of surface nitrogen due to *chlorophyll* shows small degree of change throughout the depth profile.

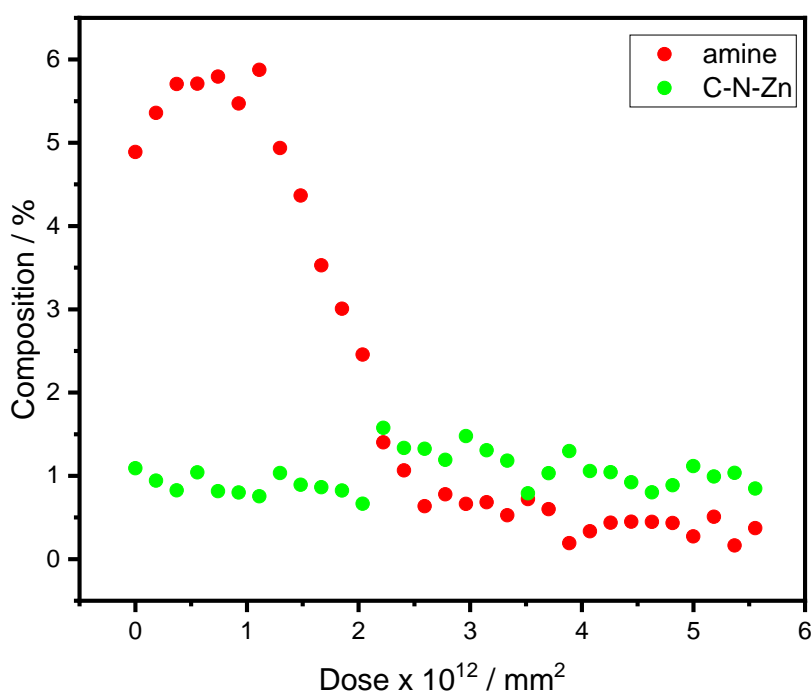


Figure 4-41: Surface concentrations of two nitrogen environments as a function of number of clusters.

The carbon spectra similarly transition as the C-N component characteristic of PDMA at approximately 285.8 eV seen initially decreases in intensity and the C-C component at 285.0 eV increases.

It was thought that this data suggests that the majority of the material detected on the surface initially, before etching, is PDMA polymer brush. The polymer brush looks to be largely removed by ion etching. However, there seem to be *chlorophyll* left on the surface. This could be because the Ar3000+ clusters are too gentle to break up the *chlorophyll* and it gets left behind as the polymer brush is removed, or whether there is an uneven deposition of *chlorophyll* and leading to left with thicker islands of *chlorophyll* to continue depth profiling through. This data also proved that the *chlorophyll* has become attached to the polymer brush, which was evidenced by the emergence of -C-N-Zn peak at 398.5 eV. However, there is an excess of zinc ions, as pure *chlorophyll* should be only 1.5 at% zinc, or in another words, in pure *chlorophyll* C:Zn is 55:1, and by the end of the profile it was observed C:Zn = 10:1, which attributed to possible contamination from the solution of *ZnChla*.

4.4 Conclusion

Surface-grafted PDMA brushes were synthesised via ATRP. The structures of PDMA brushes and their BIBB-APTES initiators were confirmed by XPS N 1s and C 1s spectra. Ellipsometric measurements reveal that the average height of the initiator was around 1 nm, while the heights of the brushes can reach round 15 nm after 15 min of polymerisation time with maximum height of 30 nm after 1 h. AFM images of PDMA brushes and their BIBB-APTES initiators confirm the successful growth of the polymer brushes with a good agreement with ellipsometric height measurements. *ZnChla* was successfully attached to PDMA brushes.

Adsorption isotherms of *ZnChla* on PDMA were acquired and demonstrated that monolayer coverage was achieved with a *Chla* concentration of 15 μM . When the PDMA brushes were treated with 1-iodooctadecane, the binding of *Chla* was found to be blocked, decreasing as the degree of quaternization increased. These findings are consistent with the hypothesis that *Chla* binding to PDMA brushes is via coordination of the tertiary amine in the pendant groups of the polymer to the metal centre in the *Chla*. There is no shifts in the position in the *Chla* absorption bands after binding to PDMA brushes suggesting that the amount of aggregation is small. This approach seems to provide a promising route to the formation of pigment-polymer antenna complexes.

CHAPTER 5: PLEXCITONIC COMPLEXES: PLASMONICS

5.1 Introduction

Localised surface plasmon resonances (LSPRs) that are generated by the resonant coupling of light to the plasmonic modes of sub-wavelength metallic nanostructures are widely exploited in various applications such as sensors and essential research on LHCs.^[33] Under certain conditions, the combination of plasmon mode and excitons may exchange energy faster than their decay rates. This allows the system to enter the strong coupling regime where new hybrid light-matter states (plexcitons) are generated.^[2] The new plexcitonic states are evidenced by a splitting of the plasmon band in the absorption spectrum. A range of systems, including those based on dye molecules, quantum dots and J-aggregates, have all been shown to exhibit strong coupling.

In a previous study, Lishchuk *et al.* demonstrated that LSPRs of arrays of gold nanostructures were strongly coupled to pigment-protein antenna complexes from bacteria^[32] and plants.^[241] Light harvesting antenna complexes organise pigment molecules (*chlorophylls* and carotenoids) precisely in space, controlling the orientations of their transition dipole moments and achieving high packing density, without concentration quenching of excitons. The integration of these remarkable properties with strong light-matter coupling opens a new route to the control of excitation transfer in molecular films, but proteins are fragile and costly to synthesise, making them unsuitable for applications in device production. The aim of this chapter is to investigate the properties of biomimetic light-harvesting structures based on synthetic polymers.

Recently, they Lishchuk *et al.* described the design of pigment–polymer antenna complexes in which the peptide scaffold used in photosynthetic light-harvesting complexes surface grafted PCysMA chains. These polymer scaffolds were used to support *chlorophyll* molecules.^[33]

The approach of Lishchuk *et al.* relied upon a lengthy synthetic modification to the *chlorophyll* molecule, to enable covalent coupling to pendant amine groups on PCysMA repeat

units. This chapter aims to examine the feasibility of achieving a similar strong coupling, but using simpler approaches based on the coordination of pigment molecules to pendant tertiary amine groups in poly(dimethylaminoethyl methacrylate) (PDMA) brushes, as illustrated in chapter 1. The strategy is illustrated schematically in **Figure5-1**. PDMA brushes are grown from a suitable substrate, and then immersed in a solution of zinc *chlorophyllide* (ZnChl). It was hypothesised that the pendant dimethylamino groups in the polymer might coordinate to the central Zn²⁺ ion in *ZnChla*. Drop-casting and spin-coating of *ZnChla* and J-aggregates in the absence of a polymer scaffold were also investigated; such sample preparation methods are expected to yield thick, dense layers of pigment molecules that would be expected to exhibit strong plasmon-exciton coupling and provide good positive controls. In addition, the possibility of achieving strong plasmon-exciton coupling between excitonic NR-PDMA antenna complexes and plasmonic arrays of AuNPs structures was investigated.

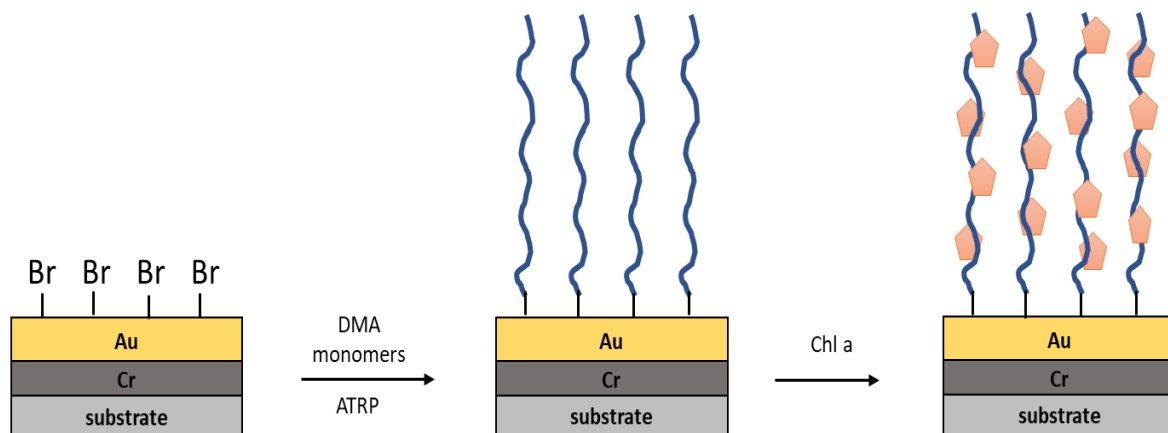


Figure 5-1: Schematic illustration of the growth of PDMA brushes onto brominated gold film and subsequent attachment of ZnChla.

5.2 Materials and methods

5.2.1 Materials

Glass substrates (Coverslips glass slides, MENZEL-GLAZER/ 22*60# 1.5) were purchased from VWR, UK. 1, 10-diiodooctane 98% was supplied by Alfa Aesar, UK. Deionised water (15 M Ω cm⁻¹) was obtained from an Elga PURELAB Nano-pore system. Dry THF was obtained from an onsite Grubbs dry solvent system. All these materials were used as received without any further purification

5.2.2 Sample cleaning and handling

Glass coverslip slides were cleaned as described in chapter 3. Briefly, Piranha solution (30% H₂O₂: 98% H₂SO₄, 1:3, v/v) was used to clean all substrates and glass ware. Caution: *Piranha solution can result in a violent reaction with organic matter and should be handled with extreme caution!* Non-glass ware and other tools were cleaned with acetone, sonicated in isopropanol and washed with ethanol.

5.2.3 Formation of BIBB-APTES films

BIBB-APTES films were prepared in two steps as described in detail in the chapter 3. Briefly, 2% solution of APTES in ethanol is used to functionalise glass substrates to form APTES SAMs. This was followed by the attachment of BIBB in a mixture of TEA and DCM to form Bromine-functionalised initiator substrates.

5.2.4 Preparation of polycrystalline gold film

Piranha cleaned glass slides were coated by thermal evaporation with ca. 2-5 nm thick chromium adhesive layer. This was followed by a deposition of thickness of 20-25 nm gold film (the nominal thickness is the reading of the evaporator QCM thickness monitor, i.e., the film

mass thickness). Edwards Auto 306 bell jar vacuum coater system was used to deposit both chromium and gold under a pressure of 5×10^{-7} mbar with evaporation rates of ca. 0.1 nm/s for both metals Cr and Au. The samples were allowed to cool for 30 min and rinsed with ethanol prior to use. Then, the samples were immersed in 1 mmol solution of octadecanethiol in degassed ethanol overnight prior to rinse with ethanol and dry with nitrogen.

5.2.5 Interferometric lithography fabrication of gold nanostructure arrays

A Coherent Innova 300C FreD frequency-doubled argon ion laser was employed as the light source for photolithography, emitting UV light at 244 nm. To create a coherent beam, a spatial filter with an aperture of 10 μm was employed to focus the laser beam through a lens and the edge of the coherent beam was cut using a mask with an appropriate aperture. The laser beam was directed into a Lloyd's mirror interferometer. The angle between the sample and mirror was set at 50° or 60° . A double-exposure process was used, and the sample was rotated 90° between exposures. Doses of 21.5 J cm^{-2} and 18.3 J/cm^2 were used during the first and second exposures, respectively. After lithographic processing, samples were etched by immersion in a 0.2 M solution of 2-mercaptoethylamine hydrochloride in 8% v/v of 35% of ammonia solution in ethanol. Finally, the samples were rinsed with ethanol and dried with nitrogen. The resulting arrays were annealed using a muffle furnace (Carbolite, UK) in air at 500°C for 120 min. The heating rate was ca. 7°C min^{-1} . The annealed samples were allowed to cool at room temperature.

5.2.6 Functionalisation of polycrystalline gold thin films and plasmonic arrays of gold nanostructures using DTBU

Cr/Au-coated coverslips and plasmonic arrays of gold nanostructures were immersed in a 2 mM solution of DTBU in nitrogen-degassed ethanol. The reaction was allowed to proceed in a

fridge at temperature of 4 °C for 24 h to form bromoisobutyrylundecanethiolate (BIBUDT)-functionalised Au surface. The samples were then removed from the solution and rinsed with ethanol and blown dry under nitrogen stream.

5.2.7 Growth of PDMA via ATRP brominated surfaces

PDMA brushes were grown from BIBB-APTES initiated glass substrates as mentioned with more details in chapter 3. Briefly, DMF was used as a solvent for DMA monomers. HMTETA and Cu(I)Br were used to catalyse ATRP reaction at 90 °C. Then, monomer/ catalysts solution was added into Schlenk tubes with BiBB-APTES-functionalised glass substrates. The reaction was performed at nitrogen atmosphere. The growth of PDMA was allowed to proceed for the desired polymerisation time (15 min and 60 min, unless otherwise is stated). The polymerisation reaction was terminated by removing the slide from the mixture. The same procedure was followed to grow PDMA from DTBU-functionalised polycrystalline gold substrate and DTBU-functionalised plasmonic arrays of gold nanostructures.

5.2.8 Extraction and derivatization of *chlorophyll a*

A detailed description of *ZnChla* synthesis can be found in chapter 3. Briefly, *chla* was extracted from spinach leaves by acetone. Then, extracted *chlorophyll a* was converted into pheophytin a (dark blue pigment) by dissolving the dark green pigment in acetic acid under stirring for 3 h. Then, zinc acetate dehydrate dissolved in methanol was used to convert pheophytin into *ZnChla* under reflux in argon atmosphere at 35 °C.

5.2.9 J-aggregates solution preparation

Poly Vinyl Acetate (PVA, molar weight 450 000) was used as a host matrix for the J-aggregated dye 5,5,6,6-tetrachloro-1,10-diethyl-3,30-di(4-sulfobutyl)-benzimidazolocarbo-cyanine (TDBC). PVA was dissolved in water. TDBC was then dissolved in the PVA-water solution. TDBC/PVA films were deposited on a plasmonic arrays by spin-coating and drop-casting.

5.2.10 Drop-casting of Chl and J-aggregates onto gold nanostructure arrays

Freshly fabricated plasmonic arrays of gold nanostructures were placed on a clean horizontal glass surface. 3 μL of 250 μM *Chla* solution was carefully placed on the surface and allowed to spread so that it was uniformly distributed across the surface of the sample. The drop was allowed to dry naturally. The same procedure was used to drop-cast 5 μL TDBC solution on Au-coated glass slides.

5.2.11 Spin coating of Chl and J-aggregates onto gold nanostructure arrays

Annealed plasmonic arrays of gold nanostructures were placed on the sample holder of the spin-coater. 3 μL of a 250 μM solution of *Chla* in acetone was carefully deposited onto the surface of spinning sample. The spin-speed was 3000 rpm. The sample was left for 120 s for the solvent to evaporate. The same procedure was used to deposit 5 μL of J-aggregate on Au-coated glass slides.

5.2.12 Synthesis of 2-(10-iododecyl) Nile Red.

Nile Red (100 mg, 0.3mmol), K_2CO_3 (250 mg, 1.81 mmol) and 1,2-diiodooctane (1.18g, 3.22 mmol) were dissolved in 2 mL DMF. The reaction mixture was stirred at 60 C for 2 h under

nitrogen. The product was then extracted with ethyl acetate (30mL) and washed 3 times with water and brine (30 ml) and dried to afford dark red solid product. The produced iodinated Nile Red was purified by column chromatography using a mixture of 1:2 ethyl acetate and petroleum ether to yield 60 mg iododecyl Nile Red (INR).

5.2.13 Attachment of INR to PDMA brushes

PDMA samples were immersed in solutions of INR in THF with concentrations in the range 0.25 mM - 8 mM overnight in the dark at room temperature. On completion of the coupling reaction, samples were rinsed with ethanol and dried under a stream of nitrogen. INR-functionalised PDMA brushes were characterised by UV-Vis spectroscopy and XPS. INR-functionalised PDMA was also grown from Br-functionalised arrays of gold nanostructures using the same methods used to functionalise PDMA brushes on glass were analysed by absorption spectroscopy.

5.2.14 Surface analysis

A Cary 50 UV-vis spectrophotometer was used to obtain extinction spectra in the range 190 – 900 nm, unless otherwise is stated. *ZnChla* samples were measured by placing samples in a standard quartz cuvette with a 10 mm optical path length at room temperature. Measurements were made in duplicate. The extinctions of plasmonic arrays were measured in air. Measurements were conducted using home-made PTFE sample holder designed to facilitate precise alignment of the excitation beam with the same area on the surface during all experimental stages.

X-ray photoelectron spectroscopy (XPS) spectra were obtained using a Kratos Axis Ultra/Supra spectrometer (Kratos Analytical, Manchester, UK). All binding energies were

referenced to the 285 eV calibrated primary hydrocarbon C 1s signal. XPS data were analysed using the CASAXPS software (v. 2.18).

Tapping mode AFM measurements were performed by using a Digital Instruments (Nanoscope 5 Multimode Atomic Force Microscope), (Veeco, Santa Barbara, CA) fitted with a “J” scanner. All measurements were conducted in air at room temperature. AFM data analysis was performed using NanoScope software (v 1.5).

Water contact angles measurements were performed using a Rame Hart sessile-drop model 100-00 goniometer. The obtained contact angle values are the mean of at least three different measurements.

Ellipsometric spectra were collected using an M-2000VI ellipsometer (J. A. Woollam Co., Inc., USA) operating in a spectral range from 370 to 1000 nm, at an incident angle (Φ) of 75°, unless otherwise is stated. Modelling ellipsometric data was performed using CompleteEASE software (v.6.6). At least three measurements per sample were carried out in air to obtain an average.

5.3 Results and discussion

5.3.1 Surface analysis of clean polycrystalline gold films

Contact angle and XPS measurements and SE measurements were performed using polycrystalline Au surfaces, because these measurements are not possible for arrays of Au nanostructures, because the surface of Au nanoarrays is not uniform. It is assumed that the chemical changes to the surface are similar for both types of samples.

The water contact angle of clean thermally evaporated gold films was measured to be $89 \pm 3^\circ$. XPS study of thermally evaporated Au-polycrystalline layer shows clear and intense Au 4f 7/2 peak at 84.25 eV and Au 4f 5/2 at 88 eV, attributed to the electronic transitions of Au, as shown in **Figure 5-2**.

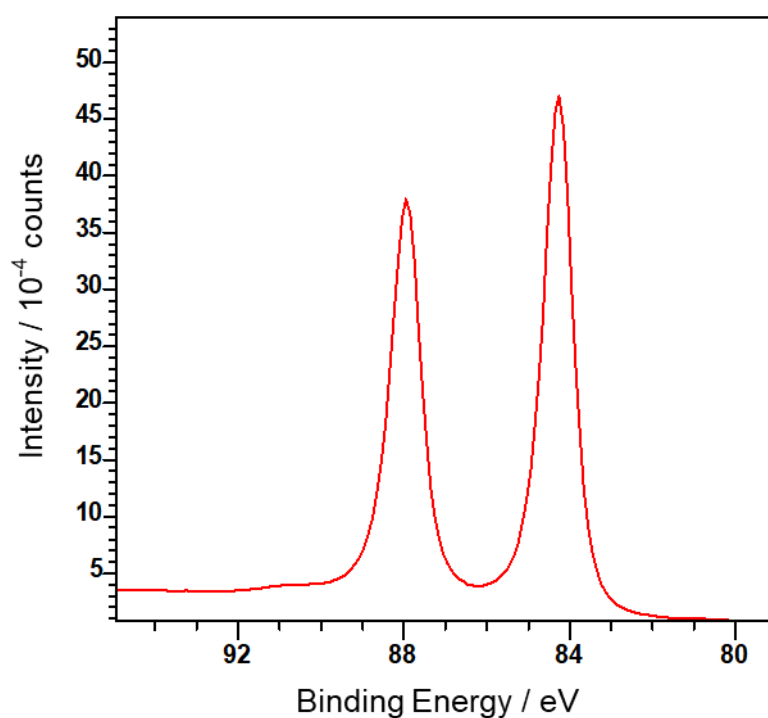


Figure 5-2: XPS high resolution Au 4f spectrum collected from clean polycrystalline gold surface.

5.3.2 Surface analysis of BIBUDT-modified polycrystalline gold films

To initiate the polymerisation of PDMA from Au substrate, the surface of the gold substrate was modified using DTBU as illustrated schematically in **Figure 5-3a**. First, SAMs of DTBU are formed by adsorption from solution on gold nanostructure arrays formed over 0.7 cm² using IL. The disulfide linkage in the adsorbate is cleaved during adsorption to yield a monolayer of BIBUDT at the Au surface. XPS analysis of BIBUDT-modified Au surface was performed. A doublet was observed at 162.5 eV and 164 eV, attributed to the S2p_{1/2} and S2p_{3/2} peaks formed by spin-orbit coupling (**Figure 5-3b**). The C1s peak was fitted with four components, which were attributed to C-C-C, C-C-S, C-C-O/C-C-Br, and -O-C=O- bonding environments. The high intensity C-C peak at 285 eV is attributed the large number of carbon single bonds (12 X -C-C-), see **Figure 5-3c**. XPS Br 3d peak was dominated by gold peak due to the overlap with gold transitions, Au 5p $\frac{1}{2}$, which is common with brominated gold surface, see **Figure 5-3d**. Also, the signal of the gold surface, Au 4f was observed clearly over the range 84 eV – 89.5 eV, see **Figure 5-3e**.

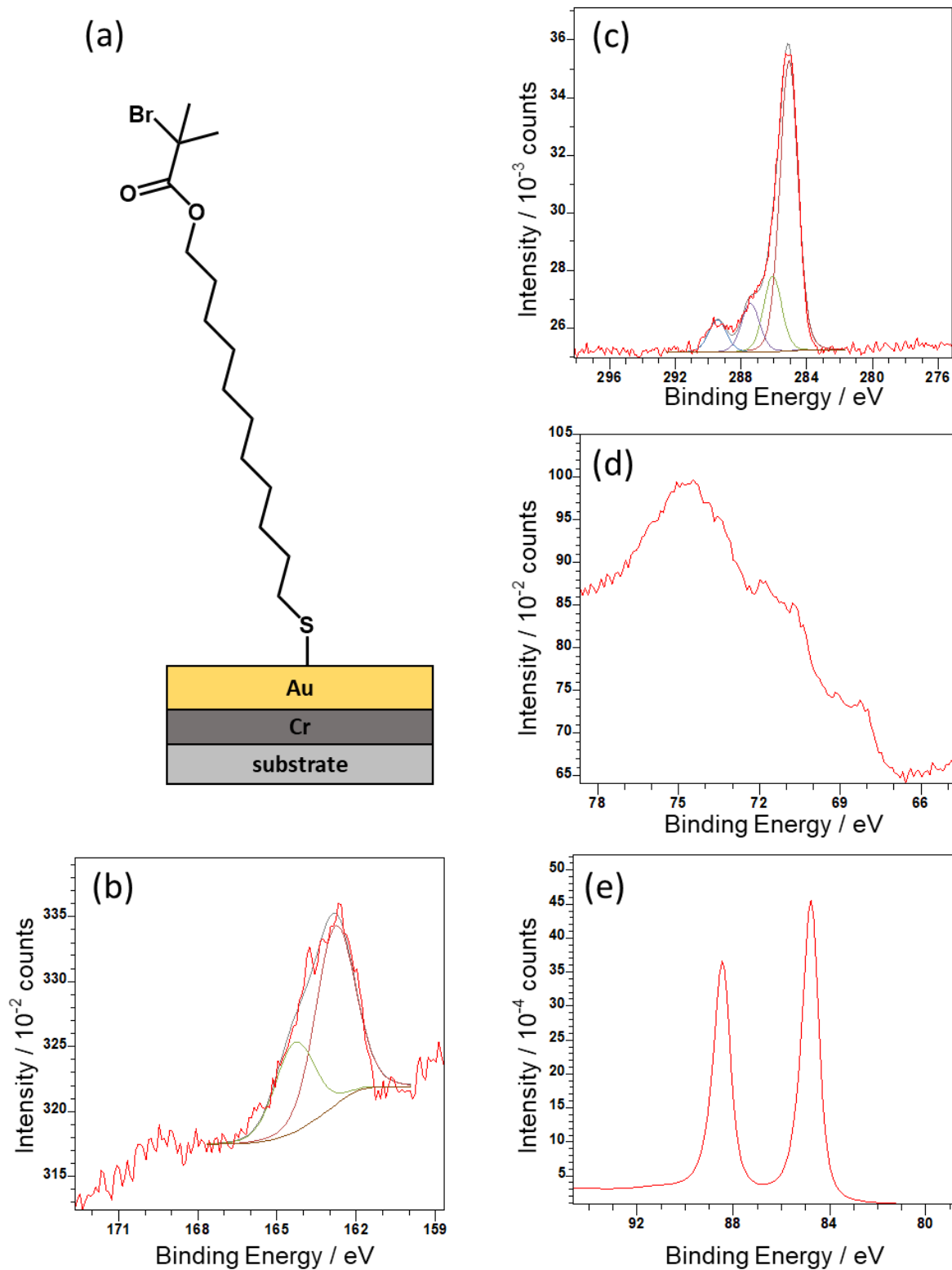


Figure 5-3: XPS analysis of BIBUDT-modified Au surface. (a) schematic of BIBUDT-modified Au surface. (b) XPS high resolution S 2p spectrum. (c) XPS high resolution C 1s spectrum. (d) XPS high resolution Br 3d spectrum. (e) XPS high resolution Au 4f spectrum.

5.3.3 Surface analysis of PDMA-functionalised polycrystalline gold films

PDMA brushes were grown from DTBU-modified Au substrate as shown schematically in **Figure 5-4a** and characterised by XPS. C 1s and N 1s XPS spectra of PDMA-functionalised Au surfaces exhibit features identical to those were previously described for PDMA grown from glass substrate in chapter 4, see **Figure 5-4 b and c**. This indicates that polymerisation proceeds equally well on gold surfaces that have been modified by attachment of initiators. The mean thickness of PDMA brushes grown for 1 h from Au surfaces was measured by ellipsometry to be 32 ± 6 nm.

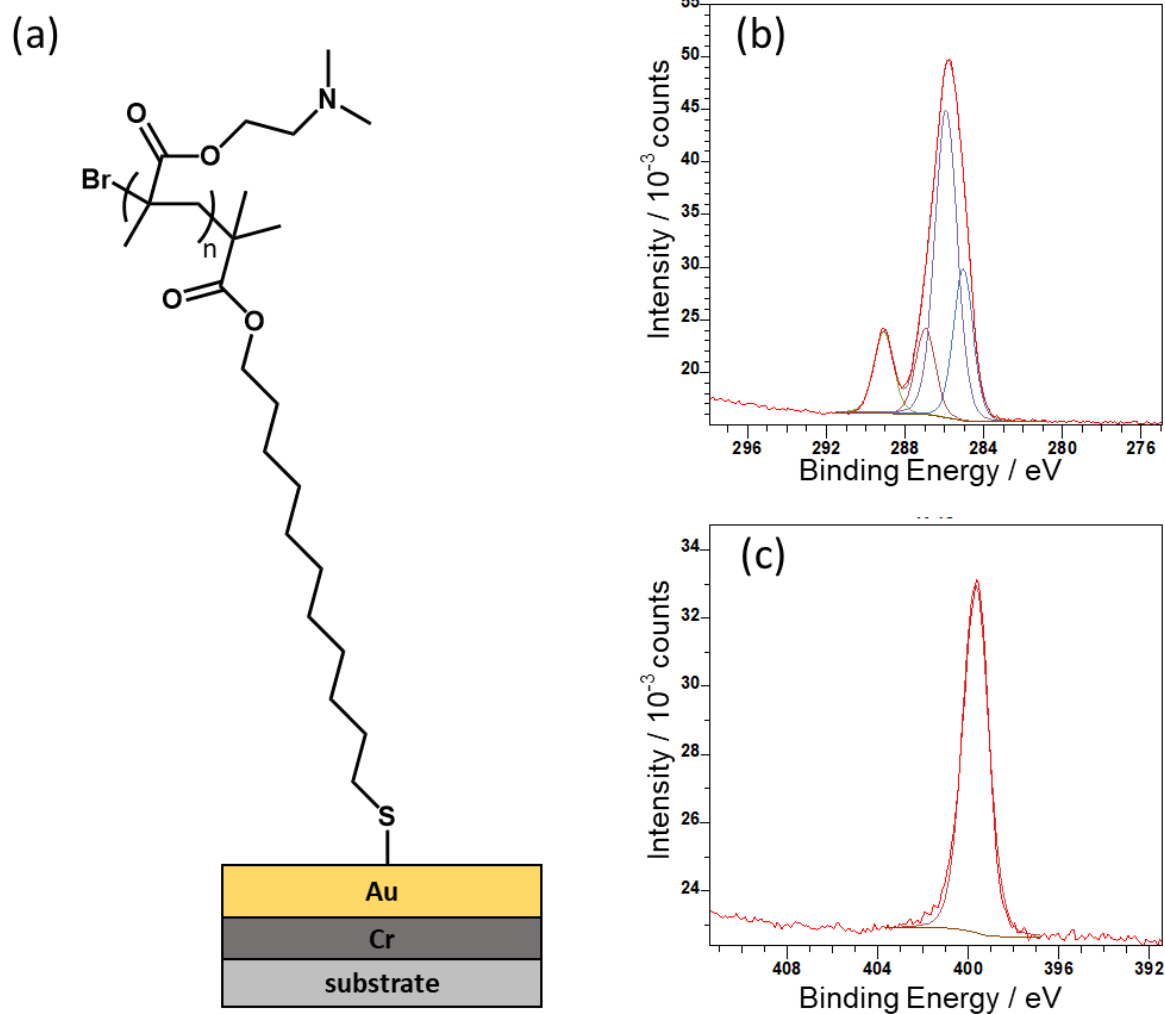


Figure 5-4: XPS analysis of PDMA grown from Au surface. (a) schematic of the growth of PDMA from Au surface. (b) XPS high resolution C 1s spectrum. (c) XPS high resolution N 1s spectrum.

5.3.4 Morphology of Plasmonic arrays

Figure 5-5 shows a tapping mode AFM height image of a typical array of gold nanostructures fabricated by IL. Close-packed clusters of AuNPs can be observed. The height of the plasmonic arrays of gold nanostructures was estimated to be 44 ± 11 nm with cluster diameter of 71 ± 33 nm and period of 255 ± 15 nm.

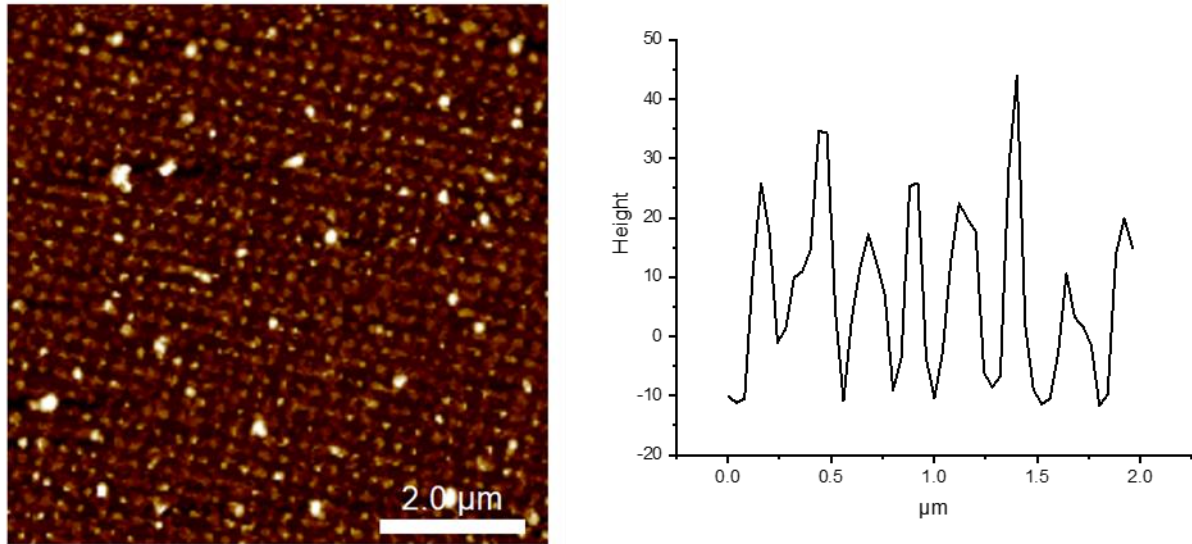


Figure 5-5: Tapping mode AFM images of typical plasmonic arrays of gold nanostructures (right, and cross section taken from this image (left).

Figure 5-6 shows typical extinction spectra of Au arrays fabricated by IL. Extinction spectra acquired for several samples displayed only very limited variability in the energy and shape of the plasmon band (**Figure 5-6a**). When spectra were acquired at varying angles of incidence (AOI) between 0 and 35°, a very degree of variation in the position of the plasmon band was observed (6 nm) without any change in the line shape (**Figure 5-6b**), indicating that extinction spectra of clean plasmonic arrays of gold nanostructures are not sensitive to the angles of incidence.

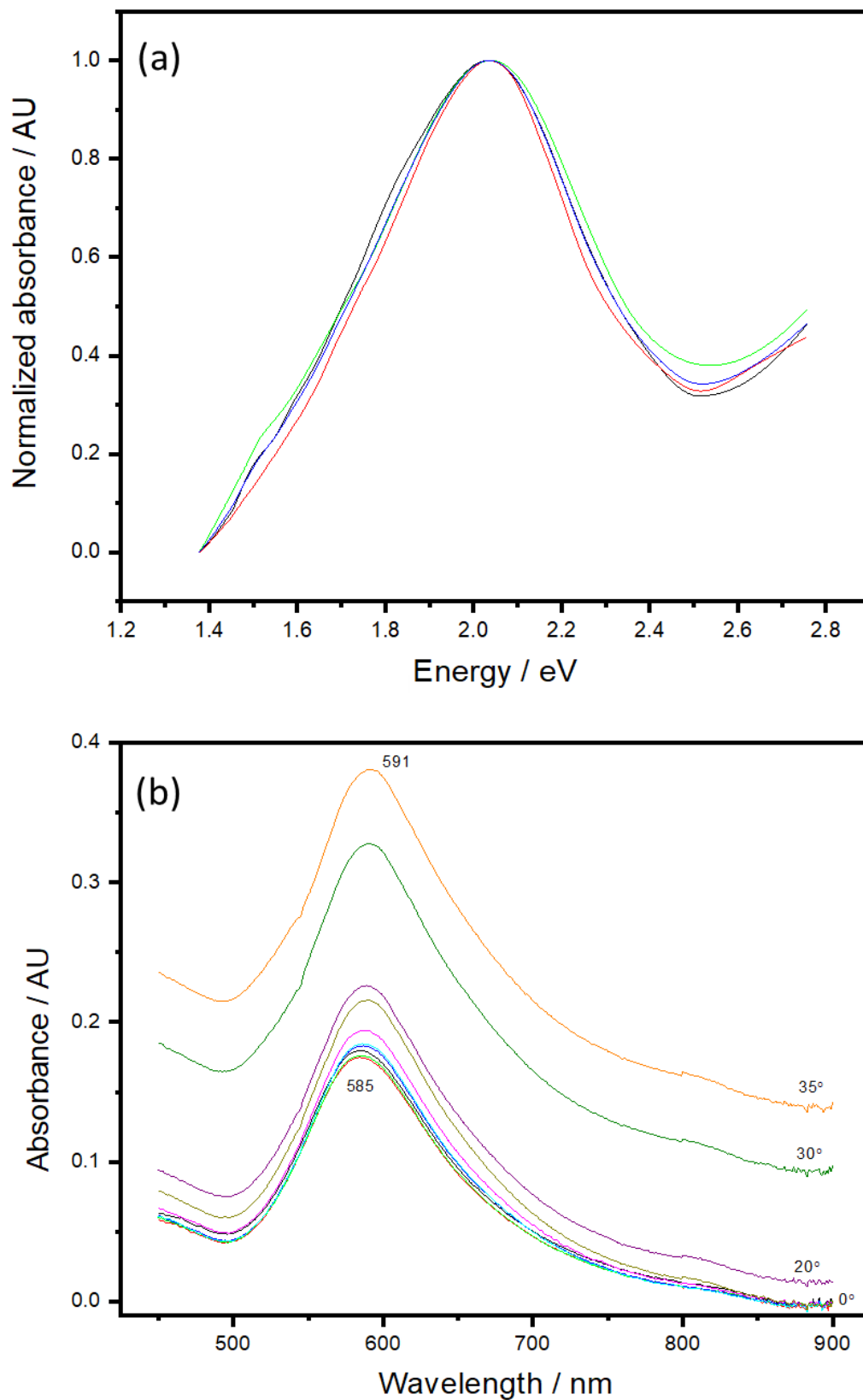


Figure 5-6: (a) Typical extinction spectra of a number of samples of Au arrays. (b) Extinction spectra of typical plasmonic arrays of Au nanostructures measured at different angles of incidence.

Figure 5-7 shows extinction spectra of plasmonic arrays of gold nanostructures before and after the growth of PDMA brushes. Typical plasmonic arrays of AuNPs exhibit an extinction maximum at 2.04 eV (black spectrum). However, a small red shift in the position of this plasmon band from 2.04 eV to 1.99 eV was measured after the growth of PDMA scaffolds for 1 h, as expected (see red spectrum). This red shift is due to the change in the local refractive index of the medium close to the plasmonic arrays from air ($n = 1$) to that of PDMA brushes ($n = 1.51$).

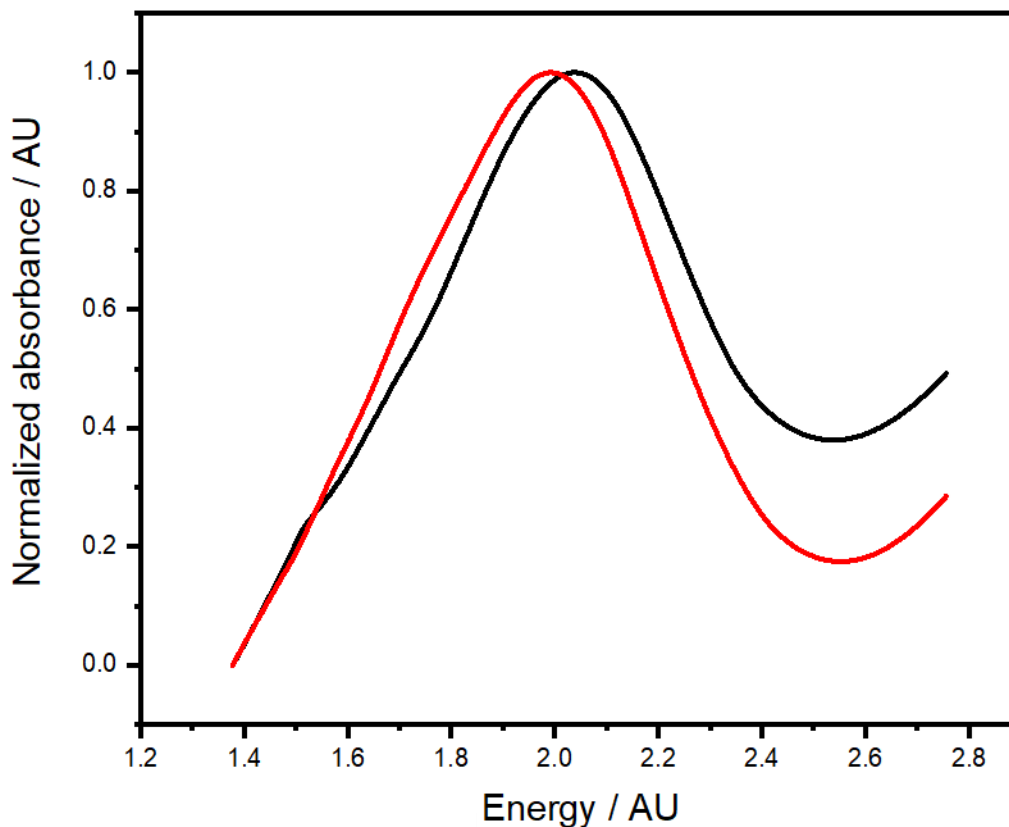


Figure 5-7: Typical extinction spectra of Au arrays before (black) and after (red) the growth of PDMA brushes (denoted by eV).

5.3.5 J-aggregates-based plasmonic complexes

The effect of the deposition of TDBC J-aggregates on the plasmonic properties of Au arrays was investigated via two ways, drop-casting and spin-coating. Drop-casting 3 μL of J-aggregates dye in PVA matrix onto a plasmonic array yielded a layer with thickness determined by spectroscopic ellipsometry to be 35 ± 5 nm. Spin-coating (3000 rpm, 120 sec) 5 μL of the dye onto a plasmonic array yielded a layer with thickness determined by spectroscopic ellipsometry to be ca. 30 nm. **Figure 5-8a** shows extinction spectra of Au arrays before and after deposition of J-aggregates. The black spectrum is the extinction spectrum of the clean Au array, with a plasmon peak at 615 nm. The red spectrum was acquired after deposition of J-aggregates. The extinction peak is now observed at 575 nm. The absorption spectrum of Au arrays after drop-casting the dyes was collected at different incident angles showing red shift of the peak position of Au arrays to 685 nm, see blue, green and cyan spectra. Also, the absorption peak of J-aggregates was observed without any shift. No sign of strong coupling was observed which could be due to the excess adsorption thick layer (50 ± 5 nm) of J-aggregates generated by drop-casting.

Figure 5-8b shows extinction spectra of clean arrays of gold nanostructures before and after spin-coating J-aggregates. The black spectrum here is the absorption spectrum of clean Au arrays with maximum absorption peak at 615 nm. The cyan spectrum is the absorption spectrum of J-aggregates with maximum absorption peak at 575 nm. A clear splitting of the plasmonic gold arrays was observed after spin-coating thin layer of J-aggregates (the thickness of the spin coated layer was evaluated by SE to be $30 \text{ nm} \pm 5 \text{ nm}$), see red spectrum. This splitting was attributed to the strong coupling between the plasmon of Au arrays and excitons of J-aggregates. This coupling is dependant to the angle of incidence as it can be seen from green and blue spectra.

The observed large shift in the LSPR caused by drop-casting of J-aggregates and the splitting of LSPR caused by spin-coating of J-aggregates on gold nanostructures proved that

the simple mixing of plasmonic materials with excitonic molecules is not sufficient to achieve strong light-matter coupling.

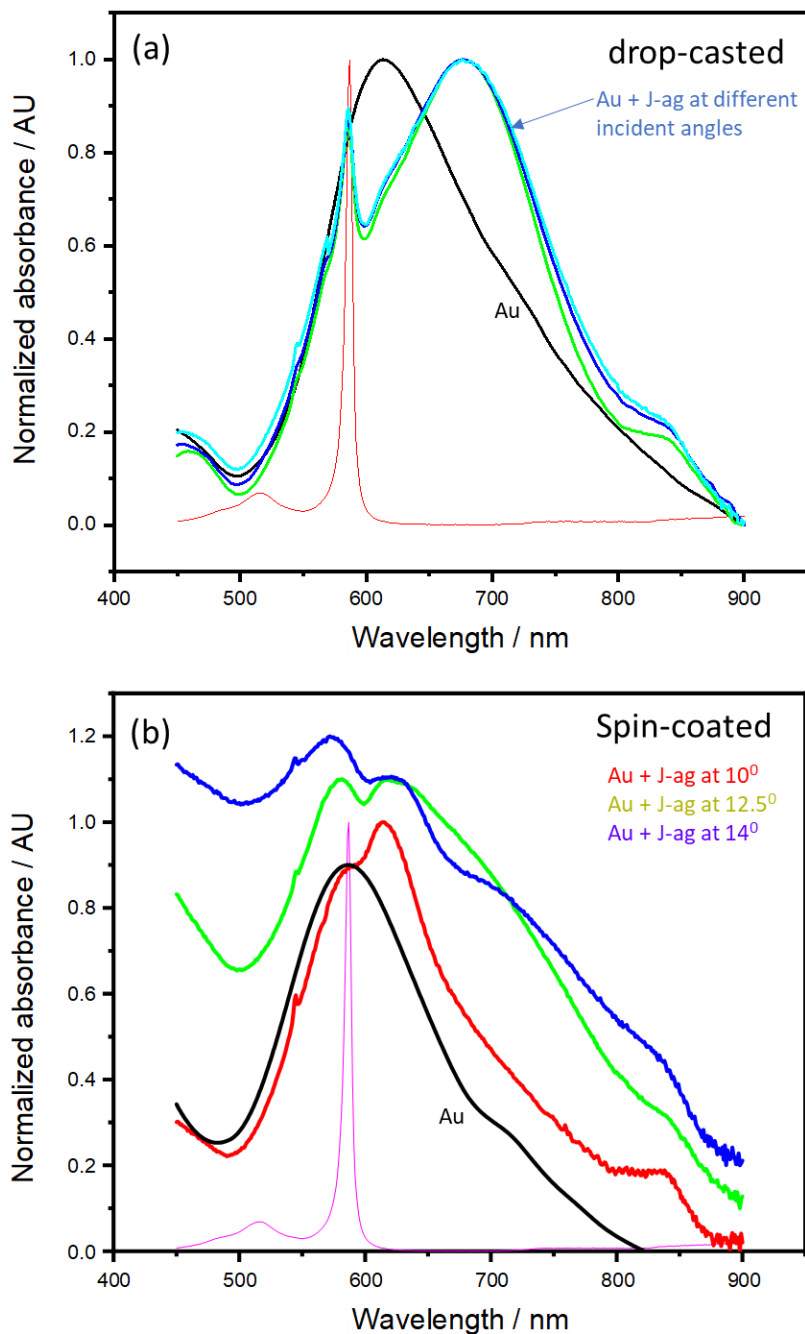


Figure 5-8: (a) Extinction spectra of Au arrays before (black) and after drop-casting J-aggregates measured at different incident angles. (b) Extinction spectra of Au arrays before (black) and after spin-coating J-aggregates measured at different incident angles. The sharp spectra observed at 585 nm in both (a) and (b) are extinction spectra of J-aggregates.

5.3.6 *ZnChla*-based plexcitonic complexes

PDMA brushes grown from gold nanostructure were used as a scaffold to organise *ZnChla* molecules in the plasmon mode. Firstly, control experiments were conducted by depositing *ZnChla* onto the plasmonic surface via drop-casting and spin-coating. **Figure 5-9a** shows the extinction spectra of clean plasmonic arrays (black spectrum) and the same plasmonic array after drop-casting of 3 μL of 500 μM *ZnChla* (green spectrum). After deposition of the *chlorophyll*, a 90 nm red shift with a broad plasmon peak was observed. Similar observations were made when 3 μL of 500 μM *ZnChla* was spin-coated onto PDMA-grafted (polymerisation time=1 h, thickness 30-50 nm) plasmonic structure. No change in the position of the spectra was observed when the extinction spectra were collected at different incident angles as shown in **Figure 5-9b**, probably because the transition dipole moments of the *chlorophyll* molecules are randomly oriented in these films. These observations were not consistent with the existence of strong plasmon-exciton coupling in these films, because in contrast to the behaviour observed for TDBC, a splitting of the plasmon band was not observed.

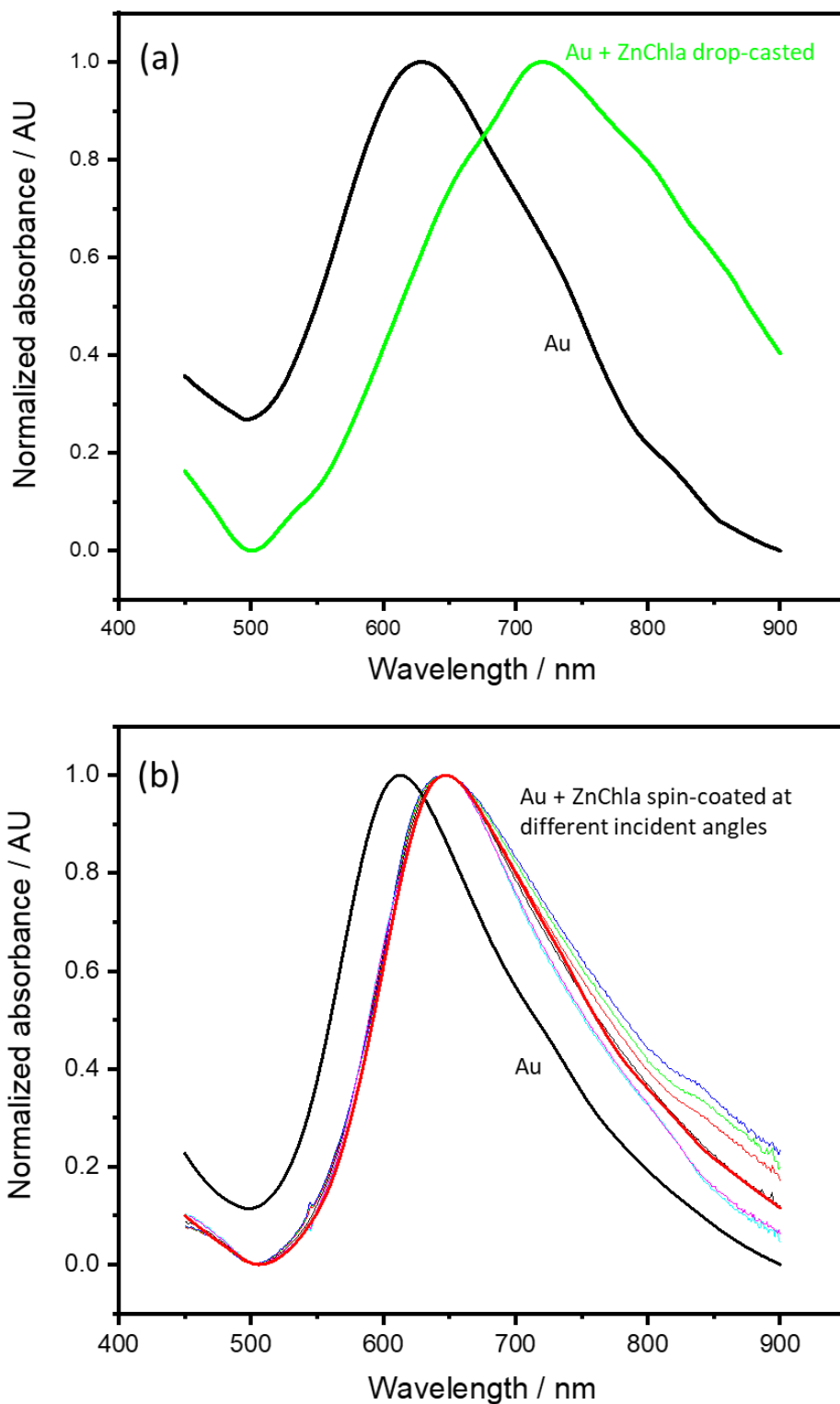


Figure 5-9: (a) Extinction spectra of Au arrays before (black) and after drop-casting ZnChla onto the surface of plasmonic arrays of AuNPs (green). (b) Extinction spectra of Au arrays before (black) and after spin-coating ZnChla onto the surface of PDMA grafted from plasmonic arrays of AuNPs (other spectra) measured at different incident angles.

In order to organise the excitonic molecules of *Chla* inside the plasmon mode volume, PDMA brushes were used to support *ZnChla* molecules. This was achieved by incubation the samples of PDMA-grafted plasmonic arrays of Au nanostructures in solutions of *ZnChla* to allow the formation of plexcitonic antenna complexes by binding *ZnChla* to PDMA through the coordination bonds as presented schematically in **Figure 5-10**.

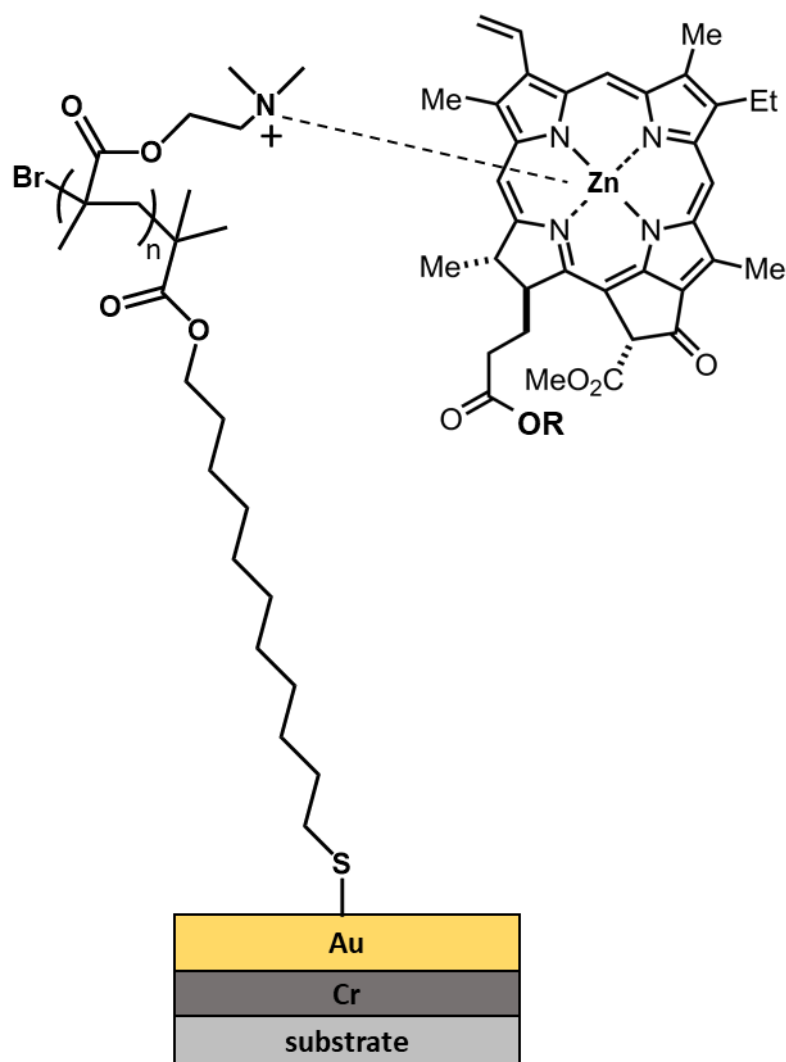


Figure 5-10: Schematic of binding *ZnChla* to PDMA grown from Au surface.

Figure 5-11 shows extinction spectra of clean Au arrays and PDMA-functionalised plasmonic arrays of AuNPs before and after the attachment of *ZnChla*. The black spectrum was acquired for clean plasmonic arrays of gold nanostructures, while the red spectrum was acquired for PDMA-grafted plasmonic arrays of AuNPs. The dotted spectrum has been acquired for *ZhChla* in a mixture of DMF and water with the ratio of 1:3. The other spectra have been acquired after attachment of *ZnChla* to PDMA from solutions with different concentrations of the dye and different PDMA thicknesses (labelled on the graph). In contrast to the simple red shift that was observed after the growth of PDMA scaffolds (**Figure 5-7**), a dramatic change in the spectrum was observed after immersion of the sample in a solution of *ZnChla* with concentration of 500 μM . The peak of the plasmon band at 2.04 eV appears to have been split into two peaks at 1.87 eV and 2.07 eV with when PDMA was polymerised for 15 min (pink spectrum). Additionally, a new feature is observed at ca. 1.5 eV. Such a feature was observed previously in spectra of *chlorophyll*-based systems that exhibit strong plasmon-exciton coupling,^[33] although its origin is unclear.

When longer brushes, grown using a polymerisation time of 1 h, were used, splitting was also observed in the plasmon band. After immersion of such brushes in a 500 μM solution of *ZnChla*, two peaks were observed in the extinction spectrum at 1.85 eV and 1.98 eV (pink spectrum). These suggest a reduced splitting of the plasmon band when the brush layer is thicker. At a concentration of 500 μM , the *ZnChla* solution has an olive-green colouration, attributed to the formation of aggregates. The most likely explanation of the different behaviour for different brush thicknesses is that for these very concentrated solutions, *ZnChla* deposits primarily as aggregates on top of the brush layer; thus, reducing the polymerisation time brings the *Chla* closer to the gold surface, effectively increasing the number of excitons in the plasmon mode volume and thus increasing the splitting strength. For thicker brush layers, the number of excitons in the mode volume is reduced and the coupling energy is reduced.

The splitting of the spectrum immersion in the *ZnChla* solution was attributed to a coupling between the LSPR associated with the gold nanostructure and the exciton in *chlorophyll* molecules. This strong coupling is a process in which the plasmon mode and the exciton are hybridised to produce new states (plexcitons) that combine the properties of light and matter. So, the splitting that has been observed here in the plasmon band is clear evidence of the formation of these new plexcitonic states.

When the concentration of *ZnChla* was reduced to 250 μM , the solution was blue-green in colour, indicating that the degree of aggregation was reduced; *ZnChla* was now dissolved in molecular form and was able to penetrate the brush layer. Consequently, higher concentrations of excitons were achieved within the brush layer and hence within the plasmon mode volume even for films grown with a polymerisation time of 1 h. The plasmon band was observed to be split, to yield new features at 1.94 and 2.05 eV (cyan spectrum).

The strong coupling is a collective phenomenon. The LSPR mode couples collectively to the excitons. In particular, the coupling energy change as a function to the square root of the density of the excitons in the plasmon mode volume, which described as $\frac{N}{V}$ in the following equation.^[33]

$$E_c \cong \sqrt{\frac{\mu^2 E_{mol}^2 N}{\epsilon_0 \epsilon_b E_{LSPR} V}}$$

When the concentration of *ZnChla* was reduced from 25 μM to 15 μM , and 7.5 μM , the separation between the two plexcitonic peaks was reduced to 0.11 eV and 0.07 eV, respectively, (light blue and blue spectra). This separation distance became hardly observed when the concentration reduced to 2.3 μM (green spectrum). As expected, the reduction of *ZnChla* concentration leads to the reduction in the coupling strength.

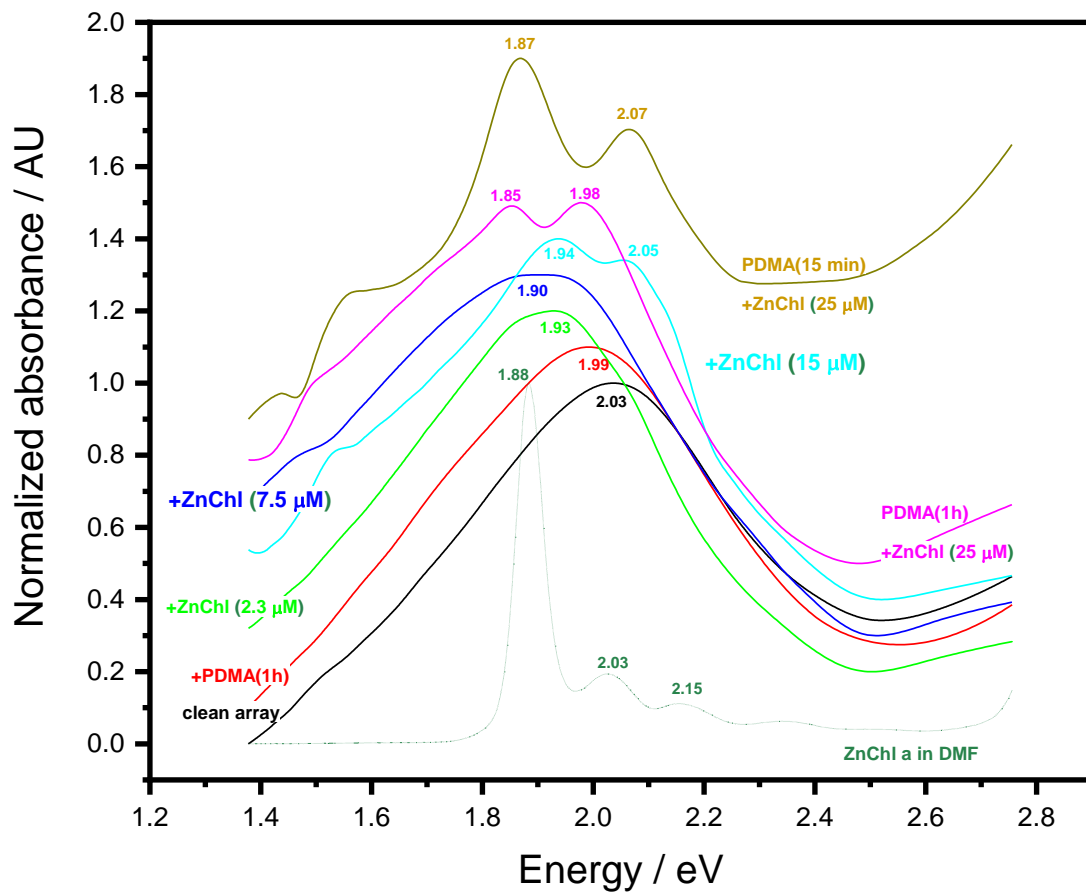


Figure 5-11: Extinction spectra of clean Au arrays and PDMA-functionalised plasmonic arrays of AuNPs before and after the attachment of ZnChla.

Modelling of plasmon–exciton coupling

The coupled plasmon–exciton systems were modelled using a simple coupled oscillator model described previously by Tsargorodska *et al.*^[32] The data was modelled based on the criterion

$$E_c \geq \frac{1}{2} (\gamma_1 - \gamma_2).$$

Modelled extinction spectra of J-aggregates-based plexcitonic complexes are shown in **Figure 5-12**. The experimental data are coloured green, and the fitted data are represented by thin red line. Deposition of J-aggregates on the plasmon arrays of gold nanostructure caused splitting of the plasmon band. This splitting was attributed to plasmon–exciton coupling with coupling energy of 0.26 eV. This coupling was correlated with changes in the angle of the incident of UV-vis beam as discussed above in **Figure 5-8**. The main fitted parameters are the energy of the plasmon and the energy of the exciton with values of 2.04 eV and 2.08 eV, respectively.

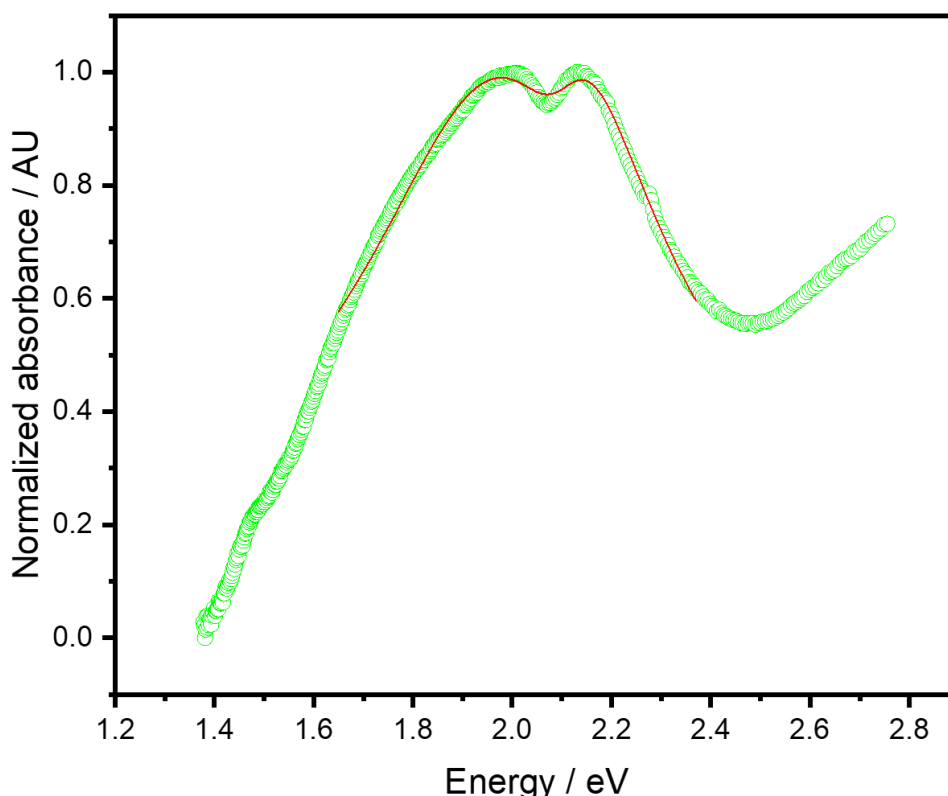


Figure 5-12: Modelling of plasmon–exciton coupling in J-aggregates-based plexcitonic systems. Green spectrum is experimental data, and red is fitted data.

Fitted extinction spectra of *ZnChla*-based plexcitonic complexes are shown in **Figure 5-13**. In both graphs, the black spectra were acquired for clean plasmonic gold nanostructures, and the sharp peaks at 1.9 eV represent Qy band of *ZnChla*. Experimental spectra after attachment of *ZnChla* to PDMA polymerised for 15 min (**Figure 5-13a**), and 60 min (**Figure 5-13b**) are coloured green, and the fitted data are represented by bold red lines. Attachment of *ZnChla* to PDMA scaffolds grown from plasmonic arrays of gold nanostructure caused splitting of the plasmon band. This splitting was attributed to plasmon–exciton coupling with coupling energy of 0.16 eV and 0.08 eV corresponding to the polymerisation time of 15 min and 60 min, respectively. The main fitted parameters are the energy of the plasmon and the energy of the exciton with values of 1.96 eV and 1.99 eV, respectively, for ~ 15 nm thick brushes, and 1.97 eV and 1.90 eV, respectively, for ~ 30 nm thick brushes.

However, such a small coupling energy is expectable for a dense layer of polymer scaffolds due to the steric hindrance of high density PDMA brushes that can reduce the efficiency of the functionalisation process, preventing the complete occupancy of PDMA binding sites with *ZnChla*. This splitting in the spectra was not observed when the density of *ZnChla* molecules was reduced within the brush layer as illustrated above.

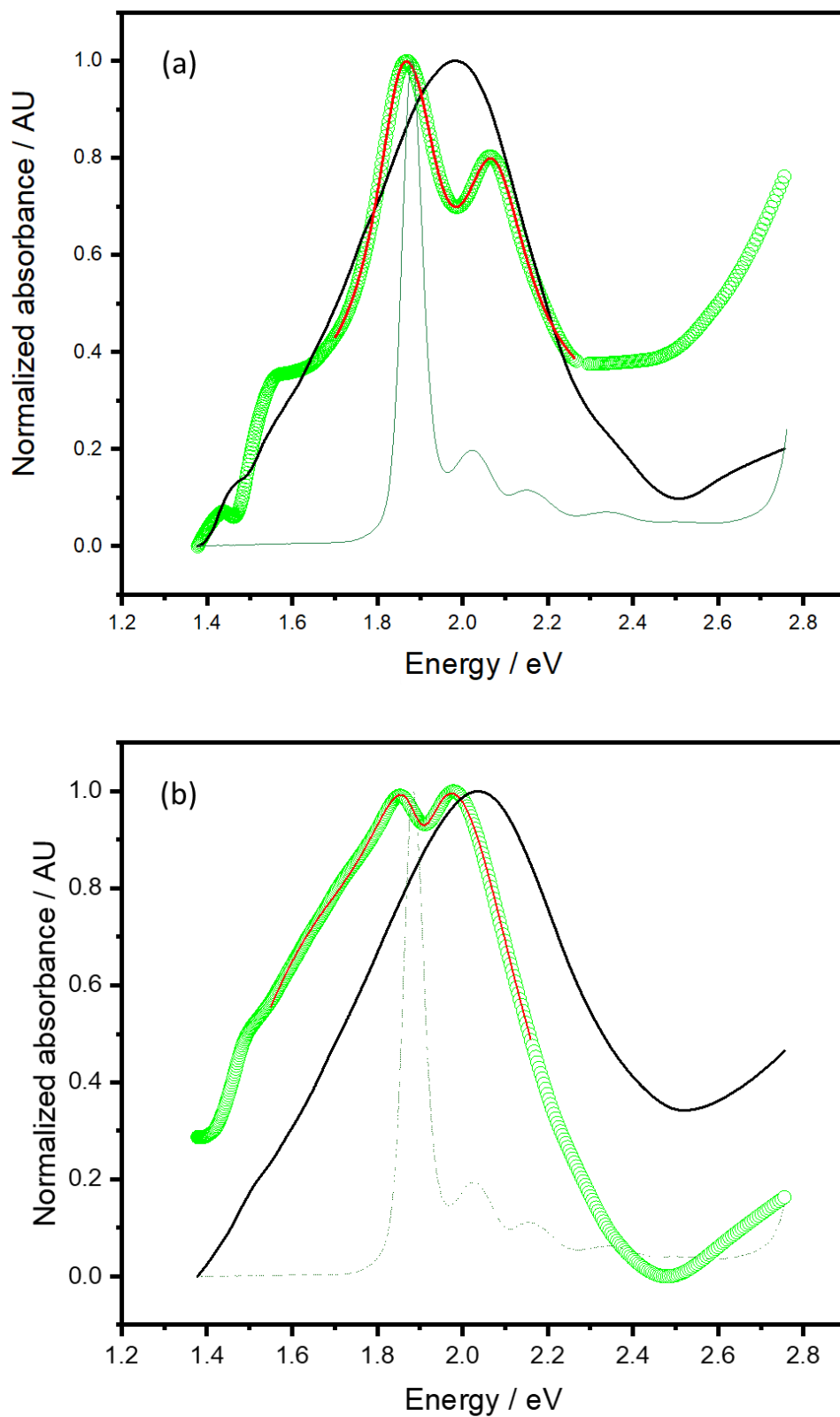


Figure 5-13: Modelling of plasmon-exciton coupling in ZnChla-based plexcitonic systems with different polymerisation times of PDMA; (a) 15 min and (b) 60 min. The black spectra are before the attachment of ZnChla and thick green spectra are collected experimentally after attachment of ZnChla. The short red lines represent the model data.

5.3.7 Iodinated Nile Red (INR)

Iodinated Nile Red dye (INR) was produced by the reaction of hydroxylated Nile Red with 1, 10-diiodooctane as shown in the **Figure 5-14**.

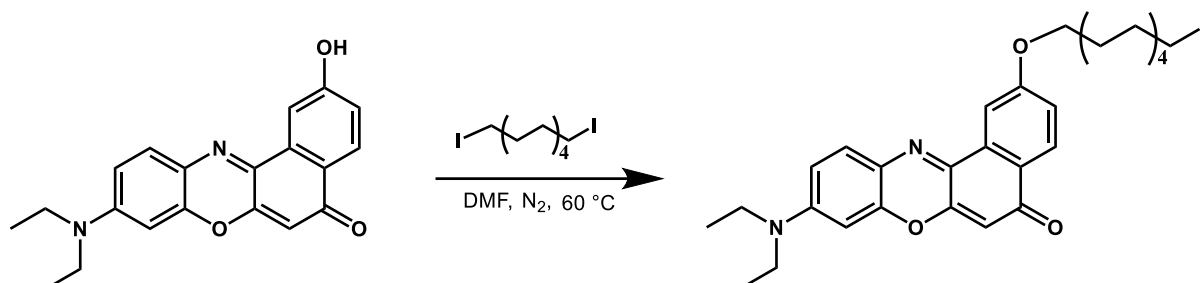


Figure 5-14: Synthesis of iodinated Nile Red via the reaction of hydroxylated Nile Red with 1, 10-diiododecane chains.

INR molecules absorb light in the visible spectral range with absorption maximum at 530 nm. Absorption intensities of INR with different concentrations were linearly increased with increasing solution concentration from 0.25 mM to 8 mM, see **Figure 5-15**. At the concentration of 4 mM and 8 mM, the dye is highly saturated, and the spectrum shows high signal to noise ratio above the absorbance intensity of 3 AU (absorbance unit), so it is not shown in the graph.

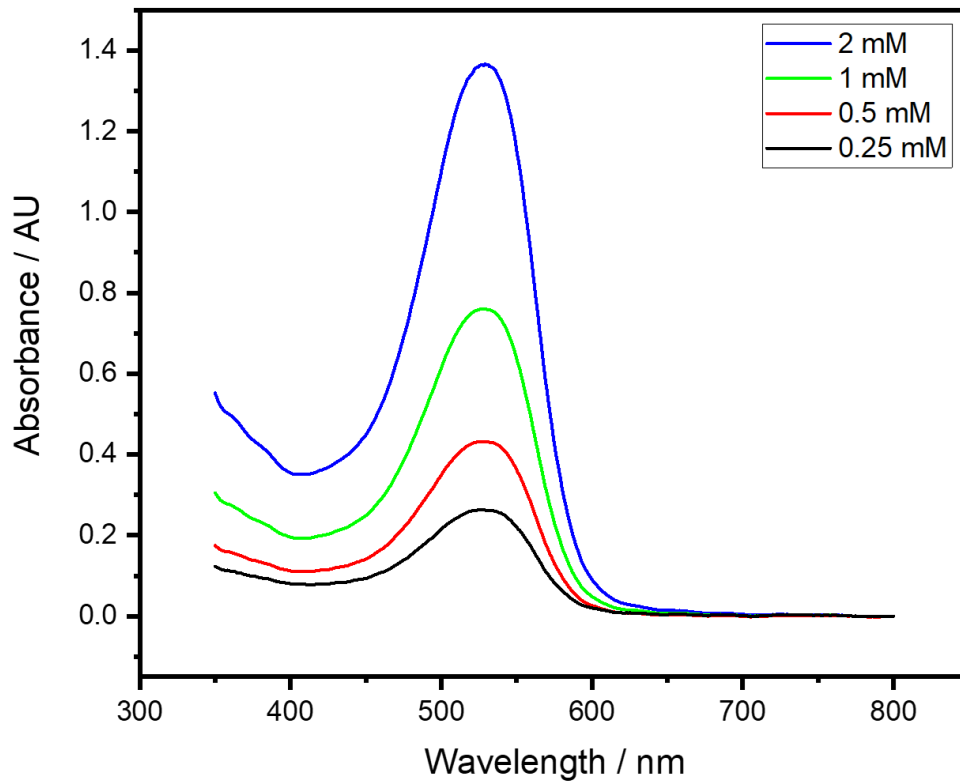


Figure 5-15: Extinction spectra of INR solutions with concentrations of 0.25, 0.5, 1, 2 and 4 mM from down to top.

Figure 5-16 shows calibration curve for the adsorption of INR onto PDMA brushes. A linear relation between the concentration of INR in the solution and the intensity of the corresponding absorbance can be observed.

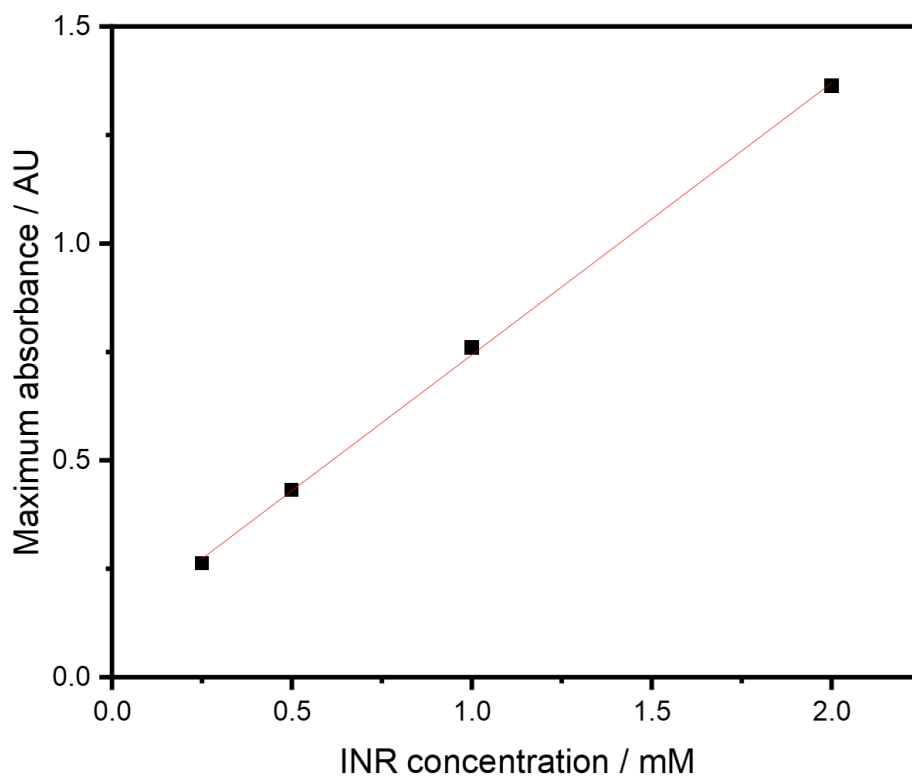


Figure 5-16: Calibration curve for INR concentrations vs maximum absorbance.

In order to study adsorption isotherm of INR adsorbed on PDMA brushes, surface-grafted PDMA brushes formed by ATRP were used as a scaffold to support INR molecules in order to design active biomimetic structure that is similar to *chlorophyll*-PDMA complex taking advantage of the ability to convert the amine group into an ammonium salt. Due to the presence of the iodinated alkyl chain attached to INR, tertiary amine group of PDMA brushes can be quaternised by INR molecules to form INR-PDMA complexes, as illustrated in **figure 5-17**.

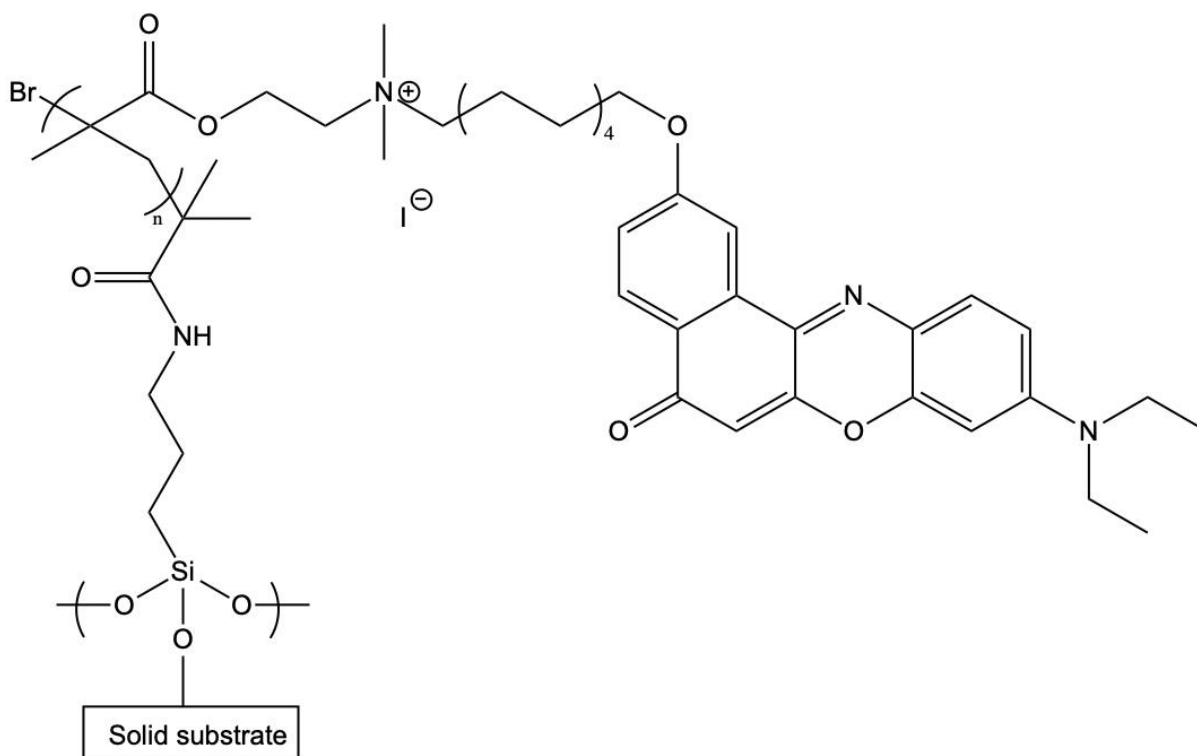


Figure 5-17: Schematic of binding ZnChla to PDMA through quaternisation mechanism.

A series of INR solutions with different concentrations ranging from 0.25-8 mM were used to functionalise PDMA brushes by immersing PDMA samples in the solutions of INR for 24h. This process allows to control the amount of INR adsorbed on PDMA brushes. INR functionalised PDMA brushes were analysed by UV-vis spectrophotometer and XPS.

Figure 5-18 shows extinction spectra of INR-functionalised PDMA brushes with different immobilised amounts of the dye. INR-functionalised PDMA brushes exhibit maximum absorption at 537 nm with red shift compared to that observed in the solutions. The absorption intensity of INR-functionalised PDMA brushes were increased with increasing the concentration of the dye to reach the maximum intensity of 0.09 using the concentration of 4 mM. No more than 0.09 absorption intensity was observed using 8 mM INR. Also, no significant shift was observed.

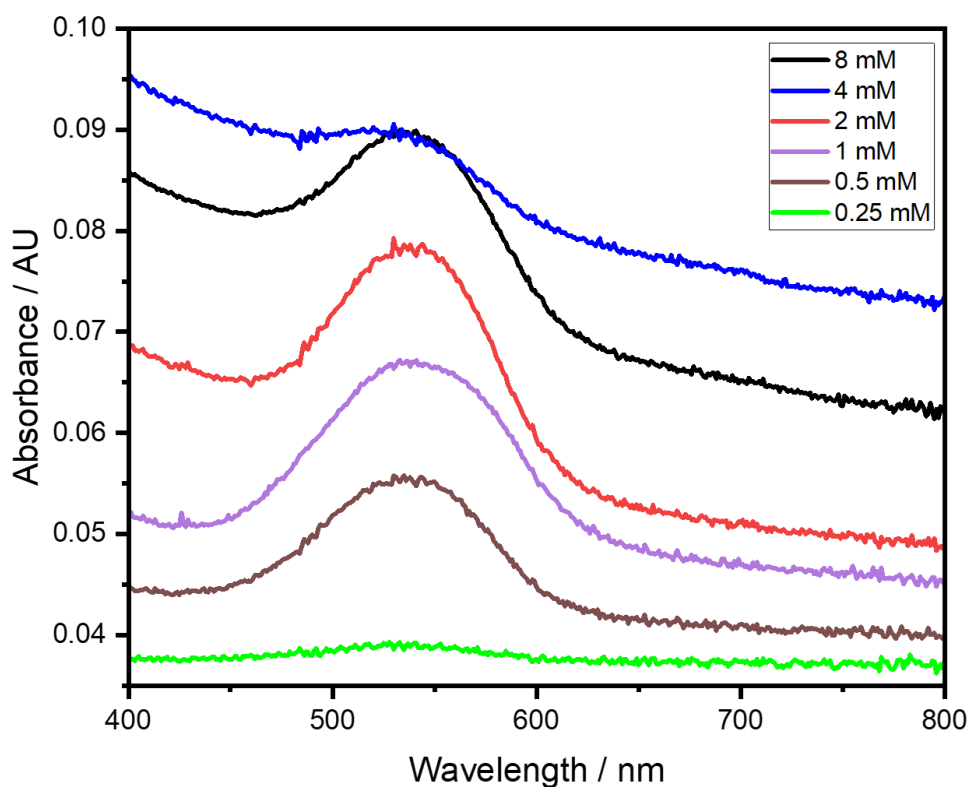


Figure 5-18: Extinction spectra of PDMA functionalised with different concentrations of INR.

The fractional coverage of adsorbed INR molecules onto the surface-grafted PDMA brushes was calculated and presented in **Figure 5-19**. There is a monotonic relationship between the concentration of the used INR solution and the amount of adsorbed INR on the surface of the structure between 0.25 mM to approximately 2 mM. Then, it tends to be more constant over the next range of concentrations. This indicates that partial coverage was obtained by varying the concentrations between 0.25 mM to less than 2 mM, while full surface coverage with INR molecules can be achieved at around 4 mM. However, the shape of the spectrum of 4 mM sample does not fit the trend set by the other samples, most probably due to an experimental error. Indeed, this sample was washed twice due to observed contamination.

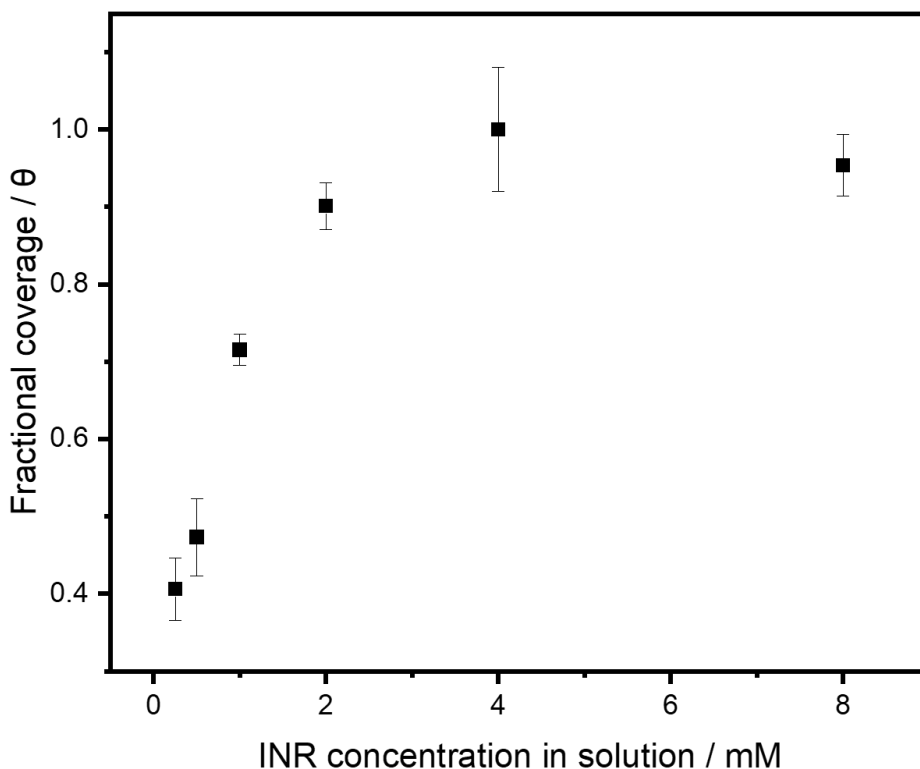


Figure 5-19: Fractional coverage of INR onto PDMA brushes.

The binding of INR to PDMA brushes was examined also by XPS. This technique is appropriate due to its ability to distinguish between normal nitrogen exists in every repeated unit of PDMA brushes and the protonated nitrogen that can be resulted from the binding of iodinated NR molecules with high analytical sensitivity. **Figure 5-20 a and b** show N 1s XPS spectra of INR-functionalised PDMA brushes with two INR concentrations, 0.25 mM and 8 mM, respectively. These spectra exhibit two components at 399.8 eV and 402.7 eV corresponding to normal nitrogen of the amine group and quaternary nitrogen, respectively, see **Figure 5-20 a**. However, the peak of the quaternary nitrogen became more pronounced using higher INR concentration of INR (8 mM), see **Figure 5-20b**. This observation suggested that INR molecules bound to PDMA chains through the quaternisation of the tertiary amine group with the iodinated chain attached to the INR. As it can be noticed here, the intensity of the quaternisation peak is relatively small compared to the peak of the normal nitrogen. i.e., there

is a small quaternisation degree, which could be due to the addition of two normal nitrogen atoms (originally from each binding INR molecule) for every quaternised nitrogen atom.

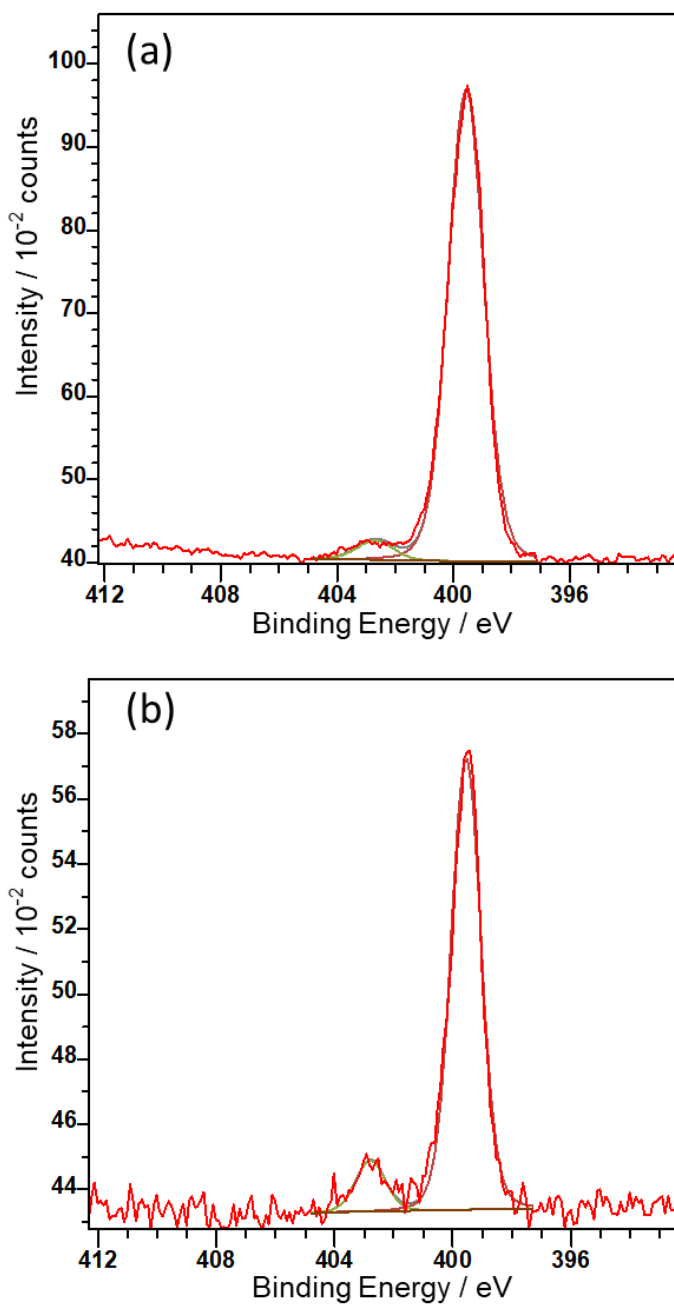


Figure 5-20: N 1s XPS spectra of INR-functionalised PDMA brushes with different INR concentrations. (a) 0.25 mM and (b) 8 mM

The binding profile of INR to PDMA brushes was obtained by examine the relation between the concentration of the used INR solution and the percentage of the quaternised nitrogen.

This profile exhibits a good agreement to the observations obtained from extinction spectra analysis as shown in **Figure 5-21**. The percentage of quaternised nitrogen atoms increased almost linearly with increasing the concentration of the solution of INR between 0.25 mM and 2 mM before it became more stable up to 8 mM.

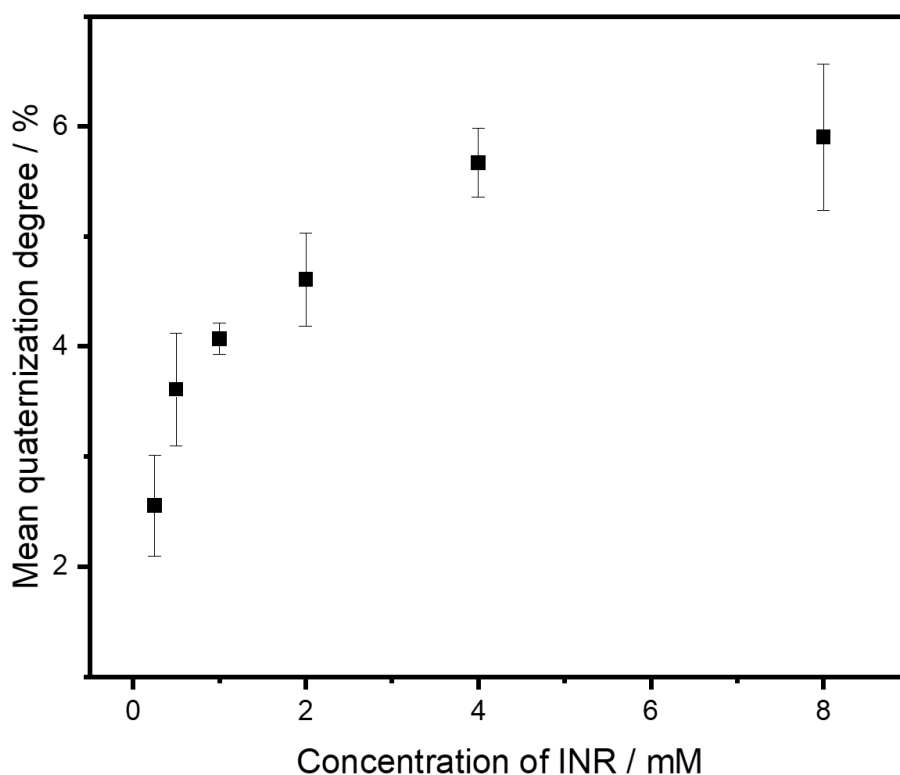


Figure 5-21: Quaternisation degree of the amine groups of PDMA brushes with different concentrations of INR.

C 1s XPS spectra were used to test for the binding of INR to PDMA brushes. **Figure 5-22** shows C 1s XPS spectra collected for PDMA functionalised with INR with concentrations of 0.25, 2 and 8 mM. As expected, the increase in the intensity of C-C peak at 285 eV was observed when the concentration of the solution of INR was increased. This observation is attributed to the large number of C-C bonds exist in each INR molecule due to the presence of long alkyl chain terminated with iodine atom.

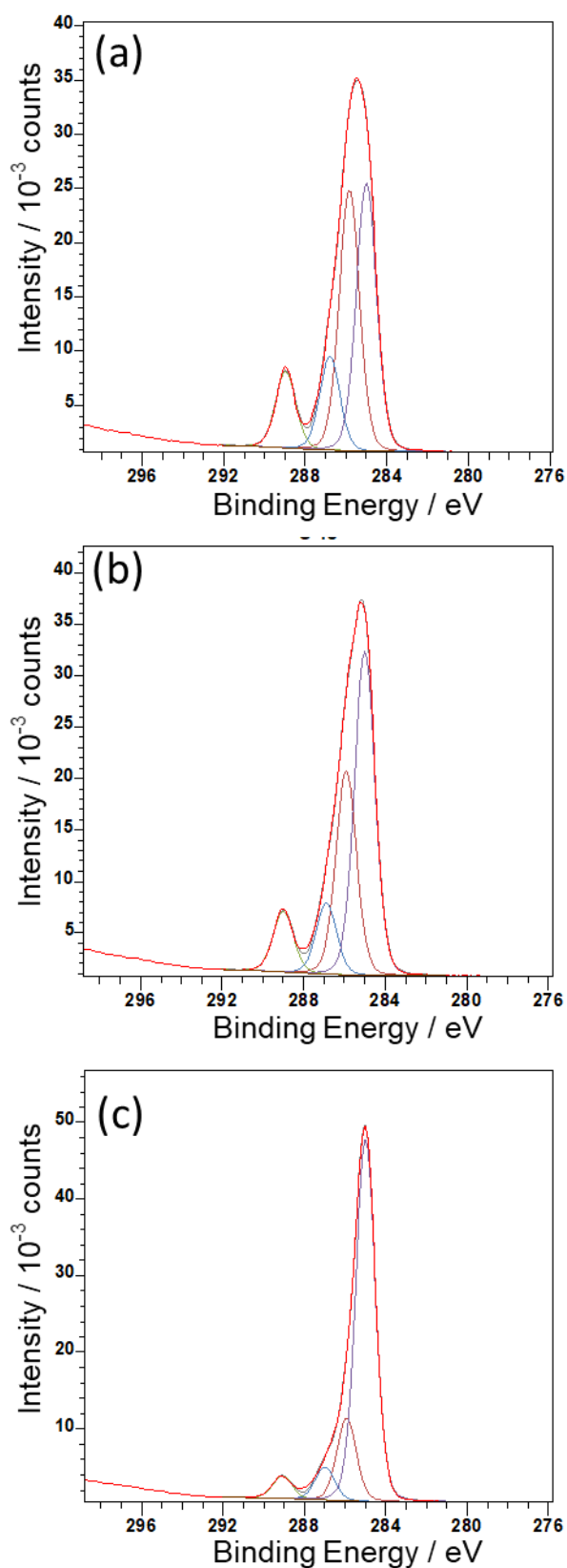


Figure 5-22: C 1s XPS spectra of INR-functionalised PDMA brushes with different INR concentrations. (a) 0.25 mM and (b) 2 mM (c) 8 mM.

Figure 5-23 shows that I 3d XPS high resolution spectra of PDMA functionalised with INR with concentration of 0.25 mM and 2 mM. As it can be seen in this figure the peak of iodine is small feature at the concentration of 0.25 mM, while it became more pronounced at the concentration of 2 mM indicating that more binding site have been occupied by INR when concentration of INR solution increased from 0.25 mM to 2 mM.

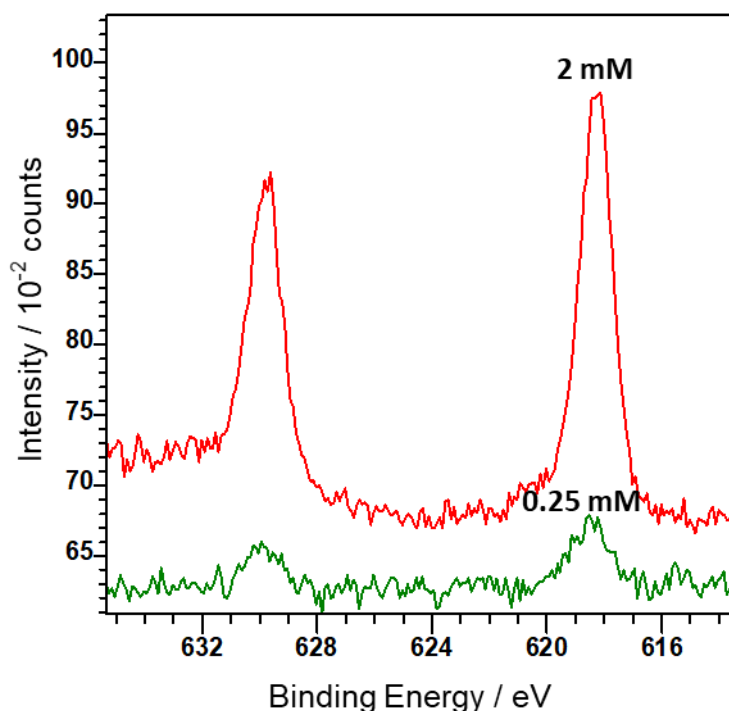


Figure 5-23: I 3d XPS spectra of INR-functionalised PDMA brushes with different INR concentrations. (top) 2 mM and (down) 0.25 mM.

Figure 5-24 shows that the percentage of iodine ions on the surface was increased by increasing the concentration of INR in the solution in which the samples were immersed. This observation indicates that the more INR molecules attached to the brushes the more binding sites on the PDMA chains are occupied by INR molecules until reaching saturation state at the concentration of 4 mM.

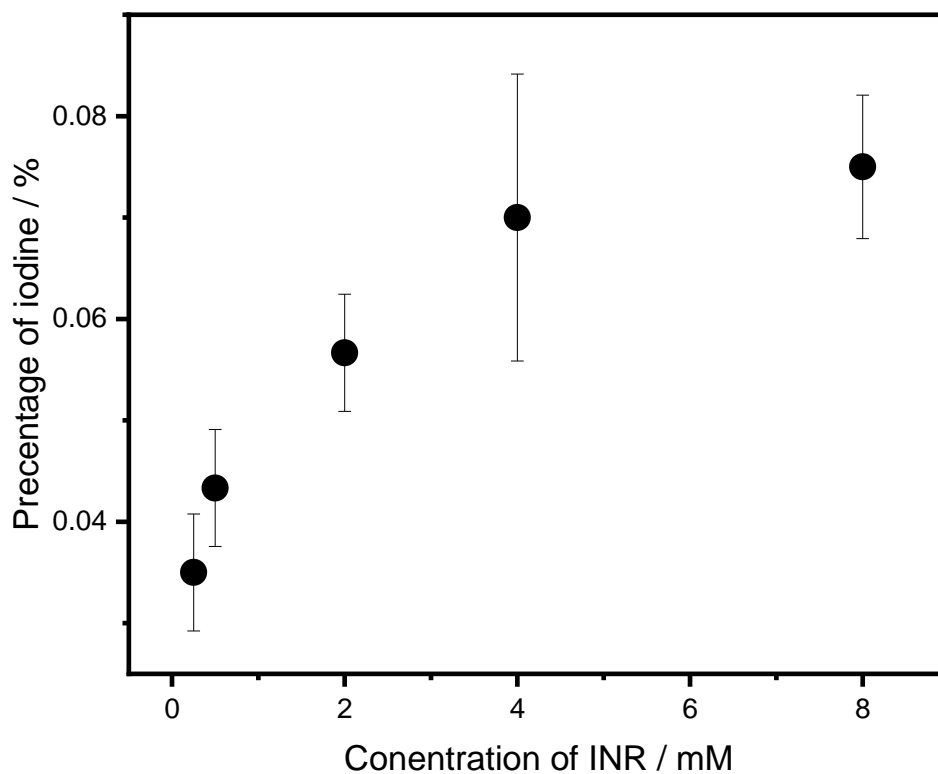


Figure 5-24: Iodine percentage on the surface of PDMA as a function of INR concentration.

There was no sign of strong plasmon-exciton coupling was observed when INR was spin-cast on the surface of plasmonic arrays of Au nanostructures. Only a red shift was obtained. However, the red shift was as the concentration of INR increased. This could indicate that the orientation of INR was not optimised for strong coupling, see **Figure 5-25**.

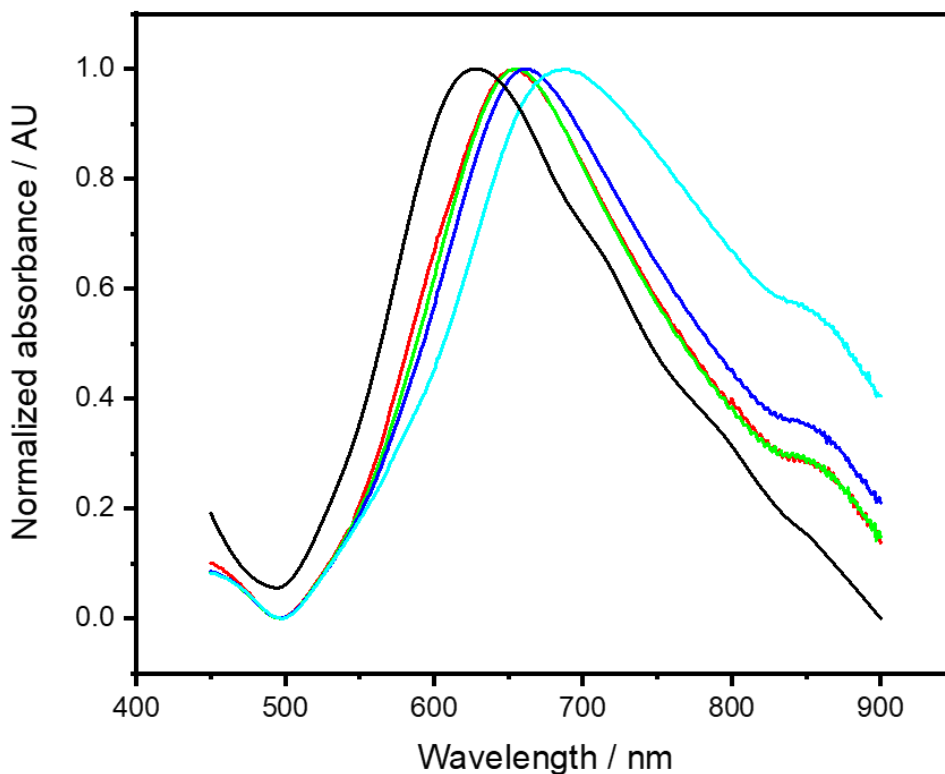


Figure 5-25: Extinction spectra of INR spin-casted on the plasmonic arrays of gold nanostructures.

Figure 5-26 shows extinction spectra of PDMA-initiated gold plasmonic arrays before and after attachment of INR. When INR-PDMA antenna complexes were deposited onto plasmonic arrays of AuNPs structures, a splitting in the absorption band was observed **Figure 5-26** blue spectrum. This splitting was found to be sensitive to the angle of incidence of the UV-vis beam at 7.5° , 2° and 0° , see magenta, dark yellow and green spectra, respectively. This observation was attributed to the coupling between LSPR of gold nanostructures and excitonic transitions of INR.

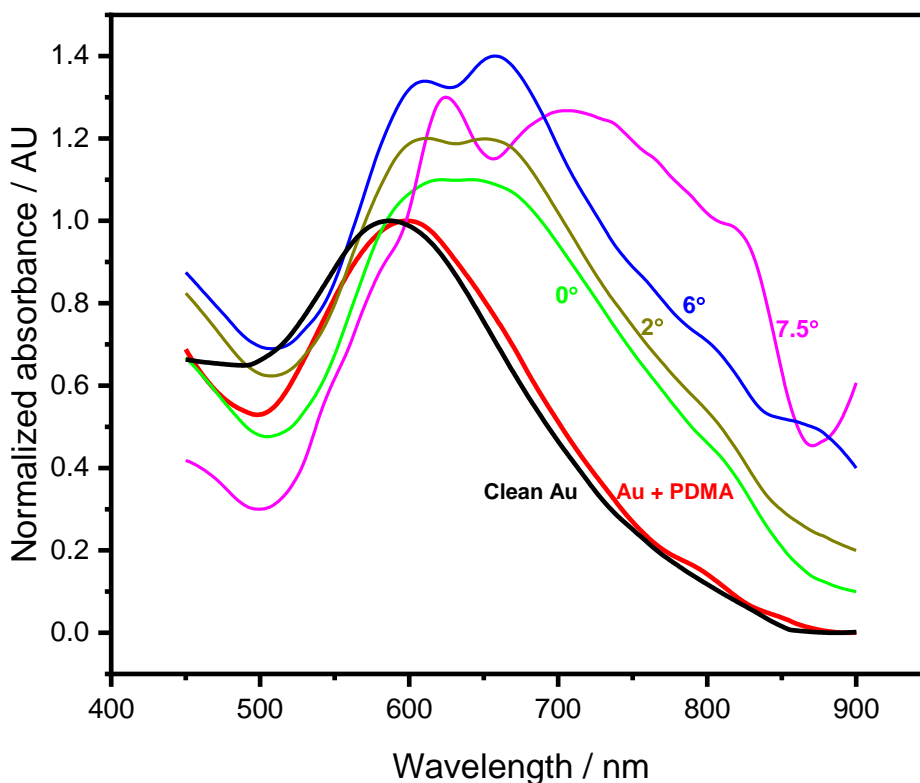


Figure 5-26: Extinction spectra of PDMA-initiated gold plasmonic arrays before and after attachment of INR.

Here, also, the coupled plasmon-exciton systems were modelled using a simple coupled oscillator model described previously by Tsargorodska *et al.*^[32] The data was modelled based on the criterion $E_c \geq \frac{1}{2} (\gamma_1 - \gamma_2)$.

Fitted absorption spectrum of INR-based plexcitonic complexes are shown in **Figure 5-27**. The black spectra were acquired for clean plasmonic gold nanostructures and green spectrum was acquired after polymerisation of PDMA. Experimental spectrum after attachment of INR to PDMA polymerised for 1 h is coloured red, and the fitted data are represented by bold blue line. Attachment of INR to PDMA scaffolds grown from plasmonic arrays of gold nanostructure caused splitting of the plasmon band. This splitting was attributed to plasmon–exciton coupling with coupling energy of 0.21 eV. The main fitted parameters are the energy of the plasmon and the energy of the exciton with values of 1.96 eV and 1.99 eV, respectively.

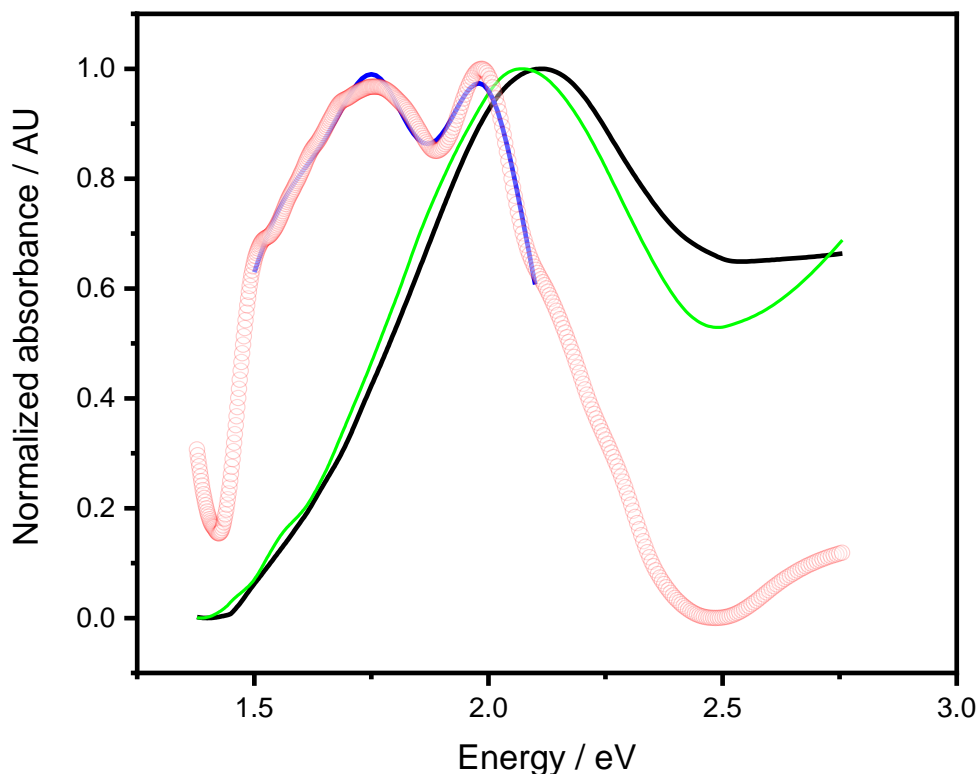


Figure 5-27: Modelling of plasmon-exciton coupling in J-aggregates-based plexcitonic systems. Green spectrum is experimental data, and red is fitted data.

However, such coupling energy is expectable for a dense layer of polymer scaffolds due to the steric hindrance of high density PDMA brushes that can reduce the efficiency of the functionalisation process, preventing the complete occupancy of PDMA binding sites with INR. While strictly this approaches the strong coupling regime, it is believed that the system is not yet fully optimised. There is scope for further optimising the coupling of the dye to the polymer by controlling the grafting density of the polymer. That may enable to achieve an increase in the concentration of dye molecules in the brush layer, thus increasing N/V and hence the coupling energy.

5.4 Conclusion

The feasibility of constructing of plexcitonic dye-polymer antenna complexes has been investigated via different methods. To set a bench-mark, J-aggregates and *chlorophyll* were spin-cast and drop-cast onto gold nanostructures. The splitting of the extinction spectra of gold nanoarrays is only observed in the case of spin-cast of J-aggregates on the surface of gold nanostructures, while a red shift is observed in the case of spin-cast of *ZnChla* on the surface of gold nanostructures. A large shift is observed when both *ZnChla* and J-aggregates were drop-casted on the surface of gold nanostructures.

Pigment-polymer plexcitonic complexes were formed by attaching pigment molecules (*chlorophyll* and Nile Red derivatives) to PDMA scaffolds grown from gold nanostructures. Splitting of the plasmon band LSPR, which is a sign of the strong plasmon exciton coupling, is observed in the case of spin-casting of J-aggregates. This splitting was sensitive to the incident angle during the measurements of UV-vis extinction spectra. Strong coupling was not observed in measurements on spin- and drop-cast films of *ZnChla*, perhaps because of problems associated with the deposition conditions. However, splitting of the LSPR was observed when *ZnChla* is attached to PDMA brushes. The coupled spectra were successfully fitted using a simple coupled oscillator model. The strength of plasmon-exciton coupling is dependent on the concentration of *ZnChla* from which the *ZnChla* was bound to the PDMA scaffold, as expected. A splitting of the absorption band was also observed when INR was attached to PDMA scaffolds, and not observed when INR spin-casted onto the plasmonic arrays of gold nanostructures. Modelling yielded a coupling energy of 0.21 eV, approaching the strong coupling regime. It is probable that the coupling strength could be increased further for both *ZnChla* and INR by further optimisation of the reaction conditions (polymerisation time, solution concentration of pigment, grafting density of polymer), and such studies would be a good subject for future work.

CHAPTER 6: GOLD NANOPARTICLE FILMS

6.1 Introduction

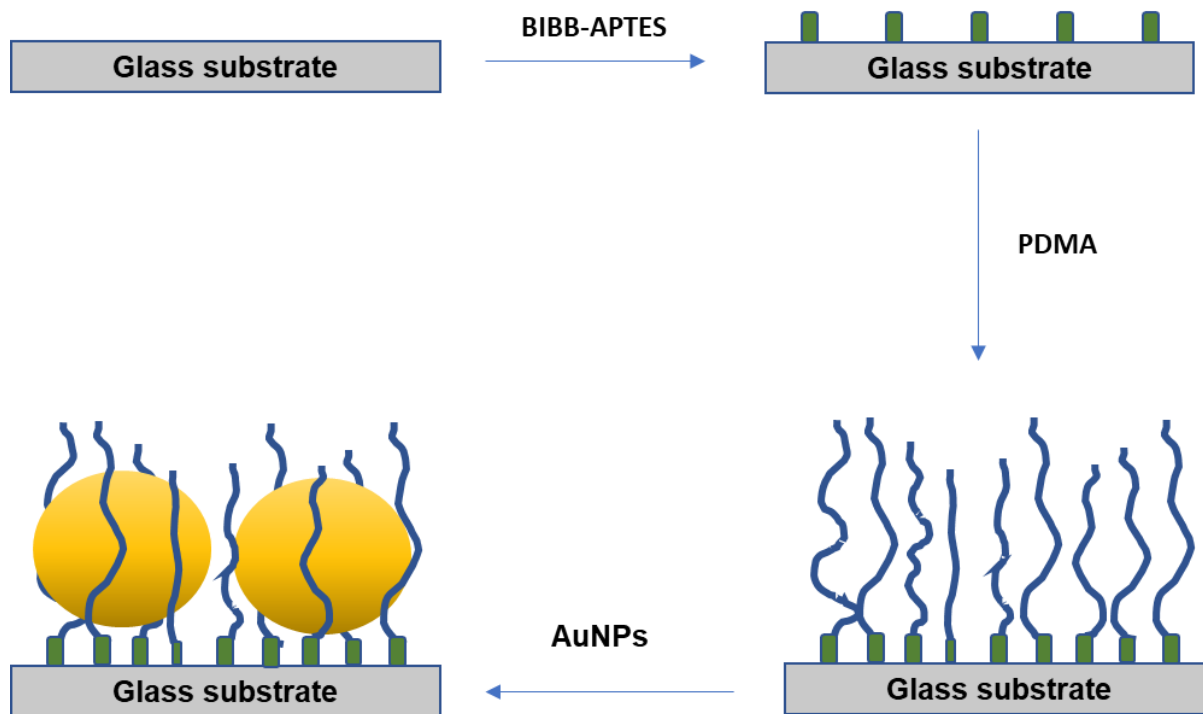
Gold NPs exhibit strong plasmon absorption band and they have consequently attracted an interest in applications in analytical science.^[242] Recently, there has been interest in a new phenomenon, strong plasmon-exciton coupling, in which plasmon modes exchange energy with molecular emitters so rapidly that their states are mixed to create new hybrid light-matter states called plexcitons.^[2] Recently, it has been shown that such strong coupling can occur in biological systems, in particular when plant LHCs or synthetic protein LHCs are coupled to plasmonic nanoarrays.^[32,241]

These observations provide inspiration for new ways to design photosynthetic materials. However, proteins are not suitable for many potential applications of molecular materials because of their fragility and the high cost of production. Thus, to exploit these new design principles, one alternative route is to translate them into the construction of synthetic polymers. In previous work, organic polymer brushes were used a suitable alternative to the peptides scaffolds that organise *chlorophyll* and carotenoids in light-harvesting complexes. Particularly, PCysMA brushes were used to support *chlorophyll* molecules coupled to gold nanostructures.^[33] However, the dependence of lithographic step in this published work potentially represents a limitation.

The aim of this chapter is to expand the work by imbedding plasmonic AuNPs into polymer brushes rather than growing the polymer brushes from a surface-bound arrays of nanostructures. This would enable the use of biologically inspired design principles in combination with strong light-matter coupling but without the need for nanolithography.

The procedures are simple, inexpensive and enable good control of film thickness. To achieve this, cationic PDMA brushes will be grown via ATRP on brominated substrates. Then, AuNPs will be imbedded into PDMA brushes by immersing PDMA samples into AuNPs solution for certain period of time. Then, *ZnChla* will be attached to the system by immersing the

samples in *ZnChla* solution in order to investigate possible the possibility of plasmon-exciton interaction. **Figure 6-1** shows simplified schematic illustration of each step of the addition of *ZnChla* to AuNPs-embedded PDMA structure.



Addition of the Zn-Chla on the plasmonic system

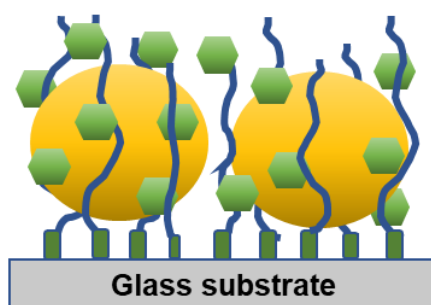


Figure 6-1: Schematic illustration of incorporation of AuNPs into PDMA and subsequent addition of ZnChla.

6.2 Materials and methods

6.2.1 Materials

Glass substrates (Cover slips glass slides, Menzel-Glazer/ 22*60# 1.5) were obtained from VWR. Copper I bromide ($\geq 98\%$) was supplied by Alfa Aesar. Chloroauric acid (gold(iii) chloride hydrate, 99.995% trace metals basis) HAuCl_4 , trisodium citrate (sodium citrate tribasic dihydrate, 99%), 3-aminopropyltriethoxysilane ($\geq 99\%$), 2-bromoisobutyryl bromide (98%), triethylamine ($\geq 99\%$), 2-(dimethylamino) ethyl methacrylate (98%), 1,1,4,7,10,10-hexamethyltriethylenetetramine (HMTETA) (97%), 1-iodooctadecane (95%), and zinc acetate dehydrate were purchased from Sigma Aldrich. Ethanol, absolute (99.8%, HPLC grade), hydrogen peroxide (30% w/v), sulphuric acid (95%), dimethylformamide (99%), and magnesium sulphate anhydrous were supplied by Fisher Scientific. Silicon wafer (150 mm) was purchase from Pi-KEM (UK). Copper bromide was stored under vacuum atmosphere and DMA was stored at 4 °C after removal of the inhibitor. Chloroauric acid was stored between 3-8 °C in the dark.

6.2.2 Samples cleaning and handling

Glass coverslip slides were cleaned as described in chapter 3. The substrates were immersed in Piranha solution (30% H_2O_2 : 98% H_2SO_4 , 1:3, v/v) for around 2 h. *Caution: Piranha solution can result in a violent reaction with organic matter and should be handled with extreme caution!* Then, the slides were washed several times with deionised water and placed in oven at 90 °C for few hours to dry. The slides were cut into small pieces ($\approx 0.5 * 1.2$ cm) and handled using a clean tweezers and kept in Eppendorf tubes until use.

6.2.3 Synthesis of BIBB-APTES films

BIBB-APTES films were prepared in two steps as described previously in chapter 3. Briefly, 2% solution of APTES in ethanol was used to functionalise glass substrates to form SAMs of APTES. This was followed by the attachment of BIBB to form Bromine-functionalised initiator.

6.2.4 Growth of PDMA via ATRP

PDMA brushes were grown from BIBB-APTES initiated glass substrates as described in detail in chapter 3. Briefly, DMF was used as a good solvent for DMA monomers. HMTETA and Cu (I)Br were used to catalyse ATRP reaction at 90 °C. 4 mL of monomer/ catalyst solution was added onto each initiator sample in Schlenk tubes, under a nitrogen atmosphere. After the desired polymerisation time, the reaction was terminated by removing the slide from the mixture.

6.2.5 Extraction and derivatization of *chlorophyll a*

A detailed description of *ZnChla* synthesis can be found in chapter 3. Briefly, *Chla* was extracted from spinach leaves by acetone and converted into pheophytin a (dark blue pigment) by dissolving the dark green pigment in acetic acid under stirring for 3 h. Then, zinc acetate dehydrate dissolved in methanol was used to convert pheophytin into *ZnChla* under reflux in argon atmosphere at 35 °C for 1 h.

6.2.6 Synthesis of AuNPs

AuNPs were prepared by reduction of HAuCl_4 (0.17, 1 mmol dm^{-3}) with trisodium citrate (0.59g, 38.8 mmol dm^{-3}) at boiling point under vigorous stirring. The appearance of deep red colour within a few minutes indicates the formation of AuNPs. The resulting suspension of

AuNPs was stored in the dark in a fridge. A full description of AuNP synthesis can be found in chapter 3.

6.2.7 Immobilization of AuNPs onto APTES-functionalised solid substrate

AuNPs were adsorbed onto APTES-functionalised glass substrate by immersing the previously formed amine-functionalised slides in AuNPs solution for the desired immobilization time in the dark at room temperature to form glass-APTES-AuNPs films. More details can be found in chapter 3.

6.2.8 Incorporation of AuNPs into brush films

AuNPs-incorporated PDMA brushes were prepared as described previously in chapter 3. Briefly, PDMA samples were immersed in AuNPs solution for 24 h unless otherwise is stated. The reaction was allowed to proceed in the dark at room temperature to form AuNPs-functionalised PDMA films.

6.2.9 Attachment of *ZnChla* to PDMA-AuNPs system.

ZnChla was attached to AuNPs-functionalised PDMA brushes by immersion of the samples (glass-BIBB-APTES-PDMA-AuNPs) in solution of *ZnChla* for 24 h in the dark at room temperature to form glass-BIBB-APTES-PDMA-AuNPs-*ZnChla* structures. Detailed description can be found in chapter 3.

6.2.10 Surface analysis

A Cary 50 UV-vis spectrophotometer was used to obtain extinction spectra in the range 400 – 800 nm, unless otherwise stated. AuNPs colloidal suspension was characterised in a

standard quartz cuvette with 10 mm optical path length at room temperature. Glass slides functionalised with APTES and AuNPs or PDMA and AuNPs were characterised in air. The measurements were conducted using a home-made PTFE sample holder which was used to perform measurements on the same area of the surface during all experimental stages.

X-ray photoelectron spectroscopy (XPS) spectra were obtained using a Kratos Axis Ultra/Supra spectrometer (Kratos Analytical, Manchester, UK). All binding energies were calibrated relative to the 285 eV calibrated primary hydrocarbon C 1s signal. XPS data were analysed using the CASAXPS (v. 2.18) software.

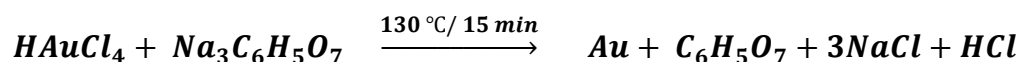
AFM images were obtained using a Digital Instruments (Nanoscope 5 Multimode Atomic Force Microscope), (Veeco, Santa Barbara, CA) fitted with a “J” scanner (maximised 125 μm). All measurements were conducted in air at room temperature. AFM data analysis was performed using Nanoscope Analysis software (v.1.5).

Ellipsometric spectra were collected using an M-2000VI ellipsometer (J. A. Woollam Co., Inc., USA) operating in a spectral range from 370 to 1000 nm, at an incident angle (Φ) of 75°, unless otherwise is stated. Modelling ellipsometric data was performed using CompleteEASE software (v.6.6). At least three measurements per sample were carried out in air to obtain an average.

6.3 Results and discussion

6.3.1 Synthesis and characterisation of AuNPs

A colloidal suspension of AuNPs was produced in one step by chemical reduction of gold salt using trisodium citrate in a simple, fast and cost-effective chemical synthesis method. In the process, tetrachloroauric acid was used as a precursor and sodium citrate was used as a reducing agent as described by the following equation.



Although there are a number of reduction agents can be used for this purpose, sodium citrate was chosen to act as a reducing and stabilization agent together. The resulting AuNPs were characterised by Uv-Vis spectroscopy. **Figure 6-2** shows a series of extinction spectra recorded for colloidal AuNP suspension with various concentrations (concentrated as-prepared 17 nM, diluted 1-1 in water and diluted 1-10 in water). All spectra exhibit a strong absorption at 523 nm. The noise in the spectrum for the concentrated solution spectrum (blue) is a consequence of the signal becoming saturated.

Using the wavelength at which the plasmon absorption occurs,^[243] and following Haiss method,^[65] the average particle size of the produced AuNPs solution is estimated to be 13 nm \pm 5 in a good agreement to DLS measurements, which reveals average particle size between 11 and 15 nm. However, the resonance energy relies on various parameters such as average particle size, dielectric constant of the medium and surface charge, etc. As it can be seen in **Figure 6-2** only the intensity of the plasmon resonance peak was reduced by dilution. Thus, the dilution reduces only the volume fraction of the particles in the solution, but peaks positions remain the same.

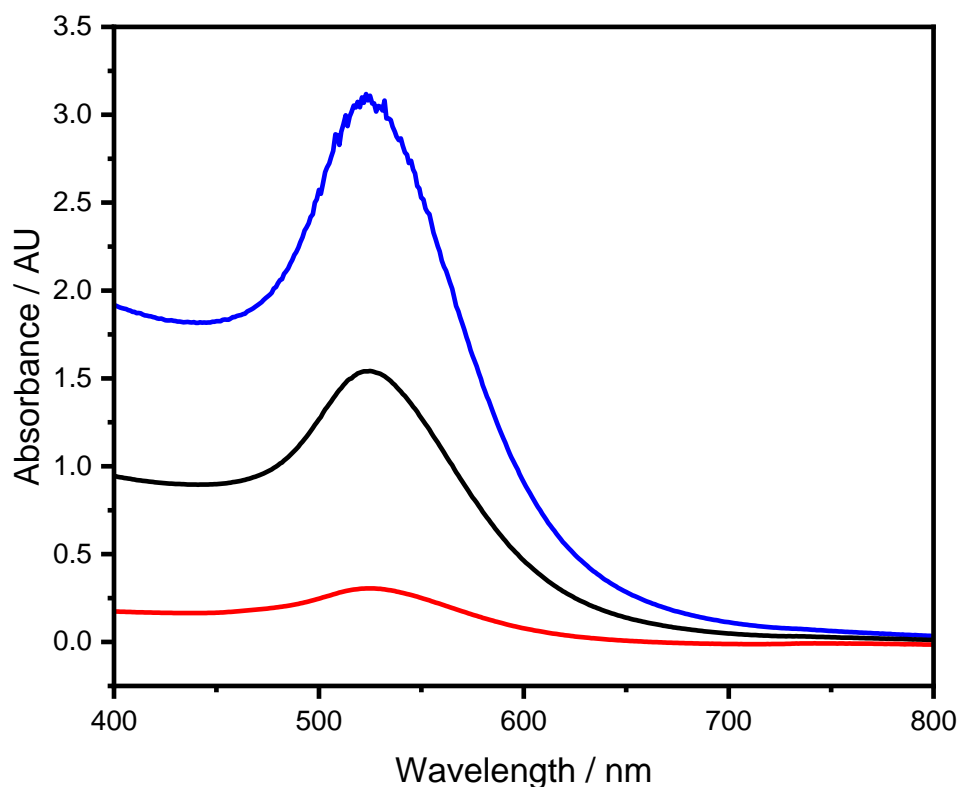


Figure 6-2: Extinction spectra of various concentrations of colloidal AuNPs prepared by chemical reduction. (Blue) concentrated as-prepared solution. (Black) diluted 1-1 solution in water. (Red) diluted 1-10 solution in water.

ATPES-functionalised glass substrates were used as a platform to support the formation of contentious AuNP layers (layer of full coverage of adhered AuNPs). The effect of the solution concentration of the immobilised AuNP was examined by UV-vis absorption measurements. **Figure 6-3** shows surface plasmon band of three different concentrations (concentrated as prepared, diluted 1-1 in water and diluted 1-10 in water) of the deposited AuNPs on APTES-functionalised glass substrates. Compared to the spectra shown in **Figure 6-2**, the maximum absorption maxima are blue-shifted due to the change of the particle's medium from water ($n = 1.33$) to air ($n = 1$). Also, a broad shoulder peaks appear at ca. 650nm. This shoulder peaks are attributed to the aggregation of the neighbouring particles as will be discussed in the relevant AFM images in **Figure 6-4**. However, the intensities of the main peak at 516 nm and

the shoulder peak at 640 nm were decreased with decreasing the concentration of the solution of immobilised AuNPs.

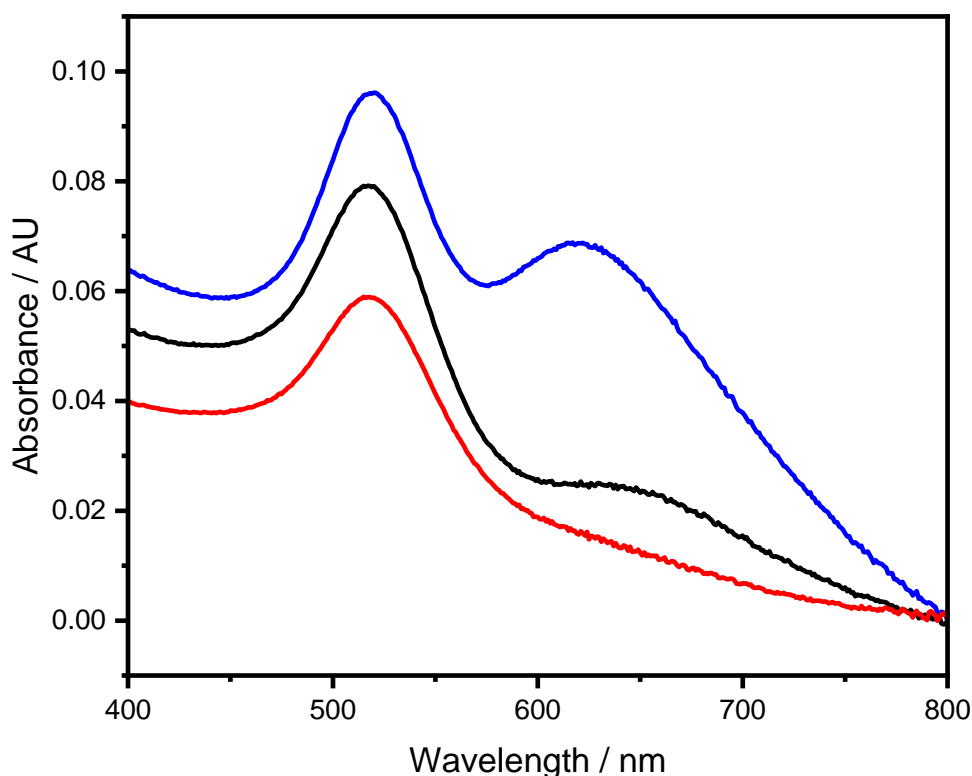


Figure 6-3: Extinction spectra of AuNPs adsorbed onto APTES-functionalised glass substrate acquired from three solutions with different concentrations (Blue) as-prepared solution. (Black) diluted 1-1 solution in water. (Red) diluted 1-10 solution in water.

The AFM height image in **figure 6-4** shows the morphologies of films of AuNPs immobilised on APTES-functionalised glass substrates After immersion of the samples in nanoparticles suspensions for 24 h. As it can be seen in both the height image and the phase image, a full surface coverage of AuNPs is obtained through the binding of the partially positive amine group ($-NH_2$) of APTES to the negatively charged AuNPs.^[244,245] The particles are close packed with small interparticle separation seem to be aggregated, leading to coupling of plasmon modes on neighbouring particles, accounting for the proud features at 640 nm in the extinction spectra shown previously in **Figure 6-3**.

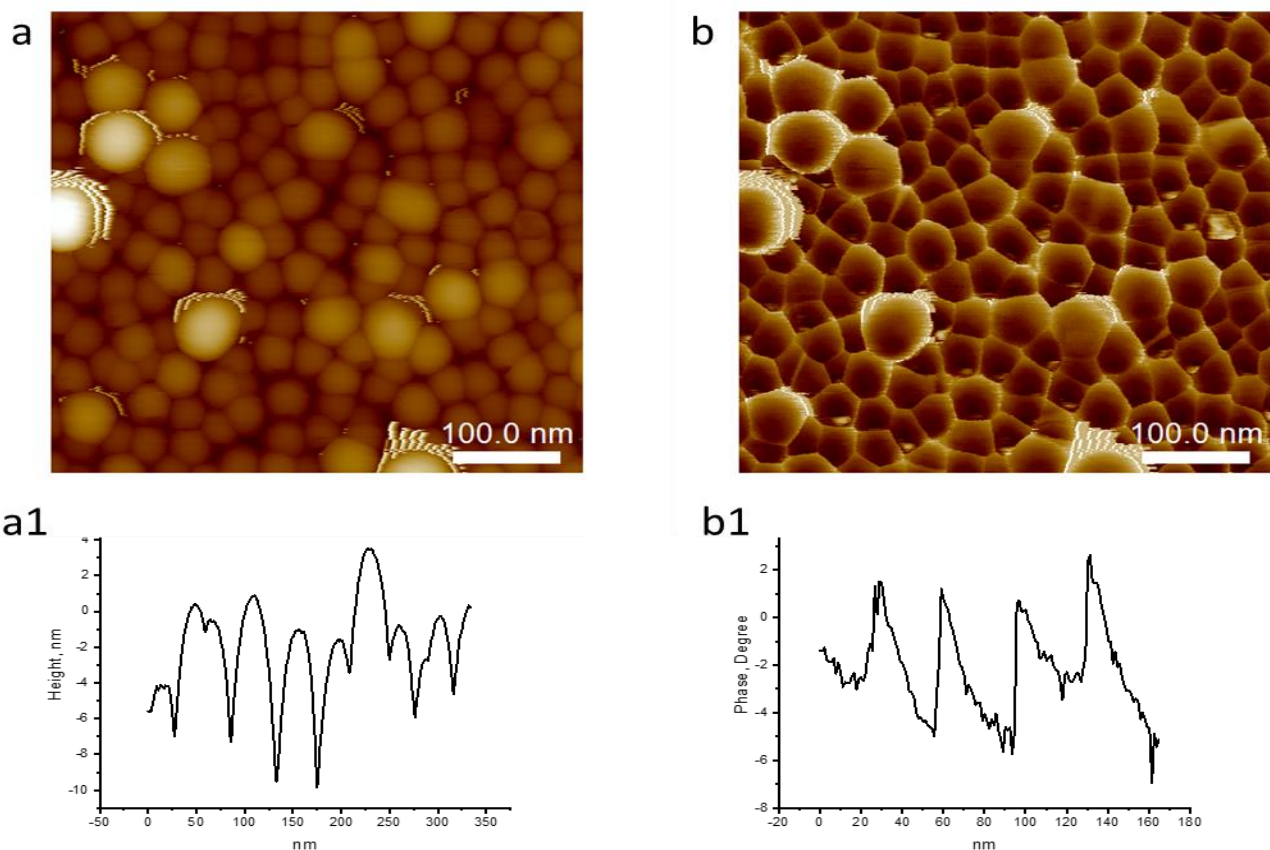


Figure 6-4: AFM tapping mode images of AuNPs adsorbed onto APTES layer (a) height image (b) phase image, and their respective cross-section spectra (a1) and (b1).

6.3.2 Incorporation of AuNPs into PDMA brushes

AuNPs were incorporated into PDMA brushes by immersing PDMA brush samples in a suspension of AuNP for 24h, allowing the negatively charged AuNPs to bind to the positively charged polymer chains through electrostatic interaction as illustrated schematically in **Figure 6-5**.

highest concentration of AuNPs. The absorption intensity was decreased as the concentration of the NP suspension was decreased, see **Figure 6-6**.

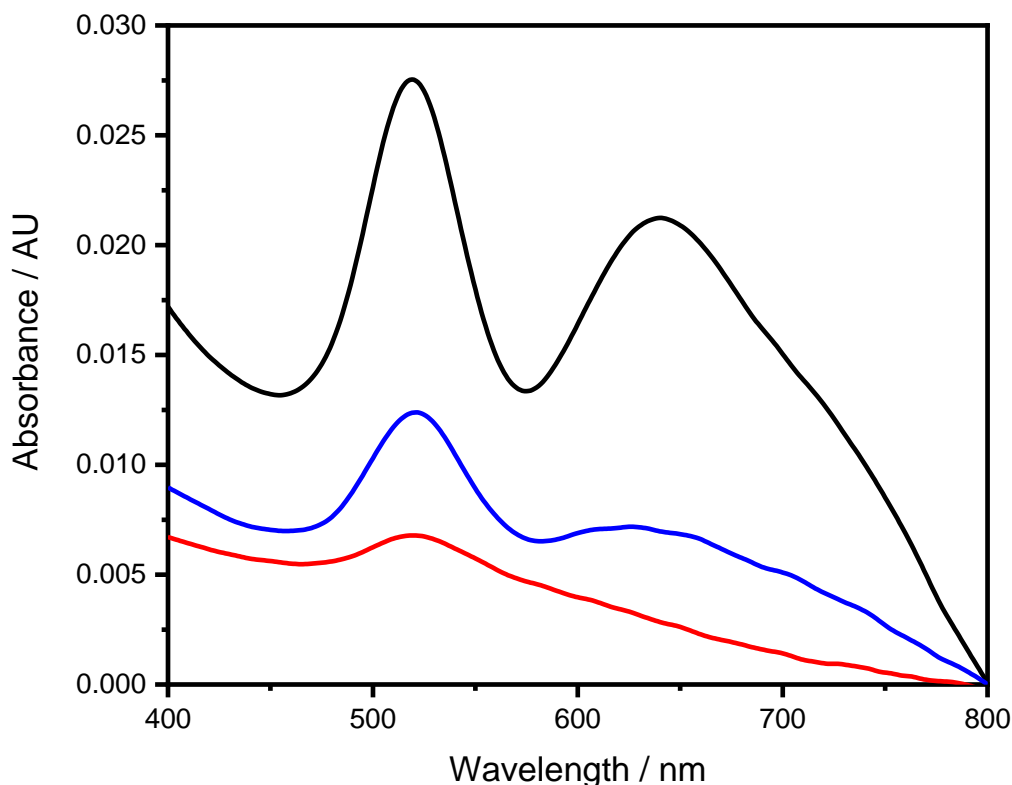


Figure 6-6: Extinction spectra of AuNPs adsorbed onto PDMA brushes from three solutions with different concentrations (Black) concentrated as-prepared solution 17 nM. (Blue) diluted 1-1 solution in water. (Red) diluted 1-10 solution in water.

The effect of PDMA brush thickness on the plasmon resonance of the embedded AuNPs into PDMA brushes was investigated. As shown in **Figure 6-7**, AuNPs embedded 15 nm thick PDMA brushes exhibit absorption maximum at 525 nm and a broad shoulder peak at 650 which is attributed to aggregation, see **Figure 6-7 black spectrum**. However, when AuNPs were embedded into 20 nm thick brush, a broad peak was observed with a maximum absorption at 640 nm, which could be attributed to the formation of high number of aggregated particles, see

Figure 6-7 blue spectrum. Using 35 nm thick PDMA resulted in the appearance of a broad peak to 665 nm with a pronounced shoulder peak at 545 nm. This apparently broad peak can be explained by the formation of two types of aggregates, with overlapping distributions of sizes but different mean radii, **see Figure 6-7 red spectrum.**

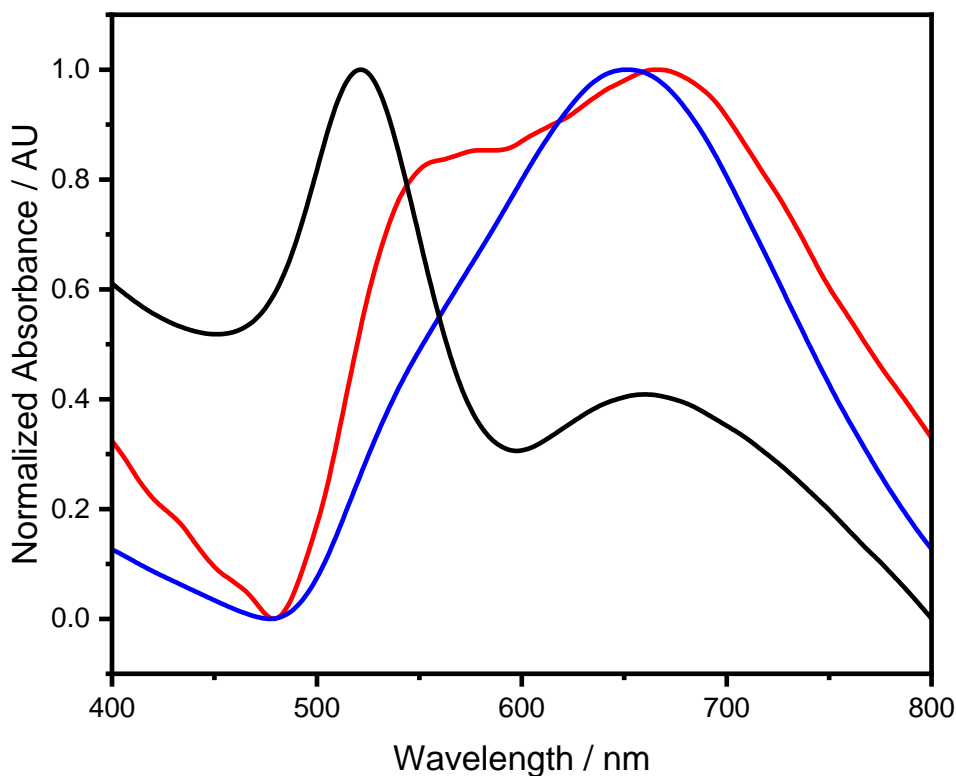


Figure 6-7: Extinction spectra of AuNPs-embedded PDMA brushes with different thicknesses of the brush (Black) 15 nm. (Blue) 20 nm. (Red) 35 nm.

A possible explanation for the change in AuNP packing with PDMA thickness is shown schematically in **Figure 6-8**. When the height of the brushes is approximately in the range of the particle size, 13-15 nm for example, a layer of particles forms in which there is a low degree of aggregation. However, when the height of the polymer increases, it becomes possible to accommodate a large number of particles, leading to an increase in the degree of aggregation.

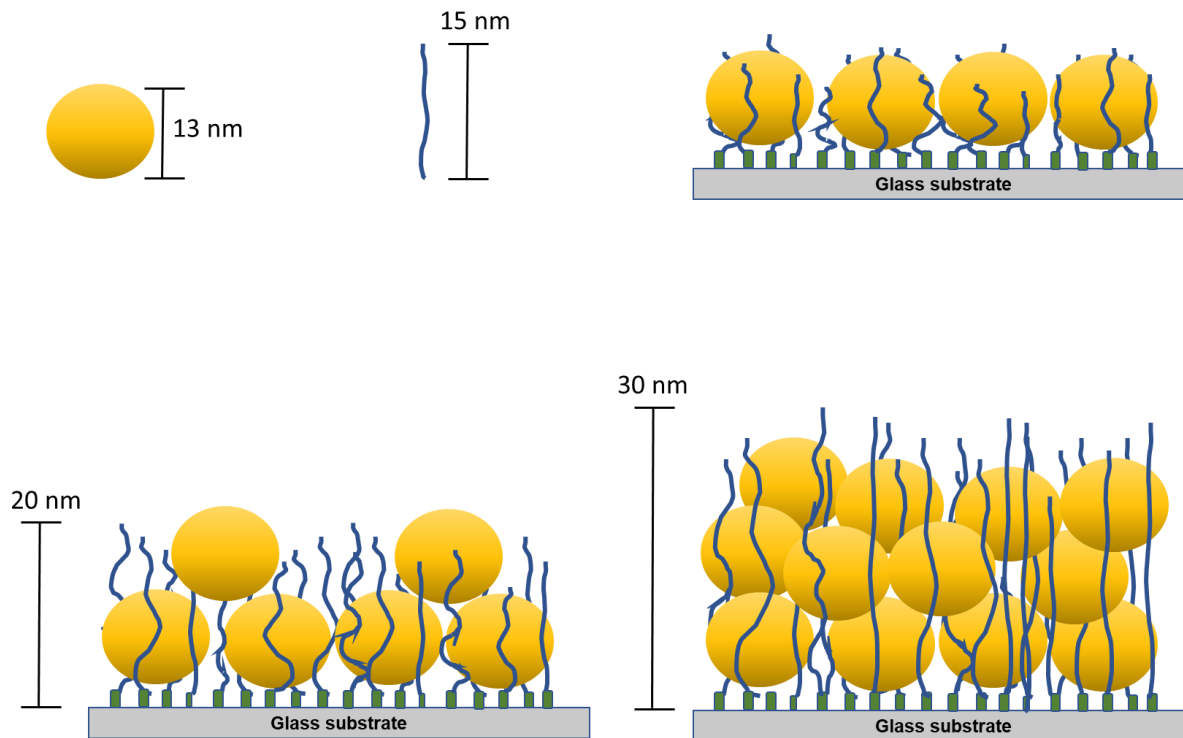


Figure 6-8: Schematic illustration of AuNPs embedded into PDMA brushes with different thicknesses ranging from 15 to 30 nm.

PDMA brushes were formed via 15 min ATRP and functionalised by incorporation of AuNP, before being characterised by spectroscopic ellipsometry in air. The glass substrate was modelled as BK7 glass from the standard material library contained in the CompleteEase software. A Cauchy dispersion model was used for modelling the non-absorbing BIBB-APTES initiator. AuNPs embedded PDMA layer were described as a mixed layer and modelled using the effective medium approximation (EMA). The first material in the EMA layer was PDMA with refractive index of ca. 1.53. The second material in the EMA model was the AuNPs. This optical multilayer-box-model is schematically illustrated in **Figure 6-9**. More details about this model can be found in Chapter 3.

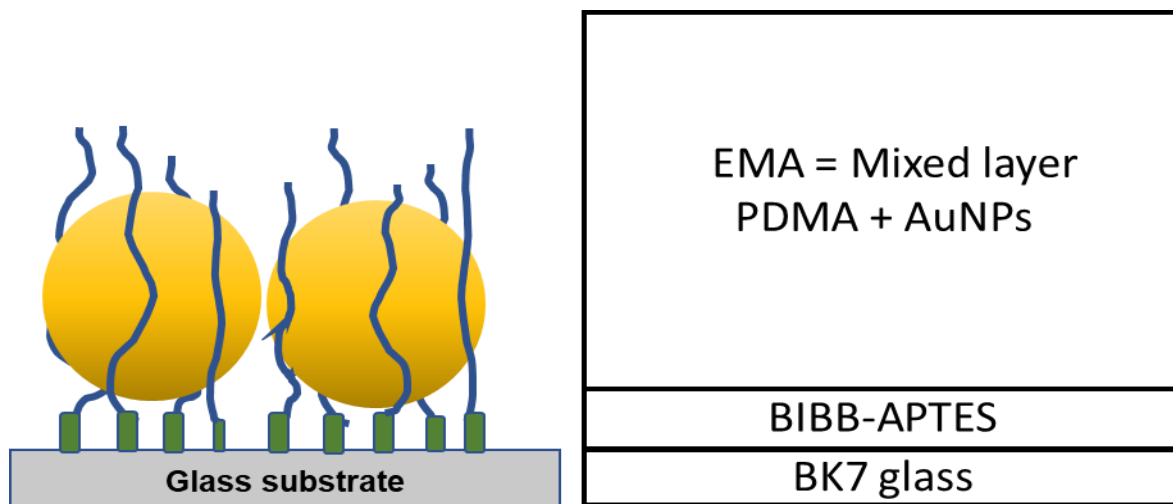


Figure 6-9: The multilayer-box-model used for ellipsometry data fitting of AuNPs-functionalised PDMA.

Approximately 15 nm to 17 nm thick layer of AuNPs-functionalised PDMA brushes was obtained. Combining this observation with the average particle size estimated from AFM image as shown above, it is reasonable to assume that a dense film of particles one particle thick was successfully incorporated into PDMA chains. Also, ellipsometry delta and psi spectra of AuNPs-functionalised PDMA measured at angle 75° exhibited a single plasmon peak at 525 nm with shoulder peak at around 630 nm without any significant shift or emergence of new peaks due to the presence of only one type of resonance frequency belong to AuNPs, see **Figure 6-10**. This observation is in a close agreement with absorption measurements shown above in **figure 6-6**.

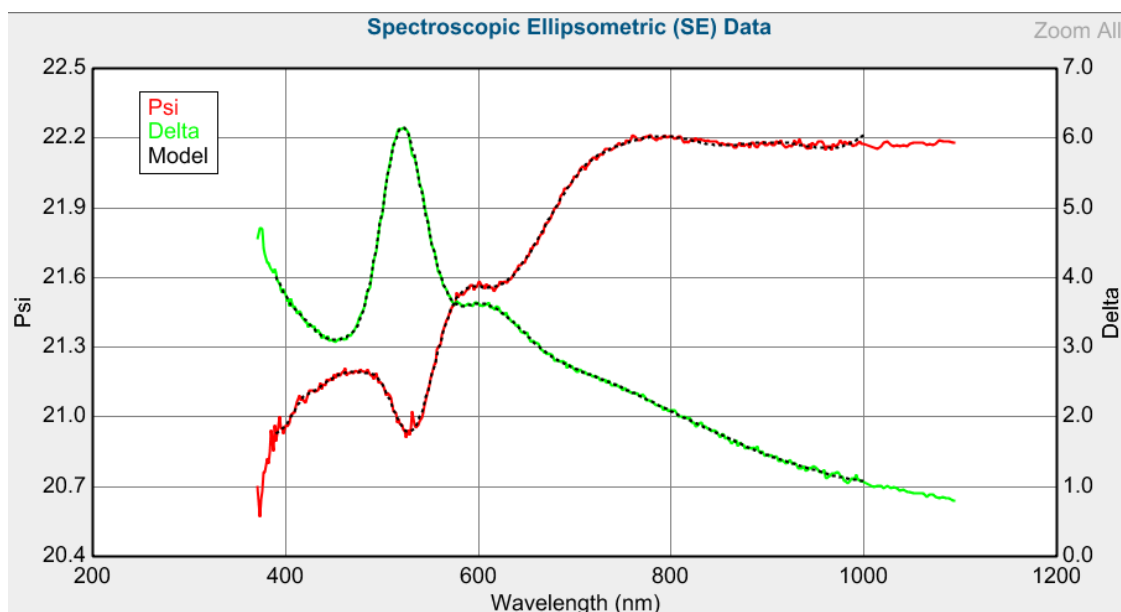


Figure 6-10: Spectroscopic ellipsometry Psi and Delta spectra acquired for AuNPs-functionalised PDMA brush.

To investigate the distribution of AuNPs in the brush films, tapping mode AFM was employed. **Figure 6-11a** shows a tapping mode topographical image of an unmodified PDMA brush film. The surface appears to be completely covered with polymer. The root-mean-square (rms) roughness was measured to be ca. 0.5 nm. **Figure 6-11b** shows tapping mode image of a similar film after immersion in a suspension of AuNP for 4 h. Isolated particles are clearly resolved, embedded within the polymer film. **Figure 6-11c** shows an AFM image of similar PDMA film after immersion in the nanoparticle suspension for 24 h. Now, isolated particles are no longer observed; instead, the image reveals a close packed layer of AuNP. The surface morphology become rougher after incorporating Au NPs into the brush layer with root-mean-square (rms) roughness of 4.2 nm after 24 h immobilization time.

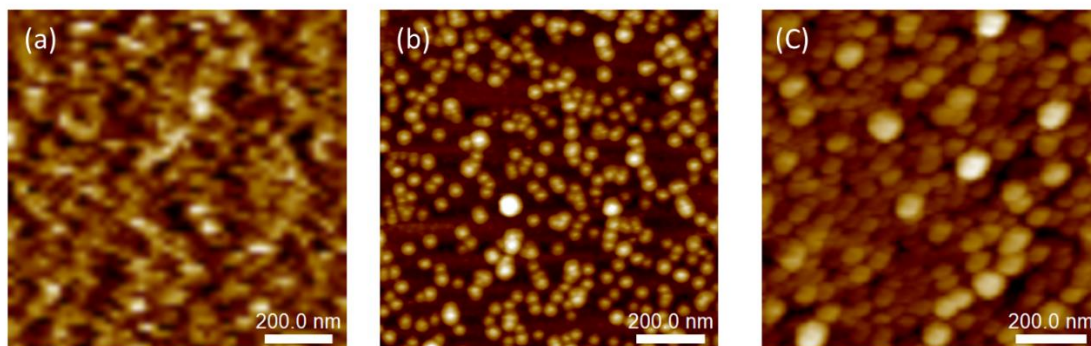


Figure 6-11: (a) PDMA brush grown from glass substrate via ATRP. (b) AuNPs-embedded PDMA brush with immobilisation time of 4 h. (c) AuNPs-embedded PDMA brush with immobilisation time of 24 h.

6.3.3 Attachment of *chlorophyll* to AuNPs-PDMA structure

To examine the possibility of attaining the efficient and fast transfer of energy in the synthesised *Chla*-functionalised PDMA complexes, AuNPs were firstly incorporated into PDMA brushes, then the brushes were functionalised by *Chla* molecules. A possible mechanism is that AuNPs are packed within the polymer chains, then *Chla* molecules are bound to the chains through coordinate bonds in close proximity to the plasmonic AuNPs allowing possible interaction as represented by the schematic diagram in **Figure 6-12**.

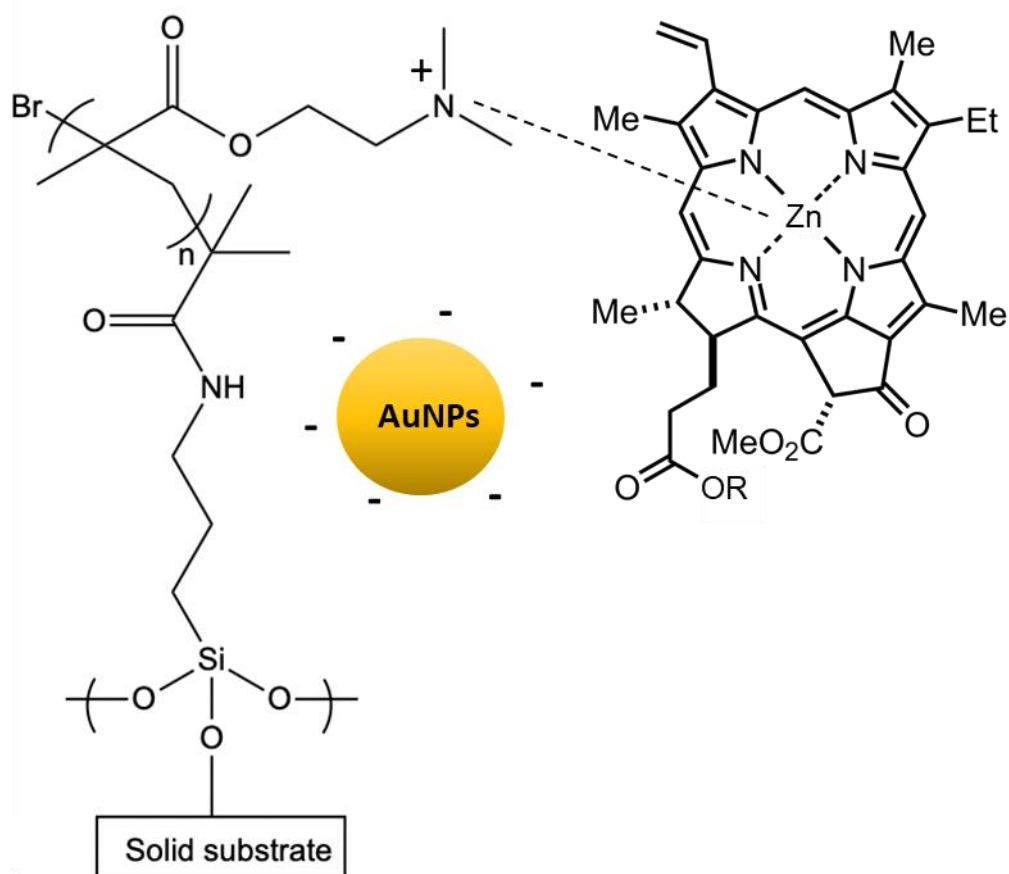


Figure 6-12: Schematic diagram showing the proposed structure of plasmon-exciton coupling in AuNPs-ZnChla supported by PDMA brushes.

The optical properties of AuNPs-embedded PDMA functionalised with *ZnChla* were characterised by absorption spectroscopy. Surface analysis of this system was carried out using spectroscopic ellipsometry, AFM and XPS. **Figure 6-13** shows the extinction spectra of AuNPs adsorbed onto PDMA brushes before (blue) and after attachment of *ZnChla* from a 100 μM suspension (red) to the plasmonic films. The spectra are shown as a function of energy, rather than wavelength. As shown in this graph, the plasmon band was redshifted to about 2.21eV. In addition to this redshift, a new shoulder peak has emerged at 2.48 eV. The redshift is attributed to the presence of *chlorophyll* molecules on the surface, which leads to change dielectric environment surrounding the plasmonic particles. The origin of the peak at 2.48 eV

(**Figure 6-13 red spectrum**) is not clear, but it was not observed when films were formed using lower concentrations such as 50 μM . At these lower concentrations, the peak at 2.21 eV associated with aggregation was also diminished. (**Figure 6-13 green spectrum**). This feature could possibly be attributed to weak plasmon-exciton coupling resulting from the interference between the plasmon resonance of AuNPs and the vibrational transitions of *ZnChla* along visible range, but this peak is not attributed to the concentration effect as it appears at 1.93 eV. However, strong plasmon-exciton interaction is not possible due to the large separation between maximum absorption resonance of AuNPs at 2.39 eV and absorption maxima of *ZnChla* at 1.86 eV.

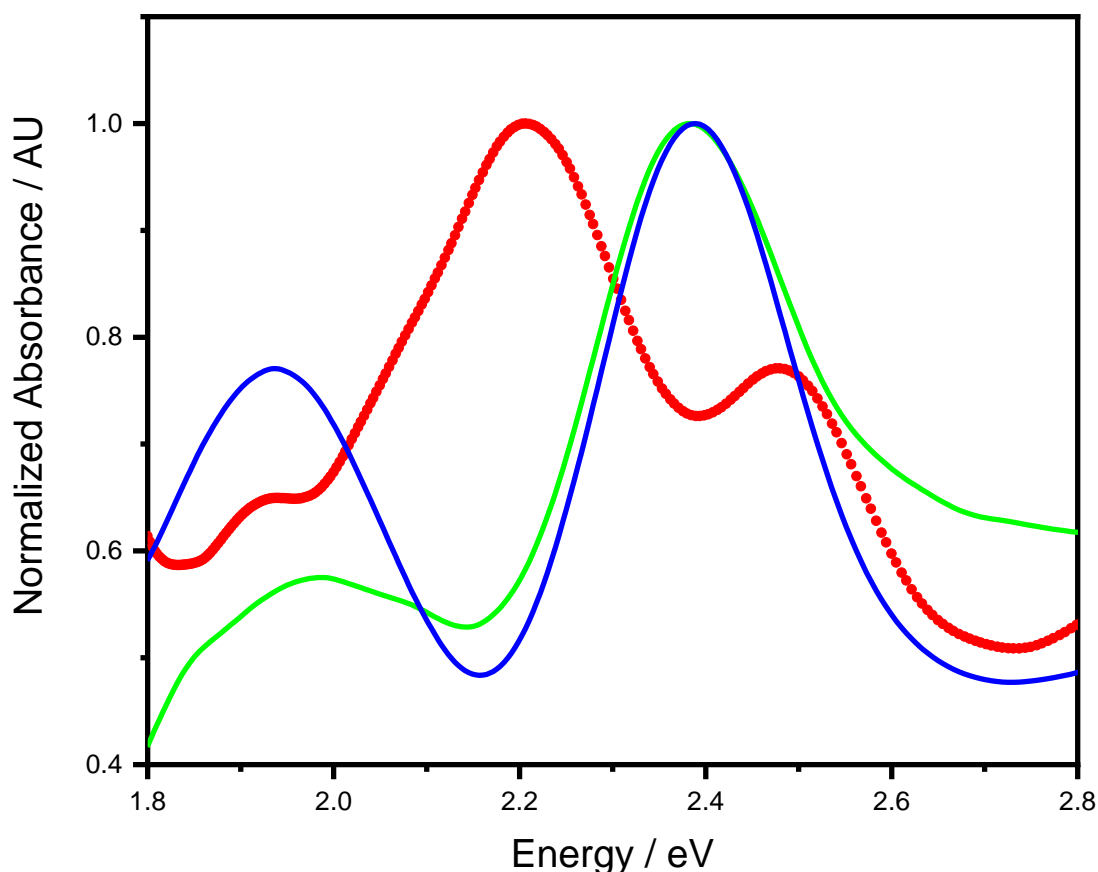


Figure 6-13: Extinction spectra of AuNPs-embedded PDMA brushes before the attachment of *ZnChla* (blue), and after the attachment of *ZnChla* with concentration of 100 μM (red) and concentration of 50 μM (green).

The optical observations obtained by Uv-vis analysis were confirmed by ellipsometry measurements. Ellipsometric amplitude (ψ) spectra of AuNP-functionalised PDMA before and after the addition of *ZnChla* were collected at variable incident angles ranging from 57 to 69. Before the addition of *ZnChla* on the system, there is only one peak at 499 nm measured at the angle of 68° corresponding to the plasmon resonance of AuNPs. This peak was gradually shifted along the range of incident angles to reach 515 nm with a broad shoulder at 590 nm at the incident angle of 58°, which was attributed to the aggregation of the particles, see **Figure 6-14a**. Ellipsometric data obtained after the addition of *ZnChla* showed new characteristics that differ from those of the surface before the addition of *chlorophyll* discussed above, see **Figure 6-14b**. Here, a shift in the position of the plasmon peak of AuNPs (from 495nm to 520nm) was observed. In addition to this, a new peak (at 431 nm) was observed at the incident angle of 68°, which was shifted to 440 nm at the incident angle of 57°. This peak could be attributed to the effect of *ZnChla* transitions on the plasmon band. Also, small features were observed at 669 nm without any shift along the range of the incident angles, which could be the Qy band of the *ZnChla*.

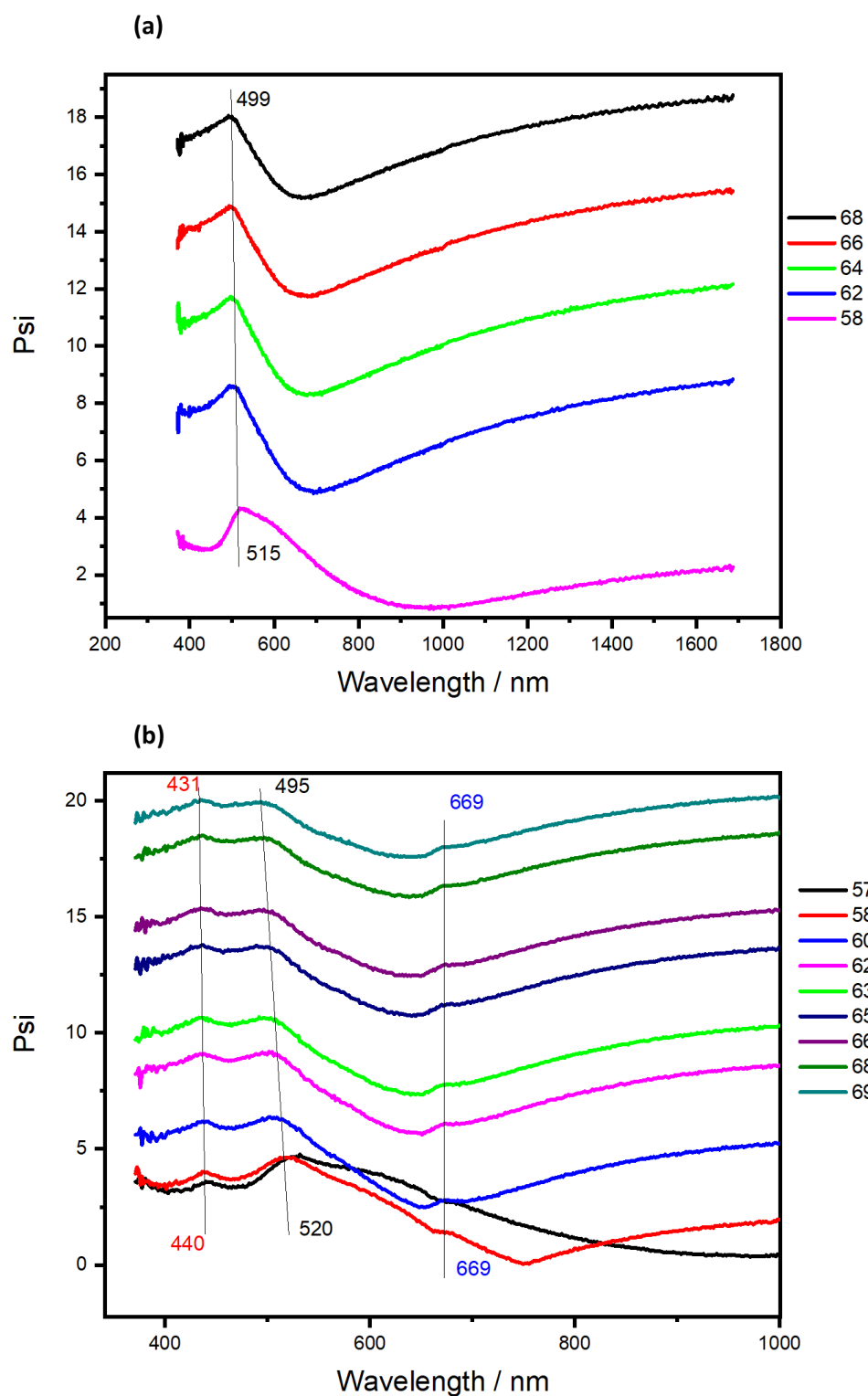


Figure 6-14: Spectroscopic ellipsometry amplitude (Ψ) spectra collected from AuNPs-functionalised PDMA brushes at variable incident angles ranging from 57 to 69, before the attachment of ZnChla (a) and after the attachment of ZnChla (b).

XPS studies of *ZnChla* attached to AuNPs-functionalised PDMA confirm the presence of *ZnChla* on the surface, which was evidenced by the appearance of Zn 2p peak at 1022 eV, see inset Zn 2p spectrum in **Figure 6-15**. The percentages of Zn 2p were diminished from 0.5 to 0.3% by reducing the concentration of *ZnChla* solution from 5.9 μM to 0 μM . At the concentration of 0 μM , the percentage of Zn observed on the surface was 0.08% which attributed to the Zn from glass substrate, see **Figure 6-15**.

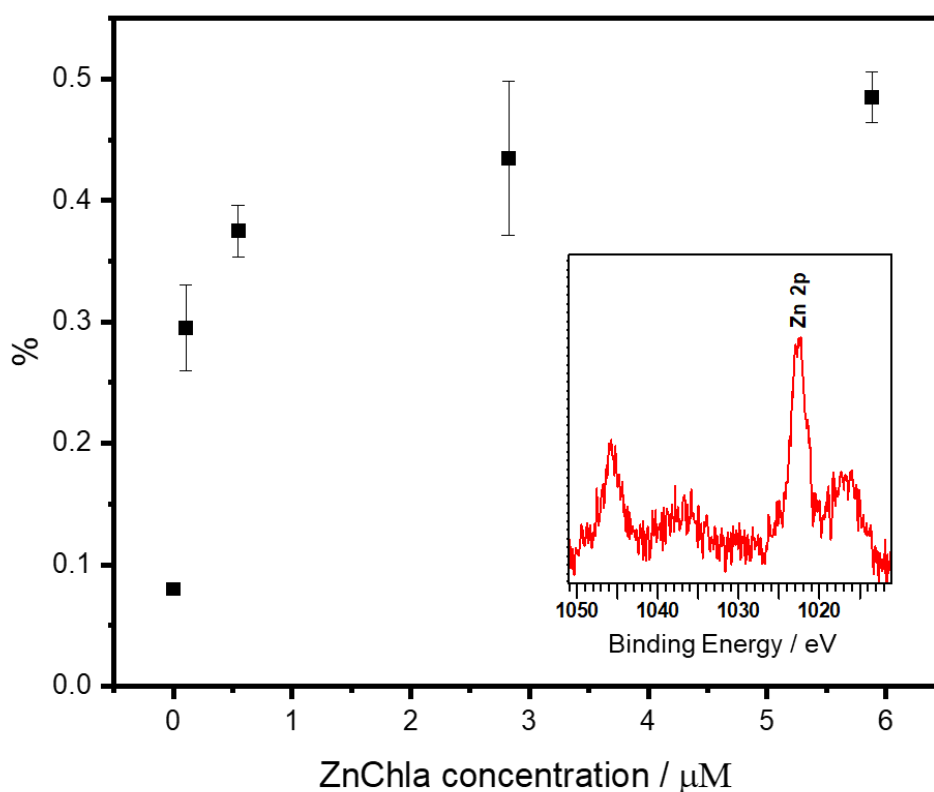


Figure 6-15: Zn 2p percentage measured by XPS analysis of AuNPs-embedded PDMA brushes after the attachment of ZnChla with different concentrations ranging from 0 μM to 5.9 μM . The inset graph is Zn 2p spectrum collected from AuNPs-embedded PDMA brushes after the attachment of ZnChla with concentration of 100 μM .

Ellipsometry data obtained after the attachment of *ZnChla* were modelled. The substrate was modelled as BK7 glass. A Cauchy dispersion model was used for modelling the non-absorbing BIBB-APTES initiator. *ZnChla* attached to AuNP-embedded PDMA layer was

described as a mixed layer and was modelled as EMA with graded layer to find out the distribution of the *chlorophyll* across the scanned area. The first material in EMA layer is PDMA with refractive index of ca. 1.51. The second material in EMA is AuNPs. The third material is *chlorophyll a*. This optical multilayer-box-model is schematically illustrated in **figure 6-16**. More details about this model can be found in Chapter 3.

The thickness of the film was measured here to be approximately 17 nm. *Chlorophyll* is more concentrated at the bottom than at the middle and top of the scanned area with percentage of .8.2%, 3.1% and 2.4%, respectively.

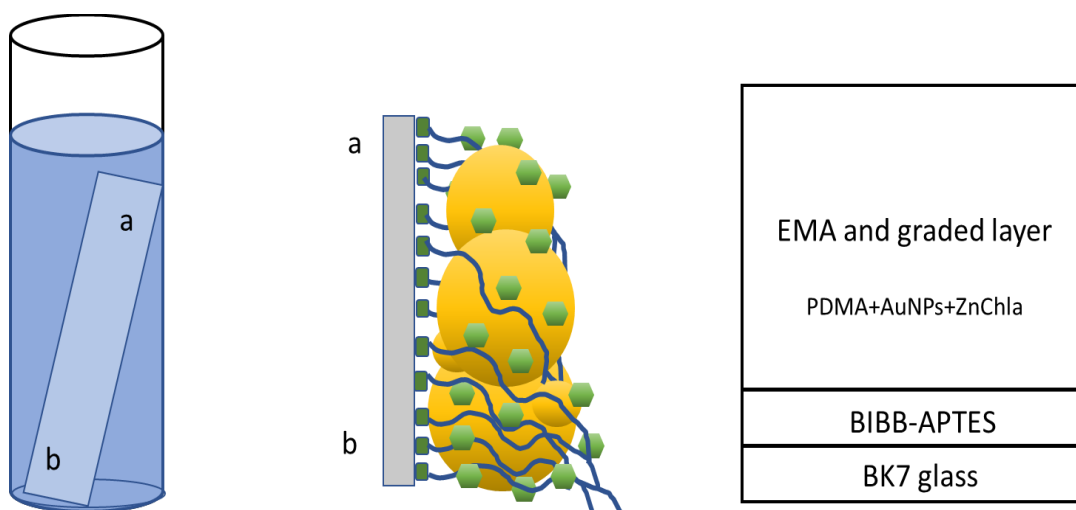


Figure 6-16: Multilayer-box-model used for ellipsometry data fitting of AuNPs-functionalised PDMA after the addition of ZnChla.

The distribution of *ZnChla* molecules was investigated by AFM height and phase tapping mode images as shown in **Figure 6-17**. *ZnChla* was found to be distributed over the surface with partial formation of blobs over the surface. The diameter of formed *ZnChla* blobs was estimated as 40 - 55 nm.

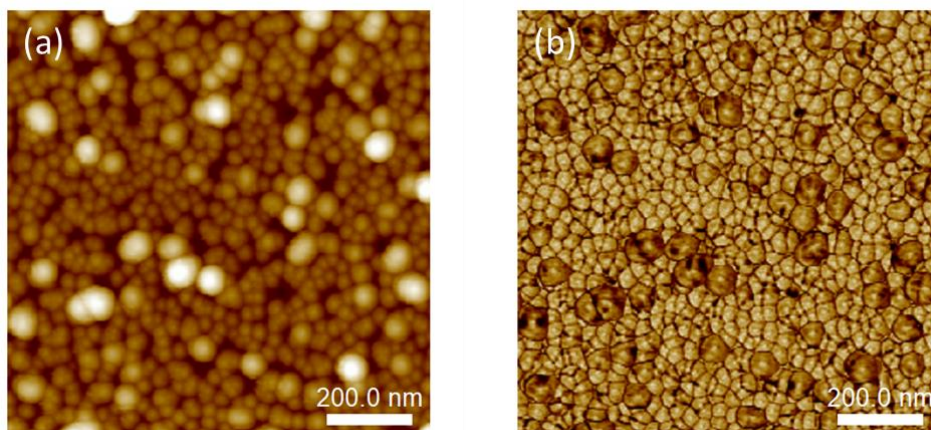


Figure 6-17: AFM tapping mode images of AuNPs-embedded PDMA brushes after the attachment of ZnChla. (a) Height image and (b) Phase image.

6.4 Conclusion

AuNPs with average particle size of 13 nm were successfully prepared in a single reduction step. Sodium citrate was chosen to act as a reducing agent and capping agent simultaneously. Incorporation of AuNPs into PDMA brushes was controlled via immobilisation time. Full coverage of AuNPs was achieved by incubation PDMA samples in AuNPs solution overnight. However, no strong plasmon-exciton coupling was achieved by attachment of *ZnChla* to the system. This most likely attributed to the long distance between AuNPs maximum plasmon resonance and maximum excitations resonances of *ZnChla*. The observed splitting of absorption band in the obtained result could be attributed to the interference between AuNPs maximum plasmon resonance with the vibrations along the range of *Chla* absorption between Soret band and Q bands. A further possibility that could be considered is that apparent splitting results from Fano coupling (previously mentioned in the introduction) between nanoparticles in close-packed films.

CHAPTER 7: ALUMINIUM NANOPARTICLE FILMS

7.1 Introduction

Aluminium is a promising candidate metal for nanoplasmonics. It is one of the most abundant elements on earth and is employed extensively in a variety of consumer goods applications.^[100] Thus, for mass-production of plasmonic devices, it offers substantial economic relative to gold and silver, and it is not subject to concern about that are significant for noble metals. Aluminium is a relatively economical and manipulatable material facilitating the mass production. Furthermore, aluminum has a plasma frequency that is higher than that of gold or silver, which effectively enables the material to exhibit large surface plasmon responses in the ultraviolet (UV) region of the spectrum, as opposed to gold or silver, which normally exhibit visible plasmons. This is pertinent, for instance, to the use of plasmonics techniques in the detection of organic and biological systems that exhibit potent UV absorptions as well as in photocatalysis^[95]. However, AINPs are known to oxidise rapidly, which diminishes its optical characteristics. When an Al particle or Al layer is exposed to air, a native coating of alumina (Al_2O_3) forms on the surface within a few minutes.^[95] The LSPR of AINPs is predicted to be redshifted by formation of an oxide shell that alters the dielectric characteristics of the nanoparticle environment, while the metallic core that is projected to undergo a spectral blue shift due to volume contraction as the oxide layer thickness increases. The total detected LSPR signal is determined by the balance of these two effects.^[100]

The goal of this chapter was to form Al nanoparticles AINPs and to try to modify their plasmon energy so that they resonate with the solet transitions in *Chla* (2.84 eV). The starting point was a well-established method for NP synthesis expected to yield particles with plasmon energy of 0.21 eV. It was then hoped to modify the synthesis route to produce particles with similar plasmon energies. To achieve this, AINPs will be prepared by chemical decomposition of alane complexes by titanium isopropoxide. Also, sono-solvo chemistry will be used to modify

the plasmon energies of AINPs. The produced AINPs by both ways will be imbedded into the brushes by immersing surface-grafted PDMA samples in the solution of AINPs for certain time.

7.2 Materials and methods

7.2.1 Materials

Quartz cover slip slides, fused, (25.4*25.4*0.25mm) were supplied by Alfa Aesar. Titanium isopropoxide (97%), alane N,N-dimethylethylamine complex, 0.5 M in toluene, 1,2-epoxyhexane (97%) were purchased from Sigma Aldrich. Toluene (99.8% HPLC) was supplied by Fisher Scientific. Dry toluene and dry diethyl ether were obtained from an onsite Grubbs dry solvent system. All these materials were used as received without any further purification.

7.2.2 Samples cleaning and handling

Quartz cover slip slides were cleaned as described in chapter 3. The substrates were immersed in Piranha solution (30% H₂O₂: 98% H₂SO₄, 1:3, v/v) for 2 h. Caution: *Piranha solution can result in a violent reaction with organic matter and should be handled with extreme caution!* Then, the slides were washed several times with deionised water and dried in piranha oven overnight. The slides were cut into small pieces with appropriate size depending on the used characterisation technique and handled using a clean tweezers and kept in Eppendorf tubes until use.

7.2.3 Synthesis of BIBB-APTES films

BIBB-APTES films were prepared in two steps. Detailed description can be found in chapter 3. Briefly, 2% solution of APTES in ethanol is used to functionalise quartz substrates to form APTES films. This was followed by the attachment of BIBB to form Bromine functionalised initiator.

7.2.4 Growth of PDMA via ATRP

PDMA brushes were grown from BIBB-APTES initiated quartz cover slip slides substrates as mentioned with more details in chapter 3. Briefly, DMF was used as a good solvent for DMA

monomers. HMTETA and Cu(I)Br were used to catalyse ATRP reaction at 90 °C. Then 4 mL of monomer/ catalysts solution was added onto each initiator sample in Schlenk tubes. The reaction was performed at nitrogen atmosphere. The growth of PDMA was allowed to proceed for the desired polymerisation time. The polymerisation was terminated by removing the slide from the mixture.

7.2.5 Synthesis of quaternised PDMA (q-PDMA)

Quaternised PDMA (q-PDMA) were prepared by immersing previously prepared PDMA-coated quartz cover slip slides in a freshly prepared solution of 1-iodooctadecane for around 18 h at room temperature. More details can be found in chapter 3.

7.2.6 Extraction and derivatization of *chlorophyll a*

A detailed description of *ZnChla* synthesis can be found in chapter 3. Briefly, *chla* was extracted from spinach leaves by acetone. Then, extracted *chlorophyll a* was converted into pheophytin a (dark blue pigment) by dissolving the dark green pigment in acetic acid under stirring for 3 h. Then, zinc acetate dehydrate dissolved in methanol was used to convert pheophytin into *ZnChla* under reflux in argon atmosphere at 35 °C for 1 hour.

7.2.7 AINPs synthesis

7.2.7.1 chemical decomposition

In Schlenk system, 13 mL of alane N,N-dimethylethylamine complex was mixed with 25 mL of dry ethyl ether. A freshly prepared titanium isopropoxide solution was used to decompose alane complex, which leads to change the colour of the mixture to a dark brown, promptly, indicating the formation of AINPs. 1,2-epoxyhexane was used to form capping layer to coat the prepared AINPs. More details can be found in chapter 3.

7.2.7.2 Sono-Solvo chemistry

Small pieces of Al foil were sonicated in a mixture of 60 mL ethanol and 30 mL of ethylene glycol using ultrasonic bath at 50 °C for 6 h. The large parts were allowed to precipitate overnight. The supernatant was collected into round bottom flask that was connected to Schleck system. After the removal of ethanol under vacuum at 110 °C, 10 mL of ethylene glycol was added to the mixture. The reaction was allowed to proceed under 197 °C for 14 days. The produced AINPs was extracted in ethanol and centrifuged to remove the large particles.

7.2.8 Incorporation of AINPs into brush films

PDMA-coated glass substrates prepared as described previously were immersed in AINPs solution for the desired immobilization time using 1.5 mL Eppendorf tubes. The reaction was allowed to proceed in the dark at room temperature to form glass-BIBB-APTES-PDMA-AINPs layers. Then the samples were rinsed with diethyl ether and dried by nitrogen stream. AINPs-functionalised PDMA brushes were analysed by UV-Vis spectrophotometer, AFM and XPS.

7.2.9 Attachment of *ZnChla* to PDMA-AINPs system

ZnChla was attached to AINPs-functionalised PDMA brushes by immersion of the samples (glass-BIBB-APTES-PDMA-AINPs) in solution of *ZnChla* for 24 h in the dark at room temperature to form glass-BIBB-APTES-PDMA-AINPs-*ZnChla* structures. Then the samples were rinsed with diethyl ether and dried by N₂ stream. *ZnChla*-functionalised systems were characterised by UV-Vis spectrophotometer.

7.2.10 Surface analysis

A Cary 50 UV-vis spectrophotometer was used to obtain extinction spectra in the range 190 – 800 nm, unless otherwise is stated. *ZnChla* samples were measured in a standard quartz cuvette with 10 mm optical path length at room temperature at least 2 times. The solid samples

were measured in air. Air measurements were conducted using home-made PTFE sample holder which was allowed to perform measurements of the same area on the surface during all experimental stages.

X-ray photoelectron spectroscopy (XPS) spectra were obtained using a Kratos Axis Ultra/Supra spectrometer (Kratos Analytical, Manchester, UK). All binding energies were calibrated relative to the 285 eV calibrated primary hydrocarbon C 1s signal. XPS data were analysed using the CASAXPS (v. 2.18) software.

AFM images were obtained using a Digital Instruments (Nanoscope 5 Multimode Atomic Force Microscope), (Veeco, Santa Barbara, CA) fitted with a “J” scanner (0–125 μM). All measurements were conducted in air at room temperature. AFM data analysis was performed using NanoScope (v 1.5) Analysis software.

Water contact angles measurements were performed using a Rame Hart sessile-drop model 100-00 goniometer. The obtained contact angle values are the mean of at least three different measurements.

7.3 Results and discussion

AINPs were synthesised by reacting titanium isopropoxide with alane complex under nitrogen atmosphere at room temperature. This reaction follows Buhro's method as represented by the following equation,



Titanium isopropoxide acts as a decomposing agent.^[201] The formed NPs are spherical particles with high pyrophoric property. To reduce the pyrophoricity of AINPs, they were capped with polyether. The resulting AINPs are negatively charged due to the presence of the oxygen atoms, where the epoxide reacts with Al, which initiate the polymerisation of the polyether by opening the ring of the epoxide leading to continuous propagation of the polymerisation reaction. Strong Al-O bonds are formed by linking the first oxygen with Al.^[201] Although there are different methodologies that have been utilised to produce AINPs as noted in the introduction, decomposing alane complexes by titanium isopropoxide was chosen because it enables the production of AINPs that are to some extent comparable to AuNPs in terms of size and shape. This was important because of the goal of trying to embed the particles in a surface-grafted polymer film in a similar way of embedding AuNPs within PDMA brushes.

Figure 7-1a shows simplified visualization of the produced AINPs. After the stabilization of AINPs with polyether, the solvent was removed to enable the measurements of extinction spectra in water. Polyether-capped AINPs shows strong absorption in deep UV spectral range at 265 nm with 1 nm blueshift for 1:1 diluted AINPs solution in water as shown in **Figure 7-1b**.

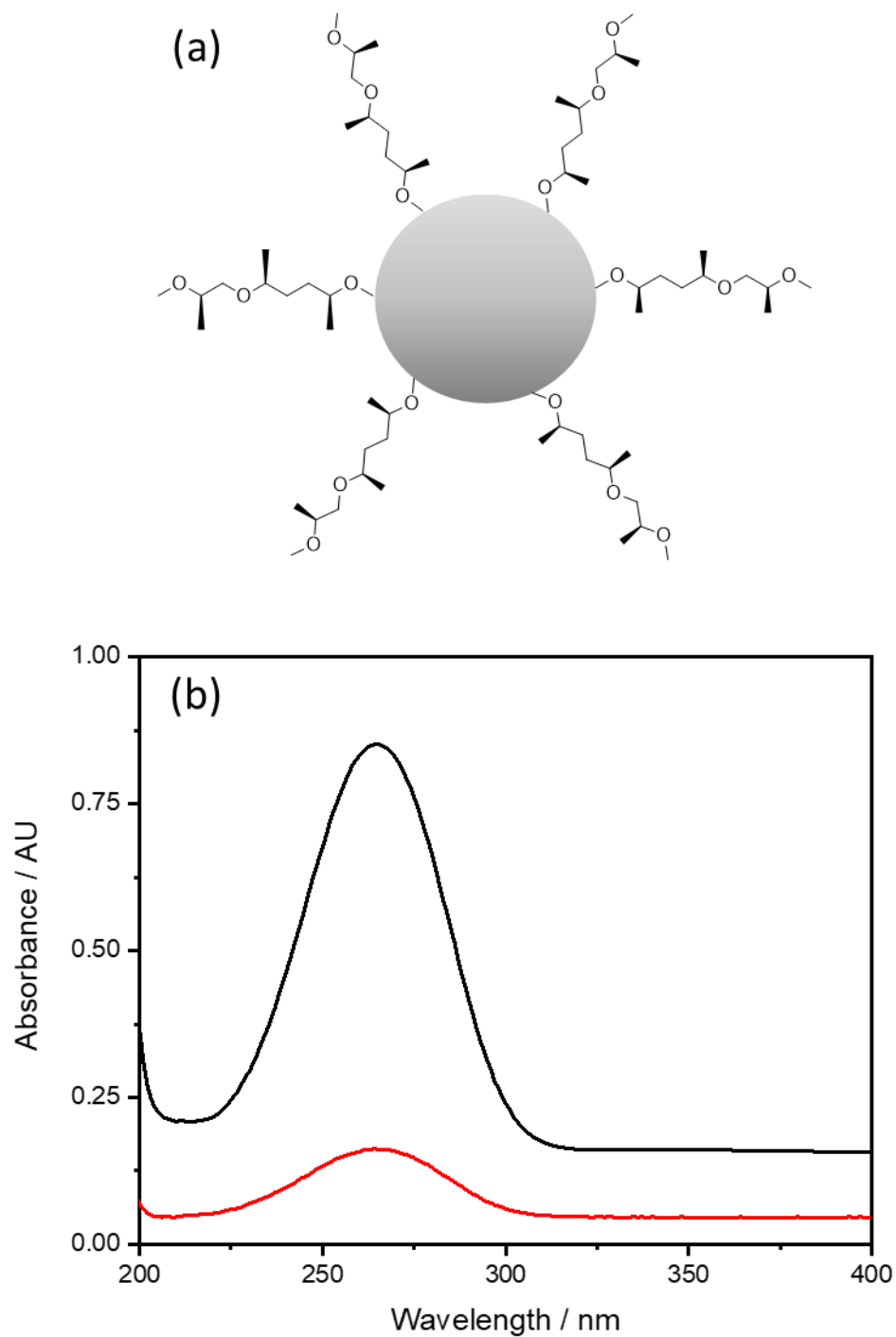


Figure 7-1: (a) proposed structure of single AINP prepared by alane decomposition and coated by polyether molecules. (b) Extinction spectra of AINPs in water. The black spectrum was acquired for a concentrated solution and The red spectrum for diluted solution.

To investigate the sensing properties of the produced AINPs and obtain refractive index sensitivity m ($m = \Delta\lambda_{LSPR} / \Delta n$), extinction spectra of AINPs were collected in air, water, ethanol, isopropanol, DCM and chloroform with refractive index of $n = 1, 1.33, 1.36, 1.38, 1.42, 1.44$, respectively. As expected, as the refractive index of the surrounding medium increased, the resonance peaks of AINPs redshifted indicating that the produced AINPs were sensitive dielectric environment. **Figure 7-2** shows the linear relationship between the refractive index of the medium and the resonance peaks of AINPs. The slope of the line, $m = 145.5$ nm/RIU (refractive index unit), is the refractive index sensitivity factor for the produced AINPs.

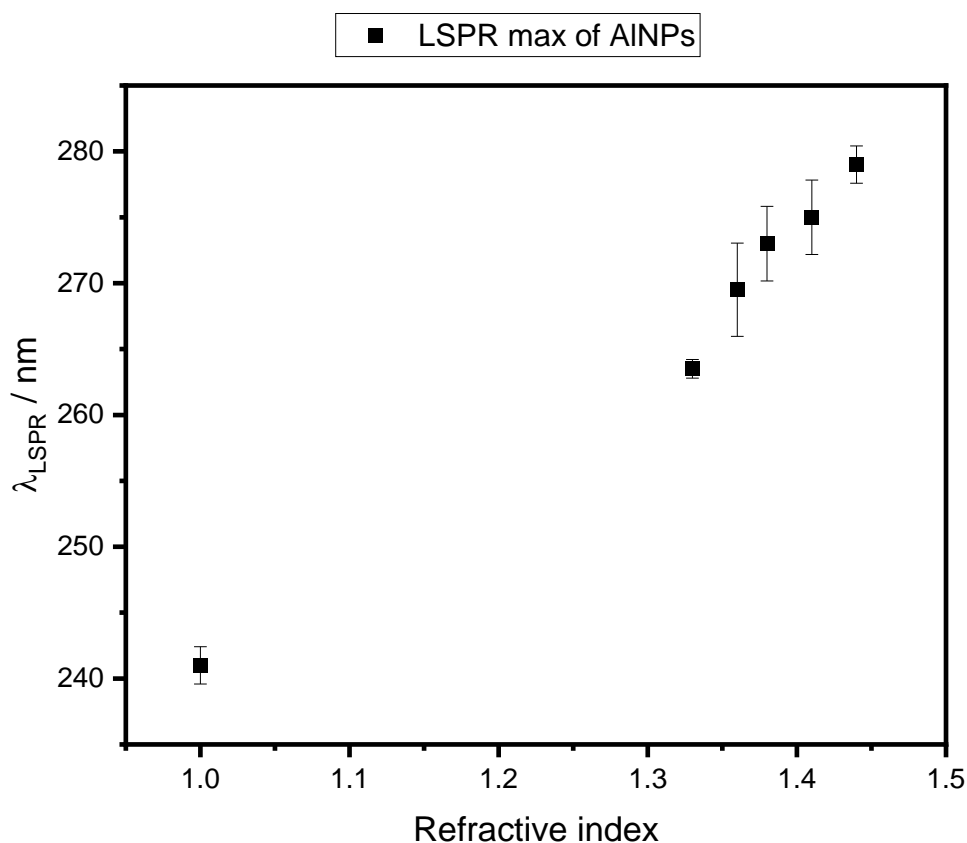


Figure 7-2: Refractive index sensitivity of the produced AINPs in different solvents.

7.3.1 Incorporation of AINPs into PDMA brushes

AINPs were incorporated into PDMA brushes in the same way that AuNPs were added to the brushes. PDMA slides were immersed in AINPs solution for 24 h. AINPs-imbedded PDMA brushes were characterised by XPS, AFM and contact angle. Due to the interference of Al and Br XPS spectra, Al 2p was identified using Br 3d spectrum. XPS Br 3d spectrum of AINPs immobilised onto PDMA brush shows high intensity peak at 74.5 eV with attributed to the presence of AINPs on the surface, while the peak at 70.8 eV was attributed to Br on the end of every repeated unit of the polymer chains, see **Figure 7-3a**. However, to confirm the attribution of the peak at 74.5 eV to AINPs rather than the substrate, Al percentage was measured also using a control sample of piranha cleaned substrate without any further modification. This analysis confirms that the percentage of Al in AINPs-imbedded PDMA brushes sample is much higher than the percentage of Al in unmodified clean substrate, see **Figure 7-3b**.

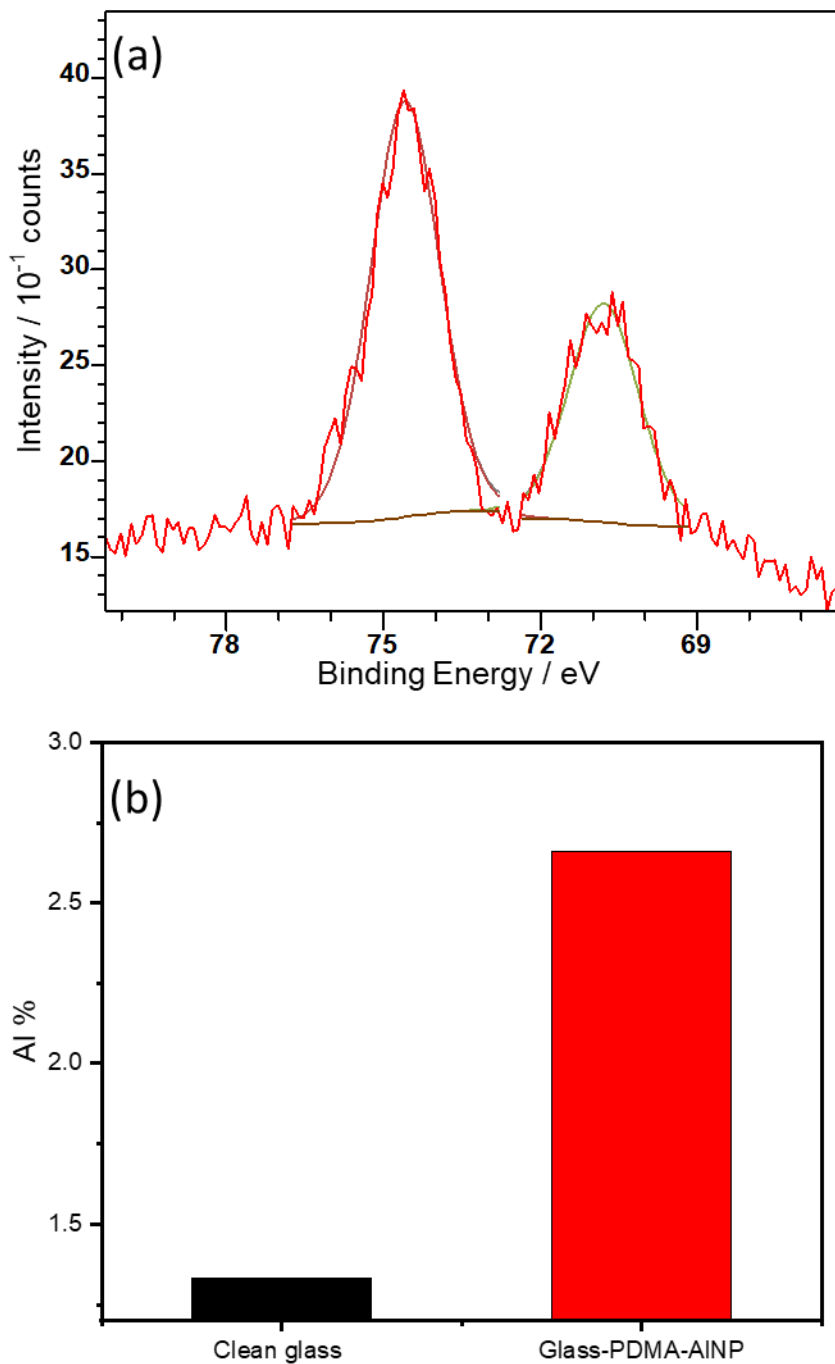


Figure 7-3: (a) XPS Br 3d Spectrum of AINPs incorporated into PDMA brushes showing Al peak at 74.5 eV. (b) AINPs percentage into PDMA brushes (red bar) compared to the percentage of Al of clean glass substrate (black bar).

AINP-embedded PDMA brushes were analysed by AFM. AFM tapping mode height images of AINP-embedded PDMA brushes confirmed the spherical shape of AINP with average particle size of 50 ± 5 nm as shown in **figure 7-4a**. However, observed AINPs in these images can be either single layer with partial coverage on the surface of PDMA brushes or multi-layers and the observed partials are located on the top layer. Although height image suggests that a sub-monolayer is presented, the phase image suggests that a small number of AINPs are adsorbed on top of closed-packed layer of AINPs. Most likely there are multiple layers which were evidenced by large number of indistinct particles underneath the most pronounced particles, see squared area in phase image (**Figure 7-4b**).

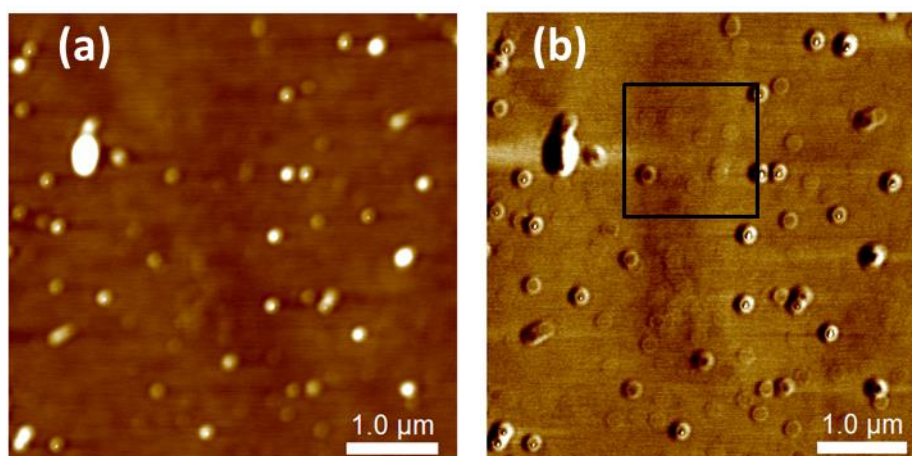


Figure 7-4: AFM tapping mode images of AINPs incorporated into PDMA brushes. (a) height image, and (b) phase image.

Extinction spectra of AINPs-imbedded PDMA brushes were collected in air. **Figure 7-5** exhibits a plasmon peak at 242 nm, shifted from the position measured for particles in solution (265 nm). This low absorbance could be attributed to fact that the particles surrounded by Al_2O_3 layer in air. Further evidence for this explanation is the change of the colour of the sample from grey to white after a very short period of exposure to air, estimated at a few minutes, see the inset photo in **Figure 7-5**.

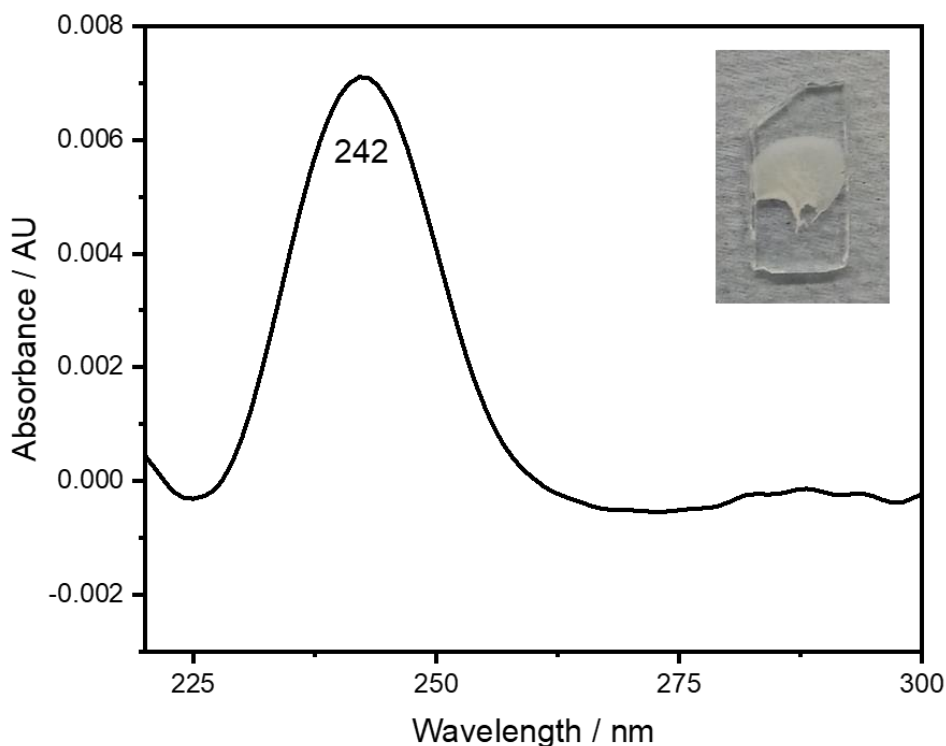


Figure 7-5: Absorption spectrum of AINPs-coated PDMA brush, and inset photo of AINPs adsorbed onto PDMA brush.

The hydrophobicity of the produced AINP-impregnated PDMA brushes was tested by varying the percentage of AINPs in the solution that was used for AINPs immobilization. The hydrophobicity of AINPs-embedded PDMA brushes was increased with increasing percentage of AINPs in the solution to reach maximum at $89^{\circ} \pm 2$ at the percentage of 100%, See **Figure 7-6**. This hydrophobicity is attributed to the hydrophobic polyether capping agent. As the degree of incorporation of AINPs into the PDMA layer increases, the hydrophobic AINPs come to dominate the properties of the film while the hydrophilic PDMA brushes make reduced contribution to the properties of the composite layer.

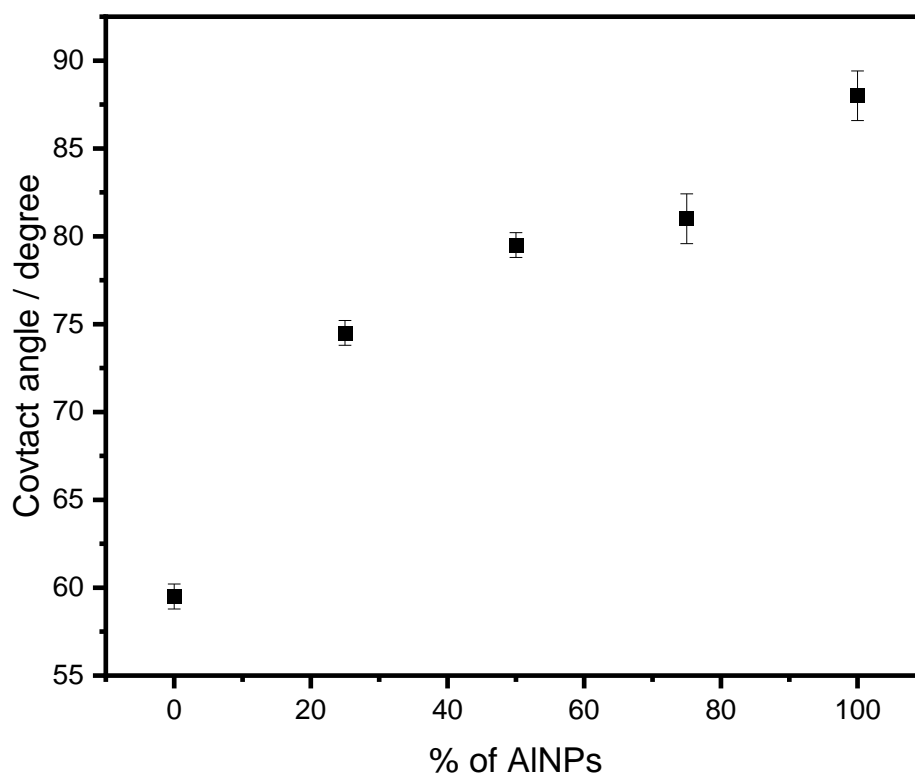


Figure 7-6: Contact angle of PDMA brushes AINP functionalised with AINPs with percentages ranging from 0 to 100%.

The addition of *ZnChla* to AINPs-functionalised PDMA caused absorption spectrum of AINPs to redshift from 242 nm to around 250 nm. However, obtaining a pronounced resonance peak after the addition of *chla* is still a challenge, where only low intensity and high signal to noisy ratio was obtained as shown in **Figure 7-7**.

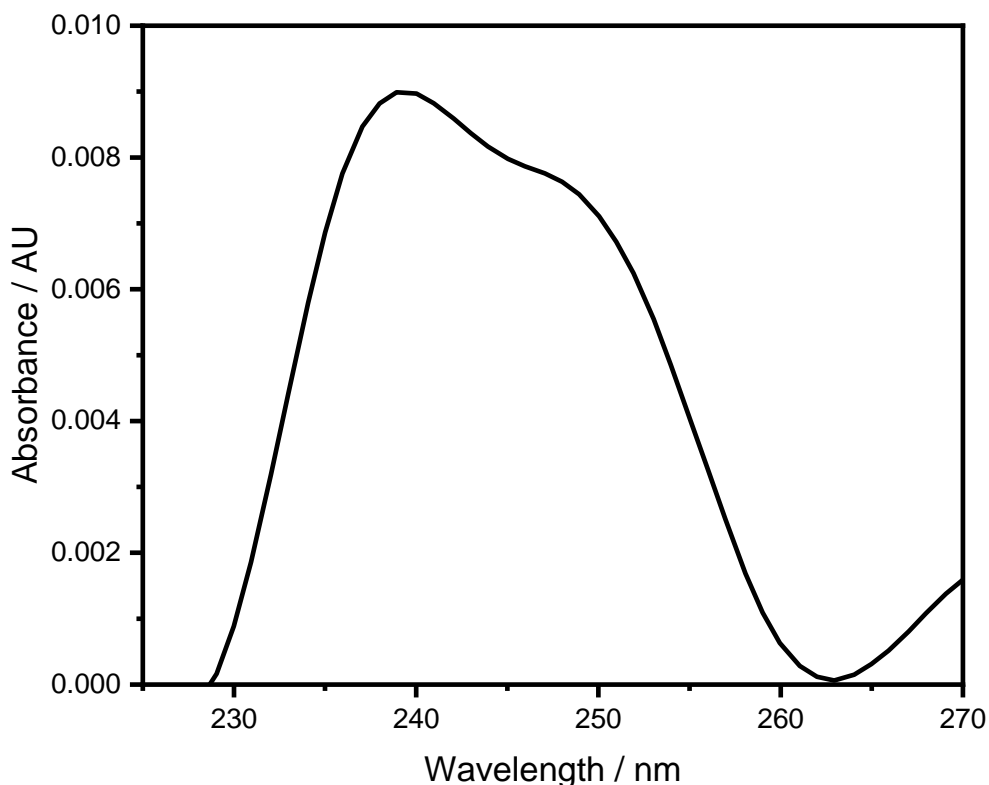


Figure 7-7: Absorption spectrum of ZnChla-functionalised AINPs-coated PDMA brush.

In order to transfer AINPs into more useful practical form by modifying maximum resonance from deep UV region to near visible spectral range, AINPs were instead synthesised following a sono-solvo chemistry method.^[202] Briefly, small pieces of Al foil were sonicated in a mixture of ethylene glycol and ethanol in 2:3 ratio. After removal of ethanol, the formed AINPs were stored in ethylene glycol for 14 days at 197 °C. Then, AINPs were extracted and centrifuged in ethanol. Following this process, dissolved Al ions in ethylene glycol/ ethanol does not show any plasmonic resonance, see **Figure 7-8a**. After 14 days of storing Al ions in ethylene glycol in a nitrogen atmosphere, AINPs were obtained that exhibited a plasmon resonance at 370 nm, as required (**Figure 7-8b**).

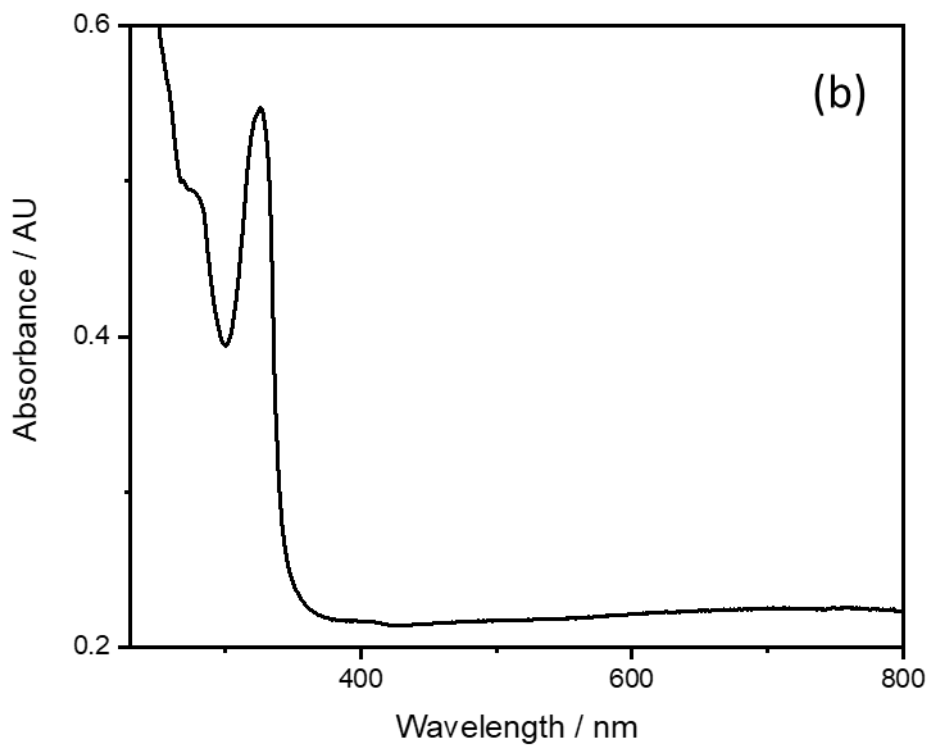
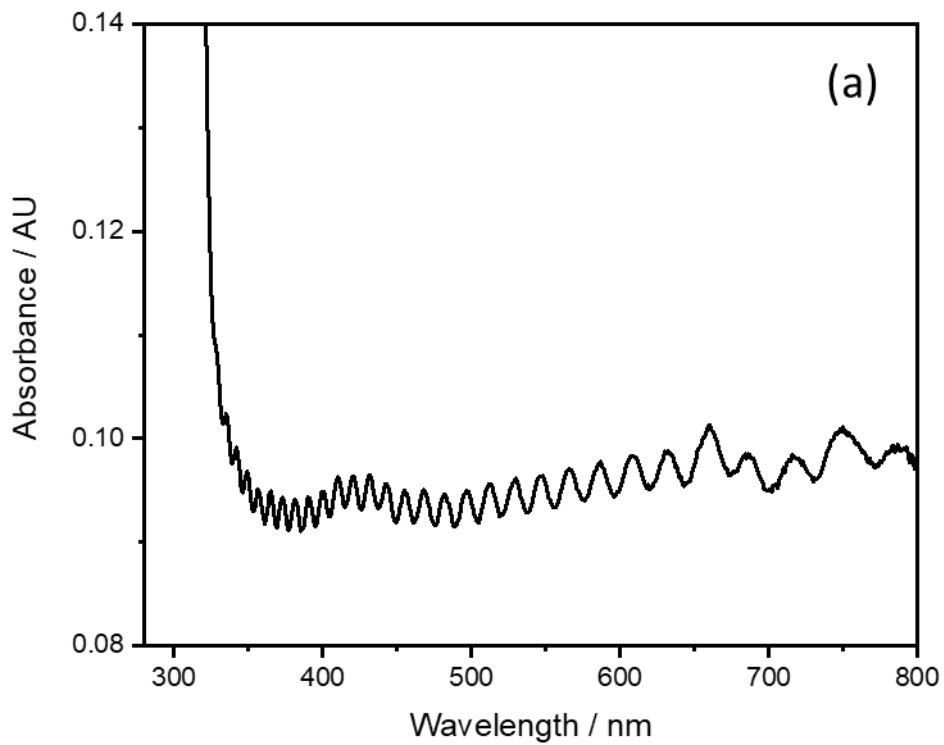


Figure 7-8: Extinction spectra of AINPs synthesised via sono-solvo chemistry (a) after 1 day inoccupation in ethanol/ ethylene glycol mixture. (b) after 14 days inoccupation in ethanol/ ethylene glycol mixture.

AINPs produced by this method are more hydrophobic compared to AINPs produced by decomposition of alane complexes with measured contact angle of $97 \pm 2^\circ$. Thus, it proved in order to incorporate these particles into PDMA films, and a plasmon absorption was not observed, see **Figure 7-9**.

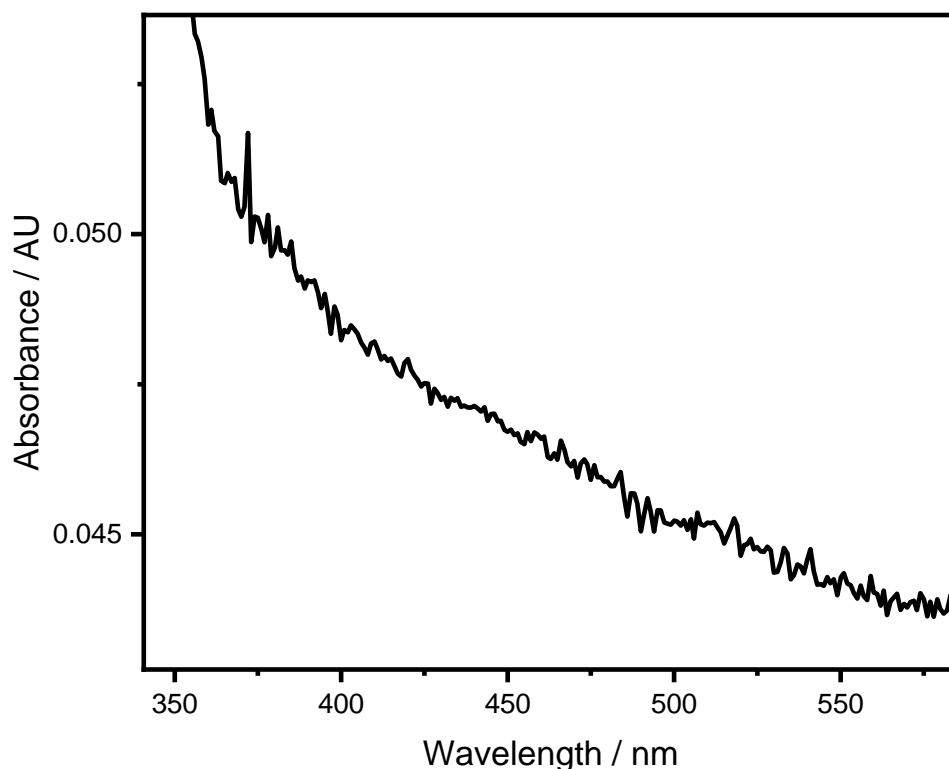


Figure 7-9: Absorption spectrum of AINPs synthesised via sono-solvo chemistry and imbedded into PDMA brush.

To reduce the effect of the hydrophobicity of AINPs, q-PDMA with long hydrophobic octadecyl chains was used. It was hoped that these chains would act as a cushion to imbed the hydrophobic AINPs. Also, as alternative to q-PDMA, polystyrene brushes were grown via ATRP and were used instead of PDMA due to their high hydrophobicity. In addition, long brushes were used to imbed large number of AINPs. In an alternative approach, AINPs were spin coated on to the brush surface using different solvents such as ethanol or acetone. To avoid the oxidation of AINPs, AINPs-functionalised PDMA films were coated with a protective

layer of titanium with different thicknesses. However, no significant enhancement was achieved. This could be attributed to the critically fast (within 1-2 min) formation of Al_2O_3 layers around AlNPs particles that can suppress the optical properties AlNPs.

7.4 Conclusion

AINPs were successfully synthesised via two methods: chemical decomposition and sono-solvo chemistry. In chemical decomposition method, alane complex was decomposed using titanium isopropoxide. The maximum plasmon resonance of AINPs prepared by this method was observed at 265 nm. However, this deep UV plasmon resonance is not ideal for sensing applications. So, sono-solvo chemistry method was used to tune the maximum plasmon resonance from deep UV spectral range to near visible range at around 370.

Although AINPs prepared by chemical decomposition were observed on the top of PDMA layer by AFM images, incorporation of AINPs (either prepared via chemical decomposition or sono-solvo chemistry) into surface-grafted PDMA brushes with controllable plasmon resonance is still challenging. This obstacle most likely caused by the very fast oxidation state that can suppress optical properties as well as high sensitivity and hydrophobicity of AINPs.

CHAPTER 8: CONCLUSION AND FUTURE WORK

8.1 CONCLUSION

In this thesis, PDMA scaffolds are used to support excitonic *chlorophyll a* molecules in order to form plexcitonic antenna complexes. The structures of PDMA brushes and their BIBB-APTES initiators were confirmed by XPS N 1s and C 1s spectra. Ellipsometry measurements reveal that the average height of the initiator is 1 nm, while the heights of the brushes can reach 15 ± 3 nm after 15 min polymerisation time, approaching maximum height of 30 ± 5 nm after polymerisation for 1 h. AFM images of PDMA brushes and their BIBB-APTES initiators confirm the successful growth of the polymer brushes with a good agreement with ellipsometry data.

Adsorption isotherms of *ZnChla* on PDMA were acquired and demonstrated that monolayer coverage is approached using 250 μ M *Chla*. When PDMA brushes are treated with 1-iodooctadecane, the binding of *Chla* is found to be blocked, decreasing as the degree of quaternization increase. These findings are consistent with the hypothesis that *Chla* binding to PDMA brushes is via coordination of the tertiary amine in the pendant groups of the polymer to the metal centre in the *Chla*. There is no shift in the position in the *Chla* absorption bands after binding to PDMA brushes suggesting that the amount of aggregation is negligible. This approach seems to provide a promising approach to the construction of pigment-polymer antenna complexes.

Depending on the successful formation of pigment-polymer antenna complexes by binding *ZnChla* to PDMA, the feasibility of constructing of plexcitonic antenna complexes on gold surfaces is investigated. The splitting of LSPR, which is a sign of the plasmon exciton coupling, is observed by spin-casting of J-aggregates on the surface of gold nanoarrays with coupling energy of 0.26 eV. This splitting is sensitive to the incident angle of UV-vis beam. Splitting of LSPR is also observed when *ZnChla* is co-ordinately attached to PDMA brushes. In this

structures, plasmon-exciton coupling is dependant to the concentration of *ZnChla* as expected. In these structures, coupling energy of 0.16 eV is measured for 15 ± 3 nm thick film, and 0.08 eV is obtained for around 30 nm thick film. However, there is scope for further optimising the coupling of the dye to the polymer by controlling the grafting density of dye molecules, which may enable to achieve an increase in the concentration of *ZnChla* molecules in the brush layer, thus increasing N/V and hence the coupling energy.

A splitting of the extinction spectra of is also observed with coupling energy of 0.21 eV when INR attached co-ordinately to PDMA scaffolds grown from gold plasmonic arrays. Although this is strictly approaching the strong coupling regime, it is believed that it could be improved by controlling the grafting density of the polymer brushes to accommodate more excitons that can lead to strong coupling.

Instead of the construction of pigment-polymer antenna on gold surface, a solution route to the formation of plasmonic structures is tested by embedding plasmonic materials within PDMA brushes. To achieve this, AuNPs with average particle size of 13 nm are successfully prepared in a single reduction step and incorporated into PDMA brushes via simple immersing of PDMA modified surface in a suspension of AuNPs. Full coverage of AuNPs is achieved by incubation PDMA samples in AuNPs solution overnight. However, no strong plasmon-exciton coupling is achieved following attachment of *ZnChla* to this system probably due to the long separation in energy between the LSPR of the AuNPs and the transitions in *ZnChla*.

A similar solution route is used to fabricate AINP-based plasmonic structure. Here, AINPs are successfully synthesised via chemical decomposition and sono-solvo chemistry. In chemical decomposition, alane complex is decomposed using titanium isopropoxide. The maximum plasmon resonance of AINPs prepared by this method is observed at 265 nm. However, this deep UV plasmon resonance is not ideal for sensing applications. So, sono-solvo chemistry method is used alternatively to tune the maximum plasmon resonance from

deep UV spectral range to near visible range at 370. However, incorporation of AINPs (either prepared via chemical decomposition or sono-solvo chemistry) into surface-grafted PDMA brushes with controllable plasmon resonance is not achieved. This obstacle most likely is caused by the very fast oxidation state that can suppress optical properties as well as high sensitivity and hydrophobicity of AINPs.

8.2 FUTURE WORK

Control of the polymer brush grafting density through patterning BIBUDT-initiated gold structures may be useful for the enhancement of plasmon-exciton coupling that was observed in *ZnChla*-PDMA antenna complexes or INR-PDMA antenna complexes grown from plasmonic arrays of gold nanostructures. It was thought that full density PDMA brushes could cause high steric hindrance, leading to difficulty in sufficient penetration of *chlorophyll* molecules into the polymer layer, reducing number of excitons inside plasmon volume, and then the coupling strength. Therefore, reduced density PDMA brushes may be useful to allow sufficient space to accommodate sufficient number of excitons that enable to achieve strong coupling. Also, pH responsiveness properties of PDMA brushes could be utilised to control conformational structure of the brush layer to program the formation of these plexcitonic systems.

Because LSPR of AuNPs are resonant close to or may overlap maximum absorption of INR, it might be useful to explore the possibility of formation of plexcitonic complexes by attaching of INR to AuNPs-impregnated PDMA brushes grown from BIBB-APTES-initiated planar substrate, glass for example. Alternatively, incorporation of AuNPs into PCysMA brushes functionalised with commercial dye, e.g., Cyanine3 NHS ester (Cy3-NHS ester), may be useful.

Designed plasmonic AuNPs-impregnated PDMA structure in theses was suppressed by fast formation of oxide layer that overlapped with plasmonic properties of AuNPs. Therefore, it might be useful to employ oxidation tolerant metal nanoparticles, silver nanoparticles for example.

REFERENCES

1. Lee H, Cheng YC, Fleming GR. Coherence dynamics in photosynthesis: protein protection of excitonic coherence. *Science* (80-) 2007;316(5830):1462–5.
2. Törmä P, Barnes WL. Strong coupling between surface plasmon polaritons and emitters: a review. *Reports Prog Phys* 2014;78(1):13901.
3. Moores A, Goettmann F. The plasmon band in noble metal nanoparticles: An introduction to theory and applications. *New J Chem* 2006;30(8):1121–32.
4. Kreibig U, Vollmer M, Kreibig U, Vollmer M. Theoretical considerations. *Opt Prop Met Clust* 1995;13–201.
5. Anker JN, Hall WP, Lyandres O, Shah NC, Zhao J, Van Duyne RP. Biosensing with plasmonic nanosensors. *Nat Mater* 2008;7(6):442–53.
6. Kelly KL, Coronado E, Zhao LL, Schatz GC. The optical properties of metal nanoparticles: the influence of size, shape, and dielectric environment. *J. Phys. Chem. B* 2003;107(3):668–77.
7. Haes AJ, Haynes CL, McFarland AD, Schatz GC, Van Duyne RP, Zou S. Plasmonic materials for surface-enhanced sensing and spectroscopy. *MRS Bull* 2005;30(5):368–75.
8. Murray WA, Barnes WL. Plasmonic materials. *Adv Mater* 2007;19(22):3771–82.
9. Pelton M, Aizpurua J, Bryant G. Metal-nanoparticle plasmonics. *Laser Photon Rev* 2008;2(3):136–59.
10. Lal S, Link S, Halas NJ. Nano-optics from sensing to waveguiding. *Nat Photonics* 2007;1(11):641–8.

11. Lenyk B, Schöps V, Boneberg J, Kabdulov M, Huhn T, Scheer E, et al. Surface Plasmon-Enhanced Switching Kinetics of Molecular Photochromic Films on Gold Nanohole Arrays. *Nano Lett* 2020;20(7):5243–50.
12. Liu J, Jalali M, Mahshid S, Wachsmann-Hogiu S. Are plasmonic optical biosensors ready for use in point-of-need applications? *Analyst* 2020;145(2):364–84.
13. Sun L, Chen P, Lin L. Enhanced molecular spectroscopy via localized surface plasmon resonance. *Appl Mol Spectrosc to Curr Res Chem Biol Sci* 2016;
14. Willets KA, Van Duyne RP. Localized surface plasmon resonance spectroscopy and sensing. *Annu Rev Phys Chem* 2007;58(1):267–97.
15. Moores A, Goettmann F. The plasmon band in noble metal nanoparticles: an introduction to theory and applications. *New J Chem* 2006;30(8):1121–32.
16. Rechberger W, Hohenau A, Leitner A, Krenn JR, Lamprecht B, Aussenegg FR. Optical properties of two interacting gold nanoparticles. *Opt Commun* 2003;220(1–3):137–41.
17. Su KH, Wei QH, Zhang X, Mock JJ, Smith DR, Schultz S. Interparticle coupling effects on plasmon resonances of nanogold particles. *Nano Lett* 2003;3(8):1087–90.
18. Lin X, Ye S, Kong C, Webb K, Yi C, Zhang S, et al. Polymeric ligand-mediated regioselective bonding of plasmonic nanoplates and nanospheres. *J Am Chem Soc* 2020;142(41):17282–6.
19. Cuevas M. Spontaneous emission in plasmonic graphene subwavelength wires of arbitrary sections. *J Quant Spectrosc Radiat Transf* 2018;206:157–62.
20. Amendola V, Pilot R, Frasconi M, Maragò OM, Iatì MA. Surface plasmon resonance in gold nanoparticles: a review. *J Phys Condens Matter* 2017;29(20):203002.
21. Boyaciyan D, Krause P, Von Klitzing R. Making strong polyelectrolyte brushes pH-

- sensitive by incorporation of gold nanoparticles. *Soft Matter* 2018;14(20):4029–39.
22. Lupitskyy R, Motornov M, Minko S. Single nanoparticle plasmonic devices by the “grafting to” method. *Langmuir* 2008;24(16):8976–80.
 23. Tsargorodska A, El Zubir O, Darroch B, Cartron ML, Basova T, Hunter CN, et al. Fast, simple, combinatorial routes to the fabrication of reusable, plasmonically active gold nanostructures by interferometric lithography of self-assembled monolayers. *ACS Nano* 2014;8(8):7858–69.
 24. Leggett GJ. Tools for low-dimensional chemistry. *Langmuir* 2018;35(24):7589–602.
 25. Lishchuk A, Kodali G, Mancini JA, Broadbent M, Darroch B, Mass OA, et al. A synthetic biological quantum optical system. *Nanoscale* 2018;10(27):13064–73.
 26. Wu F, Guo J, Huang Y, Liang K, Jin L, Li J, et al. Plexcitonic optical chirality: Strong exciton–plasmon coupling in chiral J-aggregate-metal nanoparticle complexes. *ACS Nano* 2020;15(2):2292–300.
 27. Feng Y, Gao M, Wang Y, Meng L, Sun M. Plexciton for surface enhanced Raman scattering and emission. *J Raman Spectrosc* 2020;51(3):476–82.
 28. Peruffo N, Mancin F, Collini E. Plexcitonic Nanohybrids Based on Gold Nanourchins: The Role of the Capping Layer. *J Phys Chem C* 2021;125(36):19897–905.
 29. Melnikau D, Savateeva D, Sussha A, Rogach AL, Rakovich YP. Strong plasmon-exciton coupling in a hybrid system of gold nanostars and J-aggregates. *Nanoscale Res Lett* 2013;8(1):1–6.
 30. van Burgel M, Wiersma DA, Duppen K. The dynamics of one-dimensional excitons in liquids. *J Chem Phys* 1995;102(1):20–33.
 31. Lidzey D, Bradley D, Virgili T. a. Armitage, M. Skolnick, and S. Walker. *Phys Rev Lett*

1999;82:3316.

32. Tsargorodska A, Cartron ML, Vasilev C, Kodali G, Mass OA, Baumberg JJ, et al. Strong coupling of localized surface plasmons to excitons in light-harvesting complexes. *Nano Lett* 2016;16(11):6850–6.
33. Lishchuk A, Csányi E, Darroch B, Wilson C, Nabok A, Leggett GJ. Active control of strong plasmon–exciton coupling in biomimetic pigment–polymer antenna complexes grown by surface-initiated polymerisation from gold nanostructures. *Chem Sci* 2022;13(8):2405–17.
34. Xin L, Lu M, Both S, Pfeiffer M, Urban MJ, Zhou C, et al. Watching a single fluorophore molecule walk into a plasmonic hotspot. *Acs Photonics* 2019;6(4):985–93.
35. Fassioli F, Dinshaw R, Arpin PC, Scholes GD. Photosynthetic light harvesting: excitons and coherence. *J R Soc Interface* 2014;11(92):20130901.
36. Peruffo N, Gil G, Corni S, Mancin F, Collini E. Selective switching of multiple plexcitons in colloidal materials: directing the energy flow at the nanoscale. *Nanoscale* 2021;13(12):6005–15.
37. Mohankumar M, Unnikrishnan M, Naidu GN, Somasundaran SM, Ajaykumar MP, Swathi RS, et al. Finding the Needle in a Haystack: Capturing Veiled Plexcitonic Coupling through Differential Spectroscopy. *J Phys Chem C* 2020;124(48):26387–95.
38. Jamkhande PG, Ghule NW, Bamer AH, Kalaskar MG. Metal nanoparticles synthesis: An overview on methods of preparation, advantages and disadvantages, and applications. *J Drug Deliv Sci Technol* 2019;53:101174.
39. Ealia SAM, Saravanakumar MP. A review on the classification, characterisation, synthesis of nanoparticles and their application. In: *IOP conference series: materials science and engineering*. IOP Publishing; 2017. page 32019.

40. Tiwari DK, Behari J, Sen P. Application of nanoparticles in waste water treatment 1. 2008;
41. Salavati-Niasari M, Davar F, Mir N. Synthesis and characterization of metallic copper nanoparticles via thermal decomposition. *Polyhedron* 2008;27(17):3514–8.
42. Bhaviripudi S, Mile E, Steiner SA, Zare AT, Dresselhaus MS, Belcher AM, et al. CVD synthesis of single-walled carbon nanotubes from gold nanoparticle catalysts. *J Am Chem Soc* 2007;129(6):1516–7.
43. Daniel MC, Astruc D. Gold nanoparticles: assembly, supramolecular chemistry, quantum-size-related properties, and applications toward biology, catalysis, and nanotechnology. *Chem Rev* 2004;104(1):293–346.
44. Ortiz-Castillo JE, Gallo-Villanueva RC, Madou MJ, Perez-Gonzalez VH. Anisotropic gold nanoparticles: A survey of recent synthetic methodologies. *Coord Chem Rev* 2020;425:213489.
45. Saha K, Agasti SS, Kim C, Li X, Rotello VM. Gold nanoparticles in chemical and biological sensing. *Chem Rev* 2012;112(5):2739–79.
46. Faraday M. X. The Bakerian Lecture.—Experimental relations of gold (and other metals) to light. *Philos Trans R Soc London* 1857;(147):145–81.
47. Faraday M. Experimental relations of gold (and other metals) to light./Michael FARADAY. Bak Lect relations gold (and other Met to Light Faraday—London *Philos Trans R Soc London* 1857;145–81.
48. Mie G. Contributions to the optics of turbid media, particularly of colloidal metal solutions. *Contrib to Opt Turbid media* 1976;25(3):377–445.
49. Zsigmondy RA, Norton JF. *The chemistry of colloids*. John Wiley & sons, Incorporated; 1917.

50. Svedberg T. The formation of colloids. J. & A. Churchill; 1921.
51. Turkevich J, Stevenson PC, Hillier J. Discuss. Faraday Soc. 11 55; Enüstün BV and Turkevich J 1963. J Am Chem Soc 1951;85:3317.
52. Chow MK, Zukoski CF. Gold sol formation mechanisms: role of colloidal stability. J Colloid Interface Sci 1994;165(1):97–109.
53. Frens G. Controlled nucleation for the regulation of the particle size in monodisperse gold suspensions. Nat Phys Sci 1973;241(105):20–2.
54. Brust M, Walker M, Bethell D. Schiffrin DJ and Whyman R. J Chem Soc Chem Commun 1994;1994:801.
55. Meyers MA, Mishra A, Benson DJ. Mechanical properties of nanocrystalline materials. Prog Mater Sci 2006;51(4):427–556.
56. Nadagouda MN, Speth TF, Varma RS. Microwave-assisted green synthesis of silver nanostructures. Acc Chem Res 2011;44(7):469–78.
57. Mukherjee P, Ahmad A, Mandal D, Senapati S, Sainkar SR, Khan MI, et al. Fungus-mediated synthesis of silver nanoparticles and their immobilization in the mycelial matrix: a novel biological approach to nanoparticle synthesis. Nano Lett 2001;1(10):515–9.
58. Chen H, Wang Y, Wang Y, Dong S, Wang E. One-step preparation and characterization of PDDA-protected gold nanoparticles. Polymer (Guildf) 2006;47(2):763–6.
59. Guzmán MG, Dille J, Godet S. Synthesis of silver nanoparticles by chemical reduction method and their antibacterial activity. Int J Chem Biomol Eng 2009;2(3):104–11.
60. Chattopadhyay DP, Patel BH. Nano metal particles: Synthesis, characterization and

application to textiles. *Manuf Nanostructures* 2014;184–215.

61. Zhang Q li, Yang ZM, Ding B jun, Lan X zhe, Guo Y juan. Preparation of copper nanoparticles by chemical reduction method using potassium borohydride. *Trans Nonferrous Met Soc China* 2010;20:s240–4.
62. Chah S, Hammond MR, Zare RN. Gold nanoparticles as a colorimetric sensor for protein conformational changes. *Chem Biol* 2005;12(3):323–8.
63. You Y, Lim S, Gunasekaran S. Streptavidin-coated Au nanoparticles coupled with biotinylated antibody-based bifunctional linkers as plasmon-enhanced immunobiosensors. *ACS Appl Nano Mater* 2020;3(2):1900–9.
64. Gupta S, Agrawal M, Uhlmann P, Simon F, Oertel U, Stamm M. Gold nanoparticles immobilized on stimuli responsive polymer brushes as nanosensors. *Macromolecules* 2008;41(21):8152–8.
65. Haiss W, Thanh NTK, Aveyard J, Fernig DG. Determination of size and concentration of gold nanoparticles from UV– Vis spectra. *Anal Chem* 2007;79(11):4215–21.
66. Prado AR, Oliveira JP, Keijok WJ, Milaneze BA, Nogueira B V, Guimarães MC, et al. Comparison between the synthesis of gold nanoparticles with sodium citrate and sodium tetraborate. *BMC Proc* 2014;8(S4):1–2.
67. Sun Y, Xia Y. Shape-controlled synthesis of gold and silver nanoparticles. *Science* (80-) 2002;298(5601):2176–9.
68. Pham T, Jackson JB, Halas NJ, Lee TR. Preparation and characterization of gold nanoshells coated with self-assembled monolayers. *Langmuir* 2002;18(12):4915–20.
69. Song JY, Jang HK, Kim BS. Biological synthesis of gold nanoparticles using *Magnolia kobus* and *Diopyros kaki* leaf extracts. *Process Biochem* 2009;44(10):1133–8.

70. Tokarev I, Tokareva I, Minko S. Gold-nanoparticle-enhanced plasmonic effects in a responsive polymer gel. *Adv Mater* 2008;20(14):2730–4.
71. Fang L, Li Y, Chen Z, Liu W, Zhang J, Xiang S, et al. Tunable polymer brush/au nps hybrid plasmonic arrays based on host–guest interaction. *ACS Appl Mater Interfaces* 2014;6(22):19951–7.
72. Valsecchi C, Brolo AG. Periodic metallic nanostructures as plasmonic chemical sensors. *Langmuir* 2013;29(19):5638–49.
73. Chen S, Svedendahl M, Antosiewicz TJ, Kall M. Plasmon-enhanced enzyme-linked immunosorbent assay on large arrays of individual particles made by electron beam lithography. *ACS Nano* 2013;7(10):8824–32.
74. Michel R, Lussi JW, Csucs G, Reviakine I, Danuser G, Ketterer B, et al. Selective molecular assembly patterning: A new approach to micro-and nanochemical patterning of surfaces for biological applications. *Langmuir* 2002;18(8):3281–7.
75. Al-Jaf O, Alswieleh A, Armes SP, Leggett GJ. Nanotribological properties of nanostructured poly (cysteine methacrylate) brushes. *Soft Matter* 2017;13(10):2075–84.
76. Ahmad SA, Leggett GJ, Hucknall A, Chilkoti A. Micro-and nanostructured poly [oligo (ethylene glycol) methacrylate] brushes grown from photopatterned halogen initiators by atom transfer radical polymerization. *Biointerphases* 2011;6(1):8–15.
77. Amendola V, Meneghetti M. Size evaluation of gold nanoparticles by UV– vis spectroscopy. *J Phys Chem C* 2009;113(11):4277–85.
78. Chen H, Kou X, Yang Z, Ni W, Wang J. Shape-and size-dependent refractive index sensitivity of gold nanoparticles. *Langmuir* 2008;24(10):5233–7.
79. Schaeublin NM, Braydich-Stolle LK, Schrand AM, Miller JM, Hutchison J, Schlager JJ,

- et al. Surface charge of gold nanoparticles mediates mechanism of toxicity. *Nanoscale* 2011;3(2):410–20.
80. Sun L, Han H, Liu Z, Fu Z, Hua C, Ma E, et al. Immobilization of Gold Nanoparticles in Spherical Polymer Brushes Observed by Small-Angle X-ray Scattering. *Langmuir* 2022;38(5):1869–76.
81. Nichols G, Byard S, Bloxham MJ, Botterill J, Dawson NJ, Dennis A, et al. A review of the terms agglomerate and aggregate with a recommendation for nomenclature used in powder and particle characterization. *J Pharm Sci* 2002;91(10):2103–9.
82. Sokolov S V, Tschulik K, Batchelor-McAuley C, Jurkschat K, Compton RG. Reversible or not? Distinguishing agglomeration and aggregation at the nanoscale. *Anal Chem* 2015;87(19):10033–9.
83. Luksiene Z. Nanoparticles and their potential application as antimicrobials in the food industry. In: *Food preservation*. Elsevier; 2017. page 567–601.
84. Mitsuishi M, Koishikawa Y, Tanaka H, Sato E, Mikayama T, Matsui J, et al. Nanoscale actuation of thermoreversible polymer brushes coupled with localized surface plasmon resonance of gold nanoparticles. *Langmuir* 2007;23(14):7472–4.
85. Barazzouk S, Bekalé L, Hotchandani S. Enhanced photostability of chlorophyll-a using gold nanoparticles as an efficient photoprotector. *J Mater Chem* 2012;22(48):25316–24.
86. Bekalé L, Barazzouk S, Hotchandani S. Beneficial role of gold nanoparticles as photoprotector of magnesium tetraphenylporphyrin. *J Mater Chem* 2012;22(7):2943–51.
87. Yuan H, Sun G, Peng W, Ji W, Chu S, Liu Q, et al. Thymine-functionalized gold nanoparticles (Au NPs) for a highly sensitive fiber-optic surface plasmon resonance

mercury ion nanosensor. *Nanomaterials* 2021;11(2):397.

88. Lee KS, El-Sayed MA. Gold and silver nanoparticles in sensing and imaging: sensitivity of plasmon response to size, shape, and metal composition. *J Phys Chem B* 2006;110(39):19220–5.
89. You CC, Miranda OR, Gider B, Ghosh PS, Kim IB, Erdogan B, et al. Detection and identification of proteins using nanoparticle–fluorescent polymer ‘chemical nose’ sensors. *Nat Nanotechnol* 2007;2(5):318–23.
90. Tokareva I, Minko S, Fendler JH, Hutter E. Nanosensors based on responsive polymer brushes and gold nanoparticle enhanced transmission surface plasmon resonance spectroscopy. *J Am Chem Soc* 2004;126(49):15950–1.
91. Cao J, Galbraith EK, Sun T, Grattan KT V. Comparison of surface plasmon resonance and localized surface plasmon resonance-based optical fibre sensors. In: *Journal of Physics: Conference Series*. IOP Publishing; 2011. page 12050.
92. Christau S, Möller T, Brose F, Genzer J, Soltwedel O, von Klitzing R. Effect of gold nanoparticle hydrophobicity on thermally induced color change of PNIPAM brush/gold nanoparticle hybrids. *Polymer (Guildf)* 2016;98:454–63.
93. Bhat RR, Genzer J, Chaney BN, Sugg HW, Liebmann-Vinson A. Controlling the assembly of nanoparticles using surface grafted molecular and macromolecular gradients. *Nanotechnology* 2003;14(10):1145.
94. Gupta S, Uhlmann P, Agrawal M, Chapuis S, Oertel U, Stamm M. Immobilization of silver nanoparticles on responsive polymer brushes. *Macromolecules* 2008;41(8):2874–9.
95. Gérard D, Gray SK. Aluminium plasmonics. *J Phys D Appl Phys* 2014;48(18):184001.
96. Ritchie RH. Plasma losses by fast electrons in thin films. *Phys Rev* 1957;106(5):874.

97. Powell CJ, Swan JB. Origin of the characteristic electron energy losses in aluminum. *Phys Rev* 1959;115(4):869.
98. Batson PE. Surface plasmon coupling in clusters of small spheres. *Phys Rev Lett* 1982;49(13):936.
99. Ghorbani HR. A review of methods for synthesis of Al nanoparticles. *Orient J chem* 2014;30(4):1941–9.
100. Langhammer C, Schwind M, Kasemo B, Zoric I. Localized surface plasmon resonances in aluminum nanodisks. *Nano Lett* 2008;8(5):1461–71.
101. Knight MW, King NS, Liu L, Everitt HO, Nordlander P, Halas NJ. Aluminum for plasmonics. *ACS Nano* 2014;8(1):834–40.
102. Sharma VK, Yngard RA, Lin Y. Silver nanoparticles: green synthesis and their antimicrobial activities. *Adv Colloid Interface Sci* 2009;145(1–2):83–96.
103. Tavakoli A, Sohrabi M, Kargari A. A review of methods for synthesis of nanostructured metals with emphasis on iron compounds. *Chem Pap* 2007;61(3):151–70.
104. Mohanpuria P, Rana NK, Yadav SK. Biosynthesis of nanoparticles: technological concepts and future applications. *J nanoparticle Res* 2008;10(3):507–17.
105. Paskevicius M, Webb J, Pitt MP, Blach TP, Hauback BC, Gray EM, et al. Mechanochemical synthesis of aluminium nanoparticles and their deuterium sorption properties to 2 kbar. *J Alloys Compd* 2009;481(1–2):595–9.
106. Streletskii AN, Pivkina AN, Kolbanov I V, Borunova AB, Leipunskii IO, Pshechenkov PA, et al. Mechanical activation of aluminum: 2. Size, shape, and structure of particles. *Colloid J* 2004;66(6):736–44.
107. Chandra S, Kumar A, Tomar PK. Synthesis of Al nanoparticles: Transmission electron

microscopy, thermal and spectral studies. *Spectrochim Acta Part A Mol Biomol Spectrosc* 2012;92:392–7.

108. Manikam VR, Cheong KY, Razak KA. Chemical reduction methods for synthesizing Ag and Al nanoparticles and their respective nanoalloys. *Mater Sci Eng B* 2011;176(3):187–203.
109. Gilaki M. Synthesis of magnetic Al/Au nanoparticles by co-reduction of Au³⁺ and Al³⁺ metal salts. *Pak J Biol Sci* 2010;13(16):809–13.
110. Li H, Meziani MJ, Lu F, Bunker CE, Gulians EA, Sun YP. Templated synthesis of aluminum nanoparticles-A new route to stable energetic materials. *J Phys Chem C* 2009;113(48):20539–42.
111. Haber JA, Buhro WE. Kinetic instability of nanocrystalline aluminum prepared by chemical synthesis; facile room-temperature grain growth. *J Am Chem Soc* 1998;120(42):10847–55.
112. Champion Y, Bigot J. Synthesis and structural analysis of aluminum nanocrystalline powders. *Nanostructured Mater* 1998;10(7):1097–110.
113. Fernandez A, Sanchez-Lopez JC, Caballero A, Martin JM, Vacher B, Ponsonnet L. Characterization of nanophase Al-oxide/Al powders by electron energy-loss spectroscopy. *J Microsc* 1998;191(2):212–20.
114. Kermanpur A, Dadfar MR, Nekooei Rizi B, Eshraghi M. Synthesis of aluminum nanoparticles by electromagnetic levitational gas condensation method. *J Nanosci Nanotechnol* 2010;10(9):6251–5.
115. Baladi A, Mamoory RS. Investigation of different liquid media and ablation times on pulsed laser ablation synthesis of aluminum nanoparticles. *Appl Surf Sci* 2010;256(24):7559–64.

116. Ganeev RA, Boltaev GS, Tugushev RI, Usmanov T. Nanoparticle formation during laser ablation of metals at different pressures of surrounding noble gases. *Appl Phys A* 2010;100(1):119–23.
117. Sen P, Ghosh J, Abdullah A, Kumar P. Preparation of Cu, Ag, Fe and Al nanoparticles by the exploding wire technique. *J Chem Sci* 2003;115(5):499–508.
118. Sindhu TK, Sarathi R, Chakravarthy SR. Generation and characterization of nano aluminium powder obtained through wire explosion process. *Bull Mater Sci* 2007;30(2):187–95.
119. Bousquet A, Awada H, Hiorns RC, Dagron-Lartigau C, Billon L. Conjugated-polymer grafting on inorganic and organic substrates: A new trend in organic electronic materials. *Prog Polym Sci [Internet]* 2014;39(11):1847–77. Available from: <http://dx.doi.org/10.1016/j.progpolymsci.2014.03.003>
120. Kumar R, Welle A, Becker F, Kopyeva I, Lahann J. Substrate-independent micropatterning of polymer brushes based on photolytic deactivation of chemical vapor deposition based surface-initiated atom-transfer radical polymerization initiator films. *ACS Appl Mater Interfaces* 2018;10(38):31965–76.
121. Banerjee S, Paira TK, Mandal TK. Surface confined atom transfer radical polymerization: Access to custom library of polymer-based hybrid materials for speciality applications. *Polym Chem* 2014;5(14):4153–67.
122. Mansky P, Liu Y, Huang E, Russell TP, Hawker C. Controlling polymer-surface interactions with random copolymer brushes. *Science (80-)* 1997;275(5305):1458–60.
123. Edmondson S, Osborne VL, Huck WTS. Polymer brushes via surface-initiated polymerizations. *Chem Soc Rev* 2004;33(1):14–22.
124. Ulman A. Formation and structure of self-assembled monolayers. *Chem Rev*

1996;96(4):1533–54.

125. Wei W, Faubel JL, Selvakumar H, Kovari DT, Tsao J, Rivas F, et al. Self-regenerating giant hyaluronan polymer brushes. *Nat Commun* 2019;10(1):1–13.
126. Hawker CJ, Bosman AW, Harth E. New polymer synthesis by nitroxide mediated living radical polymerizations. *Chem Rev* 2001;101(12):3661–88.
127. Barbey R, Lavanant L, Paripovic D, Schuwer N, Sugnaux C, Tugulu S, et al. Polymer brushes via surface-initiated controlled radical polymerization: synthesis, characterization, properties, and applications. *Chem Rev* 2009;109(11):5437–527.
128. Pyun J, Kowalewski T, Matyjaszewski K. Synthesis of polymer brushes using atom transfer radical polymerization. *Macromol Rapid Commun* 2003;24(18):1043–59.
129. Lorandi F, Fantin M, Matyjaszewski K. Atom Transfer Radical Polymerization: A Mechanistic Perspective. *J Am Chem Soc* 2022;144(34):15413–30.
130. Xia KM and J. Atom Transfer Radical Polymerization. *chem Rev* 2001;101:2921–2990.
131. Alswieleh AM, Cheng N, Canton I, Ustbas B, Xue X, Ladmiral V, et al. Zwitterionic Poly (amino acid methacrylate) Brushes. *J Am Chem Soc* 2014;136(26):9404–13.
132. Johnson A, Bao P, Hurley CR, Cartron M, Evans SD, Hunter CN, et al. Simple, direct routes to polymer brush traps and nanostructures for studies of diffusional transport in supported lipid bilayers. *Langmuir* 2017;33(15):3672–9.
133. MILNER ST. Polymer Brushes. *Science (80-)* 1991;251:905–14.
134. Cheng Z, Zhu X, Shi ZL, Neoh KG, Kang ET. Polymer microspheres with permanent antibacterial surface from surface-initiated atom transfer radical polymerization. *Ind Eng Chem Res* 2005;44(18):7098–104.
135. Xia J, Zhang X, Matyjaszewski K. The effect of ligands on copper-mediated atom

transfer radical polymerization. ACS Publications; 2000.

136. Fang L feng, Wang N chuan, Zhou M yong, Zhu B ku, Zhu L ping, John AE. Poly (N, N-dimethylaminoethyl methacrylate) grafted poly (vinyl chloride) s synthesized via ATRP process and their membranes for dye separation. *Chinese J Polym Sci* 2015;33(11):1491–502.
137. Matyjaszewski K, Patten TE, Xia J. Controlled/“living” radical polymerization. Kinetics of the homogeneous atom transfer radical polymerization of styrene. *J Am Chem Soc* 1997;119(4):674–80.
138. Matyjaszewski K. Inner sphere and outer sphere electron transfer reactions in atom transfer radical polymerization. In: *Macromolecular Symposia*. Wiley Online Library; 1998. page 105–18.
139. Uegaki H, Kotani Y, Kamigaito M, Sawamoto M. Nickel-mediated living radical polymerization of methyl methacrylate. *Macromolecules* 1997;30(8):2249–53.
140. Percec V, Barboiu B, Neumann A, Ronda JC, Zhao M. Metal-catalyzed “living” radical polymerization of styrene initiated with arenesulfonyl chlorides. From heterogeneous to homogeneous catalysis. *Macromolecules* 1996;29(10):3665–8.
141. Ando T, Kamigaito M, Sawamoto M. Metal alkoxides as additives for ruthenium (II)-catalyzed living radical polymerization. *Macromolecules* 2000;33(18):6732–7.
142. Wang XS, Armes SP. Facile atom transfer radical polymerization of methoxy-capped oligo (ethylene glycol) methacrylate in aqueous media at ambient temperature. *Macromolecules* 2000;33(18):6640–7.
143. Matyjaszewski K, Davis K, Patten TE, Wei M. Observation and analysis of a slow termination process in the atom transfer radical polymerization of styrene. *Tetrahedron* 1997;53(45):15321–9.

144. Milchev A, Wittmer JP, Landau DP. Formation and equilibrium properties of living polymer brushes. *J Chem Phys* 2000;112(3):1606–15.
145. Mastan E, Xi L, Zhu S. Factors affecting grafting density in surface-initiated ATRP: a simulation study. *Macromol Theory Simulations* 2016;25(3):220–8.
146. Peng CH, Kong J, Seeliger F, Matyjaszewski K. Mechanism of halogen exchange in ATRP. *Macromolecules* 2011;44(19):7546–57.
147. Edmondson S, Osborne VL, Huck WTS. Polymer brushes via surface-initiated polymerizations. *Chem Soc Rev* 2004;33(1):14–22.
148. Murata H, Koepsel RR, Matyjaszewski K, Russell AJ. Permanent, non-leaching antibacterial surfaces—2: How high density cationic surfaces kill bacterial cells. *Biomaterials* 2007;28(32):4870–9.
149. Matyjaszewski K. Atom transfer radical polymerization (ATRP): current status and future perspectives. *Macromolecules* 2012;45(10):4015–39.
150. Li X, Wei X, Husson SM. Thermodynamic studies on the adsorption of fibronectin adhesion-promoting peptide on nanothin films of poly (2-vinylpyridine) by SPR. *Biomacromolecules* 2004;5(3):869–76.
151. Samadi A, Husson SM, Liu Y, Luzinov I, Michael Kilbey S. Low-Temperature Growth of Thick Polystyrene Brushes via ATRP. *Macromol Rapid Commun* 2005;26(23):1829–34.
152. Acar AE, Yağci MB, Mathias LJ. Adventitious effect of air in atom transfer radical polymerization: Air-induced (reverse) atom transfer radical polymerization of methacrylates in the absence of an added initiator. *Macromolecules* 2000;33(21):7700–6.
153. Alswieleh AM, Cheng N, Leggett GJ, Armes SP. Spatial control over cross-linking dictates the pH-responsive behavior of poly (2-(tert-butylamino) ethyl methacrylate)

brushes. *Langmuir* 2014;30(5):1391–400.

154. Durmaz EN, Sahin S, Virga E, De Beer S, De Smet LCPM, De Vos WM. Polyelectrolytes as building blocks for next-generation membranes with advanced functionalities. *ACS Appl Polym Mater* 2021;3(9):4347–74.
155. Johnson A, Madsen J, Chapman P, Alswieleh A, Al-Jaf O, Bao P, et al. Micrometre and nanometre scale patterning of binary polymer brushes, supported lipid bilayers and proteins. *Chem Sci* 2017;8(6):4517–26.
156. Zoppe JO, Ataman NC, Mocny P, Wang J, Moraes J, Klok HA. Surface-initiated controlled radical polymerization: state-of-the-art, opportunities, and challenges in surface and interface engineering with polymer brushes. *Chem Rev* 2017;117(3):1105–318.
157. Al-Jaf O, Alswieleh A, Armes SP, Leggett GJ. Nanotribological properties of nanostructured poly(cysteine methacrylate) brushes. *Soft Matter* 2017;13(10):2075–84.
158. Cheng Z, Zhu X, Shi ZL, Neoh KG, Kang ET. Polymer microspheres with permanent antibacterial surface from surface-initiated atom transfer radical polymerization. *Ind Eng Chem Res* 2005;44(18):7098–104.
159. Madsen J, Ducker RE, Al Jaf O, Cartron ML, Alswieleh AM, Smith CH, et al. Fabrication of microstructured binary polymer brush “corrals” with integral pH sensing for studies of proton transport in model membrane systems. *Chem Sci* 2018;9(8):2238–51.
160. Leggett GJ. Tools for Low-Dimensional Chemistry. *Langmuir* 2019;35(24):7589–602.
161. Micciulla S, Soltwedel O, Löhmann O, von Klitzing R. Temperature responsive behavior of polymer brush/polyelectrolyte multilayer composites. *Soft Matter* 2016;12(4):1176–83.

162. Kocak G, Tuncer C, Bütün V. pH-Responsive polymers. *Polym Chem* 2017;8(1):144–76.
163. Jia H, Wildes A, Titmuss S. Structure of pH-responsive polymer brushes grown at the gold–water interface: dependence on grafting density and temperature. *Macromolecules* 2012;45(1):305–12.
164. Cheng N, Bao P, Evans SD, Leggett GJ, Armes SP. Facile formation of highly mobile supported lipid bilayers on surface-quaternized pH-responsive polymer brushes. *Macromolecules* 2015;48(9):3095–103.
165. De Jesús-Téllez MA, Sánchez-Cerrillo DM, Quintana-Owen P, Schubert US, Contreras-López D, Guerrero-Sánchez C. Kinetic Investigations of Quaternization Reactions of Poly [2-(dimethylamino) ethyl methacrylate] with Diverse Alkyl Halides. *Macromol Chem Phys* 2020;221(9):1900543.
166. Dong R, Molloy RP, Lindau M, Ober CK. Direct synthesis of quaternized polymer brushes and their application for guiding neuronal growth. *Biomacromolecules* 2010;11(8):2027–32.
167. He Q, Qiao Y, Mandia DJ, Gan S, Zhang H, Zhou H, et al. Enrichment and Distribution of Pb²⁺ Ions in Zwitterionic Poly (cysteine methacrylate) Brushes at the Solid–Liquid Interface. *Langmuir* 2019;35(52):17082–9.
168. Zhang Y, Gu W, Xu H, Liu S. Facile fabrication of hybrid nanoparticles surface grafted with multi-responsive polymer brushes via block copolymer micellization and self-catalyzed core gelation. *J Polym Sci Part A Polym Chem* 2008;46(7):2379–89.
169. Breul AM, Hager MD, Schubert US. Fluorescent monomers as building blocks for dye labeled polymers: synthesis and application in energy conversion, biolabeling and sensors. *Chem Soc Rev* 2013;42(12):5366–407.

170. Dai X, Zhou F, Khan N, Huck WTS, Kaminski CF. Direct visualization of reversible switching of micropatterned polyelectrolyte brushes on gold surfaces using laser scanning confocal microscopy. *Langmuir* 2008;24(22):13182–5.
171. Wu T, Zou G, Hu J, Liu S. Fabrication of photoswitchable and thermotunable multicolor fluorescent hybrid silica nanoparticles coated with dye-labeled poly (N-isopropylacrylamide) brushes. *Chem Mater* 2009;21(16):3788–98.
172. Ionov L, Bocharova V, Diez S. Biotemplated synthesis of stimuli-responsive nanopatterned polymer brushes on microtubules. *Soft Matter* 2009;5(1):67–71.
173. Nese A, Lebedeva N V, Sherwood G, Averick S, Li Y, Gao H, et al. pH-responsive fluorescent molecular bottlebrushes prepared by Atom Transfer Radical polymerization. *Macromolecules* 2011;44(15):5905–10.
174. Madsen J, Canton I, Warren NJ, Themistou E, Blanz A, Ustbas B, et al. Nile blue-based nanosized pH sensors for simultaneous far-red and near-infrared live bioimaging. *J Am Chem Soc* 2013;135(39):14863–70.
175. Fouz MF, Mukumoto K, Averick S, Molinar O, McCartney BM, Matyjaszewski K, et al. Bright fluorescent nanotags from bottlebrush polymers with DNA-tipped bristles. *ACS Cent Sci* 2015;1(8):431–8.
176. Kopeć M, Tas S, Cirelli M, van der Pol R, de Vries I, Vancso GJ, et al. Fluorescent Patterns by Selective Grafting of a Telechelic Polymer. *ACS Appl Polym Mater* 2019;1(2):136–40.
177. Li N, Lu J, Xia X, Xu Q, Wang L. Synthesis of third-order nonlinear optical polyacrylates containing an azobenzene side chain via atom transfer radical polymerization. *Dye Pigment* 2009;80(1):73–9.
178. Madsen J, Warren NJ, Armes SP, Lewis AL. Synthesis of rhodamine 6G-based

compounds for the ATRP synthesis of fluorescently labeled biocompatible polymers. *Biomacromolecules* 2011;12(6):2225–34.

179. Khalyfa A, Kermasha S, Alli I. Extraction, purification, and characterization of chlorophylls from spinach leaves. *J Agric Food Chem* 1992;40(2):215–20.
180. Hosikian A, Lim S, Halim R, Danquah MK. Chlorophyll extraction from microalgae: a review on the process engineering aspects. *Int J Chem Eng* 2010;2010.
181. Hu X, Tanaka AT and R. Simple extraction methods that prevent the artifactual conversion of chlorophyll to chlorophyllide during pigment isolation from leaf samples. *Plant Methods* 2013;9(1):19.
182. Blankenship RE. *Molecular mechanisms of photosynthesis*. John Wiley & Sons; 2021.
183. Koca N, Karadeniz F, Burdurlu HS. Effect of pH on chlorophyll degradation and colour loss in blanched green peas. *Food Chem* 2007;100(2):609–15.
184. Gouterman M. Spectra of porphyrins. *J Mol Spectrosc* 1961;6:138–63.
185. Houssier C, Sauer K. Circular dichroism and magnetic circular dichroism of the chlorophyll and protochlorophyll pigments. *J Am Chem Soc* 1970;92(4):779–91.
186. Herrero M, Mendiola JA, Cifuentes A, Ibáñez E. Supercritical fluid extraction: Recent advances and applications. *J Chromatogr a* 2010;1217(16):2495–511.
187. Simon D, Helliwell S. Extraction and quantification of chlorophyll a from freshwater green algae. *Water Res* 1998;32(7):2220–3.
188. Wright SW, Jeffrey SW, Mantoura RFC. *Phytoplankton pigments in oceanography: guidelines to modern methods*. Unesco Pub. Paris, France; 2005.
189. Iriyama K, Ogura N, Takamiya A. A simple method for extraction and partial purification of chlorophyll from plant material, using dioxane. *J Biochem* 1974;76(4):901–4.

190. Dikio ED, Isabirye DA. Isolation of chlorophyll a from spinach leaves. *Bull Chem Soc Ethiop* 2008;22(2):301–4.
191. Nurhayati N, Suendo V. Isolation of chlorophyll a from spinach leaves and modification of center ion with Zn 2+: study on its optical stability. *J Mat Sains* 2011;16.
192. Inskeep WP, Bloom PR. Extinction coefficients of chlorophyll a and b in N, N-dimethylformamide and 80% acetone. *Plant Physiol* 1985;77(2):483–5.
193. Strain HH, Cope BT, Svec WA. [42] Analytical procedures for the isolation, identification, estimation, and investigation of the chlorophylls. In: *Methods in enzymology*. Elsevier; 1971. page 452–76.
194. Omata T, Murata N. A rapid and efficient method to prepare chlorophyll a and b from leaves. *Photochem Photobiol* 1980;31(2):183–5.
195. Sato N, Murata N. Preparation of chlorophyll a, chlorophyll b and bacteriochlorophyll a by means of column chromatography with diethylaminoethylcellulose. *Biochim Biophys Acta (BBA)-Bioenergetics* 1978;501(1):103–11.
196. Özkan G, Ersus Bilek S. Enzyme-assisted extraction of stabilized chlorophyll from spinach. *Food Chem* 2015;176:152–7.
197. Sakai S, Noji T, Kondo M, Mizuno T, Dewa T, Ochiai T, et al. Molecular assembly of zinc chlorophyll derivatives by using recombinant light-harvesting polypeptides with his-tag and immobilization on a gold electrode. *Langmuir* 2013;29(17):5104–9.
198. Takeuchi Y, Amao Y. Biohydrogen production from sucrose using the visible light sensitization of artificial Zn chlorophyll-a. *Bioconjug Chem* 2003;14(1):268–72.
199. Martinez V, Henary M. Nile red and nile blue: applications and syntheses of structural analogues. *Chem Eur J* 2016;22(39):13764–82.

200. Tajalli H, Gilani AG, Zakerhamidi MS, Tajalli P. The photophysical properties of Nile red and Nile blue in ordered anisotropic media. *Dye Pigment* 2008;78(1):15–24.
201. Chung SW, Gulians EA, Bunker CE, Hammerstroem DW, Deng Y, Burgers MA, et al. Capping and passivation of aluminum nanoparticles using alkyl-substituted epoxides. *Langmuir* 2009;25(16):8883–7.
202. Castilla M, Schuermans S, Gérard D, Martin J, Maurer T, Hananel U, et al. Colloidal Synthesis of Crystalline Aluminum Nanoparticles for UV Plasmonics. *ACS photonics* 2022;9(3):880–7.
203. Ruckenstein E, Li ZF. Surface modification and functionalization through the self-assembled monolayer and graft polymerization. *Adv Colloid Interface Sci* 2005;113(1):43–63.
204. Brinker CJ. Dip coating. In: *Chemical Solution Deposition of Functional Oxide Thin Films*. Springer; 2013. page 233–61.
205. Sahu N, Parija B, Panigrahi S. Fundamental understanding and modeling of spin coating process: A review. *Indian J Phys* 2009;83(4):493–502.
206. Kumar AKS, Zhang Y, Li D, Compton RG. A mini-review: How reliable is the drop casting technique? *Electrochem commun* 2020;121:106867.
207. Lee K, Duchamp M, Kulik G, Magrez A, Seo JW, Jeney S, et al. Uniformly dispersed deposition of colloidal nanoparticles and nanowires by boiling. *Appl Phys Lett* 2007;91(17):173112.
208. Group VM. *Scanning Probe Microscopy Training Notebook*. Digital Instruments. 2000;000:0–56.
209. Inc VI. *Scanning Probe Microscopy Training Notebook* [Internet]. 2006 [cited 2019 Jun 28];1–257. Available from: [https://clms.cnsi.ucla.edu/cnsi/clms/download/SPM Training](https://clms.cnsi.ucla.edu/cnsi/clms/download/SPM%20Training)

Intro?file_id=652824

210. Bullen RAW and HA. Basic Theory Atomic Force Microscopy (AFM) [Internet]. 2006 [cited 2019 Jul 1]; Available from:
https://asdlib.org/onlineArticles/ecourseware/Bullen/SPMModule_BasicTheoryAFM
211. Kabza K, Gestwicki JE, McGrath JL. Contact Angle Goniometry as a Tool for Surface Tension Measurements of Solids, Using Zisman Plot Method: A Physical Chemistry Experiment. *J Chem Educ* 2000;77(1):63–5.
212. Njobuenwu DO, Oboho EO, Gumus RH. Leonardo Electronic Journal of Practices and Technologies Determination of Contact Angle from Contact Area of Liquid Droplet Spreading on Solid Substrate. 2007;(10):29–38. Available from:
<http://lejpt.academicdirect.org>
213. Henck SA. In situ real-time ellipsometry for film thickness measurement and control.pdf. *J Vac Sci Technol* 1992;10:934–8.
214. Fujiwara H. Spectroscopic ellipsometry: principles and applications. 2007.
215. Cahan BD, Spanier RF. A high speed precision automatic ellipsometer. *Surf Sci* 1969;16(C):166–76.
216. Woollam JA. Accurate [Internet]. [cited 2023 May 26]; Available from:
<https://www.jawoollam.com/wp-content/uploads/alpha-se-brochure.pdf#page=10&zoom=auto,-265,133>
217. Parnell AJ, Martin SJ, Dang CC, Geoghegan M, Jones RAL, Crook CJ, et al. Synthesis, characterization and swelling behaviour of poly(methacrylic acid) brushes synthesized using atom transfer radical polymerization. *Polymer (Guildf)* [Internet] 2009;50(4):1005–14. Available from: <http://dx.doi.org/10.1016/j.polymer.2008.11.051>
218. G.E. Jellison J. Spectroscopic ellipsometry data analysis: measured versus calculated

- quantities. *Thin Solid Films* 1998;313–314:33–9.
219. Blaine Johs JAW, Herzinger CM, Hilfiker J. Overview of Variable Angle Spectroscopic Ellipsometry (VASE), Part II: Advanced Applications. In: Proceedings of a conference held. 1999. page 19.
220. Arwin H, Poksinski M, Johansen K. Total internal reflection ellipsometry: principles and applications. *Appl Opt* 2004;43(15):3028–36.
221. J.D. A. X-ray Photoelectron Spectroscopy (XPS). In: Andrade J.D. (eds) *Surface and Interfacial Aspects of Biomedical Polymers*. Springer, Boston, MA. 1985.
222. Alov N V. Fifty years of x-ray photoelectron spectroscopy. *J Anal Chem* 2005;60(3):297–300.
223. Blomfield CJ. Spatially resolved X-ray photoelectron spectroscopy. *J Electron Spectros Relat Phenomena* 2005;143(2-3 SPEC. ISS.):241–9.
224. XPS: Depth Profile | Covalent Metrology Analytical Labs [Internet]. [cited 2023 Jan 22]; Available from: <https://covalentmetrology.com/techniques/xps-depth-profile/>
225. X-Ray Photoelectron Spectroscopy | XPS Depth Profiling | Thermo Fisher Scientific - UK [Internet]. [cited 2023 Jan 22]; Available from: <https://www.thermofisher.com/uk/en/home/materials-science/learning-center/surface-analysis/monatomic-depth-profiling.html>
226. Behera S, Ghanty S, Ahmad F, Santra S, Banerjee S. UV-visible spectrophotometric method development and validation of assay of paracetamol tablet formulation. *J Anal Bioanal Tech* 2012;3(6):151–7.
227. Mäntele W, Deniz E. UV–VIS absorption spectroscopy: Lambert-Beer reloaded. *Spectrochim Acta - Part A Mol Biomol Spectrosc* [Internet] 2017;173:965–8. Available from: <http://dx.doi.org/10.1016/j.saa.2016.09.037>

228. Perkampus H. UV-VIS Spectroscopy and its Applications. 2013.
229. Abraham RJ, Rowan AE. Nuclear magnetic resonance spectroscopy of chlorophyll. 1991;
230. Hedley GJ, Ruseckas A, Samuel IDW. Light harvesting for organic photovoltaics. Chem Rev 2017;117(2):796–837.
231. Bardeen CJ. The structure and dynamics of molecular excitons. Annu Rev Phys Chem 2014;65:127–48.
232. Blankenship RE. Molecular Mechanisms of Photosynthesis. Wiley–Blackwell. 2014;
233. Shimokawa T, Smith WL. Essential histidines of prostaglandin endoperoxide synthase. His-309 is involved in heme binding. J Biol Chem 1991;266(10):6168–73.
234. Jia P, Kong D, Ebendorff-Heidepriem H. Flexible plasmonic tapes with nanohole and nanoparticle arrays for refractometric and strain sensing. ACS Appl Nano Mater 2020;3(8):8242–6.
235. Kishor R, Ghoshal AK. APTES grafted ordered mesoporous silica KIT-6 for CO₂ adsorption. Chem Eng J 2015;262:882–90.
236. Xu J, Wang C, Zhou S, Zhang R, Tian Y. Low-temperature direct bonding of Si and quartz glass using the APTES modification. Ceram Int 2019;45(13):16670–5.
237. Heinig MF, Bastos da Silva Fanta A, Wagner JB, Kadkhodazadeh S. Aminopropylsilatrane linkers for easy and fast fabrication of high-quality 10 nm thick gold films on SiO₂ substrates. ACS Appl Nano Mater 2020;3(5):4418–27.
238. Lichtenthaler HK, Buschmann C. Chlorophylls and carotenoids: Measurement and characterization by UV-VIS spectroscopy. Curr Protoc food Anal Chem 2001;1(1):F4-3.
239. Sims RA, Harmer SL, Quinton JS. The role of physisorption and chemisorption in the

oscillatory adsorption of organosilanes on aluminium oxide. *Polymers (Basel)* 2019;11(3):410.

240. Al-Ghouti MA, Da'ana DA. Guidelines for the use and interpretation of adsorption isotherm models: A review. *J Hazard Mater* 2020;393:122383.
241. Lishchuk A, Vasilev C, Johnson MP, Hunter CN, Törmä P, Leggett GJ. Turning the challenge of quantum biology on its head: biological control of quantum optical systems. *Faraday Discuss* 2019;216:57–71.
242. Wang P, Lin Z, Su X, Tang Z. Application of Au based nanomaterials in analytical science. *Nano Today* 2017;12:64–97.
243. Bhattacharya S, Narasimha S, Roy A, Banerjee S. Does shining light on Gold colloids Influence aggregation? *Sci Rep* 2014;4(1):1–5.
244. Kyaw HH, Al-Harhi SH, Sellai A, Dutta J. Self-organization of gold nanoparticles on silanated surfaces. *Beilstein J Nanotechnol* 2015;6(1):2345–53.
245. Scarpettini AF, Bragas A V. Coverage and aggregation of gold nanoparticles on silanized glasses. *Langmuir* 2010;26(20):15948–53.

